UNIVERSITY OF SOUTHAMPTON

FACULTY OF ENGINEERING AND THE ENVIRONMENT

NOISE GENERATION AND PROPAGATION WITHIN AN AIRCRAFT AIR DISTRIBUTION SYSTEM

by

Michael Sanderson

Thesis for the degree of Master of Philosophy

November 2015

UNIVERSITY OF SOUTHAMPTON

ABSTRACT

FACULTY OF ENGINEERING AND THE ENVIRONMENT

Master of Philosophy

NOISE GENERATION AND PROPAGATION WITHIN AN AIRCRAFT AIR DISTRIBUTION SYSTEM

by Michael Sanderson

The flow in an air distribution system is heavily affected by the wide range of complex components used to control the air. The complexity of the system inevitably leads to increased turbulence and interaction between flow over different components. The work presented in this thesis aims to provide improved understanding of the way in which these interactions occur and the effect that they have on the noise produced in the system. For this purpose, a series of simulations have been performed on a clean duct and ducts with single and double orifices using a Reynolds averaged Navier-Stokes turbulence model. These simulations allowed for an investigation of the velocity and turbulent kinetic energy fields within the duct and the effect of the separation distance of the orifice pairs to be quantified. Further work was conducted on a single orifice configuration, where the turbulence levels upstream of the orifice were controlled using a ring placed at varying separation distances from the orifice. The effect of the varying turbulence levels on the pressure fluctuations, turbulence and noise sources was investigated using large eddy simulation. The presence of additional upstream turbulence, produced by the ring, was seen to increase the turbulence levels and pressure fluctuations downstream of the orifice. The noise source was investigated for all separation distances between the ring and orifice and was found to be dominant in a region close to the upstream corner of the orifice on the upstream face. The propagation of both existing noise and the noise produced by the orifice were investigated in the plane wave range for a single orifice. In the first investigation, sound waves were introduced in the duct upstream and allowed to propagate through the orifice. Following this, idealised sound sources were placed on the surface of the orifice in a position corresponding to the previously identified dominant noise source. The upstream and downstream propagation of this source was then quantified and showed that the effect of the orifice causes a slight predominance of the propagation in the upstream direction, primarily at lower frequencies.

Table of Contents

List of Figures

List of Tables

Declaration of Authorship

I, Michael Sanderson, declare that the thesis entitled *Noise Generation and Propagation Within an Aircraft Air Distribution System* and the work presented in the thesis are both my own, and have been generated by me as the result of my own original research. I confirm that:

- this work was done wholly or mainly while in candidature for a research degree at this University;
- where any part of this thesis has previously been submitted for a degree or any other qualification at this University or any other institution, this has been clearly stated;
- where I have consulted the published work of others, this is always clearly attributed;
- where I have quoted from the work of others, the source is always given. With the exception of such quotations, this thesis is entirely my own work;
- I have acknowledged all main sources of help;
- where the thesis is based on work done by myself jointly with others, I have made clear exactly what was done by others and what I have contributed myself;

Signed:

Date:

Acknowledgements

There are many people that have helped and supported me throughout my period of study. Foremost, i would like to thank my supervisory team, Professor Xin Zhang, Dr Zhiwei Hu and Dr Edward Peers for their fantastic technical help and encouragement through the hard times. I would also like to thank Dr Prithiraj Bissessur for his support and advice throughout my project.

I would like to thank my friends from the ANTC: Ryu, James and Toni for their help over the years, not matter how trivial the question, and all those others that I had the pleasure of sharing an office and muffin mornings with.

The unconditional support from my family and my wonderful girlfriend Malin has been invaluable to me. They have seen me at my best and worst as part of this study and I know I wasn't always the easiest person to live with.

Finally, I would like to acknowledge the financial support for this project from the Engineering and Physical Sciences Research Council (EPSRC) and Airbus U.K, without which this work would not have been possible. I would like to acknowledge my use of the IRIDIS high performance computing facility at the University of Southampton in enabling me to realise the great number of simulations undertaken in this project.

Nomenclature

A	Duct cross sectional area	$[\mathrm{m}^2]$
A_o	Orifice area	$[\mathrm{m}^2]$
a	Speed of sound in air	$[\mathrm{m.s}^{-1}]$
B	Separation distance between orifices	[.]
B_{ij}	Subgrid stress tensor	$[\mathrm{kg.m}^{-1}.\mathrm{s}^{-2}]$
C	Coefficient of discharge	[.]
C_D	Coefficient of drag	[.]
C_{DES}	Constant in DES turbulence model	[.]
C_k	Universal constant in the turbulent energy spectrum	[.]
C_p	Coefficient of pressure	[.]
C'_s	Dynamic Smagorinsky coefficient	[.]
C_s	Smagorinsky coefficient	[.]
D	Duct diameter	[m]
d	Orifice diameter	[m]
d_i	Ring internal diameter	[m]
d_o	Ring external diameter	[m]
d_w	Distance to wall	[m]
E	Turbulent kinetic energy spectrum	$[\mathrm{kg.m}^2.\mathrm{s}^{-2}]$
e_0	Total energy per unit mass	$[\mathrm{m}^2.\mathrm{s}^{-2}]$
F_i	Dipole term in FW-H equation	[.]
F_τ	Force generated by a fluctuating wall shear stress	$[\mathrm{kg.m.s}^{-2}]$
f	Frequency	[Hz]
f_c	Mode cut-off frequency	[Hz]
f_f	Friction factor	[.]
f_s	Function to define the surface of a solid body	[.]
G	LES filter function	[.]
$\widetilde{H}$	Heaviside operator	[.]
h	Radial height of the orifice	[m]
h_x, h_y, h_z	Cell length scale in the x, y and z directions, respectively.	[m]
$h_{\max}$	Maximum of x, y and z cell length scale.	[m]
h_{wn}	Cell length scale in wall normal direction.	[m]
I	Acoustic intensity	$[\mathrm{kg.s}^{-3}]$

J'_m	Derivative of Bessel Function	[.]
J_m	Bessel Function	[.]
j'_m	Roots of derivative of Bessel Function	[.]
K	Flow coefficient	[.]
K_h	Heat conductivity	[kg.m.s^{-3}.K^{-1}]
k	Turbulent kinetic energy	[m^2.s^{-2}]
L	Duct length	[m]
L_c	Characteristic length scale	[m]
L_x	Development length for duct flow	[m]
$\mathbf{L}$	Lamb vector	[m.s^{-2}]
l	Turbulence length scale	[m]
M	Mach number	[.]
$\dot{m}$	Mass flow rate	[kg.s^{-1}]
m	Circumferential wavenumber (equal to k_θ)	[m^{-1}]
n	Radial wavenumber	[.]
n_i	Normal vector components	[.]
P_A	Acoustic power	[kg.m^2.s^{-3}]
P_{ij}	Compressive stress tensor	[kg.m^{-1}.s^{-2}]
P_s	Surface component of acoustic power	[kg.m^2.s^{-3}]
P_v	Volume component of acoustic power	[kg.m^2.s^{-3}]
p	Pressure	[kg.m^{-1}.s^{-2}]
p_θ	Circumferential component of the acoustic pressure	[kg.m^{-1}.s^{-2}]
p_r	Radial component of the acoustic pressure	[kg.m^{-1}.s^{-2}]
p_s	Surface acoustic sources	[kg.s^{-3}]
p_v	Volume acoustic sources	[kg.s^{-3}]
p_z	Streamwise component of the acoustic pressure	[kg.m^{-1}.s^{-2}]
Q	Positive second invariant of the velocity gradient tensor	[s^{-2}]
Q_{C}	Source term of Curle's analogy	[s^{-2}]
Q_{PH}	Source term of Powell's analogy	[s^{-2}]
q_i	Heat flux components	[m^2.s^{-3}]
R	Duct radius	[m]
R_{gas}	Specific gas constant	[m]
Re_D	Reynolds number based on duct diameter	[.]
Re_{cell}	Cell Reynolds number	[.]
Re_t	Turbulent Reynolds number	[.]
r, θ, z	Components of cylindrical coordinate system	[m, deg, m]
r_f	Separation distance in the filter function	[m]
S	Surface area	[m^2]
S_{ij}	Mean rate of strain tensor	[m^2]
St	Strouhal number	[.]
T	Absolute temperature	[K]

T_D	Time scale based on the duct diameter and bulk velocity	[s]
T_{ij}	Lighthill stress tensor	[.]
t	Time	[s]
t^*	Retarded time	[s]
t_a	Non-dimensional time scale based on the speed of sound and an arbitrary 1m length scale	[.]
t_o	Orifice thickness	[m]
t_r	Ring thickness	[m]
$\mathbf{u}$	Velocity vector	[m.s^{-1}]
u, v, w	Velocity components of u_i in x, y and z directions, respectively	[m.s^{-1}]
u_∞	Bulk velocity	[m.s^{-1}]
u_c	Characteristic velocity scale	[m.s^{-1}]
u_n	Normal component of velocity to a solid surface	[m.s^{-1}]
u_τ	Friction velocity	[m.s^{-1}]
u_{ij}	Velocity gradients	[s^{-1}]
V	Volume	[m^3]
v_i	Source velocity components	[m.s^{-1}]
W	Width of the buffer zone	[m]
$\mathbf{x}$	Observer position vector	[m]
x, y, z	Cartesian components of co-ordinate system, x_i	[m]
x_R	Streamwise reattachment location	[m]
x_s	Orifice surface coordinate	[m]
$\mathbf{y}$	Source position vector	[m]
y^+	Non-Dimensional wall distance	[.]

Greek symbols

α_{mn}	Zeros of the derivative of the Bessel function	[.]
β	Constant for the shape of the buffer zone damping function	[.]
γ	Ratio of specific heats	[.]
$\ddot{\Delta}$	Redefined LES filter width for dynamic model	[m]
Δ	Sub-grid length scale	[m]
$\widehat{\Delta}$	LES filter width	[m]
δ	Boundary layer thickness	[m]
δ_{ij}	Kronecker delta function	[.]
ε	Turbulence dissipation rate	[m^{2}s^{-3}]
κ	Wavenumber	[m^{-1}]
κ_c	Filter cut-off wavenumber	[m^{-1}]
κ_r	Radial wavenumber	[m^{-1}]
κ_v	Von Kármán constant	[.]
κ_z	Axial wavenumber	[m^{-1}]
κ_{zmn}	Axial wavenumber of the mn mode	[m^{-1}]
κ_θ	Circumferential wavenumber (equal to m)	[m^{-1}]

λ	Wavelength	[.]
μ	Coefficient of dynamic viscosity	[kg.m^{-1}.s^{-1}]
μ_{mn}	Eigenvalues of the derivative of the Bessel function	[.]
μ_t	Dynamic turbulent viscosity	[kg.m^{-1}.s^{-1}]
ν	Coefficient of kinematic viscosity	[m^2.s^{-1}]
ν_{sgs}	SGS eddy viscosity	[m^2.s^{-1}]
ν_t	Kinematic turbulent viscosity	[m^2.s^{-1}]
$\widetilde{\nu}$	Transported variable in the Spalart-Allmaras model	[m^2.s^{-1}]
ρ	Density	[kg.m^{-3}]
σ	Damping coefficient used in the buffer zone damping function	[.]
$\sigma_{\max}$	Constant for the strength of the buffer zone damping function	[.]
σ_{ij}	Viscous stress tensor	[kg.m^{-1}.s^{-2}]
τ_{sgs}	SGS stress tensor	[kg.m^{-1}.s^{-2}]
τ_w	Wall shear stress	[kg.m^{-1}.s^{-2}]
Ψ	Low Reynolds number correction term	[.]
ψ	Rate of energy dissipation per unit volume	[kg.m^{-1}.s^{-2}]
$\mathbf{\Omega}$	Vorticity vector	[s^{-1}]
ω	Specific turbulence dissipation rate	[s^{-1}]

Overbar symbols

$\dddot{\cdot}$	Filtered quantity from dynamic Smagorinsky model
$\bar{\cdot}$	Time averaged quantity
$\hat{\cdot}$	Filtered quantity
$\widetilde{\cdot}$	Favre weighting of a time averaged or filtered quantity

Subscripts

cell	Cell value
i, j, k	Subscript for Cartesian co-ordinate system
rms	Root mean squared value
max	Maximum value
∞	Freestream value

Superscripts

$'$	Fluctuating component of the quantity
$''$	Density weighted fluctuating component of the quantity
$'''$	Residual fluctuating component of the quantity

Mathematical symbols

$\mathcal{L}_{ij}$	Resolvable stress tensor	[kg.m^{-1}.s^{-2}]
∇	Vector differential operator	[.]

Abbreviations

1-D	One Dimensional

2-D	Two Dimensional
3-D	Three Dimensional
ADS	Air Distribution System
AMG	Algebraic MultiGrid method
BFS	Backward Facing Step
CAA	Computational AeroAcoustics
CADWIE	Control of Approach Drag Without Impact on the Environment
CFD	Computational Fluid Dynamics
CFL	Courant-Friedrichs-Lewy condition
CPU	Central Processing Unit
CTU	Convective Time Unit
DDES	Delayed Detached Eddy Simulation
DES	Detached Eddy Simulation
DES97	Original Detached Eddy Simulation formulation from 1997 [8]
DNS	Direct Numerical Simulation
FFT	Fast Fourier Transform
FW-H	Ffowcs Williams-Hawkings
GIS	Grid Induced Separation
HWA	Hot Wire Anemometry
IDDES	Improved Delayed Detached Eddy Simulation
LAGOON	Landing Gear nOise database and CAA validatiON
LEE	Linearised Euler Equation
LES	Large Eddy Simulation
LLM	Log Layer Mismatch
LNS	Linearised Navier-Stokes Equation
MSD	Modelled Stress Depletion
N-S	Navier-Stokes
PBC	Periodic Boundary Conditions
PDE	Partial Differential Equation
PIMPLE	Merged PISO-SIMPLE solution algorithm
PPW	Points Per Wavelength
PSD	Power Spectral Density
RANS	Reynolds Averaged Navier-Stokes
S-A	Spalart-Allmaras turbulence model
SGS	Subgrid Scale Model
SPL	Sound Pressure Level
TI	Turbulence Intensity
TKE	Turbulent Kinetic Energy
TPP	Timesteps Per Period
URANS	Unsteady Reynolds Averaged Navier-Stokes
WMLES	Wall modelled Large Eddy Simulation

Chapter 1

Introduction

1.1 Background and motivation

In the vicinity of the world's major airports, there is a conflict between the needs of the local residents and the needs of the aircraft operators. The noise produced by aircraft at these airports is a topic of discussion and has been for many years. Significant progress has been made in reducing the noise pollution of modern aircraft [9], however, much still remains to be done and this fact is well recognised by the aerospace community. Self-imposed goals have set targets on the reduction of air pollution and noise emissions in the future and are regularly updated as progress is made [10, 11]. The current driving goals have set a target of a reduction of 65% in the noise radiated by aircraft close to airports by the year 2050, when compared to the relative noise in 2000.

With air travel becoming an ever more commonly used method of transport, there is also a desire to make the passenger experience as comfortable as possible. Following large reductions in engine noise, through the development of the turbofan engine, the application of high bypass ducts and serrated nozzles, one of the current focuses for this improvement is in interior noise reduction. One of the primary sources of cabin noise is the air distribution system (ADS), which, whilst required for ventilation, can also be a source of annoyance for passengers. The ADS is responsible for controlling the aircraft environment, through air-conditioning and pressurization of the cabin. It is a complex system comprised of many modules, which must be capable of providing equal air distribution throughout the cabin, despite varying distances to the air supply unit. There are three main components which make up an ADS; the mixing unit, ducting system and the air-outlet assemblies into the cabin area. A schematic of the ADS system within the front part of a two deck aircraft is shown in Figure 1.1.

Noise within the ADS comes from two primary sources. The first of these is the driving machinery, such as the motors and compressors, which will produce and radiate noise throughout the duct system. All of the components within the ducting will influence the sound propagation via scattering (reflection, transmission and damping of acoustic

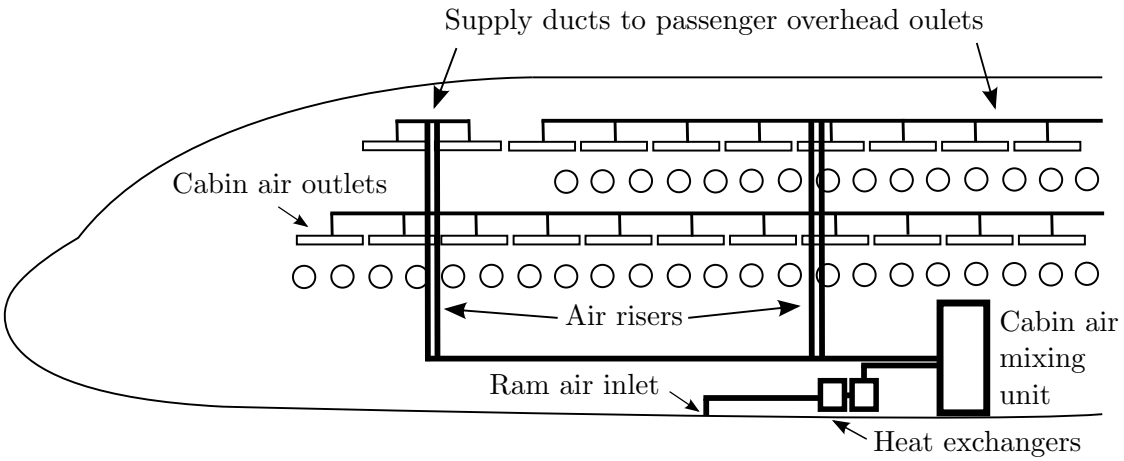

Figure 1.1: Schematics of the ADS in the front part of the aircraft for a two deck aircraft.

waves), an effect known as the passive acoustic properties of the component. The second source of noise is flow generated noise. This is caused by the bluff body components, such as de/humidifiers, straighteners, silencers and orifices (see Figure 1.3) producing acoustic waves through interaction with the air flowing through the ducting. The noise produced by these sources is known to vary greatly when interacting with the wake shed from other components upstream.

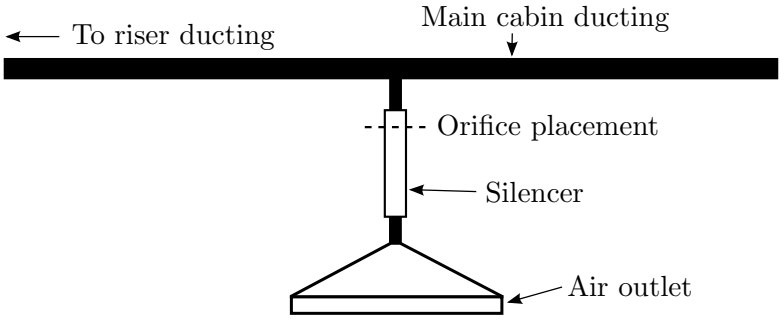

Figure 1.2: Schematics of two typical orifice designs used within an aircraft ADS.

One of the critical components within the ADS, and one of the most widely studied is the flow orifice. This is a simple device, with the primary purpose of providing a reduction in pressure within a section of ducting, in order to adjust the mass flow rate to each air outlet (other uses may be as a flow rate meter or a device to restrict flow). An orifice provides a temporary constriction in the ducting, resulting in an increased flow velocity and a reduction in pressure. Within an ADS, orifices will be placed at junctions, where it is desired that the flow is split to direct air around the cabin, see Figure 1.2. In a well designed ADS, the orifices will ensure that the same volumetric flow rate of air will reach all passengers, regardless of their seating position relative to the mixing unit. The positioning of the orifice within the ADS tends to be close to the air outlets into the cabin, and therefore, close to passengers. Due to installation constraints, it may not always be possible to reduce the noise sufficiently using a silencer and this can lead to increased noise levels within the cabin.

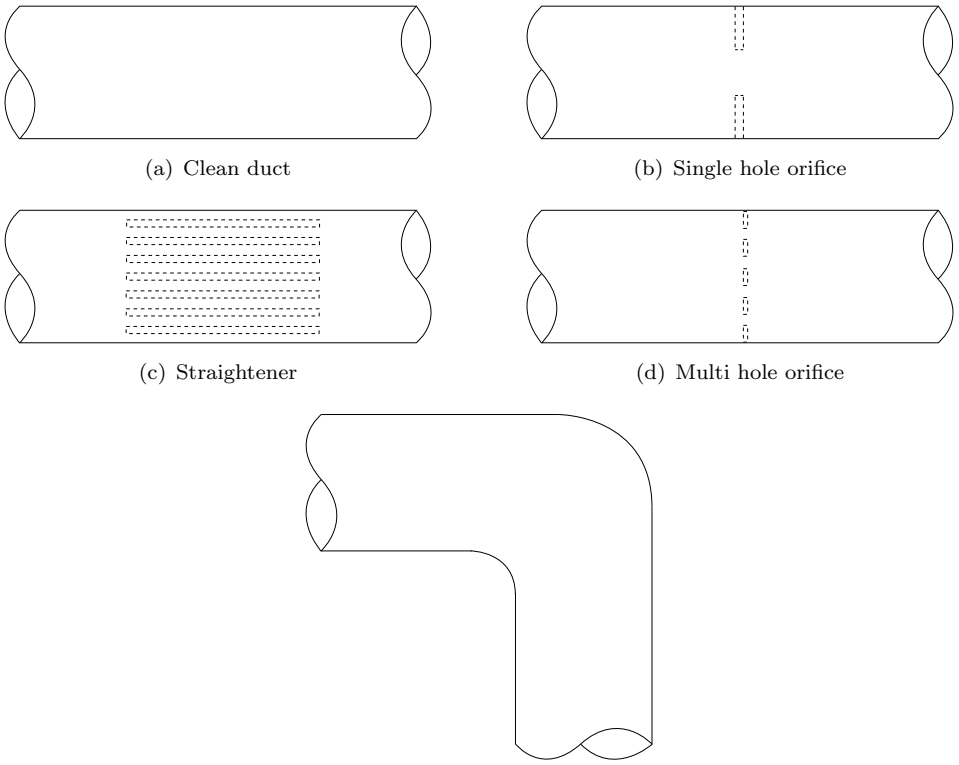

(a) Clean duct

(b) Single hole orifice

(c) Straightener

(d) Multi hole orifice

(e) Bend

Figure 1.3: Schematics of typical components within an aircraft ADS.

In an effort to improve cabin acoustics, analytical, experimental and numerical approaches have been previously used to investigate the acoustic properties of an ADS. In industry, the most commonly utilised methods of noise prediction are empirical and semi-empirical models, which can provide fast and relatively accurate results, when the flow conditions and geometries are similar to those from which the models were developed. However, these methods face difficulties when a highly turbulent incoming flow is present. Despite some semi-empirical methods providing accurate results in uniform steady flows, there can be a under-prediction of up to 20dB in the predicted noise levels, when a highly turbulent incoming flow interacts with in-duct components. Currently, there is no cost-effective method for predicting the noise of a full ADS when subjected to varying levels of incoming turbulence [12].

1.2 Research objectives

In order to reduce the noise produced by and propagated through an aircraft ADS, it is important to understand the acoustic properties of the components within the system. The aim of this work is to establish a better understanding of how turbulence and noise interact with in-duct components of an ADS. This will include a fundamental investigation of the physical mechanisms governing the noise generated by an orifice in a clean flow and the mechanisms governing the additional noise produced when a turbulent

incoming flow is present. The foundation for the improvement of our understanding is numerical simulations, which provide a valuable tool for giving an insight into the flow and noise generation mechanisms, even in areas where it is difficult to perform experimental measurements. Specifically, the work in this thesis can be broken down into the following sections:

- Initial case studies are performed on clean duct, single orifice and double orifice configurations. An unsteady Reynolds averaged Navier-Stokes (RANS) solver is used to estimated the velocity and turbulent kinetic energy field in the wake of components. The separation distance between orifices in the double orifice configuration is varied, and the effect of this is quantified in terms of the turbulence field in-between and in the wake of the orifices.
- Investigations into the noise generated by a single orifice plate with a clean inflow and varying incoming turbulence levels. The noise generation mechanism of the orifice self noise (the mechanisms with no incoming turbulence) is identified. The turbulence levels upstream of the orifice are varied using a turbulence generating physical body, which allows for the noise generation mechanism from the additional turbulence to be identified.
- Noise propagation studies of the noise sources identified on the surface of the orifice have been conducted using a linearised Euler Equations solver. The sound sources are idealised as monopole and dipole sources placed onto the orifice faces and the upstream and downstream propagation is quantified.
- Noise propagation studies have also been conducted to determine the passive acoustic properties of the single orifice configuration. This investigation analyses the transmission and reflection of various frequency downstream propagating plane waves by orifices of varying internal diameter. Furthermore, the effect of mean flow, wave amplitude and orifice thickness have been quantified.

1.3 Main contributions

The contributions from this work are as follows:

- Investigation of the effect of varying separation distances, between ADS components, on the turbulence levels and turbulence generated sound sources within the duct. Identification of the critical separation distances for maximum production of turbulence.
- Application of Curle's analogy to the solid surfaces of an orifice geometry in a fully developed duct flow in order to identify the source distribution of the orifice self noise. Estimated the relative strength of the sound sources on different parts of the orifice face and the duct walls.

- Systematic investigation into the effects of varying levels of additional turbulence on the noise generation by a ducted orifice. Upstream turbulence levels are quantified, using the turbulence intensity and length scales, and linked to the noise produced by the orifice. Curle's analogy is applied to the solid surfaces of the orifice geometry to identify the source distribution of the additional noise produced by turbulence.
- Propagation of orifice noise sources is studied using idealised sound sources placed onto the face of the orifice. Propagation is characterised in terms of the frequency of the source on the face.

1.4 Thesis outline

This thesis is organised as follows: Firstly, an extensive literature review is provided in Chapter 2. This includes a review of duct flows, orifice flows and jet flows and the governing equations of fluid motion and sound generation. The literature review is followed by a description of the computational methodology and numerical methods associated with flow and turbulence modelling in Chapter 3. A brief overview of the experimental data used for validation is also presented. Chapter 4 details simulations of the interactions between components of an ADS and the effect this has on the velocity, turbulence and sound fields near to the components. Chapter 5 details simulations of the noise generated by a single orifice encountering varying levels of incoming turbulence. Chapter 6 focuses on high-order computations of the scattering of sound by the orifice. This includes an investigation of the propagation of sound sources from the orifice faces and of downstream travelling sound waves introduced upstream of the orifice. Finally, conclusions are drawn and future work is suggested in Chapter 7.

Chapter 2

Literature Review

2.1 Introduction

In this chapter, a comprehensive literature review, relevant to the current research topic, is presented. This includes a discussion of the previous work into duct flows, free and confined jets, and orifice sound generation and propagation. A critical review of turbulence generation methods is also presented.

2.2 Duct flow

A pipe which is free of obstructions represents a relatively simple aerodynamic flow. For flow entering a pipe, either after an obstruction or from another component, there is a region where the flow develops from its initial state, to a fully developed flow profile. This distance is known as the entrance length and is depicted schematically in Figure 2.1. As the flow moves through the pipe, viscous effects cause the mean velocity profile to change with streamwise distance, until the boundary layer has grown to fill the pipe, where the flow is deemed to be fully developed. At this point, the mean flow properties are independent of the streamwise location. The typical entrance length for a turbulent duct flow is approximated by [13]:

$$\frac{L_x}{D} = 4.4 Re_D^{\frac{1}{6}} \tag{2.1}$$

where L_x is the streamwise distance at which the flow becomes fully developed, D is the duct diameter and Re_D is the Reynolds number based on the duct diameter. The requirement for fully developed flow is important in many analytical and semi-empirical models for the aerodynamic and acoustic fields within a duct flow [14, 15].

The friction between the flow and the walls causes a loss of the kinetic energy of the flow and induces a pressure drop along a section of duct. The theoretical pressure drop

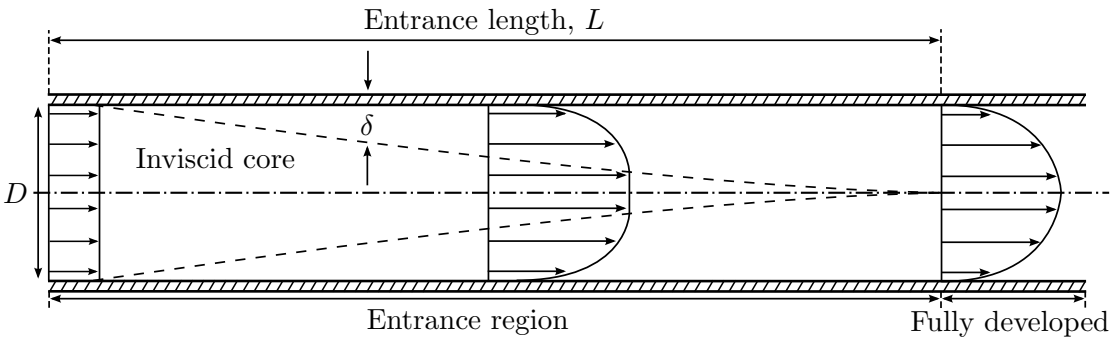

Figure 2.1: Schematic showing the development of the flow along the streamwise length of the duct, from uniform flow at the inlet to its fully developed state.

through a clean pipe containing a fully developed incompressible flow can be calculated using the friction factor estimated from a Moody's chart [16]:

$$\Delta p = \frac{\rho_\infty f_f L u_\infty^2}{2D} \tag{2.2}$$

where Δp is the total pressure drop, ρ_∞ is the upstream mean density of the fluid, f_f is the friction factor which depends on Re_D, L is the length of the duct, u_∞ is the bulk fluid velocity and D is the duct diameter.

2.3 Axisymmetric free jets

Jet flows have been extensively studied both experimentally and theoretically. This type of flow has applications in a wide range of industrial systems including combustion, jet propulsion and cooling systems. The following section provides a brief overview of the main characteristics of free axisymmetric jet flows.

An axisymmetric jet is produced when a fluid passes through a circular nozzle into an external fluid which can either be stationary (like in jet engine flow) or co-flowing (like a co-flowing exhaust pipe in a river). At the exit of the contraction, the jet forms a high velocity core, separated from the ambient fluid by a thin axisymmetric shear layer. Initially, nozzle jets have a top hat velocity profile which develops with downstream distance. The thin shear layers which are present in the top hat jet profile flows (approximately 5% of the jet diameter [17]) are unstable to incoming perturbations of any azimuthal mode number and wave number [18], which grow exponentially due to the Kelvin-Helmholtz instability process (caused by the presence of an inflectional point in the mean streamwise velocity distribution). From this process, large scale vortical structures are formed within the shear layer, which merge together as the jet travels further downstream. The shape and characteristics of these structures are heavily dependent on the initial disturbances. It has been seen that the initial disturbance level has a strong effect on the development of the mean jet characteristics, while the initial shear layer thickness shows a weaker effect [19, 20]. It has also been shown that transitional shear

layers, as opposed to fully turbulent shear layers, result in higher amplitude, organised disturbances close to the nozzle exit [21]. This is caused by a larger amplification of the the axisymmetric disturbances, giving rise to quasi-periodically spaced, axisymmetric rings of concentrated vorticity.

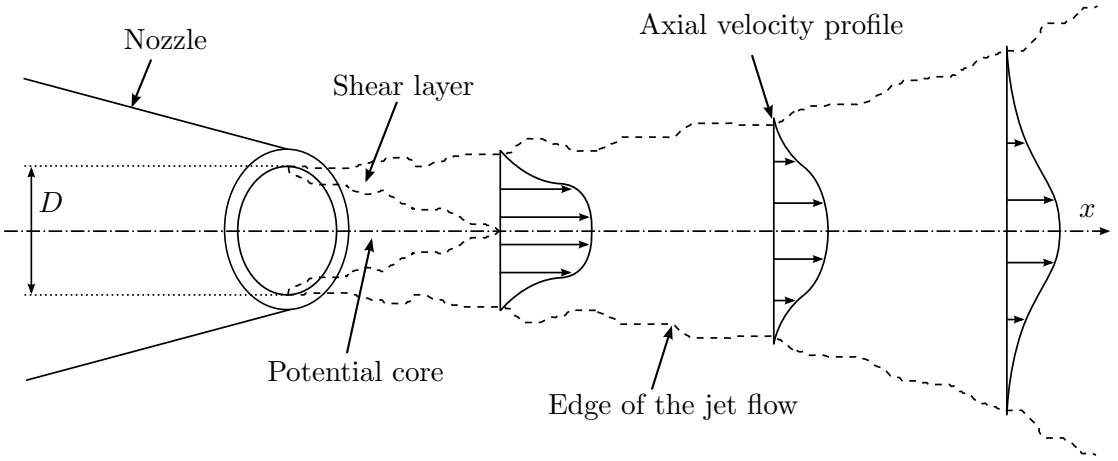

Figure 2.2: Schematic representation of the development of a jet from an axisymmetric nozzle.

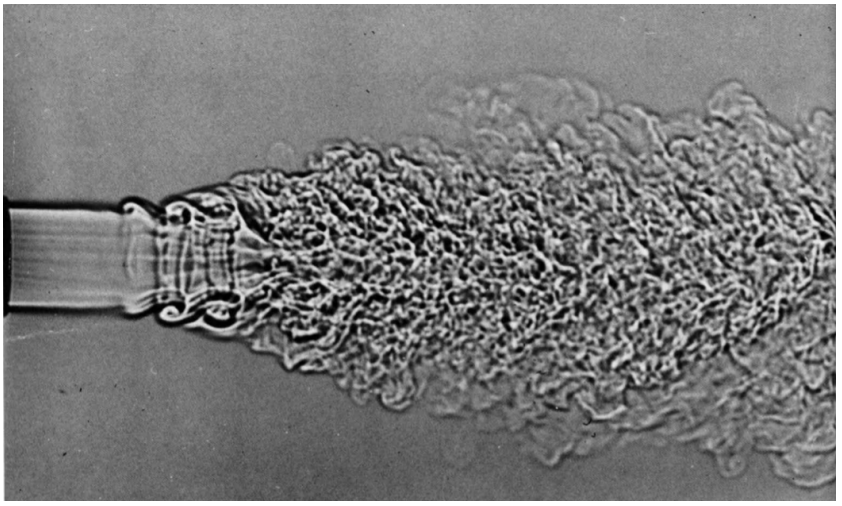

Figure 2.3: Shadowgraph image of the instability of a round jet. One diameter downstream of the nozzle exit, the image shows instability of the shear layer, the formation of vortex rings and the transition to turbulence. Image taken from Landis and Shapiro [1].

The merging of vortical structures within the shear layer results in a significant growth of the shear layer thickness in the radial direction, both towards the outside and towards the centreline of the jet. The growth means that the shear layer reaches the jet axis at a distance of approximately 4-5 diameters from the nozzle exit, see Figures 2.2 and 2.3. The region inside the axisymmetric shear layer is called the jet potential core and is characterised by an unchanged axial velocity.

The preferred mode of a jet is defined as the vortex passage frequency at the end of the

potential core. This mode can be described by its non dimensional frequency (Strouhal number), $St = fD/u_\infty$, where f is the frequency, D is the nozzle diameter and the u_∞ is the bulk velocity at the jet exit. Experimental data in literature places this over quite a broad range ($0.25 < St < 0.85$), which can be attributed to the variation of the initial shear layer instability frequency [22], upstream noise coming from the experimental set-up, which may cause a wide range of frequencies to be highly amplified [23], and to the importance of measurement location [24].

Further downstream, in the intermediate region of the jet, the large scale coherent structures interact with each other. Eddy structures within the shear layers engulf fluid from the external environment and increase the entrainment activity [25]. As the flow approaches the end of the potential core, the helical instability becomes increasingly important and dominates within the fully developed region [26]. This is in contrast to the initial region, where for the first 2-3 jet diameters downstream, the axisymmetric modes are dominant [27, 28] and the two modes are seldom seen to coexist. As the axial distance increases, the helical structures moves radially outwards [25] and increase the jet spreading due to local ejection of turbulent fluid and bulk entrainment of the ambient fluid.

In the fully turbulent region, after approximately 20 diameters downstream from the nozzle exit, the mean velocity profiles exhibit a self-preserving behaviour. The width of the jet increases linearly with streamwise coordinate and, due to conservation of axial momentum, the velocity along the jet centreline decays as x^{-1}. However, the turbulence intensity profiles require a much larger downstream distance before reaching the self-preserving state, which is especially true of the radial and tangential fluctuations. This can be explained by considering that energy is directly transferred from the mean flow to the streamwise fluctuations, whereas the transfer of energy to the other components occurs through the pressure-strain terms [23]. This means that it can take around 50-70 diameters for the jet to truly be considered self-preserving. The process described above holds for both laminar and turbulent jet flows.

In axisymmetric free jet flows, the production of sound is governed by turbulent fluctuations. When the initial shear layer emanating from the nozzle is laminar, a significant proportion of the sound spectra is generated by the pairing of vortices within the shear layer [29, 30]. When the turbulence intensity within the initial shear layer is increased, the vortex pairing noise is seen to be reduced [29, 31]. The same effect is seen for a thicker shear layer [32]. At low Reynolds numbers, jet noise is seen to be dominated by tones within the spectra, however, as the Reynolds number is increased, the broadband noise from turbulence is seen to drown out the fundamental jet tone and its harmonics [33].

2.4 Aerodynamics and acoustics of orifice plates

Orifices find many uses within industrial applications, including flow rate measurement, pressure reduction and flow restriction. When utilised in an ADS, the primary function of an orifice plate is to control the pressure within a section of the ADS. An orifice plate consists of a thin plate with an opening through which a fluid may flow. There are two common sharp edged circular orifice designs; single hole and multi-hole as shown in Figure 2.4. In the case of the single hole orifice, the opening is usually concentric with the outer ducting.

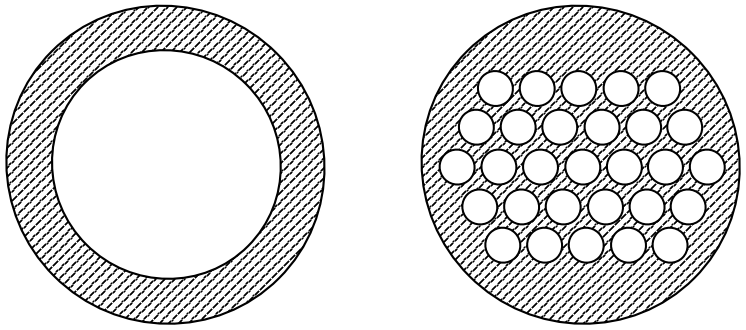

(a) Single hole orifice (b) Multiple hole orifice

Figure 2.4: Schematics of two typical orifice designs used within an aircraft ADS.

2.4.1 Orifice jets and confined jets

When a fluid approaches the opening of an orifice, the pressure is increased slightly upstream of the plate. As it accelerates to pass through the reduced area of the orifice, the pressure decreases and a jet flow appears. The pressure of the fluid downstream of the orifice is decreased. The jet reaches its minimum diameter at a small distance downstream of the opening, known as the vena-contracta. The location of the maximum velocity falls at $x/h \approx 2.9$ (where h is the radial height of the orifice, taken as $\frac{D-d}{2}$), after which the centreline velocity sees a local minima at approximately $x/h = 59$ [7].

The jet flow and development of the shear layers within an orifice flow show differences to that of a nozzle flow. Firstly, the initial velocity profile within an orifice flow is saddle-back, rather than the top-hat profiles noted in nozzle flows. Furthermore, the shear layers are seen to be thinner than in a nozzle jet. Coherent structures have been identified in all previous orifice jet studies. These structures were shown to have a higher energy content in the orifice jet [34], but be less well defined [35]. The shape of the structures was found to be similar, although the orifice jet had a higher degree of three dimensionality, which was attributed to the separation from the sharp edge of the orifice and due to the thinner shear layer which is less stable. For an orifice jet, it was found that higher initial turbulence intensity levels reduced the strength and occurrence of the coherent structures [35].

A confined jet, such as a ducted orifice jet, displays a number of critical differences to that of a free orifice jet. The primary difference is that the length scale of a confined jet, increases with downstream distance until the geometry prevents any further spreading. From this point, the jet length scale is fixed to the size of the confinement [36]. Secondly, contrary to the convective instability of a free jet, confined jets often exhibit periodic oscillatory patterns, due to the high sensitivity of shear layers to incoming disturbances. This can lead to strong self-sustained oscillations for impinging shear layers and jets.

2.4.2 Orifice aerodynamic flow features

The flow through an orifice is characterised by regions of separated flow both upstream and downstream of the plate as shown in Figure 2.5. Upstream of the orifice, divergence from the fully developed mean profile is seen at distances of less than x/D = -1.84, with a fully developed profile still being present at x/D = -3.77 [7]. Upstream separation is located at approximately $x/h \approx$ -0.46. Downstream of the orifice, the jet is seen to reattach at $x/h \approx$ 10 - 11.4 [7, 37–39]. Secondary separation is also seen on the rear face of the orifice, where the reattachment point is located at $x/h \approx 1.94$. The location of these separation and reattachment points are weakly dependent of the velocity of the flow. The maximum backflow velocity is seen at a location of $x \approx x_R/2$ (with x_R being the primary recirculation length) where values approach 30% of the centreline velocity.

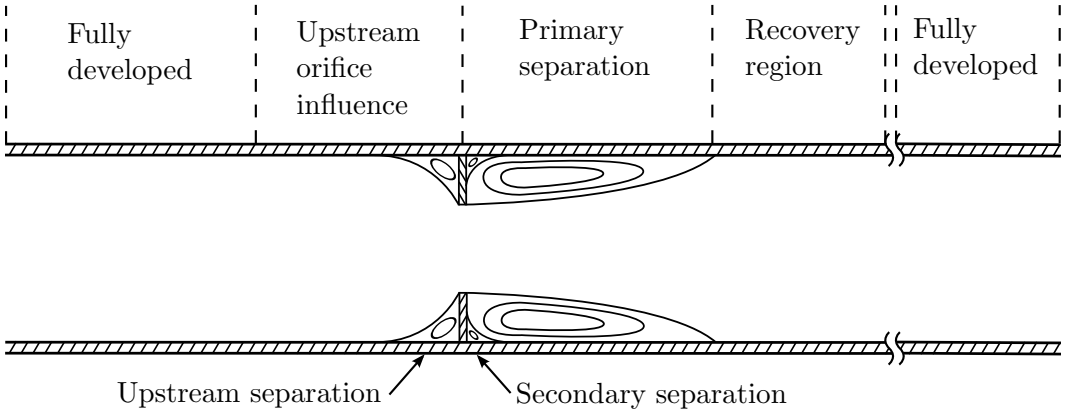

Figure 2.5: Schematic of the typical flow features found in orifice flows.

At downstream distances greater than the reattachment length, the mean velocity profiles show the mass flow displacing towards the centreline, followed by a displacement towards the wall and finally approaching the fully developed profiles by x/D = 48.96. The variation of mass flow distribution along the axial direction follows the changes in the radial centrifugal force to which the fluid is subjected, which is caused by the reversal in streamline curvature between points upstream and downstream of the reattachment point [7].

Further downstream of this point, the velocity continues to drop and the pressure within the ducting continues to increase. The differential in pressure across the orifice is proportional to the square of the velocity and is derived from Bernoullis equation by assuming a steady, incompressible flow with no losses:

$$\dot{m} = KA_o\sqrt{2\rho_\infty(p_1 - p_2)} \tag{2.3}$$

where $\dot{m}$ is the mass flow rate, A_o is the orifice area, ρ_∞ is the mean upstream fluid density and p_1 and p_2 are the upstream and downstream static pressures, respectively. In reality, there is a permanent pressure drop across an orifice, caused by frictional and turbulence losses within the fluid. The losses vary with the Reynolds number and are accounted for using a flow coefficient, K:

$$K = \frac{C}{\sqrt{1 - \left(\frac{d}{D}\right)^4}} \tag{2.4}$$

where C is the coefficient of discharge, relating the actual mass flow rate to that of an ideal nozzle, which expands an identical fluid from the same initial conditions to the same exit conditions. For orifices at relatively high Reynolds numbers, the coefficient of discharge is seen to converge to approximately 0.59-0.62 [40].

2.4.3 Orifice sound generation

The acoustic field created by a ducted orifice geometry is a complex interaction between the flow generated in the nearfield of the orifice and the interaction of the wake with the surrounding walls. The sound power radiated by an orifice is seen to be a function of the internal diameter of the orifice and the Mach number [41]. Holmgren [41] found that the relationship between the sound power and the internal orifice diameter scaled between $u_i^{4.5}$ - $u_i^{7.5}$, which reflects the different relative strengths of the sound sources based on the internal orifice diameter.

There is some debate over the dominant noise generation mechanism for a ducted orifice, however, all previous work does agree that the noise generation is of dipole type, suggesting that there are mechanisms which exert unsteady forces on the walls and play a major role in the noise generation [14, 42]. There have been proposals of two main mechanisms for generating noise from an orifice geometry. The first of these, suggests that the unsteady forces on the orifice itself is the primary cause of the noise generation. From Curle's theory, it is known that the strength of a dipole is related to the fluctuating force acting on the solid body. However, as it is difficult to measure the fluctuating force experimentally, the assumption is often made that the fluctuating force is proportional to the steady force and hence the pressure drop across the component.

Using the above assumptions, Ribner [43] estimated the sound power radiated from an unsteady force field induced by a solid body in a flow field by relating the acoustic power to the steady hydrodynamic force. Gordon [15, 44] was able to make use of this relationship, by obtaining the characteristic frequency of the unsteady force on a spoiler and orifice by measuring the flow speed near in-duct elements and the thickness of the wake induced by the elements. It was observed that when a spoiler was inserted into the duct that the broadband noise radiated from the exit plane was increased. Furthermore, the sound power was seen to change from a u_i^8 law, to a u_i^6 law with the presence of the solid body. The source location for this additional noise was noted to be on or near to the spoiler. It was also observed that the total sound power generated by the spoiler could be related to ∇p^3 and this relation held for a range of spoiler geometries. The close proximity of the spoiler to the exit plane of the duct does however limit this relation to cases where the downstream pressure can be assumed atmospheric.

Nelson and Morfey [14] also investigated the flow induced noise of a rectangular duct with spoiler using the pressure drop method. In this experimental setup, the spoiler was placed far from the end of the duct. The spoiler and the turbulence it produced were modelled as a distribution of dipole sources, the strength of which was determined using the fluctuating force acting on the spoiler. The fluctuating force was estimated from the steady drag force expressed in terms of the drag coefficient, which was a function of the pressure drop. The sound power was seen to vary with u_i^4 - u_i^6 depending on the cut-on frequencies of the modes. This change of power law value across the frequencies shows similarities to the properties noted by Davies and Ffowcs-Williams [45], although the values are different, due to the assumptions of dipoles and quadrupoles, respectively.

The work of Nelson and Morfey has been extended to include other in-duct components where the sound generation mechanism is similar. Oldham and Ukpoho [46] noted that if the open area ratio and the characteristic dimension of the components were input to Nelson and Morfey's model, the method was capable for predicting flow induced noise from all kinds of duct elements. In general though, the collapse is seen to be quite poor; within 20dB at low frequencies and only slightly improved at high frequencies.

A limited number of attempts have been made to link the unsteady forces on the face of the orifice to the noise spectra using computational methods. Åbom[47] investigated the sound radiated by a ducted thin orifice plate and suggested that the main sound source was the pressure fluctuations on the plate. Results at different flow speeds were seen to collapse with the scaling laws suggested by Nelson and Morfey [14]. Cissoni *et al.* [48] also agree with this conclusion, finding that for flow around a ducted teeth shaped obstacle, the frequencies of the fluctuating force on the surface of the obstacle were the same frequencies seen in the farfield spectra.

The second mechanism proposed is that the turbulent jet from the orifice, creates pressure fluctuations due to the fluctuating forces from its interaction with the duct walls [49]. It has been shown that turbulent flow produces noise most efficiently in the presence of

an obstacle, such that the sound is not produced where the turbulence is formed, but instead is produced where the turbulence interacts with the solid obstacle [50]. This theory was confirmed in model experiments [51], however, the sound source when no obstacle was present in the duct was not clearly identifiable. This second mechanism becomes more important at higher Mach numbers, especially when the jet Mach number exceeds unity, due to the additional noise produced by moving shock waves. It has also been suggested that the breakdown of coherent jet structures before the jet reattached to the wall may be a significant noise source [52]. A broad peak in the spectra was found to be related to the randomness of the breakdown process of the deformation and acceleration of the coherent jet column structures.

Additional directly radiated noise is produced due to the unsteady motion of the jet structures, as discussed in Section 2.3, however, this noise only appears as narrowband tones and is dominated by the dipole noise over most of the noise spectrum. The connection between the turbulent structure of the jet and the noise produced during the interaction with obstacles is a point which is still subject to research. The tonal noise can be attributed to a number of feedback mechanisms, the best known of which is very similar to that introduced for cavity flows [53]. Upstream travelling disturbances (either hydrodynamic fluctuations or acoustic waves, depending on the problem) caused by the impingement of a shear layer or jet stream on a solid body, interact with the original shear layer introducing additional disturbances. This causes further structures to form which convect with the mean flow until they too impinge on the downstream body. This feedback then triggers a new set of upstream travelling disturbances, thereby inducing a resonance loop. The period of these excitations for a high speed jet flow was found to match the time it takes for a structure to convect downstream, plus the propagation time for an acoustic wave to travel back to the nozzle exit [54].

Additional feedback mechanisms have been described that are possible without impingement, such as where the downstream vortex roll up and vortex merging was sufficient to induce disturbances in the shear layer at a nozzle exit [55]. Other mechanisms include the feedback loop caused by the upstream convection of disturbances, from the jet interaction with the wall, within the recirculation region behind an orifice [56], the periodic impingement of vortices from the orifice jet on the duct wall [49], the flapping of the jet within the confined duct [57] and, a particularly relevant mechanism for ducted orifices, where feedback caused by acoustic reflections within the ducting can lead to strong self-sustained oscillations, known as whistling [58, 59]. Whistling is related to the creation of an acoustic pulse from the interaction of vortices with the orifice plate, which then reflects from the boundaries of the geometry and comes back to strengthen the creation of new vortices on the orifice plate. Whistling is mainly important for thick plates, due to the increase in frequency when using a thin orifice plate which pushes the noise outside the frequency range of interest [24]. It should be noted that all of the feedback mechanisms are in some way connected to the confinement of the jet, where

the wavelength of the self-sustained oscillations is always connected to the impingement length [60].

The studies listed so far do not make any attempt to account for the interaction noise produced when two in-duct elements are placed at a sufficiently close distance. In this case, the turbulence in the wake produced by the upstream element will interact with the downstream element creating additional interaction noise. Mak [61] developed an equation for the prediction of sound generation by multiple elements in close proximity in a low speed duct. An additional term was introduced into Nelson and Morfey's [14] equation to account for the coherence and phase difference between the two spoiler sources, the distance between sources and the ratio of the mean drag forces. This equation contained a number of parameters which needed to be obtained through experiment, making the method difficult to apply. The method was further extended by Han [62] who modified terms within Mak's equation to account for interaction between more additional elements, unfortunately further complicating the model. Mak and Au [63] have recently attempted to develop a model, based on numerical results, for the prediction of the sound power level generated by a spoiler using the turbulent kinetic energy field in the nearfield. However, their results show an insensitivity to the inlet turbulence intensity when varied from 1-25% which appears be the result of insufficient upstream mesh density or incorrect specification of the physical structure of the turbulence at the inlet boundary.

One possible explanation for the interaction noise may be impingement noise from the upstream turbulence. When a highly turbulent fluid stream impinges upon a surface, additional unsteady forces are produced which radiate sound in the form of an acoustic dipole [64]. A number of papers have studied the effect of the noise generated by impingement and have found that the turbulence intensity [65, 66] and the length scale of the turbulence [67, 68] have a direct affect on the interaction noise. The noise produced by an impinging jet is seen to increase as the distance between the nozzle and the plate is decreased [69]. The noise is suggested to be from two mechanisms, firstly, the impinging of large coherent structures on the downstream body and secondly, the initial instability of the shear layer [70]. When a streamlined body is introduced into a turbulent jet flow, a similar increase in noise is found. Paterson and Amiet [71] found that even at relatively low turbulence intensity levels (TI $\approx$ 5%), the noise from incident turbulence dominated the turbulent boundary layer noise, the stall noise and the vortex shedding noise in an aerofoil flow. It was again noted that the turbulence intensity and length scale were critical parameters governing the noise increase.

There have been a series of computational studies focusing on multiple in-duct elements placed in tandem. However, the vast majority of these computational studies have focused on the validation of numerical methods using the challenging orifice geometry [72–74]. Despite performing experiments and making comparisons to the computational work, these papers do not directly contribute to the improved understanding of

orifice flows and the interaction noise created by tandem in-duct elements. One computational study has attempted to characterise the interaction noise mechanisms [12]. A double orifice configuration with varying separation distances between the orifices was simulated with LES. There was a link seen between the noise and the eddies shed from the upstream orifice, which developed and impinged on the downstream orifice face. The impingement of upstream turbulent eddies on the surface of a body was also described as a cause of additional surface pressure fluctuations in a turbulent boundary layer containing roughness elements. [75].

2.4.4 Orifice sound propagation

The sound propagation characteristics of an orifice are known as the passive properties of the orifice. When a sound wave is propagating through an orifice, part of the wave is reflected and part of the wave is transmitted to continue its propagation downstream. In the mouth of the orifice, some of the acoustic energy is absorbed as it is converted to vorticity at the sharp corners of the orifice [76].

When there is no mean flow present, the acoustic problem is linear and only small amounts of vorticity are created within the thin boundary layer next to the inside edge of the orifice. When the amplitude of the sound waves increases, the problem become non-linear and the absorption of acoustic energy is increased as alternate vortex shedding appears from the orifice edges. These vortices convect downstream at the speed of sound before being dissipated.

When a mean flow is introduced in the ducting, the vorticity which is generated on the inside edge of the orifice will be convected at the mean flow velocity. The mean flow also introduces acoustically induced vortex shedding into the linear problem. This vortex shedding cycle has been studied previously [77, 78]. It is seen that vorticity is generated around the upstream face of the orifice reaches its maximum magnitude as the flow through the orifice changes direction. At this point, the vorticity is shed as a vortex from the downstream face. The vortex is only seen to convect a short distance downstream before it is dissipated. The sound absorption was found to take its maximum value when $M < 0.2$ and for an orifice diameter to duct diameter of 0.3 [79, 80]. This was found to be valid for frequencies below the first circumferential cut-off frequency. The absorption of energy was seen to be higher with low frequency incident waves and the transmission and reflection coefficients were found to be strongly dependent on the orifice internal diameter and frequency [77].

The linearity of the scattering problem has been shown to depend on the mean flow rate, where the absorption significantly increases with increasing flow rate [78]. Non-linear effects at low Mach numbers have also been reported when the magnitude of the acoustic velocity fluctuations exceed 10% of the mean velocity in the orifice [59].

In the plane wave frequency range, below the first cut-on mode, models have been developed to account for the scattering by thin orifice plates [47, 81]. The scattering is

seen to be heavily dependent on the Mach number and the ratio of the area at the vena-contracta to the orifice area. The scattering in both models was found to be frequency independent and showed that as the Mach number is increased, the reflection coefficient increases and the transmission coefficient decreases.

2.5 Incoming flow turbulence generation

The primary objective of this work is to identify a link between the incoming turbulence levels and the noise produced by components of an ADS. Therefore, a method must be found to ensure that sufficient turbulent fluctuations can be produced and that the magnitude of the fluctuations can be controlled. Furthermore, it is important that any noise produced by the generation method is small in comparison to the noise produced by the orifice. Within this section, the advantages and disadvantages of different turbulence generation methods will be discussed in terms of their suitability for the current problem.

In fluid flows, especially for convection driven flows, the inflow boundary conditions can have a significant effect on the results. Under certain conditions, it is safe to assume that the flow within the domain can only be weakly linked to the turbulent characteristics of the inlet. This occurs when the turbulent features produced by the body of interest are much stronger and of larger scale than those present at the upstream boundary. However, when there is little distinction between the scales of the inflow and body generated turbulence, then the accuracy of the inflow specified scales becomes critical [82].

Ideally, a turbulent inflow boundary condition would be capable of producing a velocity distribution with spatial scales that vary between the mesh sizing and the integral length scale of the problem in question. Furthermore, these fluctuations should satisfy the constraints of the governing equations, and be divergence free, so as not to introduce any acoustic disturbance. When it is desirable to use turbulent inflow conditions, it is important to find a physically reasonable and computationally effective turbulent inflow method.

There are a number of different methods for developing turbulence, most of which are applicable to internal flows. The simplest and cheapest method is to superimpose random velocity fluctuations onto the mean inlet profile. Whilst this method is simple, it does not reproduce the physical structure of turbulence and the fluctuations are rapidly damped due to their lack of structure [82]. The simple random signal quickly becomes laminar as it convects downstream [83]. Another easy method for generating turbulence is to use a lengthened inlet region, upstream of the body of interest, to develop the flow. Jarrin *et al.* [84] suggested that the minimum theoretical distance for developing a turbulent flow from a laminar flow, in an LES simulation, is $110\delta_h$ for a plane channel flow (δ_h is half the depth of the channel). For the ADS ducting, it would be unreasonably computationally expensive to use such a long upstream length to develop the flow.

Instead of creating a long inlet region, with all of the computational expense that this entails, in certain cases it is possible to employ a recycling method, whereby the flow from some plane within the simulation is mapped back on the inlet of the domain. There are three major recycling methods; periodic boundary conditions, pre-computed and internal mapping methods. Periodic boundary conditions, allow for temporally developing flows, such as homogeneous isotropic turbulence, to develop when given sufficient simulation time. This method can be useful for simulations of ducting where no components are present (e.g. clean ducts), however, when a component is introduced to the system, a downstream length of greater than the entrance length is required to ensure the flow can fully develop before re-entering the component of interest. Whilst the entrance length may be sufficient for developing the mean velocity profile, the turbulence generated by the component may persist further downstream and cause interactions with the component as the flow is cycled through the system. Therefore, this method is only suitable for repeating geometries or where it is appropriate to approximate infinite lengths in the directions in which these boundary conditions are used. Pre-computed recycling, involves recording data from a plane within a fully developed periodic simulation and updating this saved information onto the inlet of the main simulation. The drawback of this method is large amount of data storage and the additional overheads of applying this new boundary information regularly. The internal mapping method employs a scaled mapping of the velocity field from a plane in the interior of the domain onto the inlet plane, where scaling is used to enforce a specified mean flow rate. The mapping introduces the possibility of intensifying errors as the flow circulates between the inlet and the sampling plane, as well as spurious periodicity in the streamwise direction due to a repeating inflow condition [84, 85]. Although when used correctly, the outcome is very similar to the pre-computed methods, with a significant improvement in efficiency.

Another commonly used method is turbulence synthesis, which generates turbulence by superimposing artificially generated fluctuations on the statistically averaged properties. Synthetic methods do not have the same drawbacks of disturbance amplification and periodicity as the recycling methods, due to the random motions being inherently unperiodic. This method has been used on a range of applications including turbulence in urban environments [86] and upstream turbulence in a wind turbine application [87]. There are some disadvantages to these methods, in particular the need for experimental or DNS data of the structure of the flow to be given as input conditions, and that in some cases, there is a large unwanted pressure signature left by the addition of the turbulence which can dominate and corrupt the smaller pressure fluctuations associated with noise.

A final method of turbulence generation is to introduce a physical body into the flow upstream of the region of interest to introduce realistic turbulent fluctuations into the flow. Admittedly, this is a method commonly used in experimental techniques and receives relatively limited attention in computational studies due to the wide range of inflow conditions discussed above. However, when it is desirable to perform a direct comparison to

experimental data, where a similar method is used, it would be advantageous to explore the use of the same method. In general, there are two main experimental methods for increasing turbulence: uniform grids and fractal grids. Grids in general effect the flow in two ways [88]. Firstly, the turbulent spectrum is altered based upon the size of the eddies in the flow relative to the dimensions of the grid. Secondly, the wake of the grid contributes turbulent energy to the flow at high frequencies. Both of these effects produce a flow which is characterised by good homogeneity and isotropy. Fractal grids are seen to produce the same effect but, due to the range of length scales, produce turbulent eddies across a larger range of scales, better distributing the turbulent kinetic energy and resulting in a slower decay rate [89]. Placing a grid within a duct can complicate the turbulence generation mechanisms, particularly if the grid dimensions are large relative to the duct geometry. This inhibits the formation and growth of turbulent eddies due to the close proximity to the duct wall and can also be influenced by the growth of the boundary layer downstream of the grid [88]. The major advantage of this method is the simplicity of the implementation, however, this is inevitably at the expense of increased computational cost due to the larger domain size and cell count when including an additional physical body.

2.6 Summary

Overall, this literature review has highlighted a number of gaps in the understanding of orifice sound generation. There are two primary noise sources mentioned in previous papers, however, no clear consensus exists throughout the literature. Furthermore, whilst the understanding of the noise sources for a single orifice is limited, there is even less known about the sources and mechanisms behind interaction noise. Further work is required in this area to resolve these issues.

Chapter 3

Research Methodology

3.1 Introduction

The primary aim of any computational aeroacoustic method is to predict the acoustic characteristics at a specified observer location, whether this be in the nearfield or the farfield of the body of interest. The aerodynamically generated noise and its propagation can be predicted using numerical methods to solve the governing equations of fluid motion and noise propagation. Within this chapter, the research methodology surrounding the use of numerical methods for solving the governing equations of fluid motion and sound propagation will be discussed, in terms of their issues and limitations, how they deal with turbulence modelling and the specific details of the numerical solvers, including boundary conditions and numerical schemes. Furthermore, a brief description of the computational software that is utilised and the methods used for validation of the computational results will be presented.

3.2 Governing equations of fluid motion

The governing equations of fluid motion take a number of forms depending on the amount of physics which needs to be included to provide a good approximation of a specific problem. Within this section, the Navier-Stokes, Euler and Linearised Euler governing equations are introduced, which form the basis for the computational methods utilised in this work.

3.2.1 Navier-Stokes equations

The equations governing the motion of a fluid, including the acoustic behaviour, are the compressible equations of the conservation of mass, momentum and energy, commonly known as the Navier-Stokes equations. In conservative form and in the absence of body forces, the equations can be written using a standard index notation as:

$$\frac{\partial \rho}{\partial t} + \frac{\partial \rho u_j}{\partial x_j} = 0, \tag{3.1}$$

$$\frac{\partial \rho u_i}{\partial t} + \frac{\partial}{\partial x_j}[\rho u_i u_j + p\delta_{ij} - \sigma_{ij}] = 0, \tag{3.2}$$

$$\frac{\partial \rho e_0}{\partial t} + \frac{\partial}{\partial x_j}[\rho u_j e_0 + u_j p - u_i \sigma_{ij} + q_j] = 0, \tag{3.3}$$

where ρ is the density, t is the time, u_i is the velocity component in the ith-direction, x_i is the coordinate component in the i-direction, p is the static pressure, σ_{ij} is the viscous stress tensor, q_i is the heat flux component in the ith-direction and e_0 is the total energy per unit mass which is equal to $e_0 = e + \frac{u_k u_k}{2}$. In order to close the conservation equations, the equation of state is required. Assuming that the fluid can be treated as an ideal gas, the equation of state takes the form:

$$p = \rho R_{\text{gas}} T, \tag{3.4}$$

where R_{gas} is the specific gas constant and T is the absolute temperature. In Newtonian fluids, such as air, it can also be assumed that the fluid motion is a linear function of the strain, i.e. gradients of the flow state variables. The viscous stress tensor represents the stress due to fluid motion, and is given by:

$$\sigma_{ij} = 2\mu(S_{ij} - \frac{1}{3} S_{kk}\delta_{ij}), \tag{3.5}$$

where μ is the dynamic viscosity, which is a function of the temperature, δ_{ij} is the Kronecker delta function which equals 1 when i=j and 0 otherwise, and S_{ij} is the rate of strain tensor, defined as:

$$S_{ij} = \frac{1}{2}\left(\frac{\partial u_i}{\partial x_j} + \frac{\partial u_j}{\partial x_i}\right). \tag{3.6}$$

The heat flux is assumed to follow Fourier's law:

$$q_j = -K_h \frac{\partial T}{\partial x_j}, \tag{3.7}$$

where K_h is the heat conductivity, which is a function of temperature.

3.2.2 Euler equations

There have been a number of notable simplifications made to the Navier-Stokes equations, to produce further sets of governing equations, applicable to a smaller and more specific range of fluid flows. One of these simplifications leads to the Euler equations,

which are essentially the Navier-Stokes equations with zero viscosity and without the heat flux terms. It is also assumed that the flow is isentropic, such that no heat is added and no energy transformations occur due to friction or dissipative effects. In conservation form and using standard notation, the mass, momentum and energy equations of the Euler equations can be written as:

$$\frac{\partial \rho}{\partial t} + \frac{\partial \rho u_j}{\partial x_j} = 0, \tag{3.8}$$

$$\frac{\partial \rho u_i}{\partial t} + \frac{\partial}{\partial x_j}[\rho u_i u_j + p\delta_{ij}] = 0, \tag{3.9}$$

$$\frac{\partial \rho e_0}{\partial t} + \frac{\partial}{\partial x_j}[\rho u_j e_0 + u_j p] = 0, \tag{3.10}$$

The Euler equations can be applied to incompressible and compressible flows by assuming that the divergence of the velocity field is zero. This can also be applied as an additional constraint when used in conjunction with an appropriate equation of state (see Eq. 3.4).

3.2.3 Linearised Euler equations

In many cases, sound propagation is minimally affected by viscosity and sound perturbations are so small, that their contribution to the convection velocity of the meanflow is negligible. These two assumptions mean that sound propagation can effectively be described by the Linearised Euler Equations (LEE). As discussed further in Section 3.5, the magnitude of acoustic waves is normally many orders lower than the mean flow variables and can be easily damped by the solver. This method of linearisation helps to maintain the accuracy of the propagating acoustic wave by solving only for the perturbed variable field. The LEE can be derived from the Euler equations by decomposing the flow variables into their mean and fluctuating components as follows:

$$\begin{aligned} u_i &= \bar{u}_i + u_i^{'}, \\ p &= \bar{p} + p^{'}, \\ \rho &= \bar{\rho} + \rho^{'}, \\ e_0 &= \bar{e}_0 + e_0^{'}, \end{aligned} \tag{3.11}$$

where $\bar{\cdot}$ indicates a mean quantity and the superscript $'$ indicates a fluctuating component. Decomposing each of the fluid properties and assuming that products of perturbations are so small that they can be neglected, we arrive at the Linearised Euler Equations:

$$\frac{\partial \rho^{'}}{\partial t} + \frac{\partial}{\partial x_j}[\bar{\rho}\bar{u}_j + \bar{\rho}u_j^{'} + \rho^{'}\bar{u}_j] = 0. \tag{3.12}$$

$$\frac{\partial}{\partial t}[\bar{\rho}u_i^{'} + \rho^{'}\bar{u}_i] + \frac{\partial}{\partial x_j}[\bar{\rho}\bar{u}_i\bar{u}_j + \bar{\rho}\bar{u}_i u_j^{'} + \bar{\rho}u_i^{'}\bar{u}_j + \rho^{'}\bar{u}_i\bar{u}_j + \bar{p}\delta_{ij} + p^{'}\delta_{ij}] = 0, \tag{3.13}$$

$$\frac{\partial}{\partial t}[\bar{\rho}e_0^{'} + \rho^{'}\bar{e}_0] + \frac{\partial}{\partial x_j}[\bar{\rho}\bar{u}_j\bar{e}_0 + \bar{\rho}\bar{u}_j e_0^{'} + \bar{\rho}u_j^{'}\bar{e}_0 + \rho^{'}\bar{u}_j\bar{e}_0 + \bar{u}_j\bar{p} + \bar{u}_j p^{'} + u_j^{'}\bar{p}] = 0, \tag{3.14}$$

By assuming zero mean flow ($\bar{u}_i$=0) the linearised Euler equations reduce to:

$$\frac{\partial \rho^{'}}{\partial t} + \frac{\partial \bar{\rho}u_j^{'}}{\partial x_j} = 0. \tag{3.15}$$

$$\frac{\partial \bar{\rho}u_i^{'}}{\partial t} + \frac{\partial}{\partial x_i}[\bar{p} + p^{'}] = 0. \tag{3.16}$$

$$\frac{\partial \bar{\rho}e_0^{'}}{\partial t} + \frac{\partial}{\partial x_j}[\bar{\rho}u_j^{'}\bar{e}_0 + u_j^{'}\bar{p}] = 0. \tag{3.17}$$

3.3 Governing equations of the aerodynamic sound analogies

This section describes the fundamental theories of aerodynamic noise generation. These are known as acoustic analogies and allow the propagation of sound waves to be separated from their generation. This is made possible by the assumption that the acoustic perturbations caused by the sound waves are so small in comparison to the mean flow acoustic perturbations, that their feedback to the mean flow can be neglected. The first acoustic analogy was derived by Lighthill [90] with extensions made to include the presence of solid boundaries by Curle [91] and arbitrary convective motion of the source by Ffowcs-Williams and Hawkings [92].

The sources of aerodynamic sound can be divided into three categories, which are all caused by different underlying flow phenomena. The sources are termed monopole, dipole and quadrupole and these sources are described briefly below.

A monopole sound source corresponds to sound generation by a fluctuating volume force. This can occur when there is unsteady mass injection into the volume or at high Mach numbers, where non-isentropic flow fluctuations are present.

A dipole sound source corresponds to sound generation by a fluctuating surface force. For stationary surfaces, this may be caused by aerodynamic features such as unsteady flow separation, vortex shedding or the impingement of vortices and eddies on a surface.

Dipole sources are also present with moving surfaces, such as an aircraft passing through a non-uniform flow field.

Finally, quadrupole sound sources correspond to the sound generation by turbulent fluctuations within the freefield flow. This type of noise is broadband in the same way as turbulent fluctuations, however, this tends to be a weak source, especially at the low Mach numbers considered here.

Sound sources may be described as compact if the acoustic wavelengths generated by a body are small in comparison to the characteristic length of the sound source. This means that for an observer in the acoustic farfield, the retarded time between the surface sources is negligible and the sound appears to radiate as a point source. For a compact source, lower frequency acoustic waves tend to be relatively unaffected by the shape of the geometry, whereas the scattering of higher frequency waves tends to be heavily influenced.

3.3.1 Lighthill's equation

Lighthill's equation [90] provides a mathematical descriptor of the non-linear source terms arising from unsteady flow interactions, as depicted in Figure 3.1. The equation is derived from the Navier-Stokes equation by taking the temporal derivative of Equation 3.15 and subtracting the spatial derivative of Equation 3.16. This results in a wave equation on the left hand side (LHS) and a distribution of equivalent sound sources on the right hand side (RHS). This equation only applies to flows without solid boundaries meaning that the equation doesn't take into account reflection, diffraction, absorption or scattering and a clear line of sight must exist between source and observer. Furthermore, the medium is assumed to be stationary and the frame of reference is fixed with respect to the undisturbed medium. In order to predict the sound produced by unbounded flows, the equations are derived by comparing the exact equations of fluctuating fluid motion, to those of a uniform acoustic medium at rest. The differences give the effect of a fluctuating external force field acting and radiating sound.

Assuming the acoustic perturbations are small, the sound speed is constant and the relationship between acoustic pressure and density in the acoustic farfield is given by $p^{'} = a^2\rho^{'}$, the wave equation can be written as:

$$\frac{\partial^2 p^{'}}{\partial x_i^2} - \frac{1}{a^2}\frac{\partial^2 p^{'}}{\partial t^2} = \Big[\nabla^2 - \frac{1}{a^2}\frac{\partial^2}{\partial t^2}\Big]p^{'} = 0, \tag{3.18}$$

from which Lighthill's inhomogeneous wave equation is given:

$$\Big[a^2\nabla^2 - \frac{\partial^2}{\partial t^2}\Big]\rho^{'} = -\frac{\partial^2 T_{ij}}{\partial x_i \partial x_j}, \tag{3.19}$$

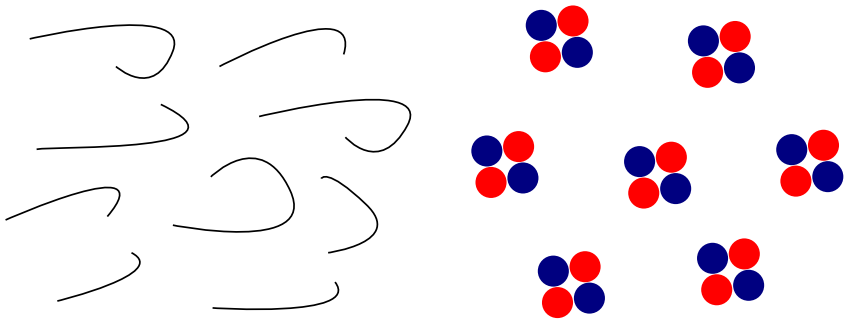

Turbulent flow

Equivalent distribution of quadrupole sources

Figure 3.1: Schematic of the distribution of quadrupole source terms in turbulent flow [2].

where the left hand side is the linear wave equation and the right hand side represents a quadrupole source distribution corresponding to a finite region of rotational flow in an unbounded flow with no solid boundaries given by the Lighthill stress tensor, T_{ij}:

$$T_{ij} = \rho u_i u_j + P_{ij} - a^2 \rho^{'} \delta_{ij}, \tag{3.20}$$

where P_{ij} is the compressive stress tensor:

$$P_{ij} = p^{'} \delta_{ij} - \sigma_{ij}. \tag{3.21}$$

These equations suggest that freefield turbulence, such as that created from a jet, is a weak sound source, especially at low Mach numbers. The sound pressure level of noise produced by the quadrupole term is proportional to u_i^8 [90], known as Lighthill's eighth power law.

3.3.2 Curle's equation

Lighthill's theory was extended by Curle [91] to include the effect of solid boundaries on the sound field. The solid body introduces reflection and diffraction effects as well as generating an additional dipole noise source. This is depicted in Figure (3.2). The far-field sound pressure generated by this noise generation mechanism is a result of the fluctuating force acting on the solid surface.

The presence of solid bodies within the flow is accounted for using a function f_s which surrounds the surfaces and takes negative values inside the surface and positive values outside the surface. This is then applied to the governing equations using a Heaviside function, $\widetilde{H}(f_s)$, which takes the value of zero when the function $f_s < 0$ and takes a value of 1 when $f_s > 0$. Then, following the same procedure as in the derivation of

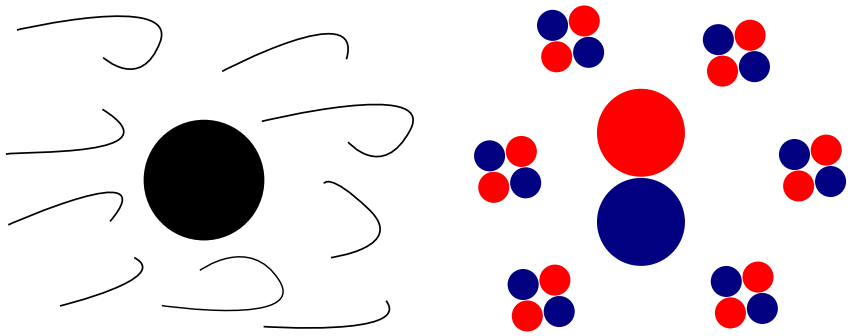

Turbulent flow around cylinder

Equivalent distribution of dipoles and quadrupoles

Figure 3.2: Schematic of the distribution of quadrupole and dipole source terms in the flow around a stationary cylinder.

Lighthill's equation, Curle's equation can be derived from the Navier-Stokes equations as:

$$\left[a^2\nabla^2-\frac{\partial^2}{\partial t^2}\right]\left(\widetilde{H}(f_s)\rho'\right)=-\frac{\partial^2(\widetilde{H}(f_s)T_{ij})}{\partial x_i\partial x_j}+\frac{\partial}{\partial x_i}\left[(P_{ij}+\rho u_i u_j)\frac{\partial\widetilde{H}(f_s)}{\partial x_j}\right]-\frac{\partial}{\partial t}\left[\rho u_i\frac{\partial\widetilde{H}(f_s)}{\partial x_i}\right], \tag{3.22}$$

where the terms on the RHS represents the contributions from the quadrupole, dipole and monopole source terms, respectively. The latter two source terms are distributed over the body and result from the production of sound from the unsteady forces exerted by the body on the fluid and the volume pulsations of the body, respectively. It has been demonstrated that the sound pressure field produced by the pressure dipole sources is equivalent to the scattering of the volume quadrupole sound field by the body [93]. As before, the frame of reference is fixed with respect to the stationary fluid through which the acoustic waves propagate.

For the dipole term, the sound pressure level is proportional to u_i^6 [94]. Therefore, at low Mach numbers, the acoustic power generated by the dipole source term is larger than the quadrupole source term by a factor of $\frac{1}{u^2}$. This means that for typical aircraft approach speeds, where airframe noise is dominant, it is possible to neglect the volume integral of the Lighthill stress tensor.

3.4 Governing equations of sound propagation in cylindrical ducts

The sound field present in a uniform duct, with rigid walls, varies with the frequency of the propagating sound wave. At low frequencies, when the cross-sectional dimensions are much smaller than the wavelength of the sound, only plane waves can propagate, from

which it can be assumed that the sound field is essentially one-dimensional. In many applications, this is a reasonable approximation, however, as the frequency increases, higher order modes are able to propagate though the duct, creating a highly complex acoustic field.

The propagation of sound waves in a stationary medium is governed by the wave equation, given here in one-dimensional space and Cartesian coordinates:

$$\nabla^2 p' - \frac{1}{a^2}\frac{\partial^2 p'}{\partial t^2} = 0, \tag{3.23}$$

where p' is the acoustic pressure, a is the speed of sound and t is the time. Due to the nature of the geometries considered in this work, it is necessary to express the wave equation in terms of cylindrical coordinates (r, θ, z, where r is the radial distance from the centreline of the duct, θ the angle relative to the horizontal axis and z is the streamwise direction along the duct), noting that $0 \leq r \leq R$ and $0 \leq \theta \leq 2\pi$ (see Figure 3.3):

$$\frac{\partial^2 p'}{\partial r^2} + \frac{1}{r}\frac{\partial p'}{\partial r} + \frac{1}{r^2}\frac{\partial^2 p'}{\partial \theta^2} + \frac{\partial^2 p'}{\partial z^2} - \frac{1}{a^2}\frac{\partial^2 p'}{\partial t^2} = 0. \tag{3.24}$$

This equation is obtained using the conservation equations (see Section 3.2) by assuming that the pressure variations are small and by neglecting the effects of viscosity and thermal conduction.

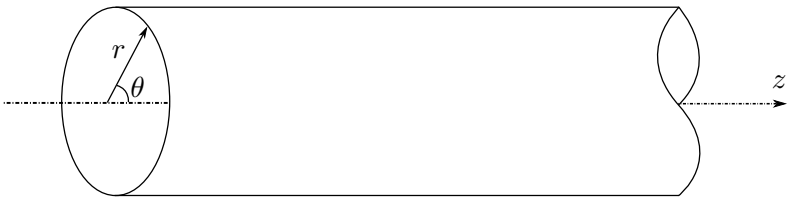

Figure 3.3: Schematic of of the cylindrical coordinate system for a clean circular duct.

By introducing the wavenumber $\kappa = \frac{2\pi f}{a} = \frac{2\pi}{\lambda}$, where f is the frequency and λ is the wavelength, another form of the 1-D wave equation, known as the Helmholtz equation, is given:

$$\frac{\partial^2 p'}{\partial r^2} + \frac{1}{r}\frac{\partial p'}{\partial r} + \frac{1}{r^2}\frac{\partial^2 p'}{\partial \theta^2} + \frac{\partial^2 p'}{\partial z^2} + \kappa^2 p' = 0. \tag{3.25}$$

It is assumed that the time-harmonic solutions of the acoustic pressure are separable in r, θ and z, such that the acoustic pressure in the duct can be expressed as:

$$p'(r, \theta, z, t) = p_r(r) p_\theta(\theta) p_z(z) e^{j2\pi f t}, \tag{3.26}$$

where p_r, p_θ and p_z are the radial, circumferential and streamwise components of the acoustic pressure, respectively.

By separating the variables, applying the rigid wall boundary conditions and noting the orthogonality of the Bessel function, the solution for the acoustic pressure field in a cylindrical duct can be written as:

$$p(r,\theta,z,t) = \sum_{m=-\infty}^{\infty}\sum_{n=0}^{\infty} A_{mn} J_m(\kappa_{rmn} a)\cos(m\theta+\theta_m)(p_{mn}+ e^{j(2\pi ft-\kappa_{zmn}z)} + p_{mn} - e^{j(2\pi ft+\kappa_{zmn}z)}). \tag{3.27}$$

where κ_{rmn} and κ_{zmn} are the radial and streamwise wavenumbers respectively, J_m are the Bessel functions of the first kind with circumferential order m, n is the radial mode number and f is the frequency.

The condition for the propagation of energy of an acoustic mode is that the wavenumber κ_{zmn} must be real, otherwise the wave will decay exponentially with distance and is known as an evanescent wave. Therefore, the mn mode will only propagate if:

$$\frac{2\pi fR}{a} > \alpha_{mn}, \tag{3.28}$$

where R is the duct radius. The first roots of the derivative of the Bessel function (α_{mn}) are given in Table 3.1. At low frequencies, only the fundamental mode will propagate, $m = n = 0$ (plane wave propagation, where the pressure is uniform across the duct for all values of z). As the frequency increases, additional modes will propagate. The frequency at which a mode begins to propagate is known as the cut-off frequency of the mode, f_c:

$$f_c = \frac{\alpha_{mn} a}{2\pi R}. \tag{3.29}$$

n/m	**0**	**1**	**2**	**3**	**4**
0	0	1.8412	3.0542	4.2012	5.3175
1	3.8317	5.3314	6.7061	8.0152	9.2824
2	7.0156	8.5363	9.9695	11.3459	12.6819
3	10.1735	11.7060	13.1704	14.5858	15.9641

Table 3.1: First roots of j'_{nm} of the derivative of the Bessel function $J'_m(\kappa_r a)$ for non-negative integer values of m and n.

Each term in Equation 3.27 represents a mode. Each value of m represents a spinning mode and each value of n represents a radial mode. The modes corresponding to $m = 0$ are axisymmetric.

The mode number m, is equal to the number of pressure maxima when viewed from the end of the duct, or the number of starts on the spiral 'screw thread' [3]. For each mode, the pitch of the spiral angle depends on the frequency. As the frequency is reduced towards the cut-off value, the axial wavelength increases. To accommodate this, the pitch of the spiral waves increases to the point that the wave fronts are spinning around

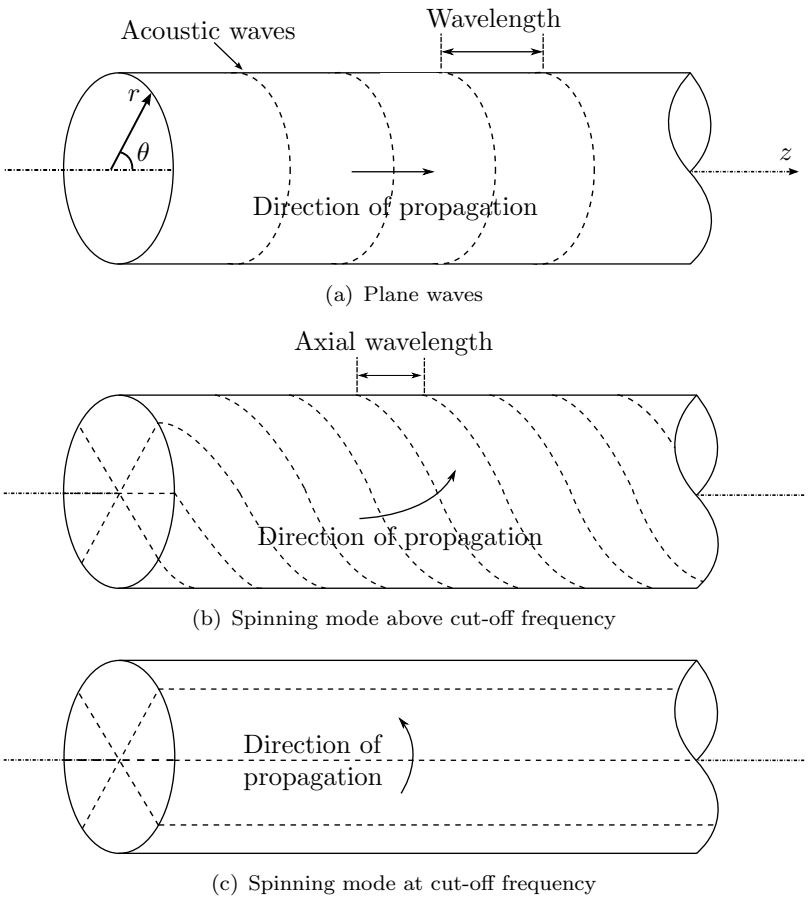

(a) Plane waves

(b) Spinning mode above cut-off frequency

(c) Spinning mode at cut-off frequency

Figure 3.4: Schematic of plane waves and higher order modes propagating in a cylindrical duct [3].

right angles to the axis of the duct. The shape of propagation of the modes also varies with streamwise distance, an example of which is given in Figure 3.4.

For each value of n, there exists a coaxial nodal cylindrical surface. The nodal lines of the first nine higher order modes are presented in Figure 3.5. For all modes, the nodal lines represent a position where the acoustic pressure is zero, with the sign of the area indicating the phase relation. The total sound power transmitted in the duct can be obtained as the summation of the sound power transmitted by each mode.

Analytical estimations of the sound field generated within a straight hard-walled clean square duct were produced by Davies and Ffowcs-Williams [45]. The sound field generated by large scale turbulence within the duct was seen to scale with u_i^6. This was also true of the small scale turbulence below the first cut-on frequency, due to the fact that at low frequencies only the plane waves propagate. At very high frequencies, all the modes were excited and the turbulence radiated in the same way as it would in free space. Thus, at these high frequencies, the sound power increased with u_i^8. The importance of mode cut-on ratio was also noted in the acoustic power produced by a turbofan engine [95].

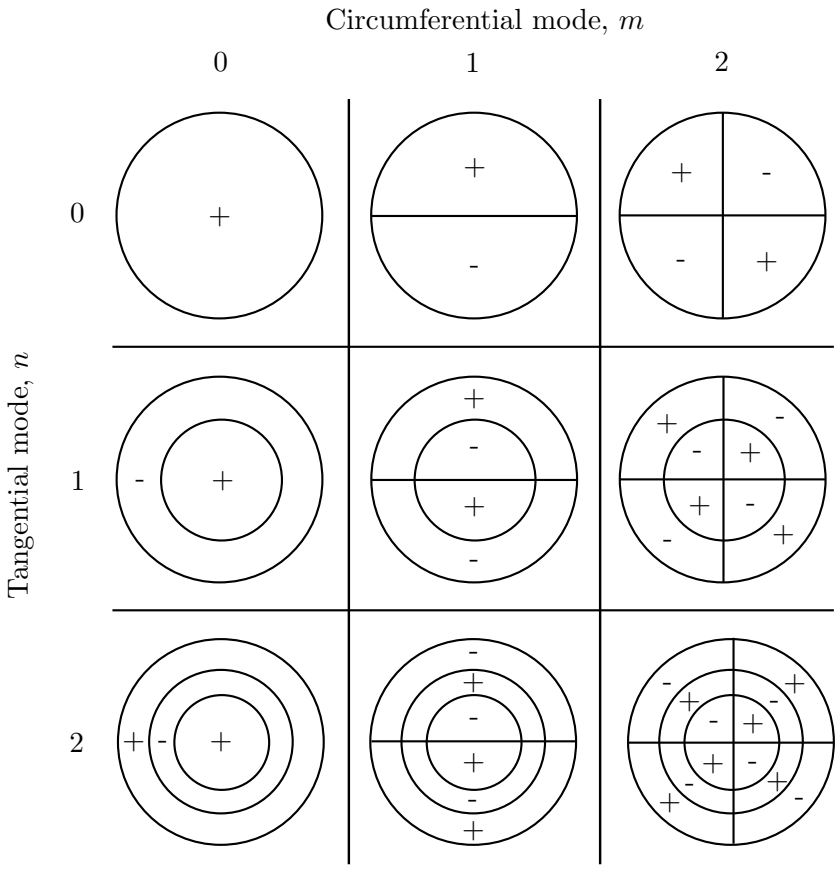

Figure 3.5: Schematic of the first nine higher order modes, where the nodal lines represent a position of zero acoustic pressure and the sign of the area indicates the phase relation [4].

3.5 Computational issues and limitations

There are fundamental differences between the challenges and needs of aerodynamic and acoustic problems. Therefore, whilst it is natural to try to adapt the methods of Computational Fluid Dynamics (CFD) to the numerical problem of the generation and propagation of sound, there are a number of characteristics of aeroacoustic problems which must be understood and accounted for, for this to be a viable solution. Within this section, the demanding nature of aeroacoustic problems will be discussed to highlight some of the difficulties that must be overcome in order to achieve accurate acoustic predictions.

One of the main differences between typical computational fluid dynamics and computational aeroacoustic (CAA) problems, is the time dependent nature of acoustic generation and propagation. In most aircraft noise problems, such as airframe and jet noise, there can be a large spectral bandwidth (e.g. 100Hz-20kHz) containing high frequency acoustic waves. Furthermore, there is a large disparity between the acoustic waves and the mean flow, where the acoustic pressure and density fluctuations can be as much as four orders of magnitude smaller than the mean flow properties. In low order simulations, the acoustic perturbations can be smaller than the magnitude of the error between the

exact and the computed mean flow solution. This has led authors in the past to suggest that the the acoustic solution could be hopelessly corrupted by numerical noise [96].

Typically, in aerodynamic problems, flow features decay quickly in the wake, and the region of interest extends only in the direction of the downstream propagating flow features. In aeroacoustic simulations, however, there is a requirement that the solution is uniformly accurate throughout the computational domain. In order to achieve this, and to predict the correct wavelength and amplitude of the propagating acoustic waves, the numerical schemes employed must be almost free of numerical dispersion, dissipation and anisotropy errors and must have very low numerical noise [97]. Numerical dissipation, which is built into low order conventional CFD codes to help flow solutions converge, has the effect of damping acoustic disturbances. This problem is most apparent for upwinding and blended schemes (combined upwind and central difference), which are unsuitable due to their high levels of inherent dissipation. Therefore, schemes used to predict acoustic behaviour should be central differencing schemes as these contain no numerical dissipation. However, whilst this is desirable for the wave propagation properties of the code, it can lead to unphysical dispersion and undamped growth of numerical oscillations in the solution. These numerical oscillations can present themselves due to either the incorrect definition of the case (boundary/initial conditions and mesh topology) or non-linear flow features within the solution field [98]. Central differencing schemes are conditionally stable depending on the cell Reynolds number:

$$Re_{\text{cell}} = \frac{u_{\text{cell}} h_{\max}}{\nu} \tag{3.30}$$

where $h_{\max}$ is the maximum dimension of the cell in the three coordinate directions and u_{cell} is the velocity within the cell. At high Reynolds numbers, or in some practical applications, it is not always possible to achieve sufficiently small cell Reynolds numbers to prevent oscillations. Therefore, additional numerical filtering is often employed to minimise this problem.

To ensure high levels of accuracy throughout the domain, there are two options; increased mesh refinement or increased accuracy of numerical schemes. If mesh refinement is used to overcome this problem, there is a requirement for a very fine computational grid, capable of resolving high frequency acoustic waves. Previous studies have suggested a resolution of between 6-20 PPW [17, 99–101] is required for accurate resolution of a sound wave, however, this is dependent on the order of accuracy of the code and the type of cells being used. The accuracy problem can also be solved using high order numerical schemes which require a smaller number of cells to resolve the same wavelength, although they tend to be more unstable and require higher levels of filtering.

Another issue with the slow decay of acoustic waves is that in many cases, the disturbances reach the boundaries of the computational domain. Therefore, due to the finite size of the computational domain, special treatments are required at the artificial boundaries, to ensure that acoustic disturbances (upstream and downstream travelling

waves in subsonic flows) leave the domain with minimal reflection. Ideally, the computational domain would be large enough such that the flow at the boundaries is steady, however, this is not always possible due to the large computational cost. The governing equations of motion allow acoustic, vortical and entropy disturbances to propagate and therefore, inlet and outlet acoustic boundary conditions must be able to deal with these three types of waves. This is additionally challenging when considering that the acoustic disturbances will propagate at the sum of the speed of sound and the mean convective flow velocity, whereas the vortical and entropy waves will be convected with the mean flow.

In aeroacoustic simulations, convergence and stability are not the only requirements for producing an accurate numerical solution. Additionally, the timestep size must be chosen based on the highest frequency wave of interest. As with the spatial resolution, the number of timesteps per period (TPP) depends on the order accuracy of the temporal scheme, with authors in the past recommending 10-20 TPP [74, 100] for a second order time marching scheme. The Courant-Friedrichs-Lewy (CFL) condition [102] provides a stability criteria for the numerical solution of certain partial differential equations. In order to ensure stability of the numerical solution solved using an explicit numerical scheme, the timestep size must be less than the time taken for a wave (in aeroacoustics, this is an acoustic wave travelling at the speed of sound plus the convection velocity) to travel to the adjacent grid point. In one dimensional space, the CFL condition takes the following form:

$$\mathrm{CFL} = \frac{a\Delta t}{\Delta x} \tag{3.31}$$

where Δt is the timestep size and Δx is the change in the spatial coordinate (grid size). When using explicit time stepping schemes, the CFL number must remain below unity throughout the simulation domain. Implicit timestepping uses an iterative steady-state like procedure to calculate the flow field at the subsequent time, allowing for solution stability when the maximum CFL values within the domain exceed 1. The maximum stable CFL number depends on the particular implicit scheme being used.

A range of simulation methodologies are available to study noise generation and propagation problems. These methods generally fall into two categories: direct and hybrid approaches. Methods that aim to compute both the unsteady flow field, sound generation and sound propagation are known as direct noise methods, where the acoustic fluctuations are propagated by the code up to the desired observer location. The computational cost of this type of method is large, meaning that simulations are restricted to moderate Reynolds numbers and relatively simple geometries such as jets [103, 104] and vortex rings [105]. The main advantage of these methods is that details of the physical mechanisms driving the sound generation may be revealed. It is possible to extend direct noise computations to the farfield by enlarging the computational domain and solving a simpler set of governing equations, such as the LEE, within this extended

region. However, the difficulty then arises to ensure the accurate and stable transfer of information at the grid interface between these sets of equations [106].

Hybrid methods aim to predict the farfield noise through the use of a separate calculation for noise propagation. This method involves calculating the unsteady flow field from a CFD calculation which then provides the sound sources for one of the acoustic analogies discussed in Section 3.3. The method then requires the choice of a Green's function to describe the effect of the field into which the sound is propagating and the careful consideration of the sampling location of the sound sources. If a solid surface is sampled to provide the sound sources, the quadrupole terms from the acoustic analogy will be neglected, however if a porous surface is used, which will include the quadrupole terms, it is possible that vorticity in the wake of the component can produce artificial noise when it convects through the off-body surface. Authors in the past have noted a strong sensitivity to the position and shape of the integration surface [107] and have attempted to understand the controlling parameters, including removing downstream faces, where the contamination from the wake convection is seen to be strongest [108].

The fact that most aeroacoustic propagation problems are linear, explains the significant use of linearised governing equations, for solving these problems at a reduced computational cost. For these solutions to be valid, the acoustic perturbations must be significantly smaller than the mean flow properties. Typical linear problems include the propagation of sound within a uniform media in the presence of reflecting surfaces, barriers, absorbing walls and ducts. There are cases, particularly at higher Mach numbers, where non-linear acoustic effects will be seen. This includes the near field of high speed jets, sonic boom propagation through atmospheric turbulence and problems which involve the scattering of non-linear disturbances into sound, such as airframe and rotorcraft noise [109].

The Linearised Euler equations (see Section 3.2.3) with source terms can be used to solve a range of general wave propagation problems [110, 111]. The issue with the LEE is the hydrodynamic instabilities which appear when used to solve sheared mean flows. This occurs when the growth of vortices within the shear layers are not damped by viscosity or non-linearities as they would be physically. Methods have been proposed to improve the stability of the LEE in sheared flows, such as the removal [112] and filtering [113] of the gradient terms within the LEE. An alternative method is the Acoustic Perturbation Equations (APE) [114], which were derived from the LEE with source terms. These equations have the advantage of improved stability, but due to their derivation for vorticity generated sound, they tend to be more suited to problems of that nature. In the propagation problems with source terms, both the mean flow and the source terms are input to the equations. This allows for better separation of the source mechanisms and convection and refraction effects and means that the methods are capable of identifying sound sources within a flow, such as a hybrid LES/LEE of a forward-backward facing step [115] and a hybrid LES/APE simulation of a jet [107].

A number of specific issues regularly appear in computational studies of orifice flows and similar geometries such as backward facing steps. It has been frequently noted that studies on this type of geometry where the separation location is fixed (denoted as type II in [116]), tend to overpredict the fluctuating component of the velocity within the recirculation regions and shear layers [12, 72, 117–119]. Furthermore, Sengissen *et al.* [72] highlighted that it was not sufficient to perform a validation to ensure accurate wall pressure spectra predictions, based only on the mean and fluctuating components of the velocity field. An overprediction of up to 5dB is also regularly seen in the comparison of pressure spectra from DES and LES simulation with experimental data [120–124]. Part of this error is attributed to the difference in the length of the experimental and computational signals. It has been shown that these errors can be reduced by shortening the experimental spectra to the same length as that of the computational signal [121]. Further difficulties include predicting the correct pressure drop through the orifice [12], defining the correct inflow conditions [125, 126], and predicting the reattachment point for geometries with fixed separation locations [115, 127]. Panjwani *et al.* [118] noted that the accuracy of a BFS simulation is a complex mix of the mesh, turbulence model and inflow conditions.

Singer and Guo [128] highlight the fact that much of the work performed on predicting radiated noise levels is not validated properly using experimental data. It is only very recently, with collaborative projects such as the CADWIE [129], LAGOON [130] and Gulfstream [131] programs, that experimental data has been made more widely available. This has helped to highlight deficiencies in many of the state of the art codes used in the aerospace industry. Furthermore, the majority of simulations still neglect installation effects, scale effects and model fidelity, causing many of the same errors seen in experimental testing.

3.6 Turbulence modelling

In contrast to laminar flows, which are smooth and deterministic, turbulent flows are unsteady, chaotic and three-dimensional in nature and can only be characterised by their stochastic properties. The transition from laminar to turbulent flow occurs when the inertial forces (non-linear terms of velocity) becomes strong enough compared to the viscous forces. This ratio is described by the Reynolds number:

$$Re = \frac{u_c L_c}{\nu}, \tag{3.32}$$

where u_c is the characteristic velocity of the flow, ν is the kinematic viscosity and L_c is the characteristic length scale (e.g. diameter of the duct). In theory, laminar flow can be maintained within a pipe up to infinite Reynolds numbers, however, perturbations are always present in reality and transition usually occurs at Reynolds numbers of $O(10^3)$.

Compared to laminar flows, turbulent flows are much more diffusive, leading to increased mixing of flow, heat transfer and friction. The presence of a solid boundary has a large effect on the turbulence within a flow and is a site for generation of fresh turbulence. The presence of the walls also limits the growth of eddies based on their proximity to the surface of the wall.

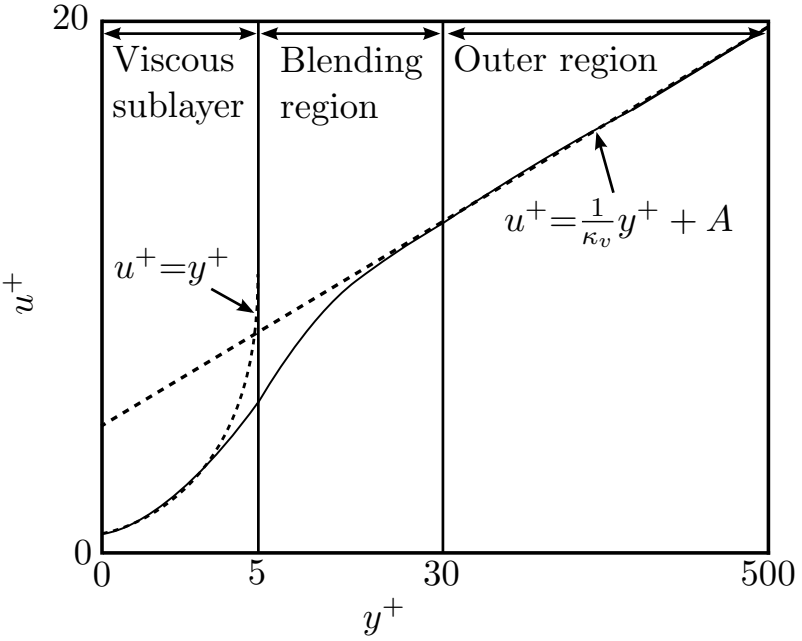

Figure 3.6: Schematic showing regions within a turbulent boundary layer.

A turbulent boundary layer shows three distinct regions [132] (see Figure 3.6) which can be distinguished by the normalised wall distance:

$$y^+ = \frac{u_\tau y}{\nu} \tag{3.33}$$

where u_τ is the friction velocity, y is the distance from the wall in the normal direction and ν is the local kinematic viscosity of the fluid. Within a turbulent boundary layer, Prandtl [133] noted that there is a thin region close to the wall which is dominated by the effects of viscosity and the viscous shear stress at the wall. Within this region, known as the viscous sublayer, no turbulence exists, as the turbulent velocity fluctuations are suppressed by the effects of viscosity. The mean velocity profile within this region has a universal form which follows the law of the wall: $u^+ = y^+$ and extends to a distance of $y^+ \approx 5$ away from the wall. The effects of turbulence begin to be seen in the range $5 < y^+ < 30$, where the laminar and turbulent motions coexist in the buffer zone or blending region. Between the blending region and the outer layer, the length scale of the eddies within this region are a function of their distance to the wall and have a mean velocity given by the log-law of the wall [134]: $u^+ = \frac{1}{\kappa_v} \log y^+ + A_{\text{const}}$, which is governed by the characteristic roughness of the surface. At distances further from the

wall, known as the outer region, the influence of viscosity becomes negligible and the size of the large eddies become independent of Reynolds number.

Turbulent flows are characterised by a large range of scales of motion and contain eddies ranging from the smallest viscous scales to the largest integral length scales. The energy is distributed throughout the range of scales, however, most of it is contained within the large scale eddies, where the energy is supplied by the mean flow. The size of these energy containing eddies is dependent on the geometry of the problem and the nature of their formation. Energy is transferred from larger eddies to smaller eddies through what is known as the energy cascade. At the smallest scales of motion, the kinetic energy of the smallest isotropic eddies is converted into heat by the effects of viscosity.

In the region between these scales lies the inertial sub-range, which contains eddies characterised by their inertia and the transfer of energy to successively smaller scales. Within this range, the spectrum of the turbulent kinetic energy is seen to be independent of the effects of viscosity (depending only on the wavenumber, κ, and the rate of energy dissipation per unit volume, ψ) and can be described by $E(\kappa, \psi) = C_k \kappa^{-5/3} \psi^{2/3}$, giving a slope proportional to $\kappa^{-5/3}$ (see Figure 3.7). C_k is a universal constant of the order of 1.5.

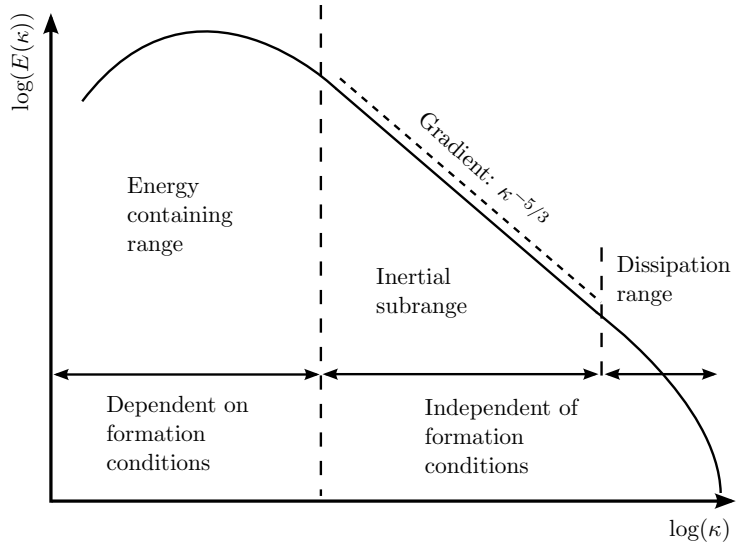

Figure 3.7: Schematic showing the ranges defined within the turbulent kinetic energy spectrum.

The high Reynolds number flows associated with most simulations of practical interest mean that direct numerical simulation (resolving all scales of turbulent motion), where the cost is proportional to Re^3, is not practical. In order to make the computational cost more manageable, the Navier-Stokes equations can either be averaged or filtered. These methods reduce the computational cost by modelling some of the scales within the turbulent energy spectrum (see Figure 3.8), however, they both introduce extra terms

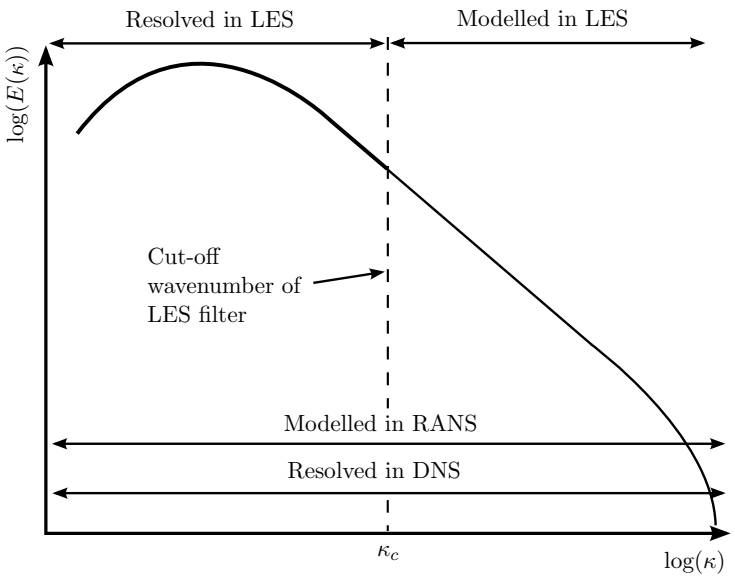

Figure 3.8: Schematic of the turbulence kinetic energy spectrum showing the resolved and modelled regions of the various turbulence modelling approaches used to approximate the spectrum. κ_c indicates the cut-off wavenumber of the LES filter.

into the governing equations which need to be modelled in order to close the system of equations.

3.6.1 Reynolds averaged Navier-Stokes modelling

The Reynolds Averaged Navier-Stokes equations (RANS) are time averaged equations of motion for fluid flow. In order to derive these, the quantities within the Navier-Stokes equations (see Section 3.2.1) are decomposed into their mean and fluctuating components:

$$\Phi = \tilde{\Phi} + \Phi'', \tag{3.34}$$

where Φ'' is the fluctuation and $\tilde{\Phi}$ is a density weighted averaged variable [135]:

$$\tilde{\Phi} = \frac{\overline{\rho\Phi}}{\bar{\rho}}. \tag{3.35}$$

For an unsteady, compressible Newtonian fluid, the RANS equations can be written in conservation form by decomposing each of the flow variables in the same way:

$$\frac{\partial \bar{\rho}}{\partial t} + \frac{\partial \bar{\rho}\tilde{u}_j}{\partial x_j} = 0, \tag{3.36}$$

$$\frac{\partial \bar{\rho}\tilde{u}_i}{\partial t} + \frac{\partial}{\partial x_j}[\bar{\rho}\tilde{u}_i\tilde{u}_j + \bar{p}\delta_{ij} + \overline{\rho u_i'' u_j''} - \bar{\sigma}_{ij}] = 0, \tag{3.37}$$

$$\frac{\partial \bar{\rho}\tilde{e}_0}{\partial t} + \frac{\partial}{\partial x_j}[\bar{\rho}\tilde{u}_j\tilde{e}_0 + \tilde{u}_j\bar{p} + \overline{u_j''p} + \overline{\rho u_j'' e_0''} + \bar{q}_j - \overline{u_i\sigma_{ij}}] = 0, \tag{3.38}$$

where $\bar{\cdot}$ indicates a mean quantity, $\tilde{\cdot}$ indicates a density weighted variable and the density weighted averaged total energy $\tilde{e}_0$ is given by:

$$\tilde{e}_0 = \tilde{e} + \frac{\tilde{u}_k\tilde{u}_k}{2} + \frac{\widetilde{u_k''u_k''}}{2}. \tag{3.39}$$

The decomposition procedure results in extra symmetric non-linear terms known as the apparent Reynolds stresses ($-\overline{\rho u_i'' u_j''}$), which introduce momentum diffusion due to turbulent motions, and the turbulent heat flux ($-\overline{\rho u_j'' e_0''}$). These non-linear terms cannot be solved analytically and require additional modelling to close the RANS equations. The most common method of modelling the Reynolds stresses is the Boussinesq eddy viscosity approximation [136], which relates the Reynolds stresses to the mean velocity gradient as such:

$$-\overline{\rho u_i'' u_j''} = 2\nu_t S_{ij} - \frac{2}{3}\rho k\delta_{ij}, \tag{3.40}$$

where the turbulent kinetic energy, $k = \frac{1}{2}\overline{u_i'' u_i''}$, S_{ij} is the rate of strain tensor and ν_t is the kinematic eddy viscosity, assumed to be an isotropic scalar quantity and only dependent on the local flow field. The turbulent heat fluxes can be modelled using a similar eddy viscosity based approach, described in [137]. A range of different turbulence models have been developed using the Boussinesq approximation. The main features of some common RANS models using the Boussinesq approximation, are detailed in Table 3.2.

Model	**Kinematic eddy viscosity**	**Transported variables**
Spalart Allmaras [138]	$\nu_t = \widetilde{\nu} f_{v1}, \;\; f_{v1}(\widetilde{\nu})$	$\widetilde{\nu}$
k-ε [139]	$\nu_t = C_\mu k^2/\varepsilon, \; C_\mu = 0.09$	k, ε
k-ω [140] k-ω SST [141]	$\nu_t = k/\omega$	k, ω

Table 3.2: Main features of three of the most commonly used RANS turbulence models.

The solution of the RANS equations is relatively computationally cheap, but all of the turbulent scales of motion are modelled, which introduces errors into the prediction. Furthermore, RANS models tend to dissipate all but the largest flow structures, making it very difficult to assess the contribution of the smaller turbulent eddies. Therefore, RANS models are only useful for providing mean flow properties or a starting point from which a more complex unsteady simulation can be initialised [142].

3.6.2 Large eddy simulation

The idea behind Large Eddy Simulation (LES) is based on Kolmogorov's theory of self similarity [143, 144]. This states that the large eddies are dependent on the geometry of the domain, whilst the smaller scales are much more universal. This gives rise to a turbulence model where the spatial and temporal scales of the largest eddies are resolved explicitly by the governing equations and the smaller scales are modelled by a Sub Grid Scale (SGS) model. This assumption means that LES is much more computationally efficient than DNS, the cost varying with $O(Re^2)$.

In LES, the Navier-Stokes equations (see Section 3.2.1) are filtered with a spatial low pass filter to split the variables into resolved and modelled parts. The filter reduces the range of scales that must be resolved by removing the scales associated with high frequencies. A homogeneous LES filter must satisfy the following set of properties when applied to the Navier-Stokes equations:

1. Conservation of constant ($\widehat{D_{\text{const}}} = D_{\text{const}}$), which implies:

$$\int_{-\infty}^{\infty} G(r_f) dr_f = 1, \tag{3.41}$$

where G is the filter function, r_f is the separation distance in the filter function and $\widehat{\cdot}$ denotes the filtered variable.

2. Linearity:

$$\widehat{\Phi_a + \Phi_b} = \widehat{\Phi}_a + \widehat{\Phi}_b, \tag{3.42}$$

where Φ_a and Φ_b are general scalar quantities.

3. Commutation with derivatives:

$$\frac{\widehat{\partial \Phi}}{\partial x} = \frac{\partial \widehat{\Phi}}{\partial x}. \tag{3.43}$$

The commutation property is valid with a constant filter width, for example an isotropic filter. When the flow is inhomogeneous, such as is the case for wall bounded flows, it is desirable to use a spatially varying filter, i.e. $G(r_f, x)$, however, the commutation error can only be neglected if the filter width changes gradually [83].

The cut-off wavenumber of the filter, κ_c, is related to the filter width, $\widehat{\Delta}$, as:

$$\kappa_c = \frac{\pi}{\widehat{\Delta}}. \tag{3.44}$$

The cut-off wavenumber must be chosen to be larger than the energy containing range, see Figure 3.8. Of the three classical filter functions (Top-hat, Gaussian and sharp spectral), OpenFOAM makes use of the implicit top-hat (box) filtering:

$$G(r_f) = \frac{1}{\widehat{\Delta}} \widetilde{H}(\frac{1}{2}\widehat{\Delta} - r_f), \tag{3.45}$$

where $\widetilde{H}$ is the Heaviside function.

The filter operator can be applied to the flowfield variables Φ as:

$$\widehat{\Phi}(x) = \int G(r_f)\Phi(x - r_f)dr_f, \tag{3.46}$$

where $\widehat{\Phi}$ is the filtered flowfield variable. Applying this filtering operator to the Navier-Stokes equations throughout the whole domain and applying a Favre density weighting operation on the filtered variables to avoid subgrid terms in the mass conservation equation [135] (see Equation 3.35), the unsteady filtered Navier-Stokes equations in conservation form can be obtained:

$$\frac{\partial \widehat{\rho}}{\partial t} + \frac{\partial \widehat{\rho}\widetilde{u}_j}{\partial x_j} = 0, \tag{3.47}$$

$$\frac{\partial \widehat{\rho}\widetilde{u}_i}{\partial t} + \frac{\partial}{\partial x_j}[\widehat{\rho}\widetilde{u_i u_j} + \widehat{p}\delta_{ij} - \tilde{\sigma}_{ij}] = 0, \tag{3.48}$$

$$\frac{\partial \widehat{\rho}\widehat{e}_0}{\partial t} + \frac{\partial}{\partial x_j}[\widehat{\rho}\widehat{e}_0\tilde{u}_j + \widehat{p}\tilde{u}_j + \tilde{q}_j + \widehat{\rho e_0 u_j} - \widehat{\rho}\widehat{e}_0\tilde{u}_j + \widehat{pu_j} - \widehat{p}\tilde{u}_j - \tilde{u}_i\tilde{\sigma}_{ij}] = 0, \tag{3.49}$$

This filtering operation introduces unknown non-linear terms into the momentum equation, arising from the convective term on the left hand side of the Navier-Stokes equations, and the energy equation (information about the modelling of the subgrid term in the energy equation can be found in [145]). The additional term within the momentum equation can be decomposed into the product of the filtered velocities and the contributions of the residual (modelled) parts:

$$\widetilde{u_i u_j} = (\widetilde{u}_i + \widetilde{u_i'''})(\widetilde{\widetilde{u}_j + u_j'''}) = \widetilde{u}_i\widetilde{u}_j + \tau_{\text{sgs}}, \tag{3.50}$$

where u_i''' is the residual fluctuation and τ_{sgs} is the residual stress tensor or the subgrid-scale (SGS) stress tensor which takes the form:

$$\tau_{\text{sgs}} = \widetilde{u_i u_j} - \tilde{u}_i\tilde{u}_j. \tag{3.51}$$

In order to close the filtered Navier-Stokes equations, the stress tensor, which represents the contribution of the residual fluid motions, has to be modelled.

3.6.3 Subgrid scale modelling

The fundamental idea behind SGS modelling, is the theory of the universal nature of the smallest scales of turbulent motion. Kolmogorov [143, 144] hypothesised that an inertial subrange exists between the energy containing scales and the viscous length scale, where the velocity field is assumed to be statistically isotropic. When the energy put into the largest eddies by the flow is in equilibrium with the energy transferred into the largest scales of the inertial subrange, then the velocity in the inertial subrange only depends on the energy dissipation rate and the local length scales.

3.6.3.1 Smagorinsky model

The Smagorinsky SGS model [146] applies the turbulent viscosity hypothesis to the deviatoric part of the SGS stress as follows:

$$\tau_{\text{sgs}} = -2\nu_{\text{sgs}} S_{ij}. \tag{3.52}$$

The SGS eddy viscosity, ν_{sgs} is analogous to the turbulent eddy viscosity, ν_t used in the closure of the RANS models. The SGS eddy viscosity is a local quantity, which is a function of the filter length scale $\widehat{\Delta}$ and the rate of strain tensor S_{ij}:

$$\nu_{\text{sgs}} = l^2|\bar{S}| = (C_s\widehat{\Delta})^2|\bar{S}|, \tag{3.53}$$

where l is the turbulence length scale, C_s is the Smagorinsky constant and $|\bar{S}| = \sqrt{2S_{ij}S_{ij}}$. There are a number of disadvantages to the Smagorinsky model, primarily that the Smagorinsky constant is heavily dependent on the flow problem being considered [125]. Secondly, in an inhomogeneous flow, the optimum value of C_s may vary throughout the flow field. Furthermore, additional assumptions are required to describe flow undergoing transition, due to ν_{sgs} being non-zero in laminar flows if the strain rate is non-zero. Finally, in order to account for the reduction of the subgrid length near the wall, due to higher mesh density within boundary layers, the length scale can be multiplied by a Van Driest damping function [147]:

$$l = C_s\ \Delta \left(1 - \exp\left(\frac{-y^+}{25}\right)^3\right). \tag{3.54}$$

3.6.3.2 Dynamic Smagorinsky model

The dynamic Smagorinsky model [148] was proposed to eliminate some of the deficiencies of the original Smagorinsky model by calculating a local Smagorinsky constant as a function of time and position. The dynamic model provides a method for determining the local C_s from the resolved velocity field. In order to produce this behaviour, a test

filter is introduced which has a larger filter width than the original filter ($\ddot{\Delta} > \widehat{\Delta}$). Applying this new test filter to the filtered Navier-Stokes equations, a subgrid-stress tensor, B_{ij} is produced, similar to τ_{sgs}:

$$B_{ij} = \overline{\ddot{u}_i \ddot{u}_j} - \ddot{\bar{u}}_i \ddot{\bar{u}}_j. \tag{3.55}$$

The resolvable stress tensor is defined by:

$$\mathcal{L}_{ij} = B_{ij} - \ddot{\tau}_{\text{sgs}} = (\ddot{\bar{u}_i \bar{u}_j}) - \ddot{\bar{u}}_i \ddot{\bar{u}}_j. \tag{3.56}$$

The dynamic Smagorinsky model is based on the Germano identity when the tensors τ_{ij} and B_{ij} are written in terms of the Smagorinsky model equation. Assuming that the Smagorinsky constant obeys the theory of scale invariance and that it does not vary rapidly in directions over which the test filter acts, the result can be written according to:

$$\mathcal{L}_{ij} = -2C_s'^2 \left(\ddot{\Delta}^2 |\ddot{\bar{S}}| \ddot{\bar{S}}_{ij} - \widehat{\Delta}^2 (|\ddot{\bar{S}}| \ddot{\bar{S}}_{ij}) \right), \tag{3.57}$$

where C_s' is the model constant which is determined dynamically and is capable of accounting for backscatter (transfer of energy from small to large scales) by taking negative values, although this effect can be neglected when resolving a portion of the inertial subrange [149]. These negative coefficients can lead to instability of the solution. Therefore, local averages of the model constant are calculated in time and space to avoid numerical instabilities [150]. Negative values of the effective viscosity can be avoided by clipping to zero. Dynamic models have also been developed for other SGS models [145, 151].

3.6.4 Detached eddy simulation

Detached eddy simulation (DES) is a hybrid RANS/LES method which offers improved accuracy over the RANS equations, without the full computational cost of LES. The original idea of DES was proposed by Spalart [8] with the motivation that RANS models could be used as an SGS model, to model the attached eddies within the boundary layer, while LES is applied only in the separated flow regions. The purpose of this method is to eliminate the difficulties associated with the use of the standard LES models in the near wall regions. The original DES formulation, now known as DES97, was created by modifying and replacing the wall distance function in the Spalart-Allmaras model. Following this, the DES methodology has been applied to a range of RANS turbulence models, using a modification of the turbulent length scale within each respective model:

$$l_{\text{des}} = \min(l_{\text{rans}}, l_{\text{les}}) = \min(l_{\text{rans}}, C_{\text{DES}}\Delta), \tag{3.58}$$

where Δ is the sub-grid length scale and l_{les}, l_{des} and l_{rans} are the turbulence length scales used in the LES, DES and RANS models, respectively.

Two problems have been identified with the original DES formulation. Firstly, under certain circumstances, problems can arise where a 'grey area' is present at the switchover between RANS and LES regions. The issue is noticeable when a meshing strategy is used within the boundary layer that is neither coarse enough to ensure that only the RANS model is activate (where spacings in the wall parallel direction are greater than the boundary layer thickness), nor fine enough to function as a type of wall-modelled LES (where the model functions as an SGS model over the bulk of the boundary layer). This situation is known as an ambiguous grid, where LES content is activated within the boundary layer, but the mesh is not sufficiently fine to support the resolved velocity fluctuations. The DES limiter (Equation 3.58) then reduces the eddy viscosity, and hence the modelled Reynolds stress, without resolved stresses to restore the balance [8]. This situation is known as modelled stress depletion (MSD). In severe cases, such as a thick boundary layer approaching separation, MSD can lead to 'grid induced separation', where the separation point is artificially moved upstream.

Three solutions have been proposed to this problem. The first is to make the DES formulation zonal, where the DES limiter is disabled in selected regions, e.g. where an attached boundary layer is expected [152]. This type of formulation is useful in simple geometries, however for complex 3-D geometries, where separation and reattachment points may not be known *a priori*, this could lead to additional errors. The second method involves making use of the blending functions that define the boundary layer within certain RANS models [153, 154] to preserve the RANS mode. Whilst this method was successful, it is specific to the k-ω family of RANS models. The final method, known as DDES [155], relies on an eddy-viscosity based function to define the boundary layers, and is therefore applicable to any eddy viscosity based RANS model:

$$f_{\text{d}} = 1 - \tanh([8r_{\text{d}}]^3), \tag{3.59}$$

where the function r_{d} is defined by:

$$r_{\text{d}} = \frac{\nu_t + \nu}{\max[\sqrt{U_{ij}U_{ij}}\kappa_v^2 d_w^2, 10^{-10}]}, \tag{3.60}$$

where ν_t is the kinematic eddy viscosity, ν is the molecular viscosity, U_{ij} are the velocity gradients and κ_v is the Von Kármán constant and d_w is the distance to the wall. These functions are used to ensure that the switchover now depends not only on the mesh, but also on the eddy viscosity field. The DES length scale is also modified:

$$l_{\text{ddes}} = l_{\text{rans}} - f_{\text{d}}\max(0, l_{\text{rans}} - l_{\text{les}}). \tag{3.61}$$

The second problem with the original DES97 implementation arises when the model is operating as a Wall modelled LES (WMLES). In this situation, the simulations produce two logarithmic layers: the inner log layer, which is modelled by the RANS model and the outer log layer, which appears because the LES model is active in the outer part of the boundary layer, once the grid spacing is smaller than the distance to the wall. When used as a WMLES, DDES has no advantages over DES97 [155] and in both models, these two log layers do not match (known as the log layer mismatch (LLM)), leading to underpredictions of the skin friction by 15-20% [156]. This motivation led to the creation of a combined DDES/WMLES model, known as improved DDES (IDDES) [5]. When applied to an orifice flow, this model would be expected to act as a URANS model in the attached boundary layer upstream of the orifice, as an LES model in the separated region and as a WMLES in the reattached boundary layer downstream of the orifice, which has inherited LES content from the separated region, see Figure 3.9.

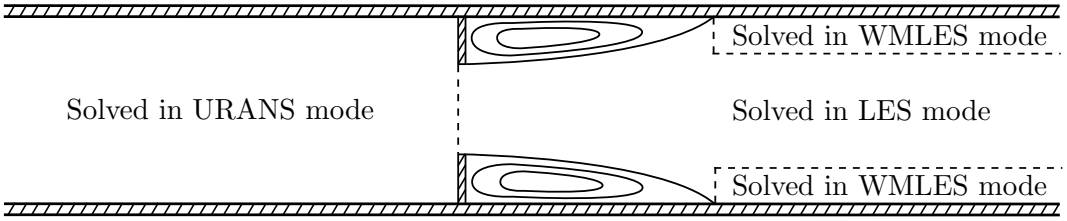

Figure 3.9: Schematic of the regions within the domain that will be solved with URANS, LES and WMLES when applying a IDDES turbulence model to an orifice geometry.

The WMLES branch of the IDDES model is only active when the inflow conditions are unsteady and impart some turbulent content to the simulation. Furthermore, the grid must be fine enough to resolve the dominant eddies within the boundary layer. The model uses a system of sensor functions that react to the presence of resolved turbulence in the simulation. The model equations presented here show how the LLM is reduced by sharpening the RANS-LES switchover and moving it closer to the wall [157]. The model blends the RANS and LES branches using a new WMLES length scale:

$$l_{\text{wmles}} = f_B(1 + f_e)l_{\text{rans}} + (1 - f_B)l_{\text{les}}, \tag{3.62}$$

where f_B is an empirical blending function which provides rapid switching of the model from RANS to LES within the range $0.5h_{\max} < d_w < h_{\max}$:

$$f_B = \min\{2\ \exp(-9\zeta^2), 1.0\}, \quad \zeta = 0.25 - \frac{d_w}{h_{\max}}, \tag{3.63}$$

and f_e is a function targeted specifically at addressing the LLM by preventing the modelled Reynolds stresses from reducing too significantly at the interface between the RANS and LES models:

$$f_e = \max\{(f_{e1} - 1), 0\}\Psi f_{e2}, \tag{3.64}$$

where Ψ is a low Reynolds number correction term introduced to compensate for the activation of the low Reynolds number terms in some RANS models, f_{e1} is a grid dependent elevating function for the RANS component of the WMLES length scale:

$$f_{e1} = \begin{cases} 2\exp(-11.09\zeta^2) & \text{if } \zeta \geq 0, \\ 2\exp(-9.0\zeta^2) & \text{if } \zeta < 0, \end{cases} \tag{3.65}$$

and f_{e2} is a function to control the intensity of the elevation of the RANS component of the model:

$$f_{e2} = 1.0 - \max\{f_t, f_l\}, \tag{3.66}$$

which happens through the following two functions:

$$f_t = \tanh[(c_t^2 r_{\mathrm{dt}})^3], \quad f_l = \tanh[(c_l^2 r_{\mathrm{dl}})^{10}], \tag{3.67}$$

where r_{dt} and r_{dl} are the turbulent and laminar analogues of r_{d} (given by Equation 3.60), which are used to detect the modelled log-law region and the viscous sublayer, respectively. The model constants c_t and c_l depend on the underlying RANS model (DDES and IDDES formulations have also been created for use with the k-ω SST model [158]) and take the values of 1.63 and 3.55, respectively, for the Spalart Allmaras model. The DDES and WMLES branches do not naturally blend, so a further function is defined to ensure smooth coupling:

$$l_{\mathrm{hyb}} = \bar{f}_d(1 + f_e)l_{\mathrm{rans}} + (1 - \bar{f}_d)l_{\mathrm{les}}, \tag{3.68}$$

where the blending function $\bar{f}_d = \max\{(1 - f_{dt}, f_B\}$, and $f_{dt} = 1 - \tanh[(8r_{dt})^3]$. These modifications have been tested on a fully developed planar channel flow, for which a sharp reduction of the LLM was achieved [5]. The implementation of the IDDES has also been tested on a more complex geometry with separation and reattachment and was seen to provide excellent agreement to LES results and an estimated factor 34 reduction in computational cost. There was however, a numerics sensitivity shown by IDDES in a channel flow validation case [157] and, for that reason, a validation of the basic flow properties of the orifice is conducted in Section 5.4.1.

3.6.5 Sub-grid length scale

The selection of the relation between the subgrid length scale and the grid spacing is a general issue with the use of any LES modelling approach which does not use

explicit filtering. This problem is significant when the computational grid is heavily anisotropic, which is typical of the wall bounded flows that are considered in this work. All simulations use a mesh spacing in the wall normal direction, which is much finer than the other two directions. This fact leads to a violation of the assumption that the small eddies within the boundary layer are a result of the energy cascade.

In literature, there are two commonly used subgrid length scale definitions, the cube root of the cell volume and the maximum of the three cell dimensions:

$$\Delta = (h_x h_y h_z)^{\frac{1}{3}} \tag{3.69}$$

$$\Delta = \max(h_x, h_y, h_z) \tag{3.70}$$

where h_x, h_y and h_z are the grid spacings in the x, y and z directions, respectively. Historically, the most widely used subgrid length scale definition has been the cube root of the cell volume [5], Equation 3.69. However, it has been argued that this formulation has no physical basis and the maximum of the three cell dimensions (Equation 3.70) has been advocated in DES literature [8, 159]. It is also the case that neither definition is successful when considering application to wall-resolved LES of wall bounded flows, when using standard meshing practices [5, 160]. A new length scale was proposed in the formulation of the IDDES model, which not only depends on the grid spacing, but also on the distance to the wall. In the region far away from the walls, it is argued that the statistical isotropy of the small eddies requires the use of the maximum cell size in the three dimensions, however, if the mesh is fairly isotropic, the cube root of the cell volume definition holds here as well. Within the region close to the wall, it is desired that that the behaviour of Δ does not completely follow the drastically decreasing value of the wall normal step size and therefore, should only depend on the wall parallel spacings. Assuming that Δ is a linear function of the wall distance and that it varies within the range $h_{\min} < \Delta < h_{\max}$, the new definition of the sub grid length scale, used in IDDES, is:

$$\Delta = \min(\max[C_w d_w, C_w h_{\max}, h_{\text{wn}}], h_{\max}), \tag{3.71}$$

where h_{wn} is the grid size in the wall normal direction and C_w is an empirical constant, which is not specific to any SGS model and should be set equal to 0.15 [5]. This new scale is compared to a common cube root cell volume sub-grid length scale in Figure 3.10.

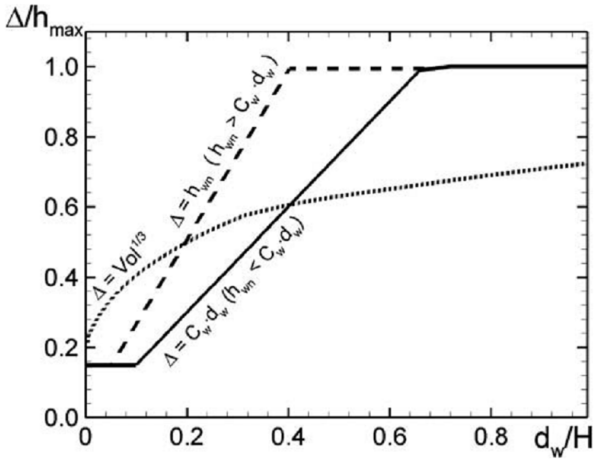

Figure 3.10: Two types of variation of the IDDES subgrid length scale across a plane channel compared to variation of the length scale based on the cube root of the the cell volume [5].

3.7 Sound source identification methodology

Whilst it was mentioned at the start of this chapter that the primary goal of any CAA simulation is to predict the noise at an observer location, it is also of significant interest to identify where this sound was produced. The identification of these sound sources is a non-trivial task, which requires a basic understanding of the noise generation mechanisms for a specific case, in order to accurately apply the correct methodology for source identification. In general, the methods can be split into two categories, surface sources and volume sources.

Sound source identification becomes challenging when you consider that it is not possible to directly measure the acoustic pressure field from a Navier-Stokes simulation, due to the fact that the total pressure field contains a combination of the hydrodynamic and acoustic pressure fields. In experimental studies, this separation can be achieved through the use of a turbulence screen placed over the microphone which rejects most of the pressure fluctuations associated with the turbulent flow. It is also possible to use an indirect method to estimate the ratio of the hydrodynamic pressure to the acoustic pressure using a coherence function [161], but this requires the coherence of the pressure fluctuations between two points to be large, which is not always true in regions where the hydrodynamic pressure fluctuations are dominant. This point was noted by Agarwal [37, 162, 163] who studied the sound generation of an orifice using wall pressure measurements. It was found that in the separated region ($x/h < 11.4$), the wall pressure fluctuations were dominated by the turbulent flow, whilst further downstream, in the region where the flow is recovering to its fully developed state, the acoustic pressure dominates the turbulent fluctuations. Therefore, the use of analogies presents an opportunity to estimate the fluctuating acoustic pressure from other quantities on the surface and within the flow, even in the presence of large hydrodynamic fluctuations.

The sound sources considered within this section will be localised sources, which have not been propagated to farfield observer locations. The difficulty with attempting to propagate the sound to the farfield arises through the enclosed space within which the orifice will radiate sound. The freefield propagation assumptions therefore do not apply to this particular geometry. There have been attempts to apply the acoustic analogies to geometries which don't satisfy the spherical freefield assumption. One approach, introduced by Powell [164], allows for the noise radiated into a hemispherical freefield to be estimated by applying Curle's solution both at an observer point above a fixed wall and at an observer point at an equal distance below the wall. This modification was successfully applied to a cavity flow [165] and a plate with roughness elements [75].

However, in a situation such as an orifice flow, where enclosing walls are present on both the upper and lower surfaces of the duct, this method is not suitable. It is possible to use a tailored Green's function to propagate the sources within the duct [166], although other issues then arise. In order to estimate the noise and allow comparison to the experimental data, it is desirable to propagate the noise to the farfield. The issue with this is caused by the use of a partially reflecting flare at the end of the duct and the influence this has on the propagation. One option is to assume the duct as having an infinite length, whereby estimations of the noise could be made at any point along the imaginary duct, although this still does not allow meaningful comparison to experimental data taken outside of the duct. Therefore, rather than propagating sound sources to a farfield observer location, the methods presented in the remainder of this section will focus on local sound source identification on the surface of the walls and within the fluid volume near the orifice.

3.7.1 Volume and surface sources

Firstly, it can be assumed that the total source of flow generated noise can be represented by the sum of the surface sources and the volume sources:

$$P_A = P_s + P_v, \tag{3.72}$$

where P_A is the total acoustic power generated by the flow and P_s and P_v represent the surface component (dipole) and volumetric component (quadrupole), respectively. The total acoustic power can be expressed by a volume integral of the sources within the volume and a surface integral of the sources on the solid surface:

$$P_s + P_v = \int_S p_s(\mathbf{y}) dS + \int_V p_v(\mathbf{y}) dV, \tag{3.73}$$

where p_s and p_v represent the acoustic sources on the surface and in the volume, respectively. Even though the sound power generated by the quadrupole sources of the flow is expected to be weak when compared to the dipole sources, due to the low Mach

number characterising this flow [167], it is still interesting to identify regions where this secondary source is strong. Therefore, what follows in this section, are two methods to estimate the volume sources, namely Proudman's analogy and the Powell-Howe analogy, and a method for estimating the surface source magnitude based on Curle's equation. A further method is presented which allows estimation of the radiated acoustic power based on the fluctuating mass flow rate through the orifice and the fluctuating pressure on the orifice surface.

3.7.1.1 Curle's analogy

It was shown in Section 3.3.2, that Curle's analogy extends the formulation of Lighthill to explicitly take into account the surface loading contributions due to the presence of solid boundaries. For the derivation, high Reynolds number and low Mach number was assumed, such that the contribution from the Lighthill stress tensor, T_{ij}, viscous dipole term and the bulk convective effect of the flow can be considered negligible. When written in terms of a reference frame moving with the body, the integral representation of Curle's formulation, solving for the density perturbation, is expressed as [92]:

$$\rho^{'} = -\frac{1}{4\pi a^2}\frac{\partial}{\partial x_i}\int_S \frac{[p^{'}\delta_{ij}n_i]_{t^*}}{|\mathbf{x}-\mathbf{y}|}dS(\mathbf{y}), \tag{3.74}$$

where $\mathbf{x}$ is the observer's position vector, $\mathbf{y}$ is the source position, n_i is the normal vector to the wall and S is the surface area of the source. The fluctuation of the hydrodynamic pressure, $p^{'} = p - \bar{p}$, is evaluated at the retarded time, $t^* = t - \frac{|\mathbf{x}-\mathbf{y}|}{a}$. At points far enough from the disturbed flow to be in the farfield of the source, it is possible to replace the spatial derivatives in Equation 3.74 with time derivatives to write the integral representation of the solution as:

$$\rho^{'} = -\frac{1}{4\pi a^3}\frac{\partial}{\partial t}\int_S \frac{(x_i-y_i)[p^{'}\delta_{ij}n_i]_{t^*}}{|\mathbf{x}-\mathbf{y}|^2}dS(\mathbf{y}), \tag{3.75}$$

This form is the most suitable for numerical evaluation [168]. From Equation 3.75, it becomes clear that the dominant source term of Curle's analogy, is the time derivative of the hydrodynamic pressure field on the solid surfaces [165]:

$$Q_{\mathrm{C}} = \frac{\partial p}{\partial t}, \tag{3.76}$$

where Q_{C} is Curle's source term. If the source is considered compact, Curle's analogy can also be written in terms of the time dependent force acting on the solid bodies:

$$\rho^{'} = -\frac{(x_i-y_i)}{4\pi a^3|\mathbf{x}-\mathbf{y}|^2}\frac{\partial}{\partial t}F_i(t), \tag{3.77}$$

where $F_i(t) = \int_S [p^{'} \delta_{ij} n_i]\ dS(\mathbf{y})$. This equation effectively states that the dipole source in a specified direction is a function of the time derivative of the net unsteady force in the specified direction exerted on the fluid by the surface of the orifice. The force consists of both a viscous and pressure force although, whilst the viscous shear stress is a valid dipole sound source [169], its magnitude is often small in high Reynolds number boundary layers. Maruta and Kotake [170] showed that the time derivative of the fluctuating wall surface pressure is well correlated with the associated acoustic pressure and that the noise source strength was proportional to the mean square time derivative of fluctuating surface pressure and its correlation area. The surface pressure field can be obtained thought the use of a transient CFD simulation and this method has been used by a number of authors in the past to estimate the farfield sound [75, 171, 172]. The formulation is not valid for short wavelengths or waves propagating at grazing angles, where the scattering and refraction of the acoustic waves becomes important.

3.7.1.2 Powell's analogy

The Lamb vector (also known as the vortex force) represents the Coriolis acceleration of a velocity field under the effect of its own rotation. The Lamb vector is a relevant quantity in aeroacoustics as it comprises the non-linearities of the Navier-Stokes equations aside from the pressure. It is capable of accounting for the flow state and is useful for identifying recirculation regions and shear layers. These properties mean that it is quantity which is used in a number of acoustic analogies. The Lamb vector is defined as the vorticity-velocity cross-product:

$$\mathbf{L} = \mathbf{\Omega} \times \mathbf{u} = (\nabla \times \mathbf{u}) \times \mathbf{u}, \tag{3.78}$$

where $\mathbf{L}$ is the Lamb vector, $\mathbf{\Omega}$ is the vorticity vector and $\mathbf{u}$ is the velocity vector. The sources of the Lamb vector are the pressure and velocity gradients.

The divergence of the Lamb vector shows a close connection to the motions in a flow, in particular to the instantaneous motions in turbulent flows. This means that the Lamb vector divergence can be used to study the coherent motions in the flow. The divergence of the Lamb vector is given as follows [173]:

$$\nabla \cdot \mathbf{L} = \mathbf{u} \cdot \nabla \times \mathbf{\Omega} - \mathbf{\Omega} \cdot \mathbf{\Omega}, \tag{3.79}$$

which consists of the sum of the flexion product $\mathbf{u} \cdot \nabla \times \mathbf{\Omega}$ and the negative enstrophy $-\mathbf{\Omega} \cdot \mathbf{\Omega}$. In regions where the Lamb vector divergence is zero, the flexion product and the enstrophy do not necessarily have to be zero, they are just locally balanced. In these regions, the sign of the Lamb vector divergence switches between positive and negative values, indicating a shift in the mechanisms which drive the momentum transfer.

The final term in Equation 3.79 indicates that for any flow containing vorticity, that the second term will be negative. Negative values of the divergence of the Lamb vector can be interpreted as localised motions which have the capacity to effect a time rate of change of linear momentum. These negative values cannot automatically be thought of as vortical structures, because shear layers within a boundary layer are capable of producing negative values as well. Positive values indicate that the motions have limited ability in this regard. Sources of Lamb vector divergence can only be produced by the flexion product, seemingly arising from the conversion of angular momentum into linear momentum (unwinding of a vortex) [173].

Powell's analogy [174] is a different formulation of Lighthill's analogy that defines the role of vorticity in the generation of sound. It allows for the connection between the hydrodynamic flow properties and the sound emission in vortical flows to be estimated. The full definition of Powell's analogy reads as:

$$\rho' = \frac{\rho}{4\pi a^2}\int_V \left[\frac{1}{|\mathbf{x}-\mathbf{y}|}\nabla\cdot\mathbf{L}\right]_{t*} dV + \frac{\rho}{4\pi a^2}\int_V \left[\frac{1}{|\mathbf{x}-\mathbf{y}|}\nabla^2 k\right]_{t*} dV, \tag{3.80}$$

where k is the kinetic energy. From Equation 3.80 it results that the Lamb vector divergence ($\nabla\cdot\mathbf{L}$) and the Laplacian of the kinetic energy ($\nabla^2 k$) are the terms contributing to the noise production. Under the assumptions of low Mach number and a compact source region, the term related to the Laplacian of the kinetic energy can be neglected. The result is that the divergence of the Lamb vector is the dominant source term in Powell's analogy [175, 176]:

$$Q_{\mathrm{P1}} = |\rho\nabla\cdot\mathbf{L}|. \tag{3.81}$$

Powell's analogy has been previously used to study the volumetric sources in an oral tract [177] and the noise produced in the breakdown of a jet [178].

3.7.1.3 Proudman's analogy

Proudman's analogy [179] is derived from Lighthill's analogy and approximates the sound power generated by statistically homogeneous and decaying isotropic turbulence. Proudman concluded that sound generation from turbulence is the consequence of two types of eddies, those with length scales in the dissipation range and those in the energy containing range. Only the sound from the large eddies is expected to make a significant contribution at high Reynolds numbers. Furthermore, a very low Mach number is assumed ($M < 0.01$) such that retarded time effects can be neglected. Further constraints are that the length scale of the turbulence, l, should be much smaller than the diameter of the duct, D and that the Mach number of the turbulence should satisfy $M \ll l/D \ll 1$.

Proudman's analogy provides a relationship for the approximate local contribution to the time averaged total acoustic power per unit volume as:

$$P_A = A_{\text{const}}\rho\Big(\frac{u^3}{l}\Big)\frac{u^5}{a^5}, \tag{3.82}$$

where u and l are the turbulence velocity and length scales, respectively, and A_{const} is a model constant. In order to make the analogy more useful in CFD simulations, it can be rewritten in terms of the turbulent kinetic energy and the turbulence dissipation rate:

$$P_A = B_{\text{const}}\rho\varepsilon\Big(\frac{\sqrt{2k}}{a}\Big)^5, \tag{3.83}$$

where, k is the mean turbulent kinetic energy, ε is the mean turbulence dissipation rate and B_{const} is the rescaled model constant. The value of B_{const} was determined to be 0.1, based on calibration using DNS of isotropic turbulence [180]. This equation allows the flow induced acoustic power to be expressed in terms of steady state variables from a CFD simulation. This makes the methods based on Proudman's analogy very computationally efficient.

One of the issues arising from the rewriting in terms of k and ε, is that it makes the model useful only for the two equation k-ε RANS model. The modification to allow the use with k-ω models is simple due to the relationship between the turbulence dissipation rate and the specific turbulence dissipation rate:

$$\omega = \frac{\varepsilon}{C_\mu k} \tag{3.84}$$

where ω is the mean specific turbulence dissipation rate and $C_\mu = 0.09$.

Using these equations, it is possible to estimate the mean volumetric noise sources from the mean fields of a CFD simulation. However, it must be noted that this method of noise prediction is only directly applicable to RANS modelled simulations. This is because the DES modifications to each of the RANS models change the transported variables in the regions where the LES model dominates. For example, the DES formulation changes the equation for the transported variables in the k-ω SST model, by increasing the dissipation of k. This then leads to a reduction in k in the LES modelled regions and means that the calculated eddy viscosity would be too small, leading to incorrect noise estimations.

A method for estimating surface sound sources from a steady k-ε simulation was proposed by Croaker *et al.* [181] for application in conjunction with Proudman's analogy. The method is based on the fluctuating surface forces and relationships from the standard k-ε model. This method was not explored further due to its limited applicability to other turbulence models.

3.8 Computational software

Within this section, details of the software utilised as part of this work will be presented. A description of the specific numerical schemes and boundary conditions used in SotonLEE and OpenFOAM will be presented, along with a discussion of the meshing considerations and methods used within Gridgen.

3.8.1 SotonLEE

SotonLEE [112, 182] is a high-order computational aeroacoustics solver developed within the ANTC (Airbus Noise Technology Centre) at the University of Southampton. It has been used to study of range of geometries and acoustic problems including ducts [110] and fan noise [111]. The code is an explicit multi-block solver which has the capability for direct acoustic solutions of the perturbed pressure field using the Linearised Euler Equations (see Section 3.2) in non-dimensionalised variables. The code is written in Fortran 95 format and employs RANS, DES and LES turbulence models.

The code solves the linearised Euler equations in curvilinear co-ordinates, and therefore requires structured grids. The code possesses very good wave propagation characteristics, with minimal dispersion, dissipation and anisotropy errors, making it very suitable for solving aeroacoustic problems. The code is fully parallelised using MPI on both Windows and Linux systems.

3.8.1.1 Numerical schemes

Within SotonLEE, spatial discretisation is performed using a finite-difference approach with the 6^{th} order pre-factored or optimised compact schemes of Hixon [183]. Time integration is performed using a low dispersion and dissipation 4^{th} order 4/6 stage Runge-Kutta explicit time stepping scheme [184]. The explicit time stepping methods calculate the flow field using information only from the previous timestep. This results in a low computational cost, although very small timesteps are required for stability. In order to damp the high frequency modes in the numerical prediction, the high-order implicit filtering technique of Visbal and Gaitonde [185] is applied.

3.8.1.2 Boundary conditions

A slip wall boundary condition is applied to the walls of both the duct and the orifice plate, which fixes the normal component of flow velocity to zero. The pressure at the wall is determined using a linear extrapolation of data from the mesh points adjacent to the wall (zero-gradient). The flow is assumed to be isentropic, so the perturbations in the non-dimensionalised density field are equal to the perturbations in the non-dimensionalised pressure field. A symmetry boundary condition is applied along the duct centreline due to the axisymmetric nature of the problem. The symmetry boundary

Figure 3.11: A schematic of the buffer zone implementation.

condition enforces that the normal velocities across the boundary are set to zero. This condition is also required when higher order spinning modes are considered with a 2.5D simulation method. Reflection of acoustic waves from the inflow and outlet boundaries are controlled using an explicit bufferzone method [186]. The buffer zone boundary condition is applied to an extra mesh region added onto the edges of the computational domain of the simulation. Within this extra region, the out-going wave, either at the inlet or outlet, is damped to a set target value by a damping function. The shape and strength of the damping function varies smoothly within the buffer zone, with the out-going wave being forced to the target value by the outer edge of the buffer zone. At the interface between the computational domain and the buffer zone, the damping function is set to zero, which means that waves enter the buffer zone without obstruction. The solution vector is explicitly damped after each timestep using the following equation:

$$\Phi^{n+1} = \overline{\Phi^{n+1}} - \sigma(\overline{\Phi^{n+1}} - \Phi_{\text{target}}), \tag{3.85}$$

where $\overline{\Phi^{n+1}}$ is the solution vector computed after each timestep, Φ_{target} is the target vector (the desired values of the velocity, pressure and density components) and σ is the damping coefficient, which varies according to:

$$\sigma(x) = \sigma_{\max} \left| 1 - \frac{W - x}{W} \right|^{\beta}, \tag{3.86}$$

within the inflow buffer zone and

$$\sigma(x) = \sigma_{\max} \left| 1 - \frac{x - W}{W} \right|^{\beta}, \tag{3.87}$$

within the outflow buffer zone, where W is the width of the buffer zone, x is the distance from the inner boundary of the buffer zone and $\sigma_{\max}$ and β are coefficients which determine the shape and strength of the damping function. For the simulations considered in this paper, the target values for perturbations within the buffer zone are set to zero, such that the outgoing waves will be damped to the mean flow. The values of $\sigma_{\max}$ and β have been fixed at 0.07 and 2, respectively (damping function varies with the square of the distance from the inner edge of the boundary). A schematic of a computational domain with buffer zone is shown in Figure 3.11.

The buffer zone serves a dual purpose in the LEE simulations. As well as damping outgoing waves, it has been used as a source region for incoming acoustic waves. This is achieved by modifying the target value, Φ_{target}, within the inflow buffer zone and updating this value at each timestep to produce the desired amplitude and frequency acoustic wave. The wave is forced throughout the inflow buffer zone, with the strength of the forcing dictated by the damping function shape from Equation 3.86. The wave shape in the circumferential direction is determined using the solution of the Bessel function, Equation 3.27. This method allows for the input of plane waves and a range of higher order circumferential and spinning modes, which are then propagated through the duct by the governing equations. A summary of the boundary conditions used in SotonLEE is presented in Table 3.3.

Variable	**Wall**	**Inlet**	**Outlet**
Velocity	$u_n = 0$	$u_i = u_\infty$	$u_i = u_\infty$
Pressure	$\frac{dp}{dn} = 0$	$p = p_\infty$	$p = p_\infty$
Density	$(\frac{\rho}{\rho_\infty})' = (\frac{p}{a\rho_\infty})'$	$\rho = \rho_\infty$	$\rho = \rho_\infty$

Table 3.3: Boundary conditions used in the SotonLEE simulations. The ∞ subscript denotes the freestream value and $\frac{d}{dn}$ is the normal derivative to the boundary.

3.8.2 OpenFOAM

Open Field Operation And Manipulation (OpenFOAM) is an open source CFD code produced and maintained by OpenCFD Ltd. The code uses a cell-centred finite volume approach to solve the three-dimensional Navier-Stokes equations on structured and unstructured meshes using any cell type. The code includes a set of efficient C++ modules which includes solvers and various utilities to perform pre and postprocessing of geometries, meshes and results data.

The code includes a wide range of turbulence modelling options (RANS, DES, LES, DNS) and the ability to solve both the incompressible and compressible governing equations, as well as other problems such as multiphase flow. OpenFOAM uses a text based input system and allows for runtime modification of cases. The solver is highly efficient and well parallelised enabling fast solutions even with complex geometries. Individual variable fields are solved using a Algebraic MultiGrid method (AMG) (for a description see [187]) designed to increase the computational efficiency and improve convergence rates. Import and export of data is available from and to a wide range of common formats, allowing flexibility in the choice of meshing and visualisation software.

There are a few drawbacks to the use of OpenFOAM. Being second order in nature, there is a requirement for fine meshes to meet the PPW requirement for propagation of acoustic waves. Furthermore, the range of implemented acoustic inflow and outflow boundary conditions is poor and there are no available acoustic propagation tools. Despite these

drawbacks however, the efficiency, flexibility, and ease of modification of OpenFOAM make it ideal for investigating these noise generation problems.

3.8.2.1 Numerical methods

There are a wide range of numerical schemes available within OpenFOAM, however, due to the low-order nature of the code, only a limited number of these are suitable for accurate aeroacoustic studies. There are some higher order schemes available to solve specific terms within the discretised equations, but due to the use of the Gaussian finite volume integration method, where values on cell faces are interpolated from cell centres, the dominant order of accuracy is always a maximum of second order.

Therefore, the ideal numerical scheme for the discretised convection terms is the second order central differencing, although, as noted previously this can introduce numerical oscillations. Therefore, in the absense of explicit numerical filtering within OpenFOAM, the 'filteredLinear3' schemes have been used to replace the 'linear' scheme in some cases where instabilities have become apparent. These schemes introduce small amounts of upwinding (typical values used in this work are 1-5%) into the central differencing scheme to damp the numerical noise. Wherever possible this has been avoided though, as the introduction of any upwinding will have a negative effect on the results. The 'backward' time marching scheme (second order implicit timestepping) is used in all cases.

3.8.2.2 Incompressible Boundary conditions

Walls are modelled using a no-slip condition and the near wall mesh is sufficiently fine in the wall normal direction in all cases to ensure that $y^+ \approx 1$. This ensures that the large velocity gradients near the wall are adequately resolved. A developed velocity profile is specified normal to the inlet face (more discussion is given in Section 4.3.2). Gauge pressure is fixed on the outlet faces. Periodic (Cyclic) boundary conditions were utilised on the inlet and outlet boundaries in one case, as described in Section 4.3.1. The turbulence parameters are defined based on a desired freestream turbulence intensity of 5%. Details of the definitions on each boundary are given in Table 3.4.

3.8.2.3 Compressible Boundary conditions

Boundary conditions for the compressible cases are very similar to the incompressible simulations. One notable exception is the specification of the driving flow as a fixed average mass flow rate (ρu) rather than a fixed velocity. The implementation of this spatially varying, fully developed, mass flow inlet adjusts the velocity field based on the density values on the inlet faces which are evaluated using a linear extrapolation of the values from the cell nearest to the boundary. The temperature field across the inlet face is fixed at 293.15K which is the experimentally measured value at a flow speed of

Variable	**Wall**	**Inlet**	**Outlet**
Velocity	$u_i = 0$	$u_i = u_\infty$	$\frac{du_i}{dn} = 0$
Pressure	$\frac{dp}{dn} = 0$	$\frac{dp}{dn} = 0$	$p = 0$
Turbulent kinetic energy	$\frac{dk}{dn} = 0$	$k = k_\infty = 1.5$	$\frac{dk}{dn} = 0$
Turbulent dissipation rate	$\frac{d\varepsilon}{dn} = 0$	$\varepsilon = \varepsilon_\infty = 43.12$	$\frac{d\varepsilon}{dn} = 0$
Specific dissipation rate	$\frac{d\omega}{dn} = 0$	$\omega = \omega_\infty = 28.75$	$\frac{d\omega}{dn} = 0$
Modified turbulent viscosity	$\widetilde{\nu} = 0$	$\widetilde{\nu} = \widetilde{\nu}_\infty = 4.38 \times 10^{-5}$	$\frac{d\widetilde{\nu}}{dn} = 0$

Table 3.4: Boundary conditions used in the incompressible OpenFOAM simulations. The ∞ subscript denotes the freestream value and $\frac{d}{dn}$ is the normal derivative to the boundary.

10m/s. Pressure and velocity are treated the same on the walls, which are assumed to be adiabatic by setting a fixed value of 293.15K for temperature. The density field is calculated from the pressure and temperature using the ideal gas equation. The other major change is the specification of an acoustic boundary condition at the outlet boundary for pressure. The non-reflective pressure boundary condition implemented into OpenFOAM is a simplification of that proposed by Poinsot and Lele [188]. The inputs for this model are the outlet pressure, p_∞, and the relaxation length, l_∞, which represents how reflective the boundary condition will be. A lower value of the relaxation length gives a higher reflection coefficient. The model firstly calculates the velocity of the outgoing pressure wave and uses this to estimate the relaxation coefficient. The relaxation coefficient value is then used to take a fraction of the difference between the target value of pressure, p_∞, and the pressure in the cell closest to the outlet, p_{cell}:

$$p_{\text{outlet}} = \zeta p_\infty + (1 - \zeta) p_{\text{cell}} \tag{3.88}$$

where ζ defines the ratio of this fraction. Whilst ideally, this boundary condition would be free of reflections, the use of a target pressure value is required to stop the pressure drifting and the problem becoming ill posed. This causes the boundary to be partially reflecting as it drives the solution towards p_∞. Other boundary conditions utilised throughout the compressible simulations are described in Table 3.5.

3.8.3 Pointwise Gridgen

The grid is a critical part of obtaining a good solution. It should be designed with the expected aerodynamic flow features in mind and the resolution should be adjusted accordingly. The critical regions of the grid include areas where there is a rapid change in flow velocity, high vorticity or separation. This makes the near wall mesh and the wake mesh important regions of the grid. In some cases it is suitable to use wall functions to model the near wall region at a reduced computational cost, however, if accuracy is

Variable	**Wall**	**Inlet**	**Outlet**
Velocity	$u_i = 0$	$u_i = u_\infty$	$\frac{du_i}{dn} = 0$
Pressure	$\frac{dp}{dn} = 0$	$\frac{dp}{dn} = 0$	$p = p_\infty$
Temperature	$T = T_\infty$	$T = T_\infty$	$\frac{dT}{dn} = 0$
Density	$\rho = \frac{p}{R_{\text{gas}}T}$	$\rho = \frac{p}{R_{\text{gas}}T}$	$\rho = \frac{p}{R_{\text{gas}}T}$
Modified turbulent viscosity	$\widetilde{\nu} = 0$	$\widetilde{\nu} = \widetilde{\nu}_\infty = 4.38 \times 10^{-5}$	$\frac{d\widetilde{\nu}}{dn} = 0$

Table 3.5: Boundary conditions used in the compressible OpenFOAM simulations. The ∞ subscript denotes the freestream value and $\frac{d}{dn}$ is the normal derivative to the boundary.

important, it is crucial to ensure the boundary layer is well resolved. It is suggested that the first cell height should allow for three points within the viscous sublayer [189], although there is little benefit to going below $y^+ = 1$ [190], and that the stretching ratio within the boundary layer should be no greater than 1.2. Good isotropy of the cells away from the wall is also required due to the calculation of the subgrid length scales within DES and LES.

Curvilinear structured multi-block grids were generated for all the meshes used throughout this work using Pointwise Gridgen V15 [191]. Gridgen is a toolkit for generating meshes with a variety of cell types (i.e., hexahedra, tetrahedra, prisms and pyramids). It provides high levels of user control over the mesh and can be used to create both 2-D and 3-D meshes. Gridgen provides four entities for grid generation; databases - geometry data that defines the shape of the object being meshed; connectors - grid curves to divide up the grid sections; domains - surface meshes; blocks - volume meshes.

Meshes are created in what is known as a 'bottom-up' meshing approach. Connectors are joined to form a domain and then the domains are combined to form blocks. Gridgen can create both structured and unstructured meshes, as well as combining regions of both in a hybrid mesh. Both structured and unstructured elliptic solvers are implemented to improve the mesh quality of the domains and blocks. As a rule, Gridgen can create meshes around almost any geometry, but this comes at the price of increased user effort and time. The ability for Gridgen to create fully structured meshes around complex geometries makes it very attractive for this research. This is particularly true for the meshes created for the LEE simulations, where smooth changes between block boundaries and minimal skewness are essential for stability of the high order code.

3.9 Iridis 4 supercomputing facility

The computational work performed in this project has been conducted using the Iridis 4 supercomputing facility at the University of Southampton. The facility has a total

computational power of 250 TFlops and consists of 770 Linux based nodes, each containing sixteen 2.6Ghz cores. Each core has a total of 4GB of available memory and high memory nodes are available for graphics visualisation. There is total of 1.04PB of storage available on the parallel file system and interprocessor communication is completed using a high-speed infiniband network.

3.10 Experimental validation

Whilst the accuracy of numerical simulations is constantly improving, there is still a need to validate each part of the computational methodology in order to ensure that the physics of the problem is being correctly captured. For this purpose, the experimental work conducted by Tao *et al.* [192], has been heavily utilised. In the following section, a brief overview of the experimental rig will be presented. Details of the individual measurements will be discussed within the results chapters of this thesis, alongside the computational results.

3.10.1 Experimental facility

Tao *et al.* [192] designed an experimental facility to allow for the aerodynamic and acoustic field around single or multiple in-duct components to be investigated. The design of the experimental facility consisted of three main parts: an air flow supply, a test section and a non-reflective end. A schematic of the overall design of the facility is presented in Figure 3.12. The flow is supplied by a centrifugal fan, capable of reaching flow velocities of 25m/s, which is vibration isolated from the test section using a flexible tube. Background noise from the fan is minimised using a silencer attached between the flexible tube and the test section. Reflections from the end of the duct are reduced through the use of a flare which increases the diameter of the duct from 100mm to 500mm. The flare was experimentally found to have a cut-off frequency of 186Hz [6].

The test section was designed to be modular, such that ADS components can be interchanged and removed. The ducting upstream of the test section has a length of 4m to ensure the that the flow approaching the components is fully developed (see Section 2.2). The internal diameter of the circular ducting is 100mm and the wall thickness is 5mm. Components are fixed into the test section using a rubber flange.

As part of the experimental work, measurements of the static pressure, unsteady wall pressure, mean velocity profile, unsteady velocity and farfield sound power were taken. Information on the techniques and positions used for each of the measurements can be found within the results chapters, specifically Sections 5.4.1.1, 5.4.2 and 5.4.3. As discussed in Section 3.7, it is not possible to achieve farfield sound measurements through the numerical simulations, without the use of a prohibitively costly computational domain size and simulation of the experimental flare. Therefore, the farfield sound power measurements from the experiment will not be considered further.

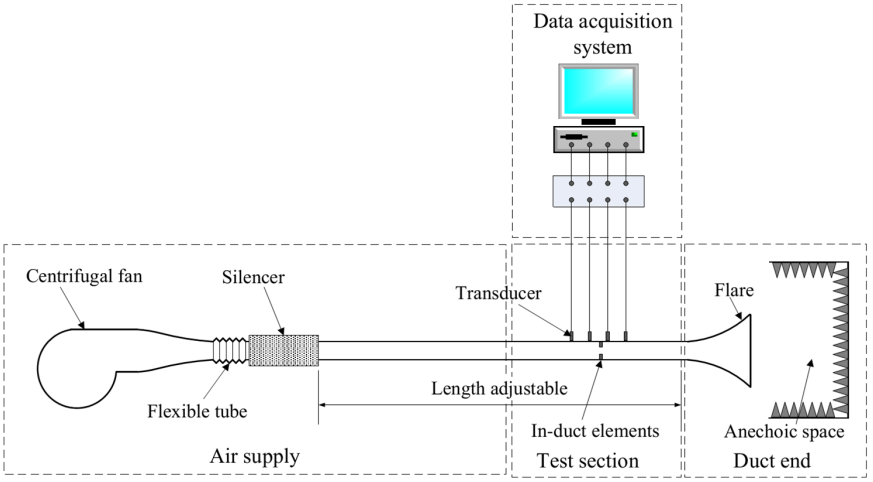

Figure 3.12: Schematic of the experimental facility for acquisition of in-duct and farfield noise measurements [6].

3.11 Summary

Within this chapter, the numerical research methodology has been presented. The information provided here is the basis for the methods used throughout the work presented in this thesis, where any specific differences are described within the relevant sections in the results chapters.

Chapter 4

Effect of Incoming Flow on the Turbulence Produced by an Orifice

4.1 Introduction

The problem of turbulence is one that cannot be avoided. The construction of an ADS can be very complicated, with systems often extending the full length of the aircraft and being made up of components ranging in size and complexity. Poorly designed systems can dramatically increase the noise produced, due to the interaction of the wake of upstream components with those downstream. It is known that the levels of turbulence in the airflow within the ADS have a link to the noise produced by the system [12]. What is not clear however, is the mechanism driving the increased noise generation.

The components within the ADS each have a primary function and their designs cannot be significantly modified. However, it may be possible to change the positioning of the components, thereby modifying their interaction, whilst still ensuring that air is distributed evenly to all passengers. Whilst some components have a minimal affect on the downstream flow, there are other components which produce highly turbulent wakes which will convect downstream, interacting with other components and producing further turbulence and noise. The different components produce wakes with varying turbulent length scales and the generation of vortices is common, due to the bluff body nature of many of the components. In order to simplify the problem, components are often studied in isolation or in pairs [12, 72–74] and the latter is the method followed in this chapter.

There are two objectives for this chapter; the first is to investigate whether increased turbulence levels, from the wake of an upstream component, result in an increase in the turbulence levels produced by a downstream body, and the second is to identify critical

separation distances between components to highlight regions of the ADS where there are likely to be high levels of noise produced.

4.2 Methodology

The geometry used for this research matches the experimental configuration designed and fabricated by Tao [6], as discussed in Section 3.10.1. Three geometries have been considered in this chapter; a clean duct, a single-orifice case and a double-orifice case with varying separation distances between the pair of orifices. The orifice geometry has been selected from the range of ADS components due to the fact that, at the time of writing this report, this was the only geometry where experimental data was available for validation of the numerical results. Furthermore, it is a component which has been extensively experimentally studied and a number of empirical relationships exists which are also useful for validation.

The circular ducting has a constant cross-sectional area along its length and a diameter, D, of 100mm. The orifices, defined in Figure 4.1, use a constant thickness, t_o, of 1.5mm and have an internal diameter, d, of 50mm. The external diameter of the orifice is constant at 100mm, which means that it is flush with the outer walls of the duct.

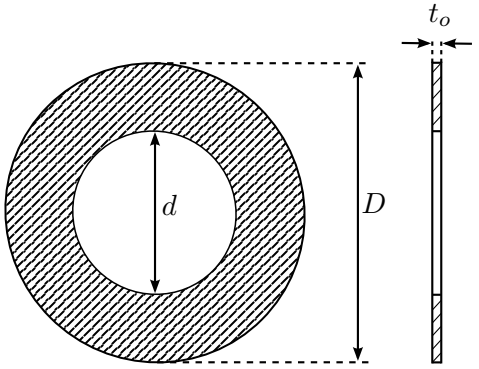

Figure 4.1: Schematic of the variable definitions for the orifice geometry.

Throughout the simulations in this chapter, the x-direction is defined as the streamwise direction along the length of the duct, with the y- and z-directions denoting the height and span from the centreline of the duct, respectively. The origin is defined as the centre of the duct along the x-axis. For the clean duct, the origin in the streamwise direction is on the inlet plane and for both orifice geometries, the origin in the streamwise direction is at the leading edge of the first orifice. The specific details of each case will be given in the following sections.

4.3 Clean duct

The purpose of the clean duct simulations was to develop a modelling procedure to be used with the more complex geometries considered later. This section includes an assessment of the suitability of the boundary conditions, initial flow conditions and turbulence models.

Two sets of boundary conditions were tested; the first being a cyclic (periodic) arrangement and the second being a velocity-inlet/pressure-outlet arrangement. A fully structured three dimensional mesh was used for this study, which is shown in Figure 4.2. The first grid point was placed at a distance of $1 \times 10^{-4}D$ away from the duct walls to provide a y^+ of $O(1)$ and uses a growth ratio of 1.15 in the wall normal direction. A total of 152 cells are used around the circumference of the duct and the maximum aspect ratio on the y-z plane is approximately 200 for the near-wall cells. A no-slip condition is used on the duct walls for both sets of boundary conditions.

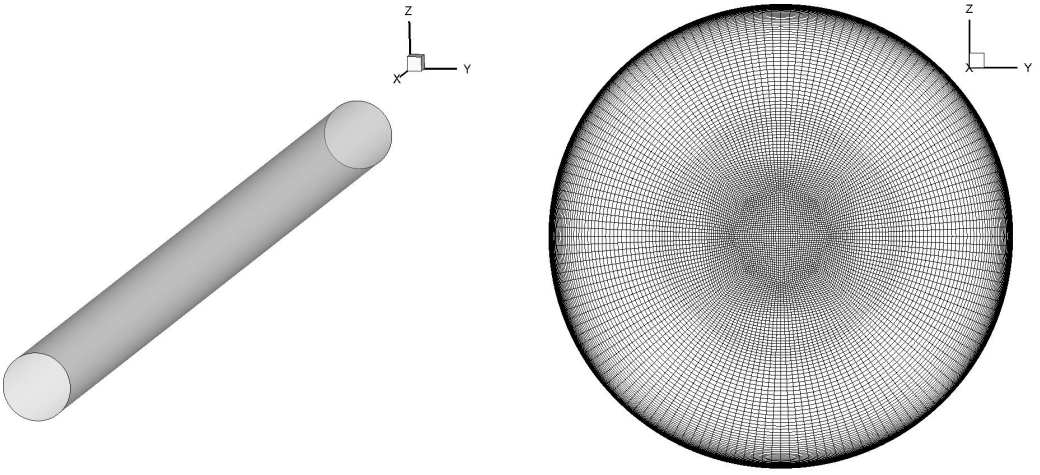

(a) Domain of the clean duct (b) Mesh in the y-z plane

Figure 4.2: Domain and mesh topology for the clean duct cases.

4.3.1 Periodic boundary conditions

The major benefit of periodic boundary conditions (PBC's) is that they remove the uncertainties introduced by the initial and boundary conditions. Therefore, the solution will always converge to the same fully developed state regardless of the initial flow field and this is a reason why they have been utilised in many similar studies in the past [84, 193, 194]. In this clean duct geometry, the PBC's, which are placed at the inlet and outlet boundaries, have the effect of creating a duct with infinite length in the streamwise direction. This produces a fully developed flow within the duct, providing that sufficient time is simulated.

One of the disadvantages of the use of PBC's is that there is no fixed inflow velocity. Over time, this means that the flow velocity within the duct will reduce due to the frictional effects from the duct walls. Therefore, in order to maintain a constant bulk velocity, it is necessary to use a driving force to counter the frictional losses. The method used in these studies, is to introduce an additional pressure gradient term into the momentum equation. This was implemented into both the 'simpleFoam' and 'pimpleFoam' solvers within OpenFOAM 2.2.2. The modifications were based on the implementation in the 'channelFoam' solver, but were extended to allow for the use of the full range of RANS/DES turbulence models available within OpenFOAM. These modifications led to the creation of two new solvers; 'simpleChannelFoam' (steady) and 'pimpleChannelFoam' (transient). These solvers are capable of maintaining a constant mass flow rate within a periodic duct by measuring the average flow rate (assuming constant density as these are incompressible solvers) and varying the magnitude of the forcing term in the momentum equation. Convergence is achieved through the use of a pressure gradient relaxation term, which limits the change in the pressure gradient at each timestep to $\frac{dp}{dx}_{\text{new}} = 0.3(\frac{dp}{dx}_{\text{max}} - \frac{dp}{dx}_{\text{current}})$.

For this study, the mesh detailed in Section 4.3 is utilised, with a streamwise length of $10D$ and comprising of approximately 0.8 million cells. In order to match the typical bulk flow velocities found in the ducting of an ADS, five RANS turbulence models were simulated at 10m/s. The simulation is progressed until the driving pressure gradient converges. The resulting fully developed mean profiles were compared to experimental data of the fully developed flow, which can be seen in Figure 4.3. Of the models tested, it was found that the Spalart-Allmaras (S-A) and k-ε models provided the best comparisons of fully developed mean velocity profile. The k-ω family of models provided a fair comparison to the experimental data, however, they predict a thinner boundary layer, resulting in a lower centreline velocity.

A further validation was conducted using the theoretical pressure drop for a clean pipe estimated from Equation 2.2. The comparison given in Table 4.1 shows that there are significant differences between the turbulence models. The prediction for the S-A and the k-ω models shows a very good comparison, particularly the k-ω SST. These models predict within 10% of the theoretical value. The family of k-ε models shows a significant overprediction of the predicted pressure losses, with values of approximately twice the theoretical value. However, this is expected, as the k-ε is known to exhibit shortcomings in internal flows, where the k-ω model performs much better [141, 195].

Overall, from the two validation quantities, the S-A and k-ω SST models have proven to best match the theoretical and experimental values for the clean duct flow. Therefore, these will be the models carried forward to further studies of the single and double orifice geometries.

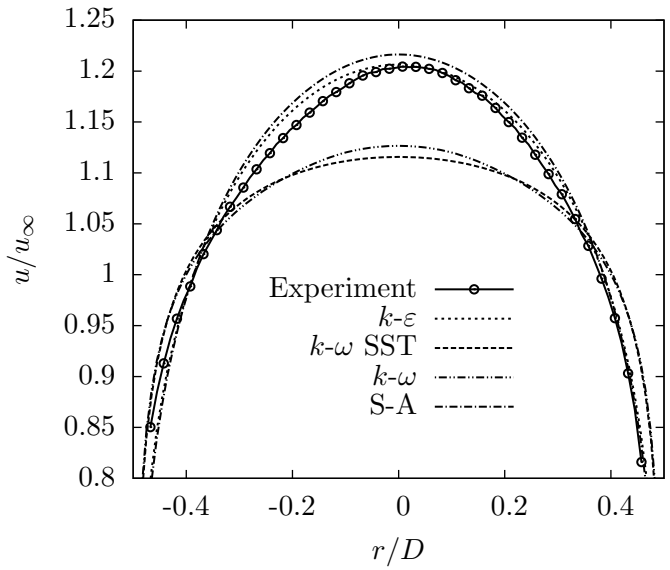

Figure 4.3: Comparison of the fully developed mean velocity profiles for a range of RANS turbulence models.

Model	**Pressure loss (Pa/m)**
Theory	11.81
Spalart-Allmaras	10.96
Launder Sharma k-ε	20.16
RNG k-ε	19.21
Realiseable k-ε	19.20
k-ω	10.74
k-ω SST	11.77

Table 4.1: Comparison of theoretical and simulated pressure losses per metre for Re_D = 67000.

4.3.2 Inlet/outlet boundary conditions

Whilst the PBC's are useful for the clean duct geometry, they have limited applicability when considering an orifice flow (unless an infinite series of equally spaced orifices are of interest). Therefore, for simulating a single orifice geometry, it is necessary that a set of independent inlet and outlet boundary conditions are applied.

Firstly, the streamwise spatial development of the different turbulence models is compared using experimental data. In order to do this, the clean duct mesh detailed in Section 4.3 is extended to a total length of $40D$ to exceed the entrance length, calculated using Equation 2.1. This resulted in a mesh of approximately 3.2 million cells. A uniform fixed velocity boundary condition was used on the inflow faces of the duct, to provide a flow velocity of 10m/s and a fixed zero gauge pressure was used at the outflow. The other boundary conditions are the same as those presented in Table 3.4.

The experimental data used for validation was collected using a pitot tube which was traversed in the spanwise direction across 76 equally spaced measurement points. Three experimental measurement locations were used, which correspond to $15D$, $39D$ and $59D$

downstream from the exit of the silencer. The results show very similar profiles at $39D$ and $59D$, indicating that the flow is fully developed by this point. This is in keeping with the entrance length calculations.

The mean numerical velocity profiles were extracted at distances of $15D$ and $39D$ from the inlet boundary and are validated using the experimental results in Figure 4.4. The development of the velocity profile for the S-A model shows a slightly unphysical pullback of the velocity on the centreline at $15D$ downstream of the inlet, but when fully developed gives a very good comparison to the experimental data at $39D$. The k-ω SST model shows an over prediction of the spatial development in the first $15D$ of the duct, and then the same underprediction of the fully developed centreline velocity is seen as in the cyclic cases. However, the shape whilst the profile is developing is a more realistic representation of the way the flow behaves within the duct. One issue which may be contributing to the differences between the experimental and simulated results is the addition of a silencer in the experiment which provides some extra development length upstream of the entry to the clean duct test section.

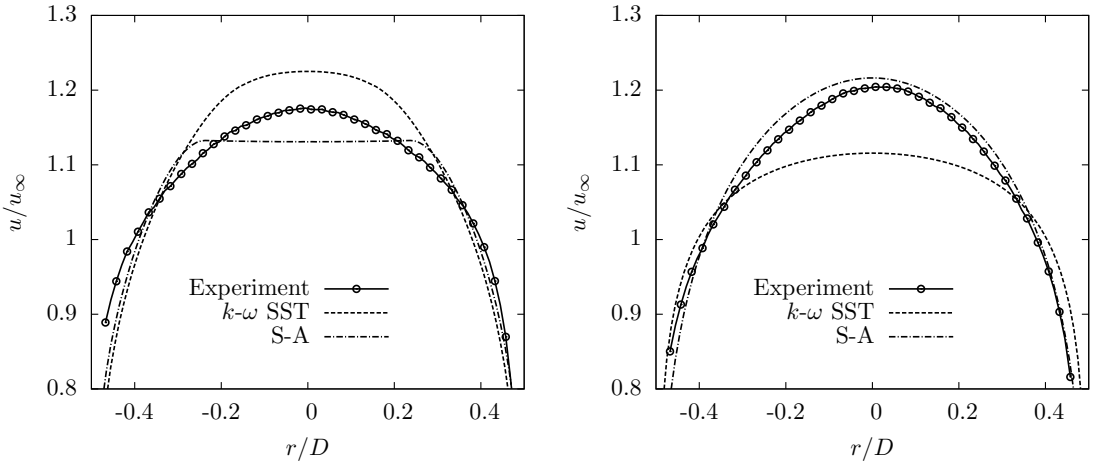

(a) $15D$ downstream of inlet

(b) $39D$ downstream of inlet

Figure 4.4: Mean velocity profiles for the streamwise development of the flow within the duct.

The importance of having a fully developed velocity profile upstream of the orifice is noted in empirical models for orifice noise [14, 15]. However, it would be impractical to simulate an inlet length of $40D$ upstream of the orifice. Therefore, it is desired that a fully developed velocity profile is specified at the inlet boundary to reduce the required development length. Initially, attempts were made to specify a fully developed profile using a theoretical one-seventh or one-eighth power law. However, the specified profile provided an incorrect gradient near y=0 and y=R and this method of specifying the profile from an analytical equation was discounted.

The second option for the specification of a fully developed profile is to equation fit the experimental data. This was done using a sixth order polynomial near the walls and a

second order polynomial in the central region of the duct. Suitable values were chosen very close to the walls, where the experimental profile could not be measured:

$$\begin{aligned} u &= u_{\max}(-97.401r^2 - 0.887r + 1.001239), \text{if } r/D \leq 0.381, \\ u &= u_{\max}(-6.53e12r^6 + 1.67e12r^5 - 1.78e11r^4 + 1.01e10r^3 - 3.21e8r^2 \\ &\quad +5.44e6r - 34425), \text{if } r/D > 0.381 \end{aligned} \tag{4.1}$$

where r is the radial distance from the centreline of the duct and $u_{\max}$ is the maximum velocity on the centreline of the duct. The result of this fitting is shown in Figure 4.5. The resulting equation was then implemented into a boundary condition which is used throughout all future simulations.

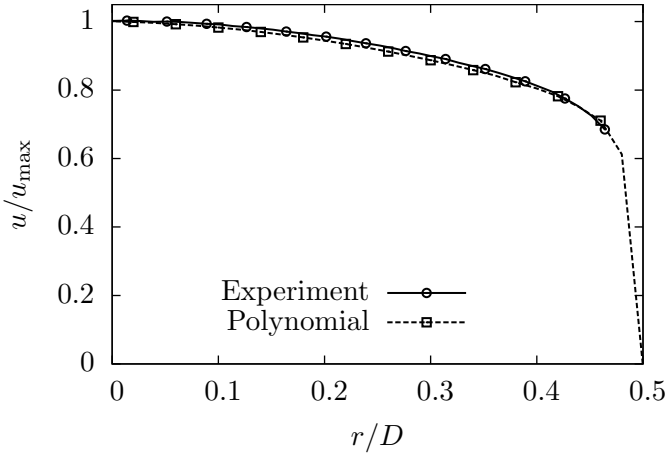

Figure 4.5: Comparison of the experimental fully developed mean velocity profile and the polynomial Equation 4.1 fitted to the data.

4.4 Single orifice

In order to understand the effect of additional upstream turbulence on an orifice, it was first necessary to establish results for the baseline single orifice. The single orifice geometry is meshed with a first cell height of $1 \times 10^{-4}D$ to provide a y^+ of $O(1)$ and uses a growth ratio of 1.15 in the wall normal direction. A total of 152 cells are used around the circumference of the duct, which has a maximum aspect ratio of 200 on the y-z plane. Across the inside edge of the orifice, seven equally spaced mesh points are used to give a resolution of 0.21mm. Mesh refinement is concentrated in the region downstream of the orifice to capture the development of the shear layers and results in a mesh size of approximately 4.1 million. The length of the domain was chosen as $10D$ upstream and $40D$ downstream of the orifice. The mesh on the y-z plane and a zoomed in image of the orifice on the x-y plane can be seen in Figure 4.6. The steady fully developed velocity profile was defined at the inlet boundary and a zero gauge pressure is fixed at outlet. No-slip conditions are applied to the walls of the duct and the orifice.

All other boundary conditions are listed in Table 3.4. Based on the previous section, the k-ω SST turbulence model is used at a flow velocity, u_∞, of 10m/s. Further to this, the simulation was initially run for $50T_D$, where $T_D = D/u_\infty$, after which averaging of the mean values was performed for a further $30T_D$.

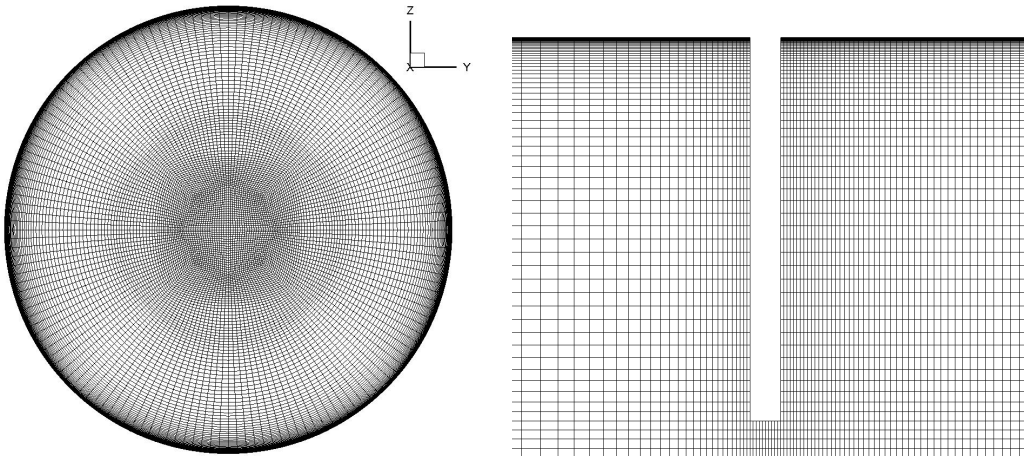

(a) Mesh slice in y-z-plane (b) Mesh slice in x-z-plane

Figure 4.6: Single orifice mesh topology.

The 'simpleChannelFoam' solver was tested on the single orifice configuration and it was found that the convergence was poor, primarily due to the inherent unsteadiness in the flowfield due to the large recirculation regions directly behind the orifice. The unsteady solver 'pimpleChannelFoam' showed better convergence, and hence only the results from this solver are presented in the remainder of this section.

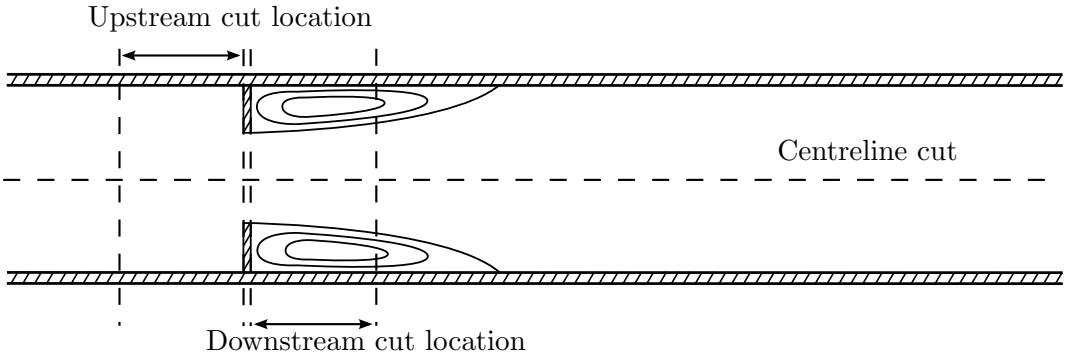

Figure 4.7: Schematic of the sampling lines within the domain for comparison of the mean velocity, k and volumetric sound sources.

Firstly, the inlet and outlet domain lengths were validated. To check the suitability of the inlet domain length, the fully developed velocity profile, from Equation 4.1, was specified at the inlet and the variation from this input profile was measured at a series of spanwise upstream cut locations as the flow travelled through the duct towards the orifice. Figure 4.7 shows the system used to extract data both from locations upstream and downstream

of the orifice along the radius and centreline of the duct. The measurements were taken along a one-dimensional line.

Figure 4.8(a) shows the difference between the input velocity profile and the calculated velocity profile at that point. The results show little upstream influence from the orifice for distances of greater than $3D$ which is in good agreement with previous experimental data [7]. A similar study was performed to check the outlet domain length, where the velocity was compared to the fully developed profiles at various distances downstream of the orifice. Figure 4.8(b) illustrates that the flow is approximately fully developed by $40D$ downstream, again in good agreement to Bull and Agarwal [7]. It would however take longer than the simulated domain length to reduce this error to zero.

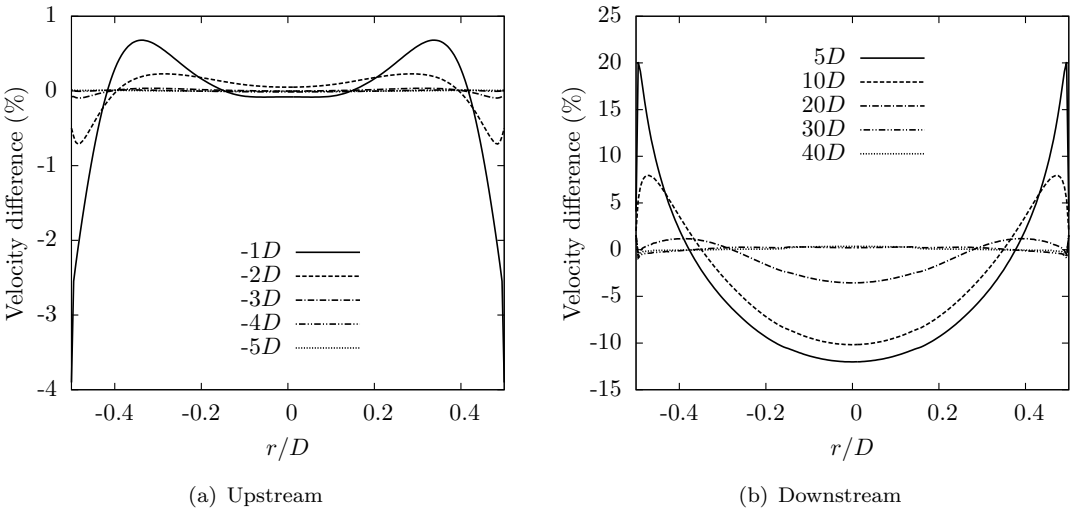

(a) Upstream (b) Downstream

Figure 4.8: Comparison of the differences between the profiles at selected cut-planes and the fully developed flow profiles.

The prominent flow features noted in previous literature in Section 2.4, can be seen in the velocity and turbulent kinetic energy contours in Figure 4.9. The jet through the centre of the orifice reaches velocities of approximately six times the freestream velocity, at the vena-contracta at approximately $0.4D$ downstream of the orifice, as shown in Figure 4.10. There is a region along the centreline, at approximately $4D$ downstream, where the velocity falls below freestream values. Directly behind the faces of the orifice, a long recirculation region exists downstream, which is predicted to reattach at approximately $2.9D$, significantly longer than the predicted $2.5D$ [163]. The difference can be attributed to an incorrect development of the shear layers, a common problem with similar geometries, such as a backward facing step, which has been attributed to a mixture of mesh resolution, turbulence modelling and initial conditions [118, 126]. The turbulent kinetic energy is plotted along the centreline of the duct and shows two peaks, the first illustrating a source of turbulence in the mouth of the orifice, caused by separation from the edges of the contraction, and the second highlighting the interaction of the axi-symmetric shear layer downstream of the jet. The acceleration of the flow results in

a large drop in pressure through the orifice of approximately $C_D = 22.5$. Comparison to the experimentally measured value of $C_D = 34.23$ shows that the pressure drop is underpredicted. This problem can also be attributed to the incorrect prediction and development of the shear layers. This is a problem that should be investigated as part of future work on this topic. Given the scope of this project and the timescale, it was not possible to address this issue in this work.

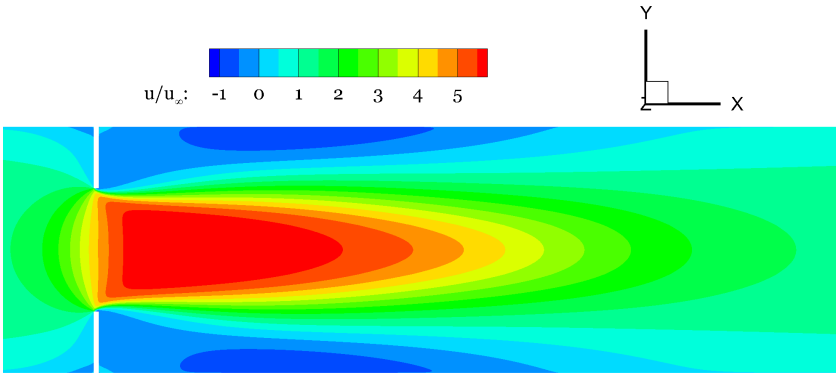

(a) Mean velocity

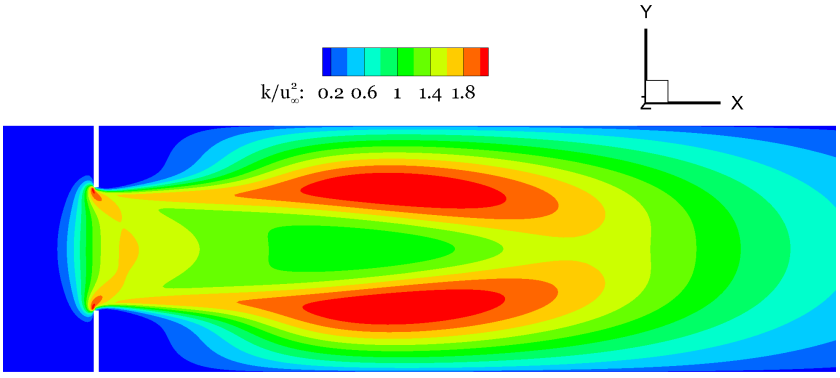

(b) Mean turbulent kinetic energy

Figure 4.9: Contours of the mean velocity and turbulent kinetic energy on the x-y plane of the mesh.

The highest levels of turbulence (and largest corresponding velocity fluctuations) are seen in the shear layers between the jet and the recirculation region. In order to better quantify the velocity and k variations downstream of the duct, a number of slices were taken at varying downstream distances of up to $5D$. The results are shown in Figure 4.11. The velocity profiles show the high velocity jet and the recirculation region close to the orifice, but at distances greater than $4D$ the flow is seen to have mostly recovered. However, when considering the k profiles, there are significantly higher turbulence levels in the duct, even at $5D$ downstream. The maximum values are seen at approximately $1D$ downstream where the shear layers have fully formed. This data shows that the additional turbulence generated by the orifice persists far downstream and will increase the turbulence levels upstream of tandem components.

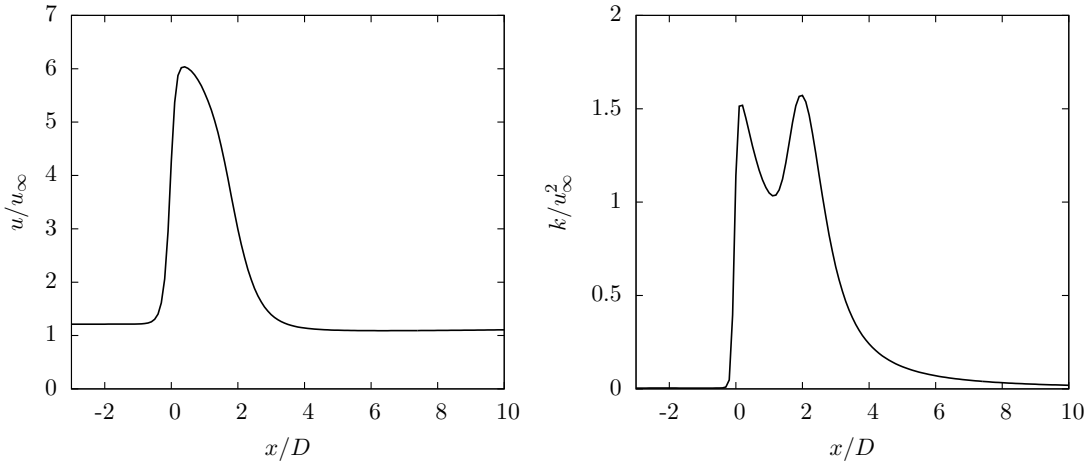

(a) Normalised velocity

(b) Normalised turbulent kinetic energy

Figure 4.10: Normalised velocity and turbulent kinetic energy on the centreline of the duct.

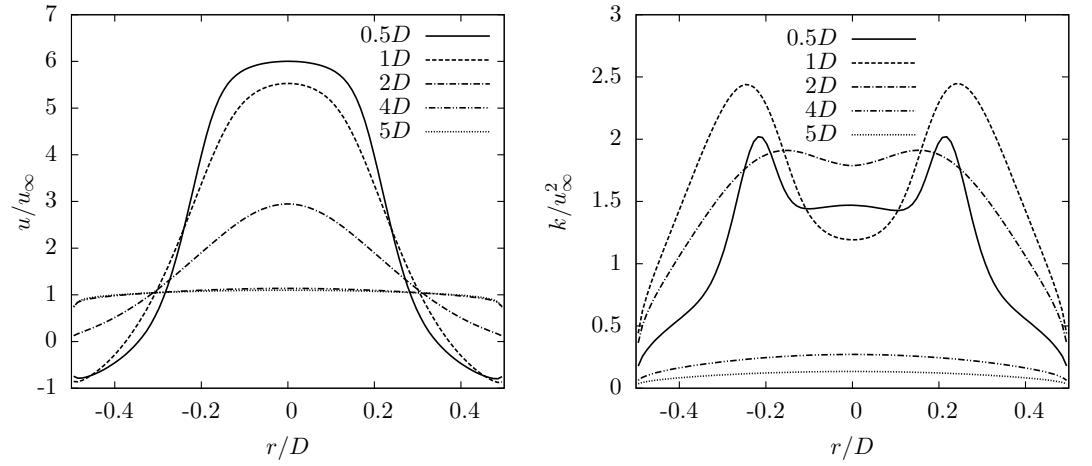

(a) Normalised velocity

(b) Normalised turbulent kinetic energy

Figure 4.11: Normalised velocity and turbulent kinetic energy profiles at cut-planes downstream of the orifice.

Estimates of the volumetric noise sources within the wake of the orifice have been made using Proudman's analogy, Equation 3.83, and are shown in Figure 4.12. This analogy correlates the k and ε fields to the sound produced by quadrupole sources within the flow. Within the downstream range investigated, the results show strong similarities, particularly in profile shape, to the k profiles, shown in Figure 4.11, and suggest that the sound generation within the volume is dominated by the k. The maximum values are seen within the shear layers up to $2D$ downstream of the orifice, with a rapid reduction in noise generation outside the shear layers. This analogy suggests that if the incoming turbulence increases the turbulence produced by an orifice, this will correspond to an increase in the volumetric noise sources within the wake.

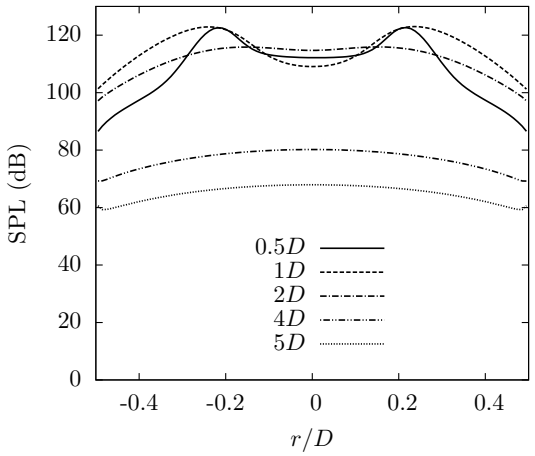

Figure 4.12: Normalised SPL profiles from volumetric sound sources at cut-planes downstream of the orifice.

Despite the shortcomings of these simulations, the results show a reasonable comparison to some of the fundamental properties of the orifice flow and provide a cost effective method for estimating the interaction effects of the in-duct components. In the following section, an additional orifice will be introduced upstream to investigate the interaction effects of tandem in-duct components.

4.5 Double orifice

A series of double orifice simulations have been performed using a pair of d=50mm orifices. The distance between the two orifices has been denoted by the variable B which is shown schematically in Figure 4.13. The measurement distance is taken from the downstream edge of the first orifice to the upstream edge of the second orifice. The separation distances have been varied between 0.5-10D and the effect of the separation has been quantified using the k profiles, velocity profiles and estimated volumetric sound source profiles.

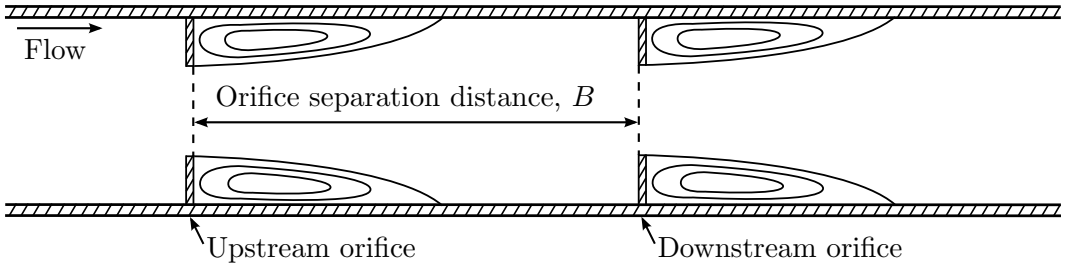

Figure 4.13: Schematic of the variable used to define the double orifice separation distance.

The double orifice geometry is meshed with a first cell height of $1 \times 10^{-4}D$ to provide a y^+ of $O(1)$ and uses a growth ratio of 1.15 in the wall normal direction. The circumference of the duct is discretised using 152 cells are used around the circumference of the duct, which has a maximum aspect ratio of 200 on the y-z plane. The mesh is refined in the streamwise direction in the regions between orifice pairs, gradually stretching the cells from 0.25mm close to the orifices up to a maximum of 3.33mm, to ensure that the development of the shear layers and the interaction of the wake with the downstream orifice is correctly captured. The cell count varies between 4.8-10.3 million depending on the length of the separation distance between the orifices. Following the studies of the required upstream domain length on the single orifice, an inlet length of $5D$ has been utilised along with a downstream domain length of $40D$. Figure 4.14 shows the mesh topology of the B=1D separation case. A fully developed velocity profile is specified at the inlet using the fitted experimental data, a zero gauge pressure is used at outlet and no-slip conditions are specified on the walls of the duct and the orifices. Other boundary conditions are given in Table 3.4. The simulations are performed using the k-ω SST model at a bulk velocity of 10m/s. The simulation was run through the transient phase for $50T_D$, after which averaging of the mean values was performed for a further $50T_D$. Additional averaging is required due to the increased flow unsteadiness. For the discussion of these results, the first orifice is denoted the upstream orifice and the second orifice is denoted the downstream orifice.

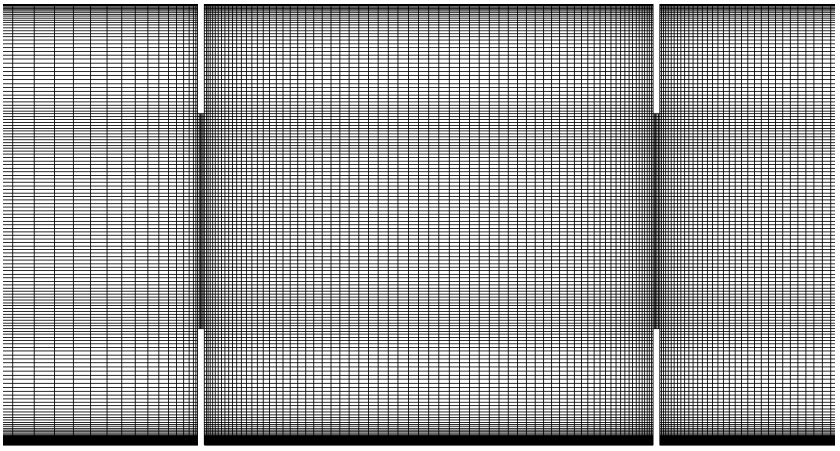

Figure 4.14: Zoomed in view of double orifice mesh.

4.5.1 Effect of separation distance on velocity

Contour plots of the velocity field for the B=1D, 2D and 4D cases are shown in Figure 4.15. The separation distance has a significant effect on the velocity field near the pair of orifices:

- The centreline velocity profiles (see Figure 4.16(a)) show that at separation distances of less than 1.5D, the shape of the jet flow through the first orifice is affected

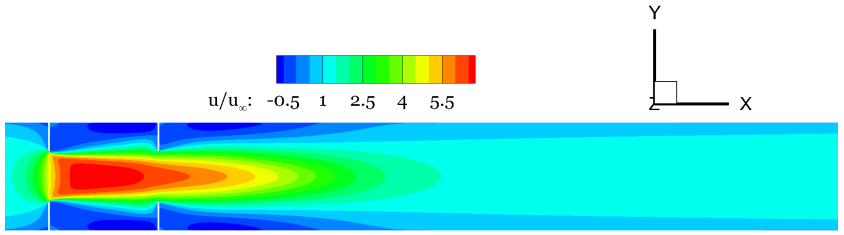

(a) B=1D

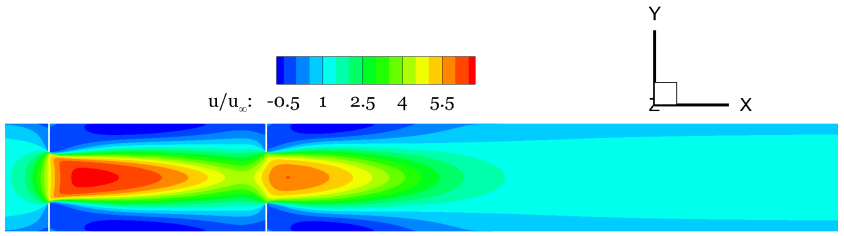

(b) B=2D

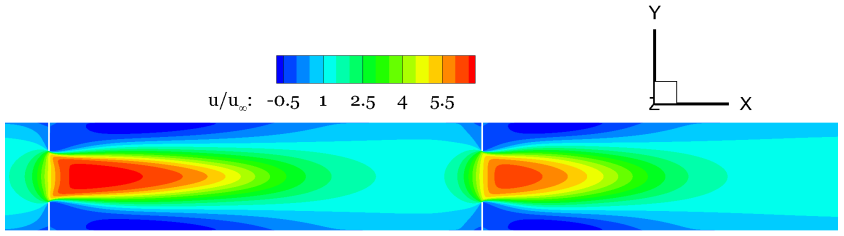

(c) B=4D

Figure 4.15: Mean velocity contours on the x-y plane for the double orifice cases at a range of separation distances.

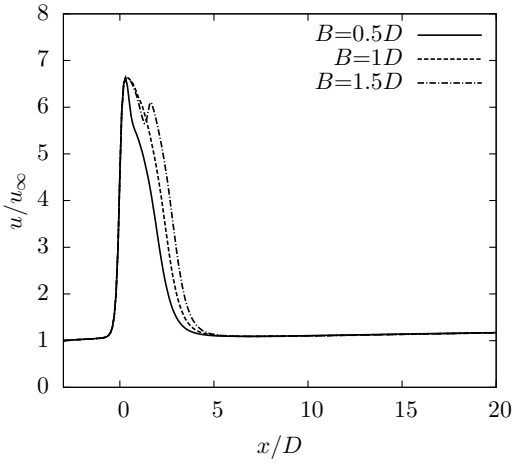

(a) $B \leq 1.5$

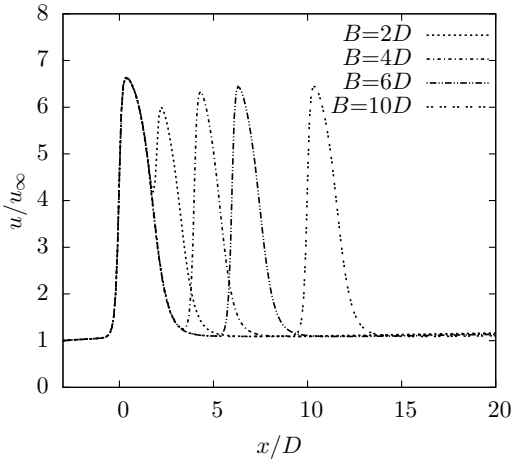

(b) $B \geq 2$

Figure 4.16: Mean normalised velocity profiles on the centreline for the double orifice cases at varying separation distances.

by the presence of the downstream orifice. This effect is not seen at separation distance of greater than 2D, (see Figure 4.16(b)) where the velocity peak for the

upstream orifice collapses regardless of the separation distance.

- At separation distances of less than $1D$, the jet through the orifices is seen to behave as a single jet (see Figure 4.16(a)). This is due to the jet passing through the centre of the downstream orifice, without expanding sufficiently to interact too heavily with the edges of the downstream orifice. At distances of greater than $1D$, the presence of a second peak through the downstream orifice is visible. This feature of the flow affects the length of the jet through the downstream orifice, which has been estimated as the downstream distance where the centreline velocity returns to 125% of its freestream value (see Figure 4.18(a)).

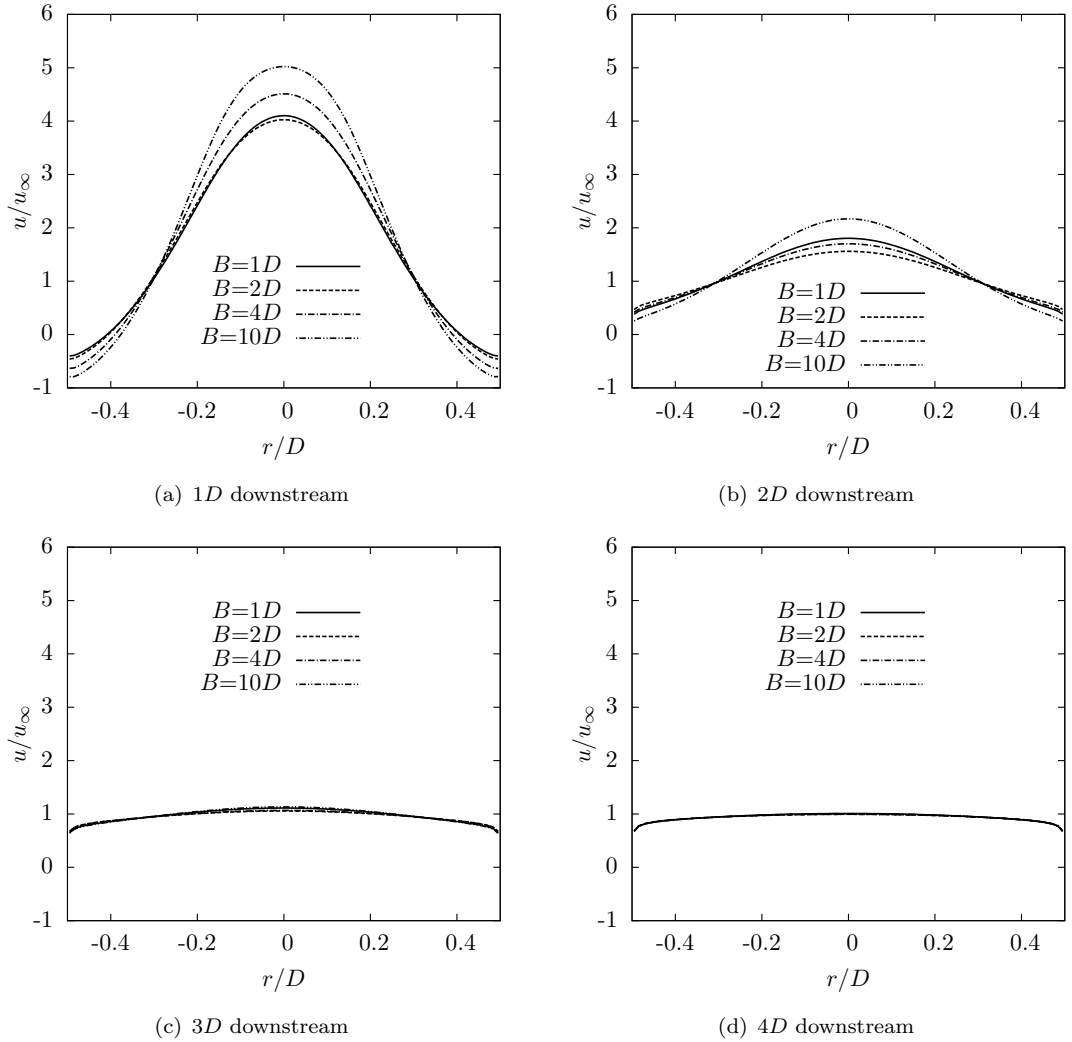

(a) $1D$ downstream

(b) $2D$ downstream

(c) $3D$ downstream

(d) $4D$ downstream

Figure 4.17: Mean normalised velocity profiles at various cut planes downstream of the downstream orifice at a range of separation distances.

- The velocity profile of the flow entering the downstream orifice has a significant effect on the peak velocities seen in the vena-contracta of the downstream orifice jet. This is evident throughout the range of separation distances considered, but most

significantly at separation distances of 1.5-2D (see Figures 4.16(a) and 4.16(b)). As the separation distance increases up to 10D the peak velocity in the jet is seen to become comparable to the single orifice case, indicating that this velocity profile is approaching its fully developed state before the downstream orifice.

- The centreline velocity is seen to recover within 4D of the downstream orifice (see Figure 4.17). This is despite differences in peak velocities and incoming velocity profiles.
- There is no effect on the flow upstream of the orifice pair caused by the presence of the downstream orifice. This suggests that when using two orifices of the same diameter, only the presence of the upstream orifice influences the flow upstream of the orifice pair.
- The pressure gradient required to drive the flow through the duct increases almost linearly from the single orifice up to separation distances of 2D. The required pressure gradient then reaches a maximum at a separation distance of approximately 4D before reducing linearly from 4-10D (see Figure 4.18(b)). This may be due to the fact that the 4D separation is the largest distance where the centreline velocity does not recover to freestream values before passing through the downstream orifice. This implies that the velocity within the duct would be high over a long section of duct, resulting in larger friction and pressure losses.

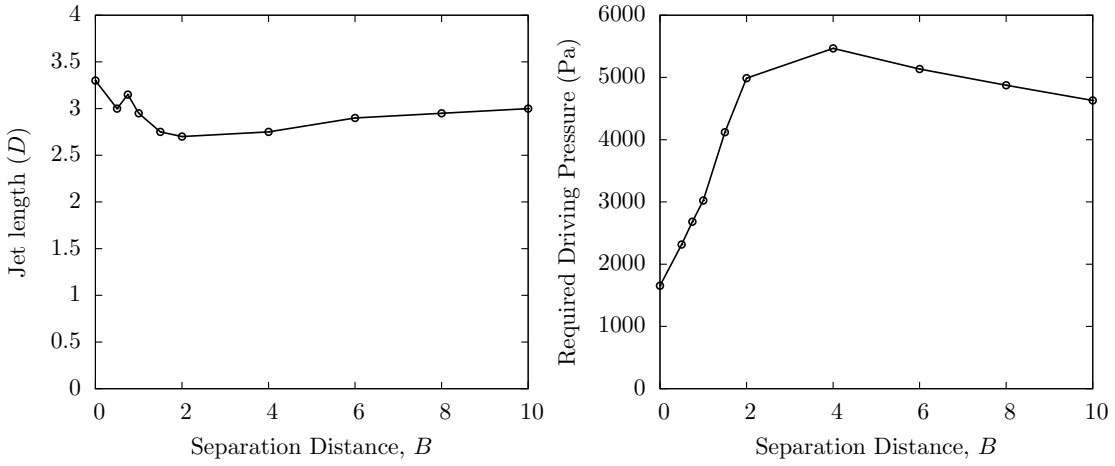

(a) Jet length

(b) Required driving pressure

Figure 4.18: Variation of the mean jet length and driving pressure for varying orifice separation distances.

4.5.2 Effect of separation distance on TKE

The interaction between orifices has a significant effect on the k fields within the duct. Contour plots of the k field on an x-y slice through the domain, for separation distances

of B=1D, 2D and 4D, are shown in Figure 4.19. A number of key points have been noted:

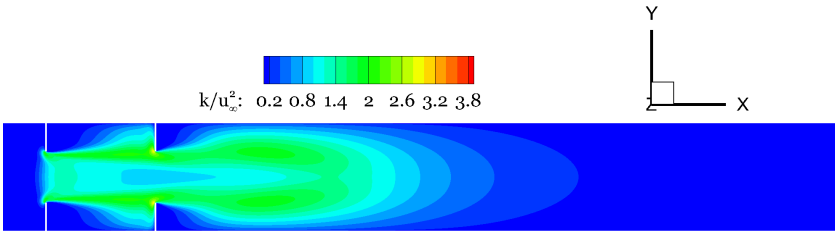

(a) B=1D

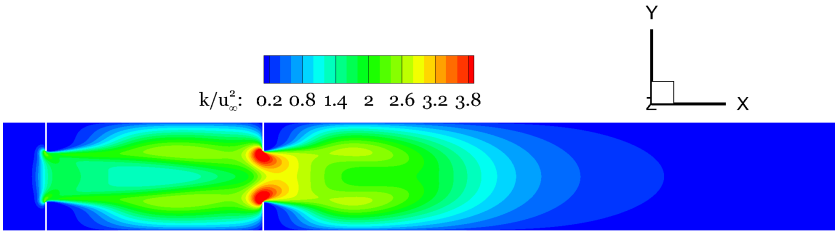

(b) B=2D

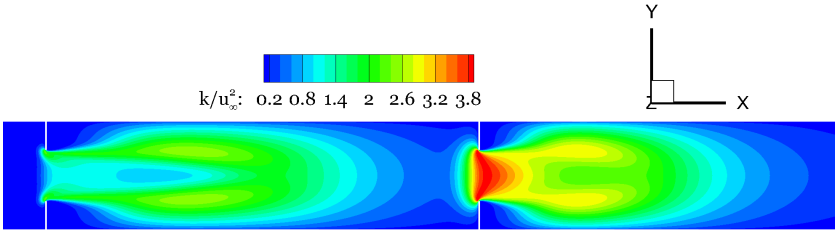

(c) B=4D

Figure 4.19: Mean turbulent kinetic energy contours on the x-y plane for the double orifice cases at a range of separation distances.

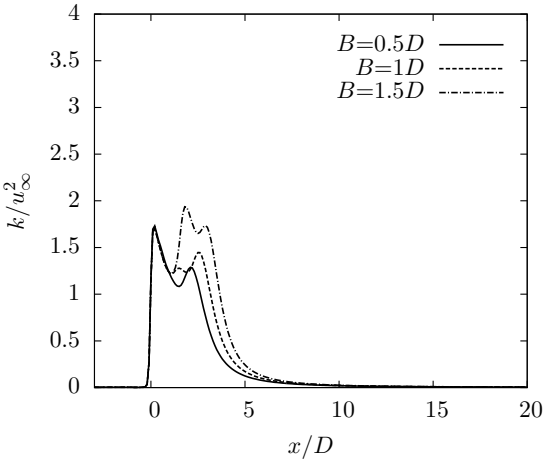

(a) $B \leq 1.5$

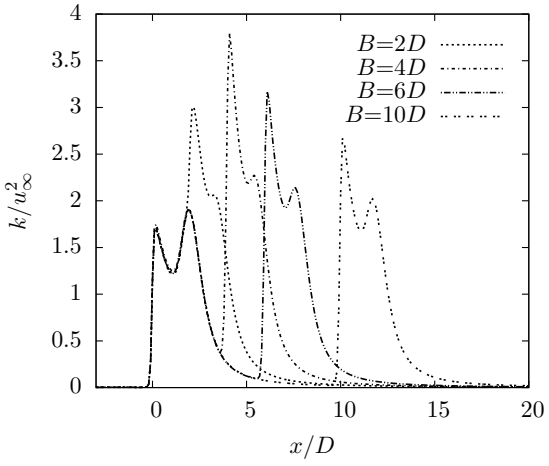

(b) $B \geq 2$

Figure 4.20: Mean turbulent kinetic energy profiles on the centreline for the double orifice cases at varying separation distances.

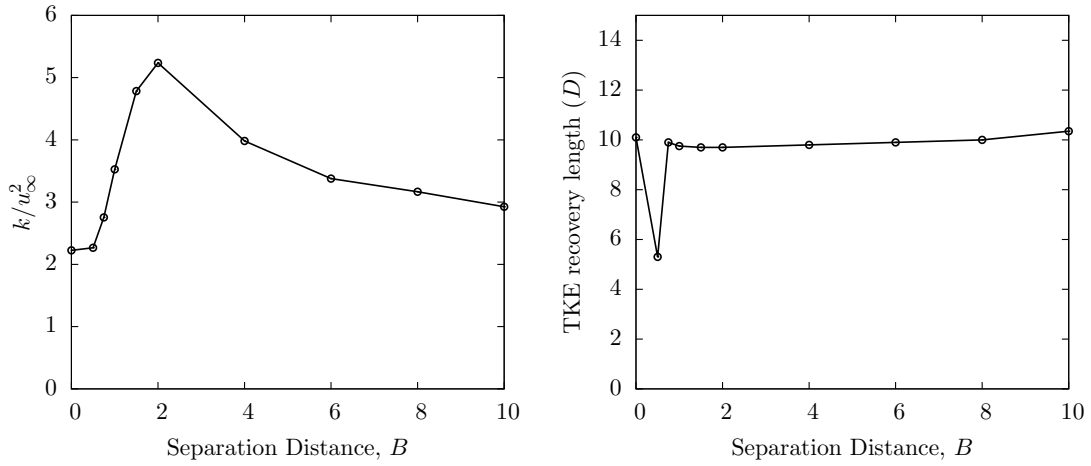

(a) Normalised maximum turbulent kinetic energy

(b) Recovery length of TKE values

Figure 4.21: Maximum normalised turbulent kinetic energy values and turbulent kinetic energy recovery lengths for varying separation distances.

- The levels of k at the inflow to the orifices significantly affect the turbulence produced by the orifices. The inflow turbulence mainly affects the first source of turbulence (the lateral flow and separation from the edges of the orifice). The second peak, at the point where the shear layer interacts, is only seen to be affected when the turbulence levels produced in the mouth of the orifice are higher than those produced by the shear layers. This suggests that it is the convection of turbulence from the mouth of the orifice that increases the levels at the shear layer interaction location.

- At separation distances greater than $2D$ (see Figure 4.20(b)), the k levels through the upstream orifice are comparable to that of the single orifice case. This is in keeping with the velocity profile measurements.

- The levels of k through the downstream orifice are increased by the turbulence in the wake of the upstream orifice at separation distances greater than $1D$. This effect is still seen at the largest separation distance measured and would be expected to have an influence even at large separation distances approaching the entrance length of the duct.

- At small separation distances of less than $1.5D$ (see Figure 4.20(a)), the k levels along the duct centreline are much lower. This is caused by the suppression of the formation of the shear layers by the close proximity of the downstream orifice.

- The maximum levels of k, within the domain (see Figure 4.21(a)), are found within the shear layers and as such are not apparent from the centreline plots. The maximum values are found at separation distances of between 2-4D, where the shear layers have the distance to fully form between the orifices but are still in

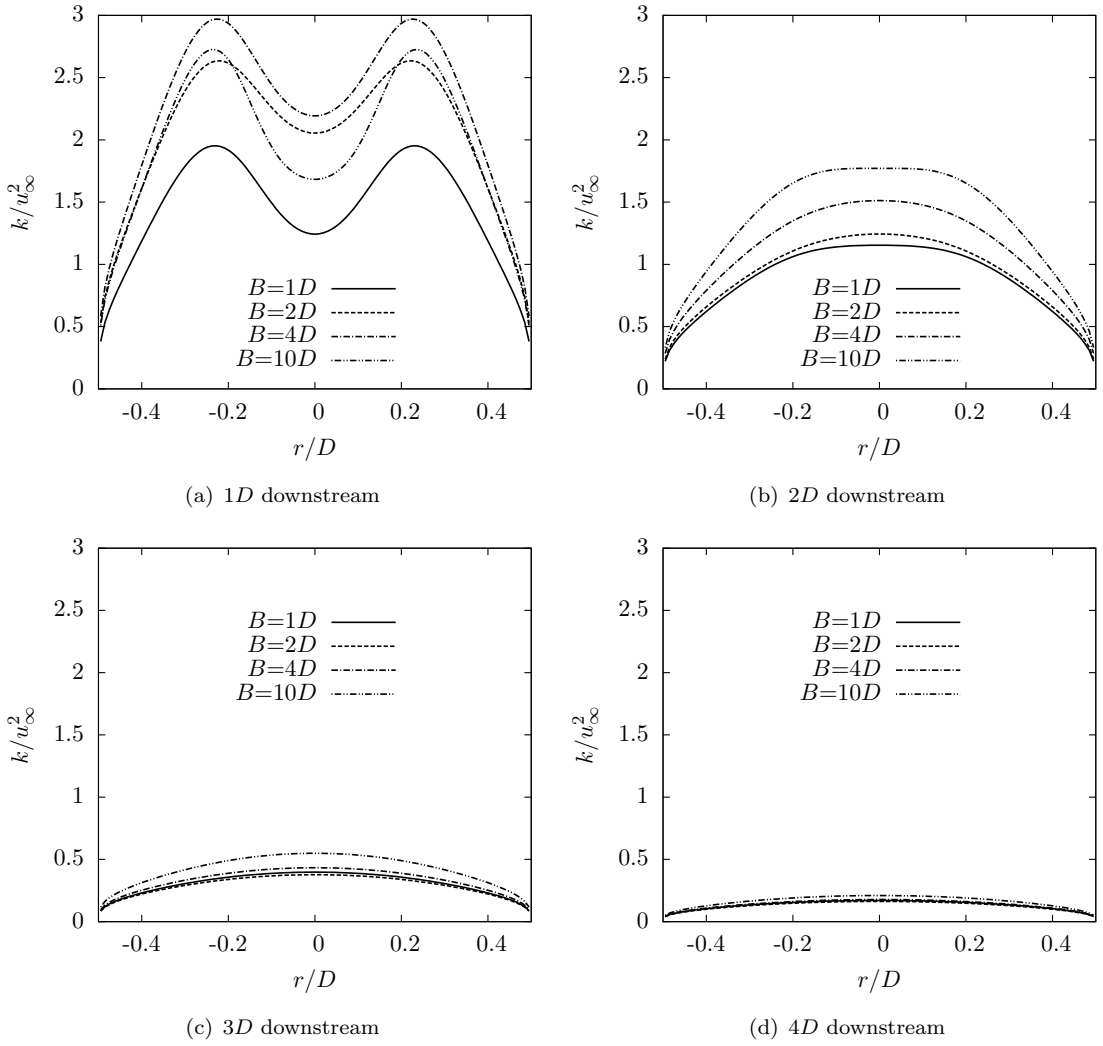

(a) 1D downstream

(b) 2D downstream

(c) 3D downstream

(d) 4D downstream

Figure 4.22: Mean turbulent kinetic energy profiles at various cut planes downstream of the downstream orifice at a range of separation distances.

close proximity to the downstream orifice. This may explain the large required pressure gradient for a separation distance of $4D$. The maximum values also support the findings that the smaller separation distances produce lower levels of turbulence after the downstream orifice. At a separation distance of $10D$, the maximum values of k are still higher than for the single orifice.

- The recovery length of the turbulent kinetic energy, defined as the streamwise distance for the centreline k to return to 500% of its freestream value (see Figure 4.21(b)), is seen to remain relatively unchanged (there is a slight increase with separation distance which can be seen in the spanwise cut profiles in Figure 4.22) for all separation distances except for B=0.5D. The reasoning for this is that the shear layer formation behind the upstream orifice is almost completely inhibited at this separation distance, to the extent that the k levels are approximately 50%

lower than the single orifice case. This provides a large reduction in the turbulence levels in the wake of the downstream orifice and a shorter recovery length.

- The k levels at cut planes in the wake of the downstream orifice for the $10D$ separation distance are seen to be the highest (see Figure 4.22). This is not because there is more k produced by the orifice shear layers at this separation distance, but can be explained by the better recovery of the velocity profile in the duct upstream of the orifice and the resulting higher jet velocity. This then leads to shear layers which extend further downstream, due to the increase in jet length, meaning that the k levels are higher at cut planes further downstream of the orifice, but lower in the immediate vicinity of the orifice (see Figure 4.22(a)).

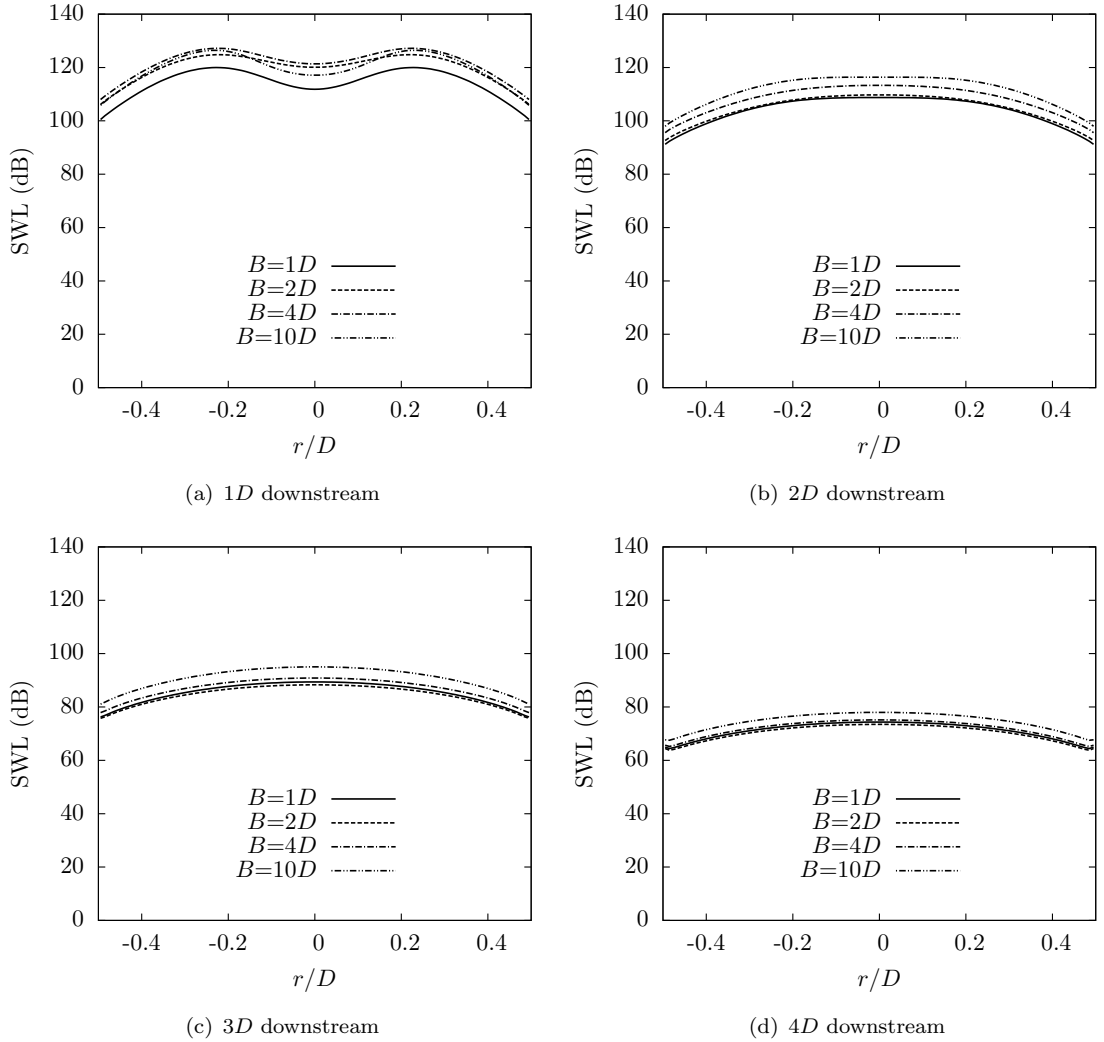

(a) $1D$ downstream

(b) $2D$ downstream

(c) $3D$ downstream

(d) $4D$ downstream

Figure 4.23: Mean estimated volumetric sound source profiles at various cut planes downstream of the downstream orifice at a range of separation distances.

4.5.3 Effect of separation distance on volumetric noise sources

The differences in the volumetric noise sources, estimated from Proudman's formula (Equation 3.83), are shown in Figure 4.23. It must be noted that the estimation provides information only on the sources of noise, not the sound power level at that particular point. The key points of interest in these results are:

- The largest sound sources are located close to the orifice and become weaker with increasing downstream distance from the orifice. As these noise quadrupole noise sources are caused by turbulence, it is logical that the shape of the profiles is very similar to the shape of the k profiles at the same locations.
- Across the span of the duct, the largest noise sources are towards the centreline and the lowest noise sources are located near to the duct walls. This is primarily due to the diffusion of turbulence from the shear layers into the centre of the duct before diffusing outwards towards the walls. The cut at $4D$ shows a relatively uniform profile across the duct.
- The noise produced by the $10D$ separation case produces the highest levels of noise except when very close downstream of the orifice. This is due to the development of the velocity profile upstream of the orifice as explained in the previous section.

4.6 Summary

Overall, there is one clear feature in the results. There is a link between the turbulence levels upstream and downstream of an orifice. The separation distance between the pair of orifices and the resulting turbulence levels and velocity profile between the orifices significantly influence the flow in the wake of the downstream orifice. When an orifice is placed at a critical distance upstream of a second orifice, the turbulence in the wake can increase the turbulence levels produced by the downstream orifice by more than twice what it would produce with a clean inflow. The volumetric noise sources, which are known to depend on the turbulence, are therefore significantly increased in the wake of the downstream orifice as well, leading to higher estimated noise levels.

One of the disadvantages of the method employed here is that it is quite specific to orifice flows in tandem. In a typical ADS system, the components that are placed upstream of an orifice will produce a different wake profile to that seen behind the orifices, such that the vortices and strong shear layers may not be present. Therefore, in order to make the study more generally applicable to all components within an ADS, a more general approach to increasing the upstream turbulence levels is required. Further quantification of the other sources of noise, such as dipole and monopole sources is also desired. For this reason, and to allow for quantification of the noise produced by the orifice, a more accurate time resolved simulation is required, with better control over the incoming turbulence levels.

Chapter 5

Noise Generation within the Air Distribution System

5.1 Introduction

In the previous chapter, it was shown that there is a link between the upstream and downstream turbulence levels in an orifice flow. What was not considered, however, was the link between the turbulence levels and the noise.

Whilst many previous computational studies on ADS interaction noise have studied orifice pairs [12, 72, 74], it is very unlikely that two components of the same type would be placed in tandem within a duct. Furthermore, the orifice pairs tend to have small separation distances (1-2D) which means that there is a strong influence from the shear layers and heavily non-uniform flow upstream of the second orifice. Whilst this type of wake could be present within a real ADS, there would be a tendency towards a more uniform upstream turbulence, due to the fact that the other components produce smaller scale turbulence due to the smaller characteristic length scales of the geometries and the lack of a high velocity jet. Therefore, whilst the orifice pair is a useful method for increasing turbulence levels upstream of the second component, it doesn't accurately represent a real system. In order to establish the link between the turbulence and the noise for the components of an ADS, it is important that a more general and controllable type of turbulence is introduced into the duct upstream of the orifice. Therefore, a different physical body has been used to create additional turbulence, without the vortices, strong shear layers and significant additional noise that is produced by an upstream orifice.

The objectives for this chapter are twofold; the first is to gain a better understanding of the noise sources present in an orifice flow without upstream turbulence, in order to identify the sources of orifice self noise. The second aim is to identify the way in which increased levels of freestream turbulence interacts with an orifice to increase the noise produced. The structure of this chapter is as follows: Firstly, the orifice geometry will be introduced, along with the method for increasing the upstream turbulence

levels. Following this, a validation of the modelling approach for an orifice without additional turbulence is performed and the source mechanisms for the isolated orifice are investigated. Finally, the higher turbulence configurations are validated and the mechanisms for the additional noise due to turbulence are investigated. Throughout this chapter, the results from the simulations have been compared to the experimental results of Tao [6] where possible. The experimental facility is discussed in Section 3.10.1 and the experimental methodology is discussed within the relevant results sections of this chapter.

5.2 Geometry and turbulence generation methodology

In this chapter, the geometry investigated is that of an isolated single orifice with varying upstream turbulence levels. The orifice geometry is the same as that shown schematically in Figure 4.1, which has an inner diameter of d=65mm, a thickness of t_o=1.5mm and an outer diameter of D=100mm, such that it is flush with the outer ducting. The only difference from the orifices considered in Chapter 4 is the larger internal diameter, which will result in a lower jet velocity, weaker shear layer gradients and lower noise levels.

Additional turbulence generation is a critical part of this project. The method adopted involves the use of a physical bluff body placed upstream of the orifice, such that the wake of the body convects downstream and interacts with the orifice. Whilst this is a simple method to implement, it does have a number of drawbacks. The addition of another bluff body can significantly increase the computational cost of the simulation, due to the increased duct length required and the additional refinement region around the upstream body/propagation region between that body and the orifice. There is also the added difficulty of dealing with the non-uniform wake profile generated by the upstream bluff body, which may be different to the turbulence found in the wake of typical ADS components. However, the main overriding advantage of this method is that it exactly matches the experimental configuration of Tao [6] and enables direct comparison and validation using the experimental data.

The bluff body chosen for this purpose is a ring geometry. The geometry is shown schematically in Figure 5.1, where the external diameter, d_o=37.5mm, the internal diameter, d_i=27.5mm and the thickness t_r=3mm. The centre of the ring was placed on the centreline of the duct and the turbulence intensity upstream of the orifice could be varied by changing the ring separation distance, shown schematically in Figure 5.2.

The ring allows two useful inflow conditions to be modelled. Firstly, when fully developed duct turbulence is desired, the ring can provide the required perturbations to accelerate the development of the turbulence in the duct section upstream of the orifice and secondly, the ring can be used to directly raise the turbulence levels upstream of the orifice, to allow for an investigation of the effect of additional turbulence on the noise produced by an orifice. The positioning of the ring is crucial to ensure that the correct

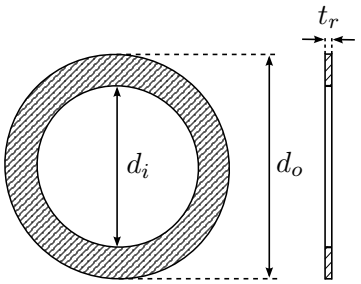

Figure 5.1: Schematic of the variables used in the definition of the ring geometry.

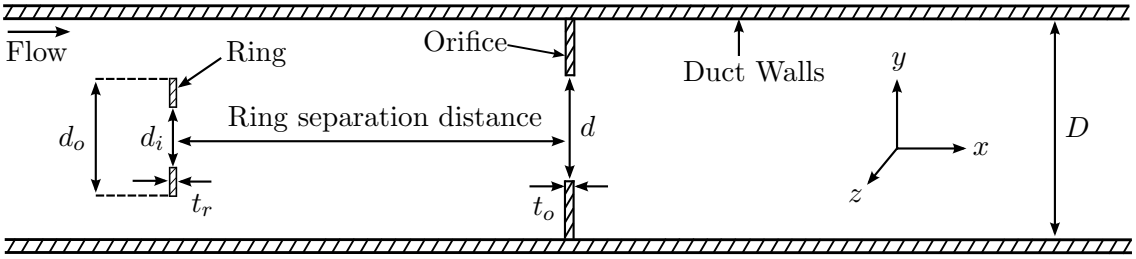

Figure 5.2: A schematic of the geometry and definitions for the single orifice cases with a ring present at varying distances upstream.

inflow conditions are produced. For the fully developed duct turbulence, the ring must be placed far upstream, such that the increased turbulence levels in the wake of the ring can decay down to typical duct levels before the flow reaches the orifice. In order to significantly raise the incoming turbulence levels, the ring must be placed sufficiently close to the orifice such that the wake has not fully decayed before it interacts with the orifice.

A total of five configurations will be investigated in this chapter, as described in Table 5.1. These are denoted positions P1-P5 and correspond to placement distances of $1.4D$, $3D$, $5.4D$, $8.4D$ and $20D$ upstream of the orifice. Positions P1-P4 are placed close enough to the orifice to raise the incoming turbulence levels and position P5 is designed to provide fully developed upstream turbulence conditions.

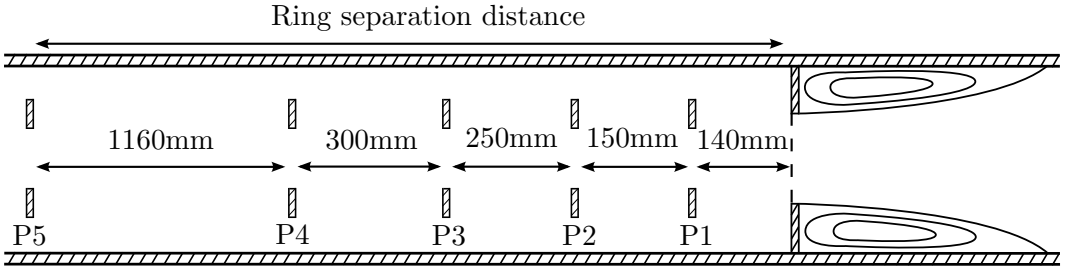

Figure 5.3: Schematic of the five separation distances between the ring and the orifice (P1-P5).

Name	Ring separation	Cell count	Transient length (T_D)	Sampling length (T_D)
Isolated orifice	N/A	9.81	39	100
Ring-P1	$1.4D$	12.48	41	100
Ring-P2	$2.9D$	12.61	43	100
Ring-P3	$5.4D$	14.49	45	100
Ring-P4	$8.4D$	16.51	49	100
Ring-P5	$20D$	19.20	60	100

Table 5.1: Details of the simulations conducted on the isolated orifice and orifice/ring pairings.

5.3 Methodology

All of the simulations performed in this chapter use the same basic modelling methodology. The second order open source code OpenFOAM is used to solve the unsteady three-dimensional compressible Navier-Stokes equations in a time resolved simulation. The use of a solver which accounts for the compressibility of the flow is essential to properly account for the noise sources and to allow for the accurate use of the acoustic analogies presented in Section 3.3 [196]. For this purpose, the 'rhoPimplecFoam' solver is utilised with some modifications to allow for the calculation of acoustic quantities of interest during the running of the simulation. The modified solver is denoted 'rhoPimplecSoundSourceFoam'. This solver uses a merged PISO [197]-SIMPLEC [198] solution algorithm for the velocity-pressure coupling. Details of the numerical schemes are presented in Section 3.8.2.1. In order to maintain accuracy within each timestep, all relaxation factors are set equal to 1 and the equations are iterated to a convergence tolerance of 1×10^{-6}.

The upstream domain length was fixed at $8D$ for all of the simulations in this chapter. In the cases for the isolated single orifice, this was $8D$ upstream of the orifice, and when rings were introduced, the $8D$ length extends upstream of the ring. This means that the total duct length is a function of the separation distance. This length was found to be more than sufficient for the inflow to experience minimal disturbance from the physical bodies placed within the domain in the studies in Section 4.4. The downstream length of $20D$ downstream of the orifice matches the domain length of the experimental facility.

All the meshes constructed for these cases use a three dimensional, multi-block structured approach, with refinement extending from a position of $1D$ upstream of the ring position, or the orifice position if no ring is used, to $15D$ downstream of the orifice position. This includes the whole nearfield region of the orifice, the convection region between the ring and orifice and the sound propagation region downstream, extending to $3D$ past the microphone positions at $12D$ downstream. The mesh sizing is controlled using a maximum cell dimension of 3.33mm throughout the region of interest which should allow for the wall pressure spectra to be resolved up to 5kHz, based on a second order spatial scheme [99, 101]. Outside of these regions, the mesh is gradually stretched up to a maximum of 10mm at the inlet and outlet boundaries. Images of the mesh in the nearfields of the ring and orifice can be seen in Figures 5.4 and 5.5. For these meshes,

the first grid point was placed at $1 \times 10^{-4}D$ away from the surface of the duct walls and orifice faces, to ensure $y^+ < 2$. The mesh across the $y-z$ plane of the duct uses a total of 100 circumferential points and, in order to avoid a singularity on the centreline, a square mesh topology is used in the centre of the duct. The choice of turbulence model was noted to be very important in this type of geometry [116] and the decision was made to utilise the IDDES model based on the backward-facing step results presented by Shur *et al.* [5]. This decision was made primarily because the meshing requirements for LES near the duct walls would have made the computational cost prohibitively large. The DES method negates some of these drawbacks without a significant impact on the accuracy [5]. The one-third power of the cell volume was used as the sub-grid length scale input to the IDDES sub-grid length scale formulation, which has been used for similar applications previously [199]. The standard values of C_{DES}=0.65 and C_w=0.15 are used in the IDDES model.

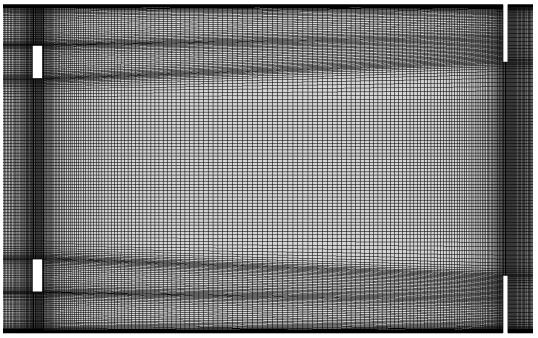

Figure 5.4: Zoomed view of the mesh on the x-y plane between the ring and the orifice for ring position P1.

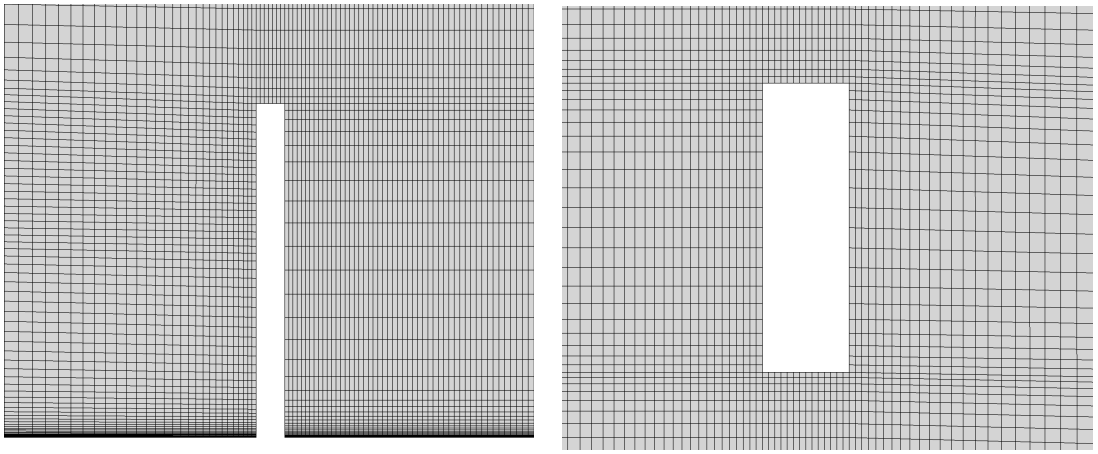

(a) Nearfield orifice (b) Nearfield ring

Figure 5.5: Zoomed view of the mesh on the x-y plane around the orifice and ring.

At the inflow, a steady fully developed mean velocity profile was used to maintain a

constant mass flow rate. As shown in Figure 5.6, this boundary condition provides a good representation of the experimental duct profile upstream of the orifice. The adiabatic walls of the orifice and the duct were treated with the no-slip condition and a partially reflecting outflow is used to drive the pressure towards the freestream value of 101325Pa (see waveTransmissive boundary condition in Section 3.8.2.3). The bulk velocity was consistent at 10m/s and the freestream temperature was fixed to 293.15K at the inlet boundary. For the coordinate system definition, x is the streamwise direction, y is the vertical direction and z is the spanwise direction. The origin for these simulations is always the geometric centre of the orifice defined on the plane of the upstream edge of the orifice.

The simulations are conducted with a timestep of 5×10^{-6} which is more that sufficient to capture the propagation of 5kHz acoustic waves at the previously recommended 20 Timesteps Per Period (TPP) [100]. This also achieves a maximum CFL < 2 which is sufficient for stability using an implicit time stepping scheme. Averaging of the results was performed following the initial transient phase of the simulations. In an orifice flow, this can be a significant amount of time, owing to the low flow speed and the very large pressure and density changes which occur upstream of the orifice in the initial stages. Mass flow monitoring on the inlet and outlet faces of the duct was performed, which gave an indication as to when the flow had converged. Further to this, the simulation was run for between 39-60T_D, where $T_D = D/u_\infty$, depending on the separation distance between the ring and orifice. Averaging of both mean and fluctuating values was performed for a further $100T_D$ across the whole computational domain. The spectra for both the experimental and numerical data were produced using a Fast Fourier Transform (FFT) with Hamming windowing. Each FFT was performed over a number of blocks, where each block contained a time history of 4096 samples. The sampling frequencies for the experimental and numerical results were 20kHz and 100kHz, respectively, resulting in frequency resolutions of 4.88Hz and 24.4Hz.

5.4 Effect of inflow conditions on the aerodynamic quantities of the single orifice

As a first step in the validation of the simulation methodology for the compressible solvers, it was necessary to validate the inflow conditions for the isolated single orifice. The fully developed steady boundary condition (which was modified to provide a constant mass flow rate from the BC used in Section 4.3.2) was shown to give excellent agreement to the experimentally measured mean velocity profiles at a distance of $4D$ upstream of the orifice, see Figure 5.6. The mean velocity profile also shows excellent agreement at a distance of $0.3D$ upstream, however, Figure 5.7 highlights a problem with under developed turbulence. The problem with the low turbulence intensity is caused

by the lack of a sufficient disturbance within the duct or sufficient development distance to cause large scale transition to turbulence.

In order to investigate the effect of an additional perturbation on the development of the flow upstream of the orifice, a ring was placed at a distance of $20D$ upstream of the orifice (P5). The upstream domain length is extended a further $8D$ beyond this, where the fully developed mean profile is applied. The effect of the upstream ring is shown in Figure 5.8. Both the mean velocity and turbulence intensity profile match better to the experimental data, indicating that the inflow conditions are significantly improved through the use of the upstream ring. For this reason, all future results presenting the validation of the fully developed inflow conditions will be for ring position P5.

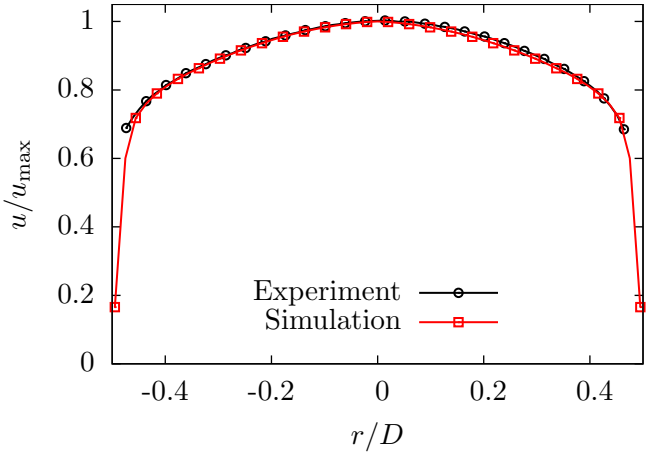

Figure 5.6: Comparison of the experimental and simulated mean velocity profiles at a position $4D$ upstream of the orifice.

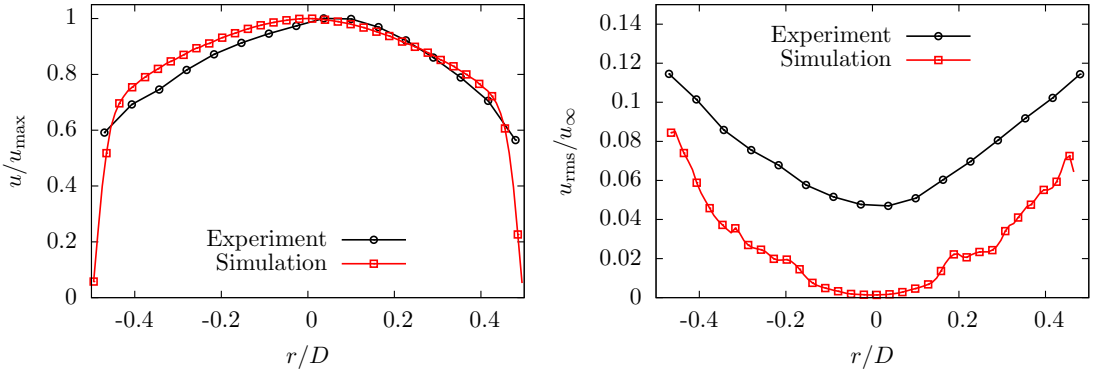

(a) Mean velocity

(b) Turbulence intensity

Figure 5.7: Comparison of the experimental and simulated mean velocity profile and turbulence intensity profile at a position $0.3D$ upstream of the orifice with a $8D$ upstream domain length (No ring).

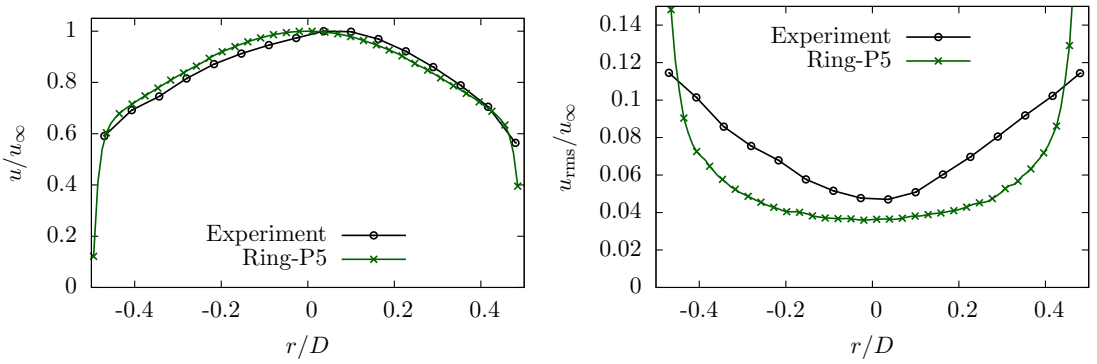

(a) Mean velocity

(b) Turbulence intensity

Figure 5.8: Comparison of the experimental and simulated mean velocity profile and turbulence intensity profile at a position $0.3D$ upstream of the orifice with a ring placed at $20D$ upstream of the orifice.

5.4.1 Aerodynamic validation

Prior to studying the wall pressure fluctuations produced by the orifice, it was necessary to validate the aerodynamic quantities from the simulation against experimental and empirical results. The primary quantities for validation purposes are the pressure drop and reattachment length. The drop in pressure through the orifice is related to the reattachment length, as this has a bearing on the area of the vena-contracta and the eventual spreading rate of the jet. Given that these quantities provide information about how well the fundamental properties of the orifice are simulated, they have been used as the data for comparison in a mesh convergence study which is presented in Appendix A.

5.4.1.1 Pressure drop and reattachment location

The data used for validation of the mean static pressure drop has been experimentally measured by Tao [6] using 55 pressure taps, separated by a distance of 10mm, see Figure 5.9. Ten pressure taps were placed upstream of the orifice and 45 downstream to cover the whole of the separated region when using the d=65mm orifice. The theoretical/empirical estimation of the pressure drop using Bernoulli's incompressible equation, with a discharge coefficient to correct the drop, is also used for validation and provides a prediction of the change in pressure between locations $1D$ upstream and $0.5D$ downstream of the orifice face.

The experimental results show that as the flow approaches the orifice, the upstream pressure slightly increases, due to the blockage by the orifice. Then, in the mouth of the orifice, the pressure sharply drops due to the acceleration of the fluid through the reduced area of the orifice opening. The pressure continues to reduce until the location of the vena-contracta, after which it gradually increases with downstream distance, until

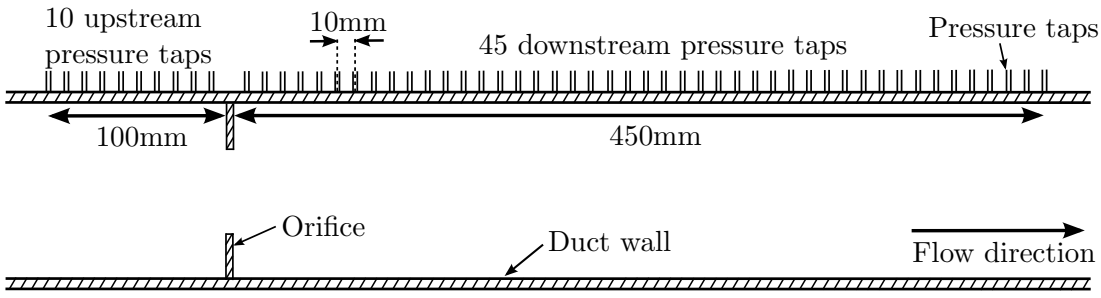

Figure 5.9: Schematic of the location of the static pressure measurement probes upstream and downstream of the orifice.

it reaches its maximum recovered pressure. The differential in pressure caused by the orifice is proportional to the square of the velocity:

$$\Delta p = \frac{1}{2}\rho u_\infty^2 C_D, \tag{5.1}$$

where Δp is the differential pressure, C_D is the drag coefficient, ρ is the fluid density upstream of the orifice and u_∞ is the bulk flow velocity. The coefficient C_D remains constant for a specific orifice regardless of the flow velocity and also accounts for the frictional losses through the duct from Equation 2.2. For the d=65mm orifice, the experimental value of C_D is equal to 7.92.

Whilst it is not possible to make a full comparison of the d=65mm simulation to the experimental data across the whole measurement range (unlike for the 60mm and 70mm orifices which were not simulated due to the lack of other measurements, such as velocity spectra), it is clear to see that the pressure drop is underpredicted by approximately 10%, see Figure 5.10. This indicates that the orifice is not sufficiently accelerating the flow in the simulations and is the same effect as was seen in the RANS simulations in Chapter 4. Another point of interest is the relative position of the vena-contracta (the point of minimum jet area), where it is seen that this is too far downstream ($0.5D$ in the experiment and $0.7D$ in the simulation). Furthermore, it is clear from Figure 5.11, that the mean reattachment point is also overpredicted by approximately 18% based on the empirical reattachment length [163].

5.4.2 Velocity validation

Unsteady velocity measurements were taken by Tao [6] using a traverse mounted single sensor hot wire probe. The probe was inserted through the duct wall at nine equally spaced locations downstream of the orifice (denoted X2-X9) ranging from 100-450mm (1-4.5D). Each measurement location was separated by a distance of 50mm ($0.5D$), as show in Figure 5.12. At each location, the hot wire probe was traversed through 76 points with a step size of 1.25mm, giving a total traversing distance of 95mm. Data were sampled using a frequency of 10kHz for a total period of 40 seconds. From the unsteady

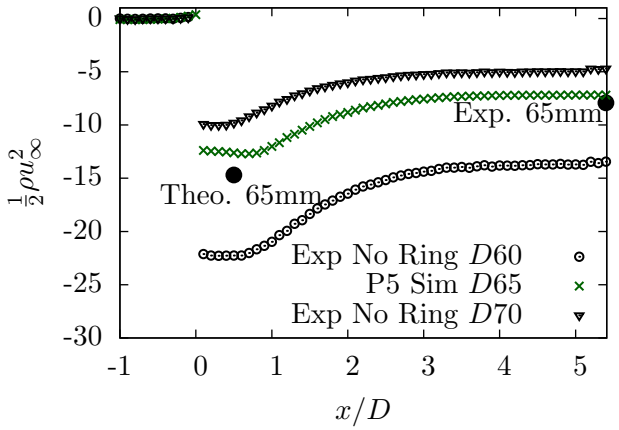

Figure 5.10: Comparison of experimental and numerical static pressure drop through the orifice measured on the wall of the duct.

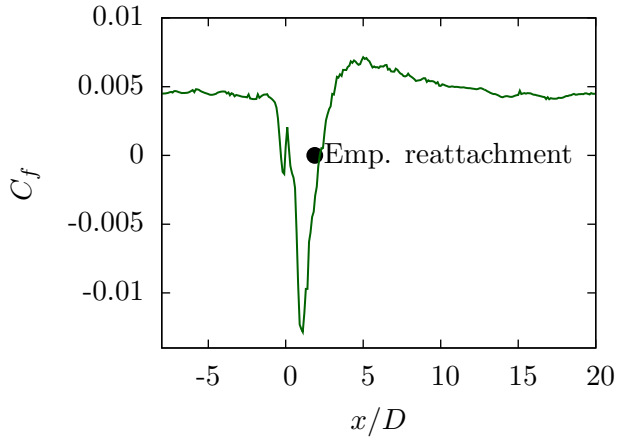

Figure 5.11: Mean shear stress measured along the duct wall, with comparison to empirical equation for reattachment point [7]. Simulated reattachment point is where the skin friction intersects the zero line for the second time.

velocity measurements, the mean velocity, turbulence intensity and power spectrum density of the velocity have been calculated.

One point worth noting is that the hot wire probe cannot measure directional data, meaning that it cannot distinguish between streamwise and recirculating flow. For that reason, the measurements directly behind the orifice face, where the flow is travelling opposite to the streamwise direction, may be inaccurate. This problem will affect the measurements of the mean velocity profile within the recirculation regions, however, the turbulence intensity will only be affected in shear layers where the velocity switches from negative to positive. This effect can be see in Figures 5.15 to 5.20.

In order to provide an overview of the flow, contours of the mean and instantaneous velocity and the mean turbulent kinetic energy are presented in Figure 5.13. In addition to showing the main features discussed in the literature review, the results show the significant unsteadiness captured by the DES model in the wake of the orifice, including

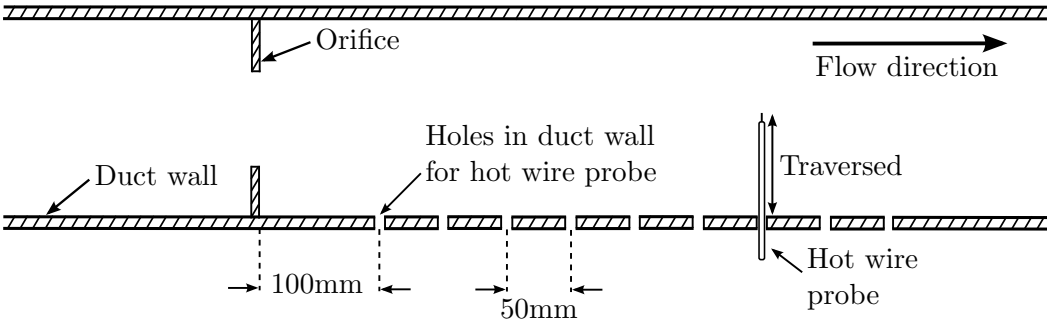

Figure 5.12: Schematic showing the velocity measurement locations which have been sampled using a hot-wire probe.

the flapping motion of the jet within the duct. The iso-contour further highlights the merging and development of the structures within the jet as they convect downstream. The same quantities can be seen in Figure 5.14 for the flow around the ring. A weaker jet can be seen and a small recirculation region is present downstream of the ring. There is also an increase in the turbulent kinetic energy in the wake of the ring, which eventually convects downstream and interacts with the orifice.

Simulated velocity data were sampled at locations matching the experimentally probed cuts. The data shown in Figures 5.15, 5.16 and 5.17 gives mean velocity and turbulence intensity data at the experimental measurement locations and the additional position $X1$ at $0.5D$ downstream of the orifice. Comparison of the experimental and simulation data shows that the mean normalised velocity is very well predicted throughout the region covering the wake of the orifice. This is true of both the shape and magnitude of the profiles. This is particularly true near the centreline of the duct, with slight discrepancies seen near the walls of the duct. This can be explained by firstly, the overprediction of the recirculation length by the simulations, and secondly, the inability of the hot-wire to distinguish the direction of the flow and the difficulties associated with measurements in regions of high turbulence intensity, such as the recirculation region. These points are confirmed as the profiles match extremely well at positions downstream of the reattachment point of the orifice ($X5$-$X9$).

Comparison of the turbulence intensity shows that the simulation has a tendency to overpredict the u_{rms} values across the span of the duct for measurement positions X2-X5. The overprediction is primarily located in the shear layers and in the recirculation region. This has previously been discussed by Deck for a BFS geometry [116]. The overprediction of recirculation length and the incorrect position of the vena-contracta, as noted in Figure 5.11, are direct results of the delayed development of the shear layers. This leads the simulation to overproduce TKE, which explains the overpredictions seen in the numerical data. The turbulence intensity on the centreline in position X2 is quite well predicted and it is only further downstream where the overpredicted turbulence diffuses into the centre of the duct that the overprediction across the span is seen. Once again, at measurement points significantly outside the recirculation region (X6-X9), the comparison of the turbulence intensity is very good.

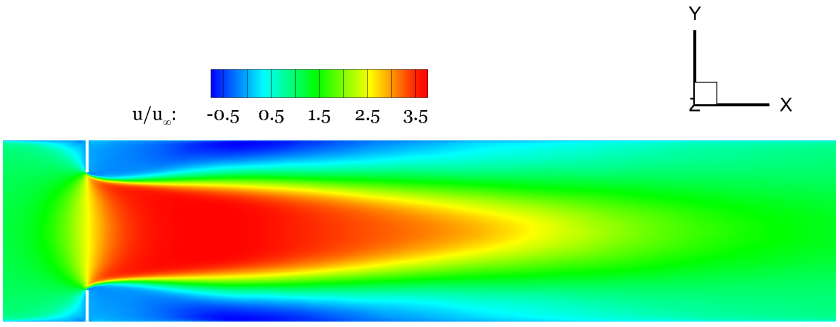

(a) Mean streamwise velocity

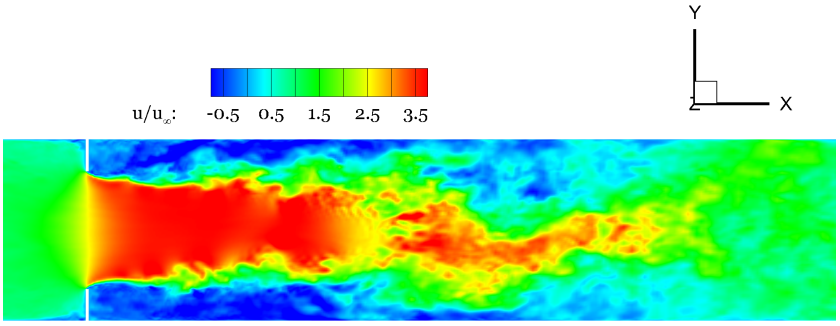

(b) Instantaneous streamwise velocity

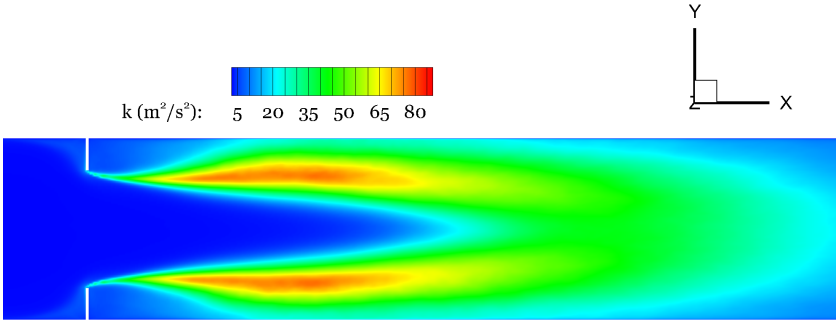

(c) Mean turbulent kinetic energy

Figure 5.13: Contours of velocity and k shown on the x-y plane of the mesh in the wake of the orifice for ring in position P5.

In order to study the velocity field in the wake of the orifice further, the magnitude of the velocity fluctuations at different frequencies is plotted in Figures 5.18, 5.19 and 5.20. The experimental and computational results both highlight the largest velocity fluctuations as being within the shear layers. There is a good comparison of the location of the shear layer by the simulation, however, the simulation data is seen to slightly overpredict the low frequency fluctuations immediately downstream of the orifice and then underpredict across the whole frequency range as the stream wise distance increases. The under prediction with increasing distance is most probably caused by a lack of resolution to maintain the fluctuations. The same may also be true of the low frequency overprediction close to the orifice, where the energy in the flow is incorrectly concentrated most at low frequencies. However, it may also be the case that the delayed shear layer development

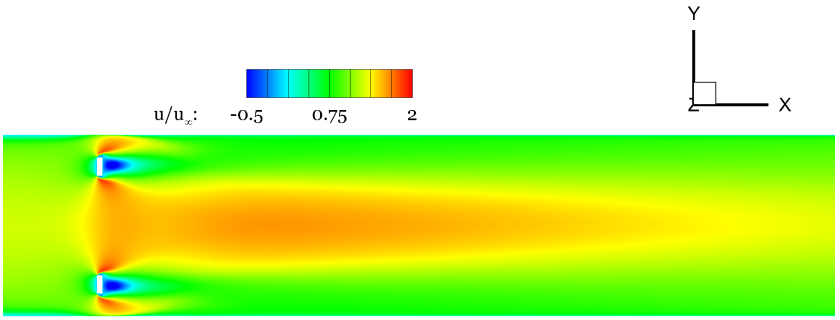

(a) Mean streamwise velocity

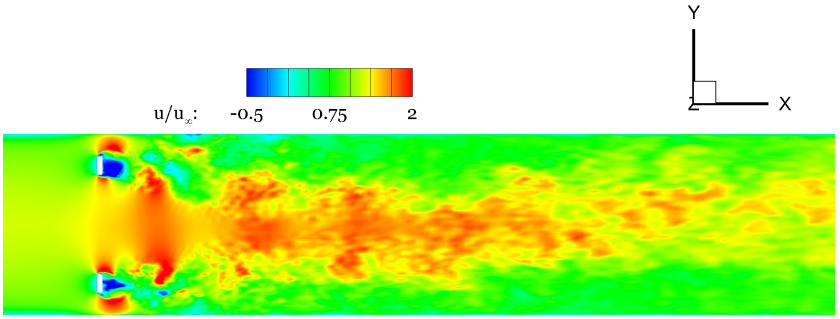

(b) Instantaneous streamwise velocity

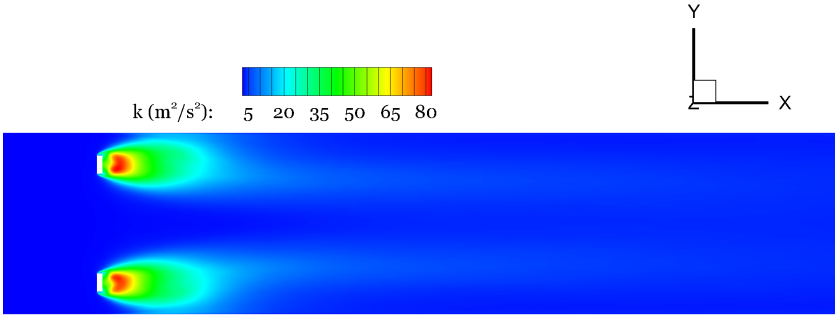

(c) Mean turbulent kinetic energy

Figure 5.14: Contours of velocity and k shown on the x-y plane of the mesh in the wake of the ring for ring in position P5.

leads to fewer smaller structures (high frequency fluctuations) in the region close behind the orifice.

5.4.3 Acoustic validation

The acoustic pressure within the duct was experimentally measured by Tao [6] using microphones which were flush mounted on the duct walls. In order to attenuate the effect of the turbulent boundary layer on the noise measurements, a 1mm hole was drilled into the duct wall, behind which the microphone was placed. This is shown schematically in Figure 5.21 and had the additional benefit of reducing the effective measurement area. The primary noise data was collected from 12 microphones mounted

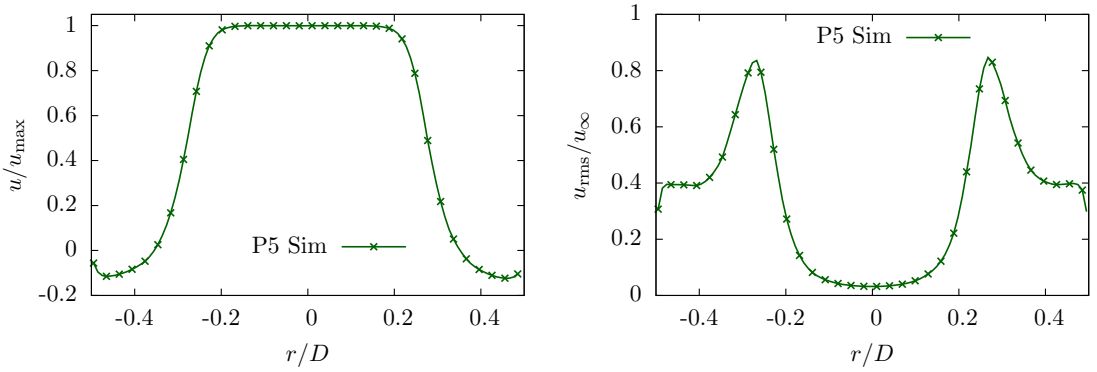

(a) Mean velocity X1

(b) Turbulence intensity X1

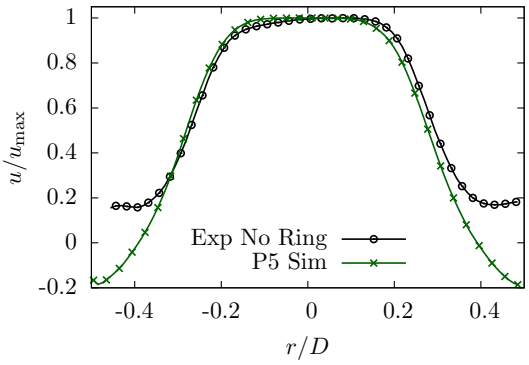

(c) Mean velocity X2

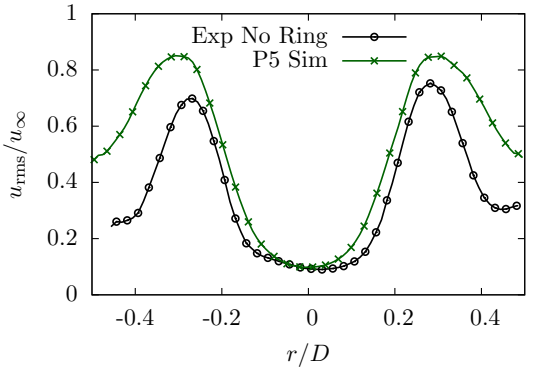

(d) Turbulence intensity X2

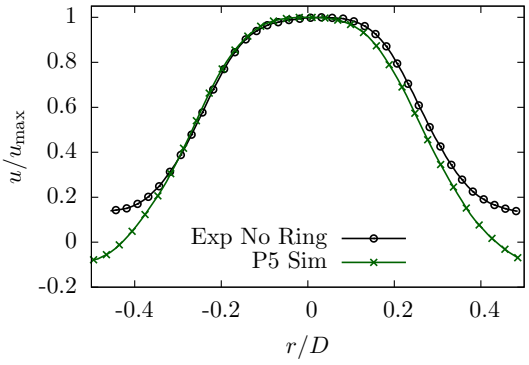

(e) Mean velocity X3

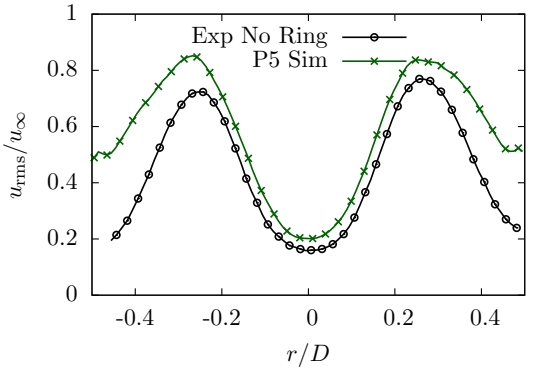

(f) Turbulence intensity X3

Figure 5.15: Comparison of mean normalised velocity and turbulence intensity profiles at spanwise cuts across the duct at positions X1-X3.

1200mm ($12D$) downstream of the orifice. The microphones were equally spaced around the duct circumference with a separation angle of 30 degrees. The large separation distance between the orifice and the measurement location was used to minimise the effect of hydrodynamic pressure fluctuations, which could corrupt the acoustic data.

Further measurement locations closer to the orifice have also been tested. The microphones were flush mounted using the same method as described in the previous paragraph and are placed at streamwise distances of between 31.5-346.5mm and 396.5-768.5mm downstream of the orifice. Within these ranges, the microphones are equally

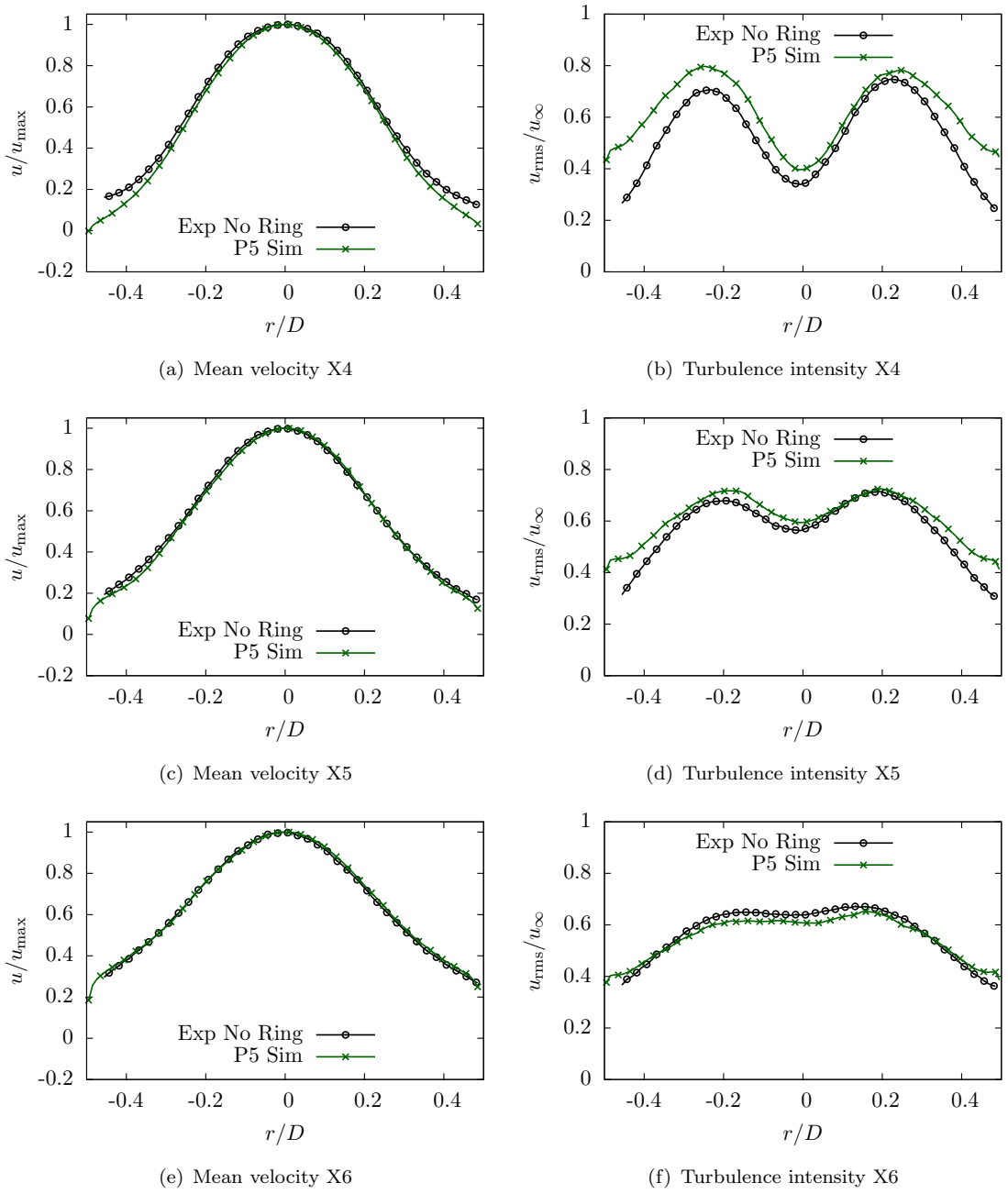

(a) Mean velocity X4

(b) Turbulence intensity X4

(c) Mean velocity X5

(d) Turbulence intensity X5

(e) Mean velocity X6

(f) Turbulence intensity X6

Figure 5.16: Comparison of mean normalised velocity and turbulence intensity profiles at spanwise cuts across the duct at positions X4-X6.

spaced, with a separation distance of 15mm. These microphones allow for a quantification of the flow in the nearfield of the orifice, including the expected tonal peaks due to vortex shedding from the orifice edges and feedback mechanisms from the interaction of the jet with the wind tunnel walls.

Experimental wall pressure measurements were firstly taken in the clean duct to measure the background noise levels within the duct. The data taken in the clean duct show a broadband spectrum, with no narrowband peaks. This suggests that in the clean duct, the pressure field is dominated by the turbulence induced by the boundary layer [6]. The

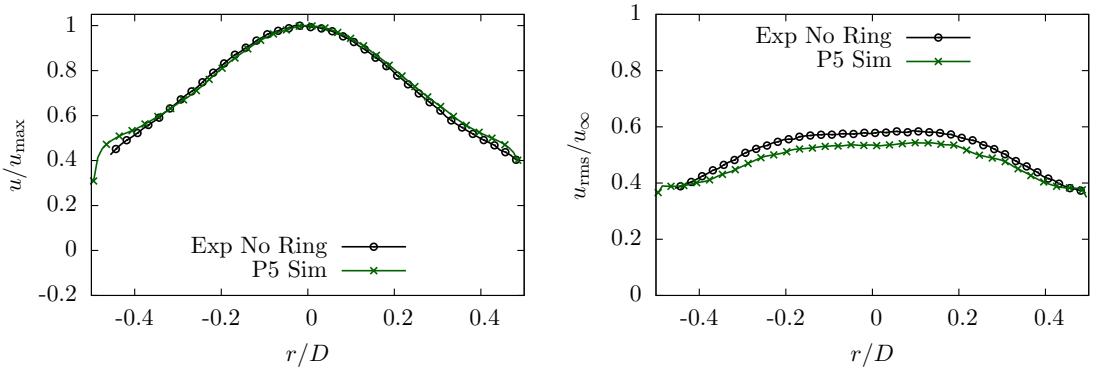

(a) Mean velocity X7

(b) Turbulence intensity X7

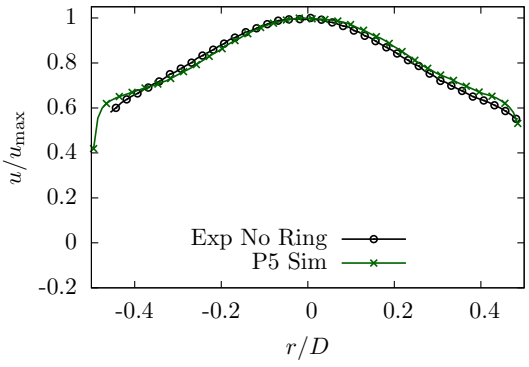

(c) Mean velocity X8

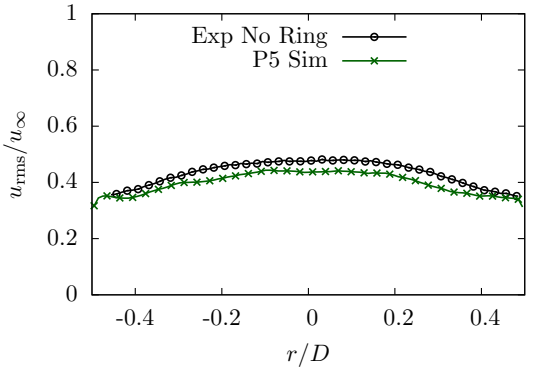

(d) Turbulence intensity X8

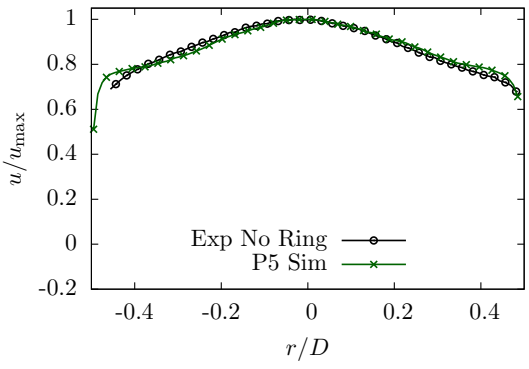

(e) Mean velocity X9

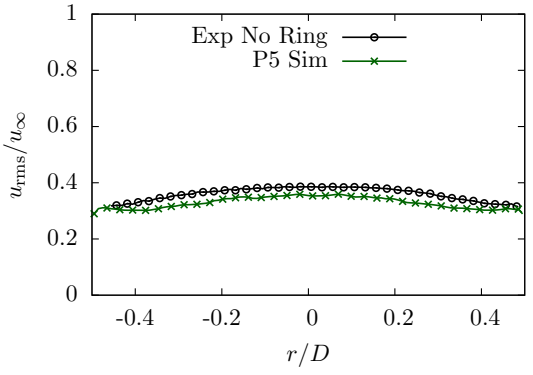

(f) Turbulence intensity X9

Figure 5.17: Comparison of mean normalised velocity and turbulence intensity profiles at spanwise cuts across the duct at positions X7-X9.

clean duct shows noise levels significantly below those seen with a component mounted in the flow, and was therefore neglected from further computational studies within this chapter.

Following the clean duct, wall pressure spectra were measured for a range of orifice sizes and flow speeds. The experimental results show that at frequencies below the first cut-on frequency of 2010Hz, only the plane wave mode propagates in the duct. In this frequency range, the spectrum has a broadband shape. At frequencies higher than 2010Hz, the higher order modes are excited. These presents themselves as narrowband peaks within

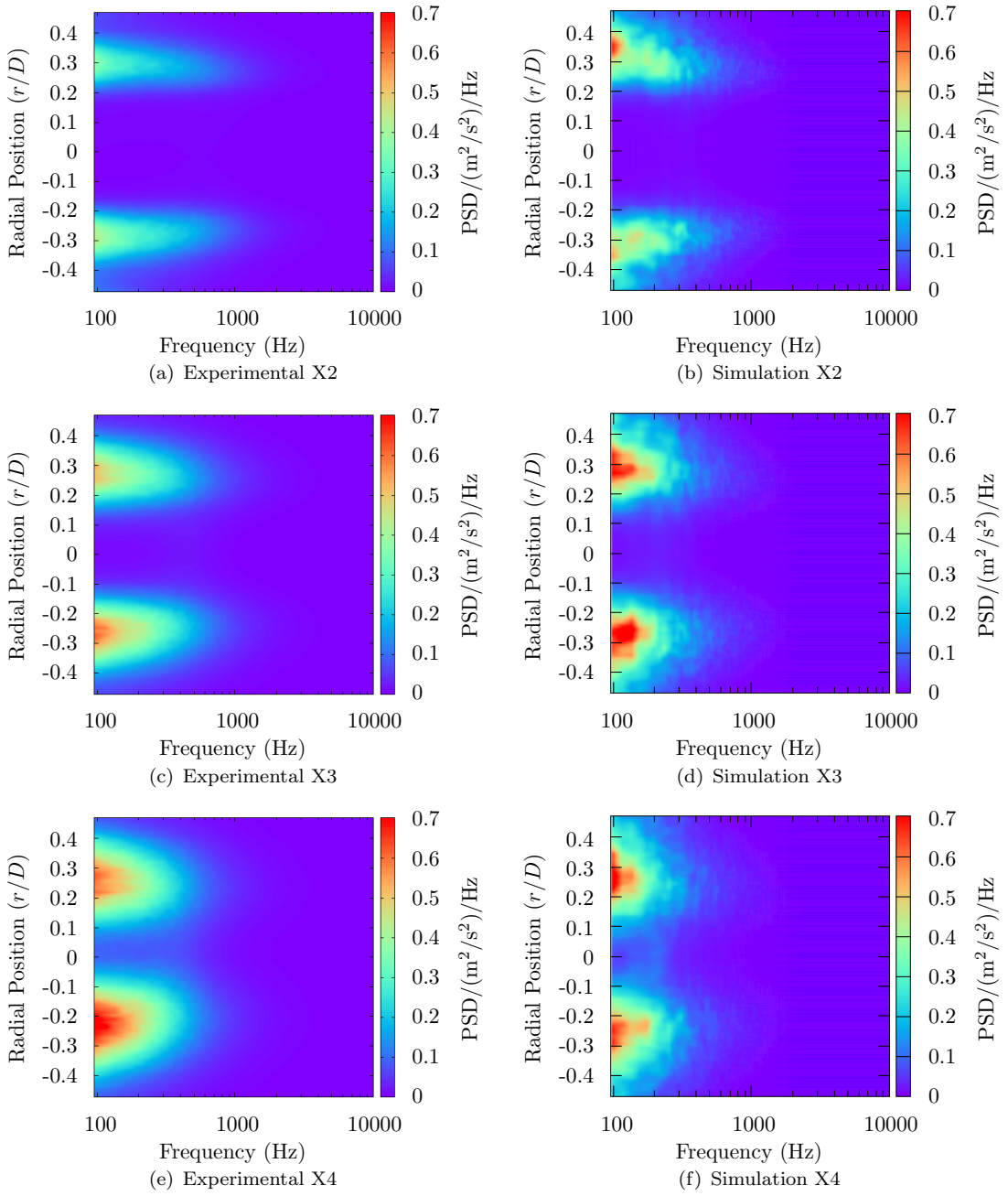

Figure 5.18: Comparison of the velocity spectra at spanwise cuts across the duct at positions X2-X4.

the spectrum, approximately corresponding to the frequencies predicted by the Bessel function (Table 3.1). All of the higher order modes dominate the plane wave mode near their cut on frequencies, although the peaks fall off rapidly as the frequency increases further. From the range of experimental data, it was seen that the higher order modes were more heavily excited (the narrowband peaks became larger) at higher flow speeds and also when the orifice diameter is reduced. However, when the orifice was very large, there were no tonal peaks present in the data. This is expected, as both increasing the bulk flow velocity and reducing the orifice diameter will increase the maximum flow

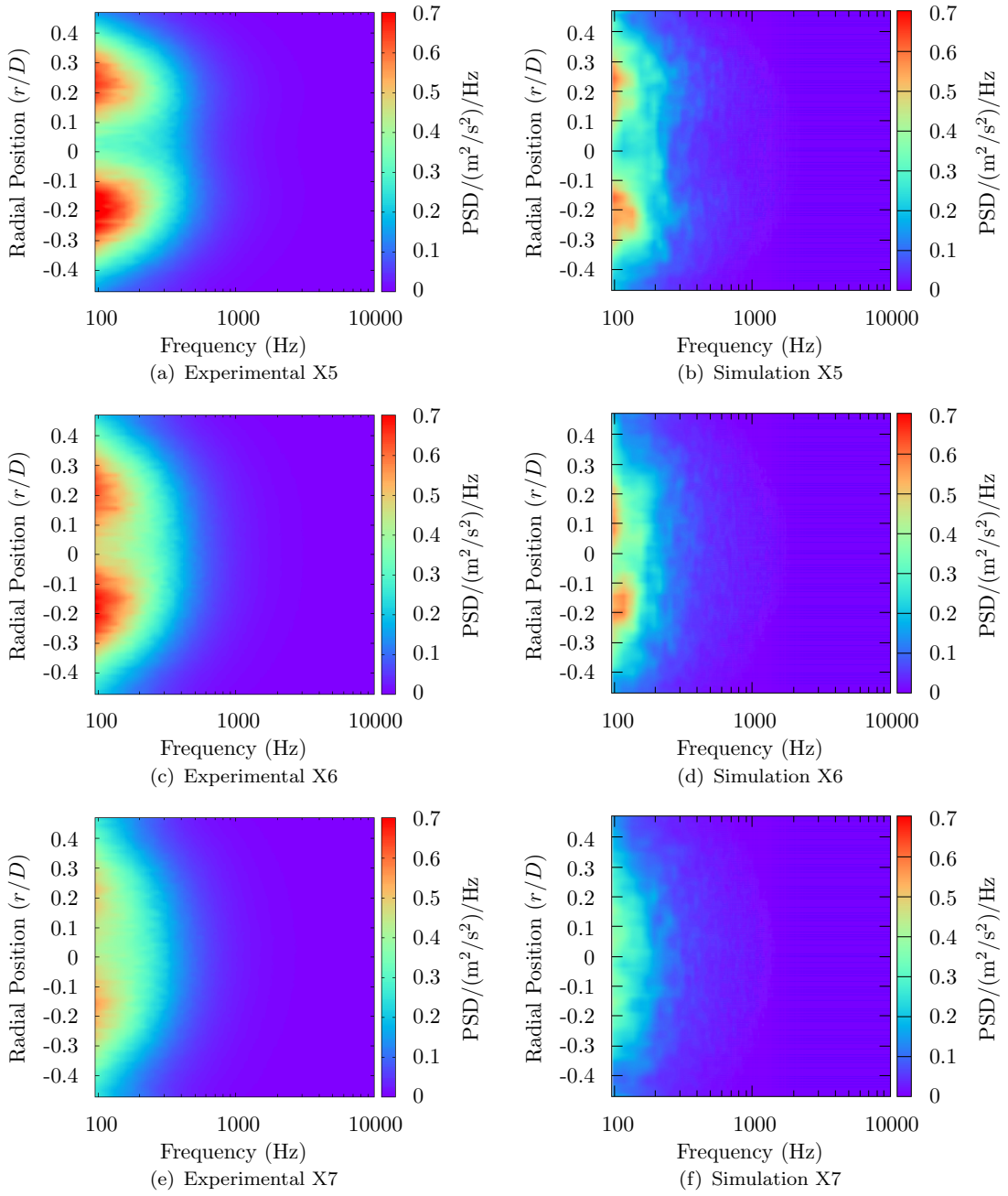

Figure 5.19: Comparison of the velocity spectra at spanwise cuts across the duct at positions X5-X7.

velocity through the orifice, resulting in higher intensity turbulence and acoustic fields downstream of the orifice [6].

A comparison of the experimental and simulation results at a distance of $12D$ downstream of the orifice, for ring position P5, is presented in Figure 5.23. The comparison is good across the whole resolved frequency range (100Hz - 5kHz) with discrepancies only seen in the magnitude of the predictions at the cut-off frequencies of the ducts modes. This suggests that the simulation is over exciting the first duct modes, maybe due to reflections from the boundaries. However, the simulated cut-off frequencies of

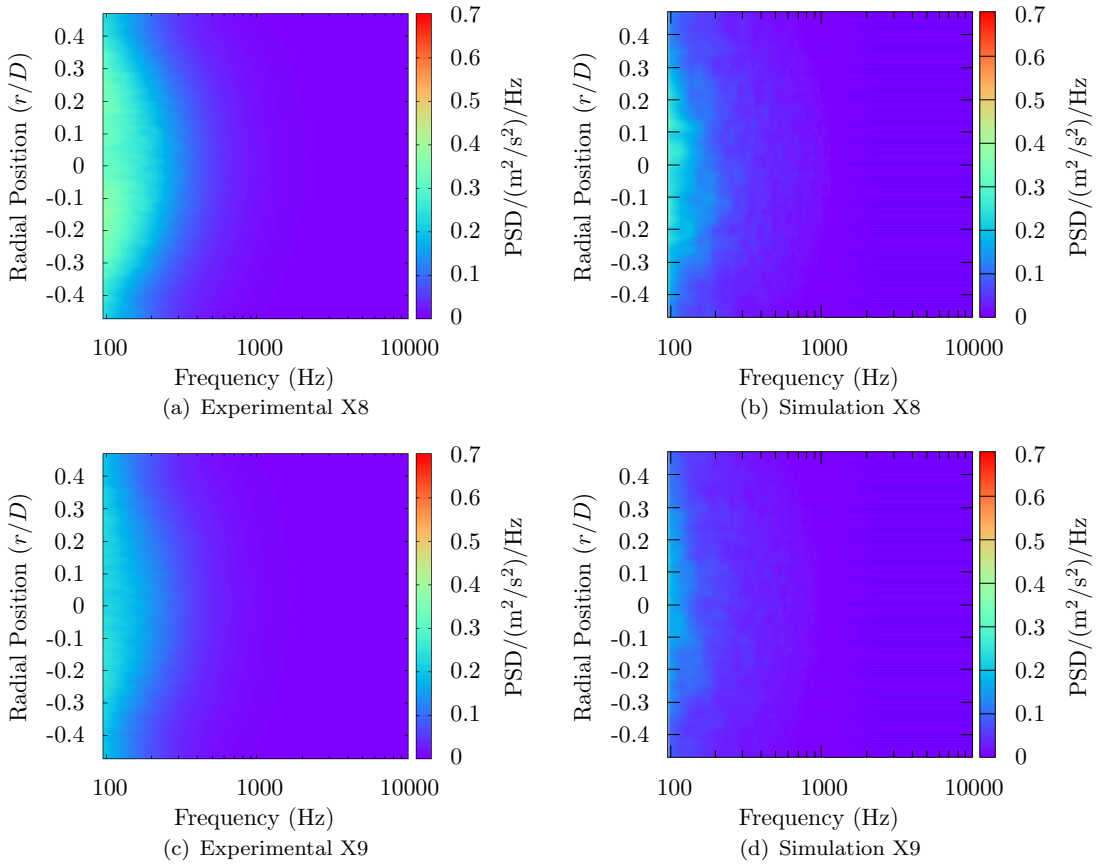

Figure 5.20: Comparison of the velocity spectra at spanwise cuts across the duct at positions X8-X9.

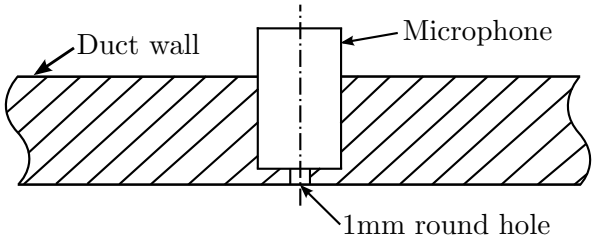

Figure 5.21: Schematic of flush mounted wall pressure microphones used in the experimental setup.

the duct modes are very well predicted, as detailed in Table 5.2, suggesting that the over prediction could be improved in future simulations. Overall, this prediction is very encouraging for the accuracy of the acoustic predictions.

	Mode 1 Freq. (Hz)	**Mode 1 (dB)**	**Mode 2 Freq. (Hz)**	**Mode 2 (dB)**
Experiment	2041	57	3403	48
Simulation	2052	65	3372	56

Table 5.2: Comparison of experimental and numerical frequency and level of duct modes, for the first two cut-off modes. Mode numbers are 1,0 and 2,0 (m,n).

One point of interest for identifying the location of the sound source is the magnitude of

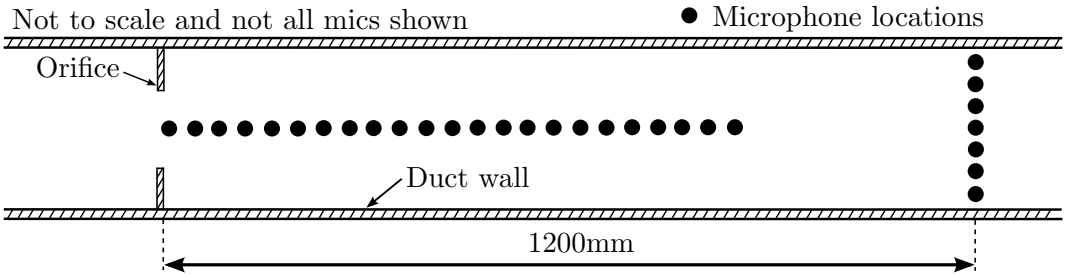

Figure 5.22: Schematic of the approximate locations of the microphones flush mounted within the experimental duct.

the fluctuations in the upstream and downstream directions. The Mach number of the flow is so small that this should have little effect on the propagation of the sound waves. The spectra of the wall pressure is shown in Figure 5.24 for locations equally spaced at $8D$ upstream and downstream of the orifice. It is clear that the fluctuations upstream of the orifice are significantly higher than those downstream. This may be caused by the presence of the ring upstream, however, it was not confirmed using results from a clean duct as the turbulence characteristics were incorrect (see Section 5.4). Furthermore, the distance to the ring is larger than the distance to the orifice, which suggests that noise from the orifice may be radiating more efficiently in the upstream direction and it is most probably located on the upstream face of the orifice. The next section will aim to confirm this suggestion.

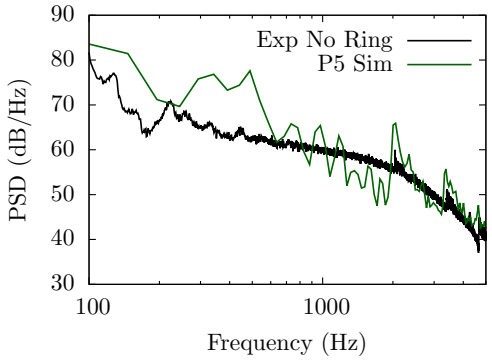

Figure 5.23: Comparison of the simulated and experimental wall pressure spectra at a distance of $12D$ downstream of the orifice for ring position P5.

5.4.4 Sound source identification

Following the literature review on the possible sources of sound in an orifice flow (see Section 2.4.3), the focus of this investigation is on two areas; the face of the orifice and the area of the duct wall where the jet impinges. For the purpose of plotting results for the entire orifice face and duct wall, the sampling locations, presented using the dashed lines in Figure 5.25, are used. On the orifice face, a normalised surface measurement distance, x_s, is used to describe the distance from the upstream corner of the orifice. In this measurement system, the point where the upstream face meets the duct wall lies

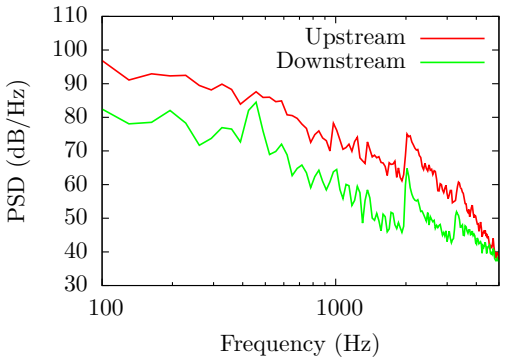

Figure 5.24: Comparison of the simulated wall pressure spectra at distances of $8D$ upstream and downstream of the orifice for ring position P5.

at -0.175, the upstream corner lies at 0, the downstream corner lies at 0.015 and the point where the downstream face meets the duct wall lies at 0.19. Along the duct wall, the sampling locations extend from the inlet of the duct at x/D=-8, past the upstream orifice face at x/D=0 and to the outlet at x/D=20.

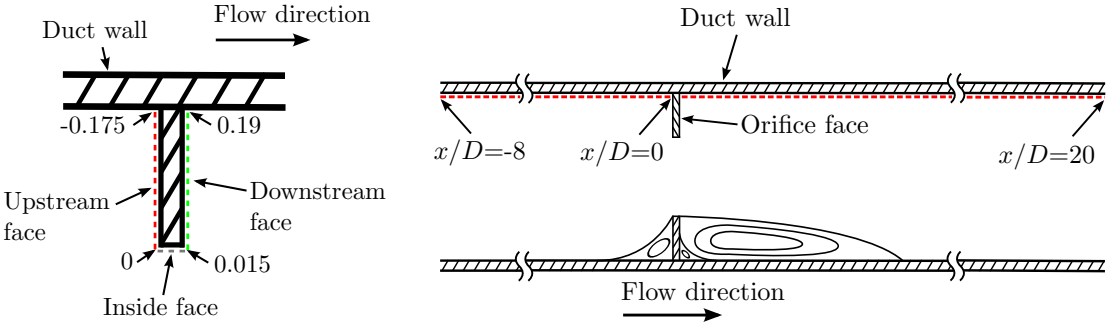

(a) Orifice face identifying the upstream, inside and downstream faces

(b) Duct wall

Figure 5.25: Schematic of normalised measurement distance, x_s, and the sampling location on the duct wall.

In order to identify the dominant noise sources, a number of noise source identification methods, which have been previously discussed in Section 3.7, have been applied to the ring case in position P5. These results are provided in the following sections.

5.4.4.1 Initial source identification

The first step in identifying the noise sources is to look at the relative magnitudes of the two previously discussed noise sources; the orifice face and the impingement point of the orifice jet on the duct wall. An attempt is made to do this through the use of the root mean square pressure and the gradient of the density field along the walls. As discussed in Section 3.7, the pressure directly measured from the computation contains both the hydrodynamic and acoustic fluctuations, therefore, measuring the RMS values of the combined pressure field will not necessarily give information on where the

sound is generated, but does help to identify regions where there is significant pressure unsteadiness.

Figure 5.26, shows the mean pressure and RMS pressure on the face of the orifice. The mean pressure plot indicates that the vast majority of the pressure drop across the orifice is seen near the upstream corner of the upstream face as the flow is accelerated when passing through the orifice opening. This large change in pressure over a short distance causes a large pressure gradient around the upstream corner of the orifice, which is the corresponding location for the maximum values of the pressure unsteadiness. Relatively large unsteadiness is also seen on the rear face of the orifice, which is postulated to be caused by the unsteadiness of the primary and secondary separation regions directly downstream of the orifice.

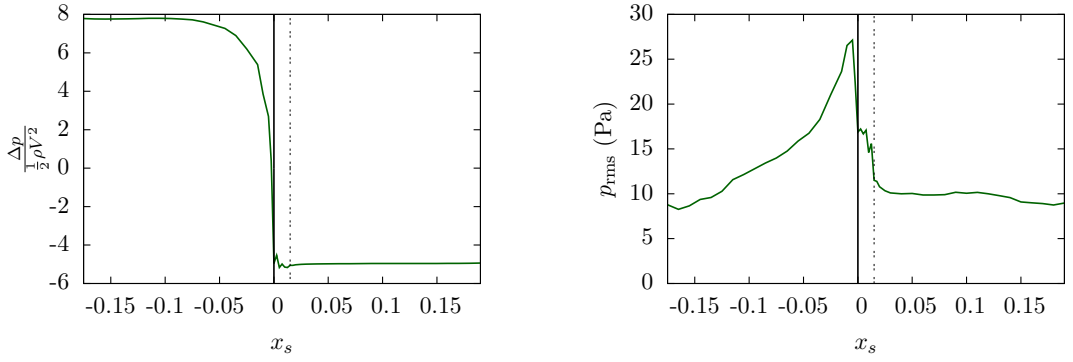

(a) Mean normalised pressure

(b) RMS Pressure

Figure 5.26: Profiles on the face of the orifice for the case with ring placed at $20D$ upstream of the single orifice. The solid line represents the upstream corner of the orifice and the double dashed line represents the downstream corner of the orifice.

The RMS pressure on the duct walls and on the duct centreline is shown in Figure 5.27. Both the duct wall and the centreline show a large pressure unsteadiness around the separated region where the jet is formed. A primary peak is located on the duct wall at approximately the location of the impingement point of the jet ($x/D \approx 2$). A primary peak is seen along the centreline at the location where the shear layers meet and is of approximately the same magnitude as the wall source. It should be noted that the high pressure unsteadiness indicated along both the centreline and duct wall is larger than what was seen on the face of the orifice. However, the centreline and duct wall indicate very similar values, suggesting that this may be the hydrodynamic pressure being affected by the large pressure drop through the orifice and may not imply a significant source of noise.

Non-uniform density distributions can play an important role in the propagation of sound. The mean density gradient (or temperature gradient) is seen to partially account for sound amplification in subsonic jets, whereby additional sources are present in the unsteady density field [200, 201]. It has also been shown that when large density

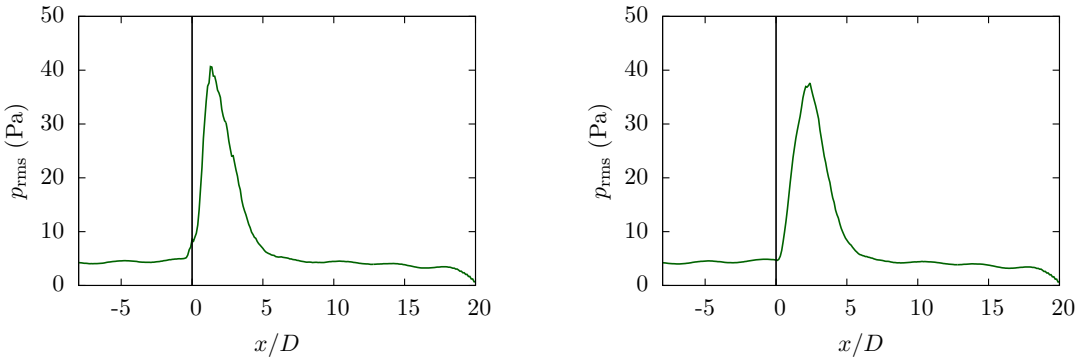

(a) Duct wall

(b) Duct centreline

Figure 5.27: Root mean square pressure fluctuations for the case with ring placed at $20D$ upstream of the single orifice. The solid line represents the upstream corner of the orifice.

gradients are present in a jet flow, an additional dipole noise source can become important [202, 203]. The gradient of the density field is shown on the orifice face and the duct wall in Figure 5.28. The plots show similar characteristics to the RMS pressure field indicating the potential presence of two dipole noise sources. The magnitude of the density change near the mouth of the orifice is expected from the large change in the pressure field through the orifice and a smaller density gradient is seen along the wall of the duct in the recovery region downstream of the orifice. This particular result strongly suggests that there is a dipole noise source located close to the orifice upstream corner.

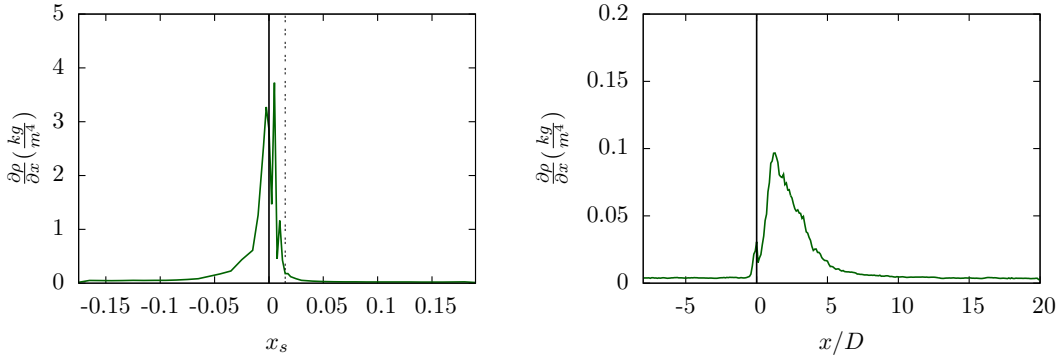

(a) Orifice face

(b) Duct wall

Figure 5.28: Mean density gradient for the case with ring placed at $20D$ upstream of the single orifice. The solid line represents the upstream corner of the orifice and the double dashed line represents the downstream corner of the orifice.

The RMS pressure values and the gradient of the density field have indicated the locations of the two suspected noise sources as regions of potential sound generation. Whilst they are not able to confirm either of these as the dominant noise source, they provide an indication as to the locations of interest for a more in-depth investigation of the orifice

noise sources.

5.4.4.2 Surface sound source identification

Curle's surface acoustic analogy, described in Section 3.7.1.1, has been applied to the two focal regions within the orifice flow; the orifice face and the duct wall. The use of acoustic analogies allows for the sound sources to be estimated, despite the dominance of the hydrodynamic pressure fluctuations in the region near to the orifice. In order to apply the analogies, the mean and instantaneous value of the square of the time derivative of the pressure were output on the surfaces of the duct and orifice. This quantity is used in the following section to estimate the acoustic sources.

Curle's analogy relates the time derivative of the hydrodynamic pressure to the acoustic pressure. However, in this work, only the source term of Curle's analogy will be considered. The magnitude of this source term is presented on the wall of the duct and orifice in Figure 5.29. The results indicate noise sources across the two regions previously identified. The dominant noise source is located on the upstream corner of the orifice face, with the secondary noise source, which is more than one order of magnitude smaller, near the jet impingement location.

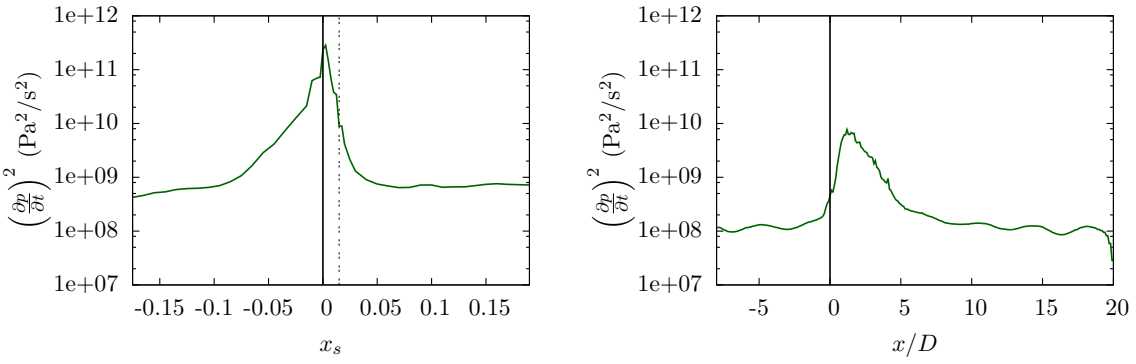

(a) Orifice face

(b) Duct wall

Figure 5.29: Profiles of the mean square of the hydrodynamic wall pressure time derivative on the face of the orifice for the case with ring placed at $20D$ upstream of the single orifice. The solid line represents the upstream corner of the orifice and the double dashed line represents the downstream corner of the orifice.

The vorticity variation has also been investigated on the surfaces and is shown in Figure 5.30. The vorticity shows two peaks around the same regions as the large source term, with the magnitude on the orifice face being significantly larger than that on the duct wall. This suggests that vorticity may be a quantity which is related to the production of sound in those regions. This will be confirmed when the effect from introducing additional turbulence is understood.

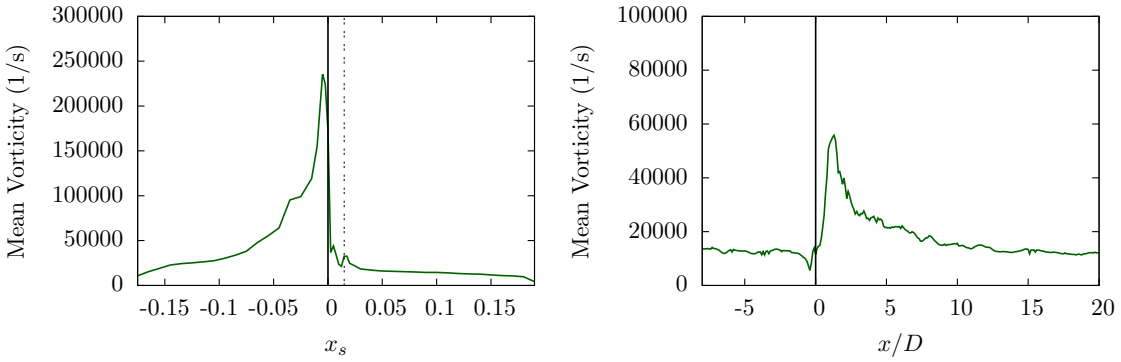

(a) Orifice face

(b) Duct wall

Figure 5.30: Mean surface vorticity for the case with ring placed at $20D$ upstream of the single orifice for ring position P5. The solid line represents the upstream corner of the orifice and the double dashed line represents the downstream corner of the orifice.

5.4.4.3 Volume sound source identification

When the volume source methods were introduced in Section 3.7, it was mentioned that the surface sources were expected to be dominant over the volume sources due to the low Mach number. However, data from these is still useful in identifying the potential contribution of the volumetric noise sources to the overall noise within the duct. The magnitude of the source term in Powell's analogy for spanwise cuts from X1-X6 is shown in Figure 5.31. Powell's analogy shows that the most significant contribution to the noise from the volumetric sources is from the shear layers. The turbulence created within the shear layers then diffuses and convects downstream creating sources in the wake of the orifice. The largest volumetric sources are present close to the orifice, with the source strength quickly diminishing outside the region of the shear layers. Overall, this analogy confirms what would be expected for this flow, given that the highest turbulence levels are experienced in the shear layers and therefore the largest corresponding noise source would be present in the same location.

One thing which must be noted about these surface and volume source results is that the estimations of the acoustic pressure are based on the sum of the frequency components of the acoustic pressure. Therefore, no indication of the strength of these sources across the frequency range can be obtained, which is crucial when dealing with noise. The following section addresses this issue by considering the variation of the noise sources with frequency.

5.4.4.4 Frequency resolved surface sound source identification

Within this section, an examination of the frequency components of both the wall pressure spectra and the source term within Curle's acoustic analogy will be made. The data has been organised into contour plots by taking the variation of the frequency plotted

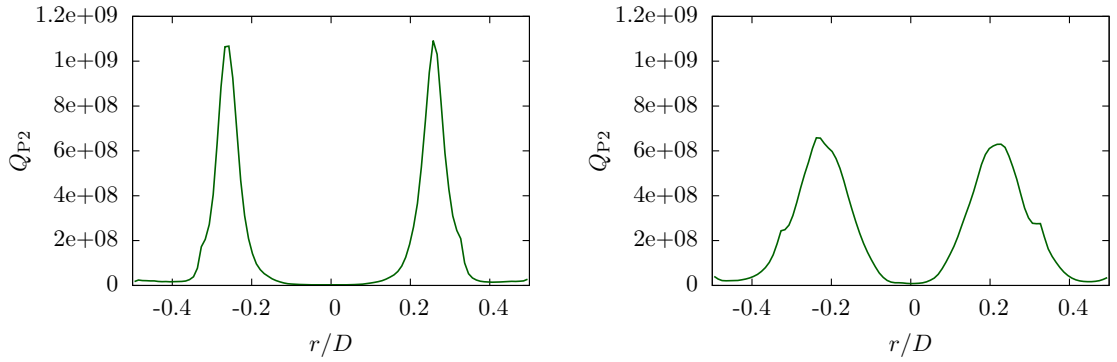

(a) Powell's source term X1

(b) Powell's source term X2

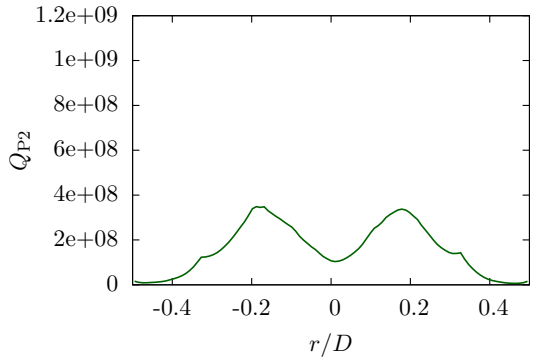

(c) Powell's source term X3

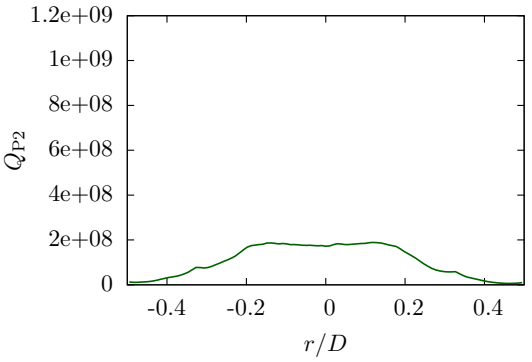

(d) Powell's source term X4

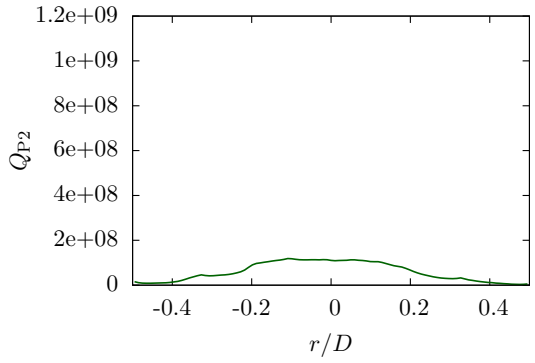

(e) Powell's source term X5

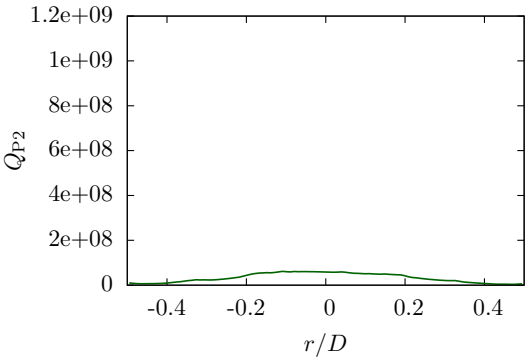

(f) Powell's source term X6

Figure 5.31: Profiles of the mean values of the source term in Powell's analogy at spanwise cuts across the duct at positions X1-X6 for ring positions P5.

against the sampled position and using the coloured contours to represent the magnitude of the PSD.

The wall pressure spectra on the orifice face and the duct wall are shown in Figures 5.32(a) and 5.33(a). From the data, it is not easy to confirm where the noise sources are located, due to the contamination by the hydrodynamic pressure fluctuations. However, there is a region along the inside edge of the orifice, which produces large pressure fluctuations across the whole frequency range. There are also high levels of unsteadiness in the low frequencies across the whole face of the orifice. A comparison between the

simulated and experimental wall pressure spectra at a single point located on the orifice face is shown in Figure 5.32(b). The data show a slight underprediction across the frequency range, but in general the magnitude and shape of the decay is very good, differing by less than 8dB up to 5kHz.

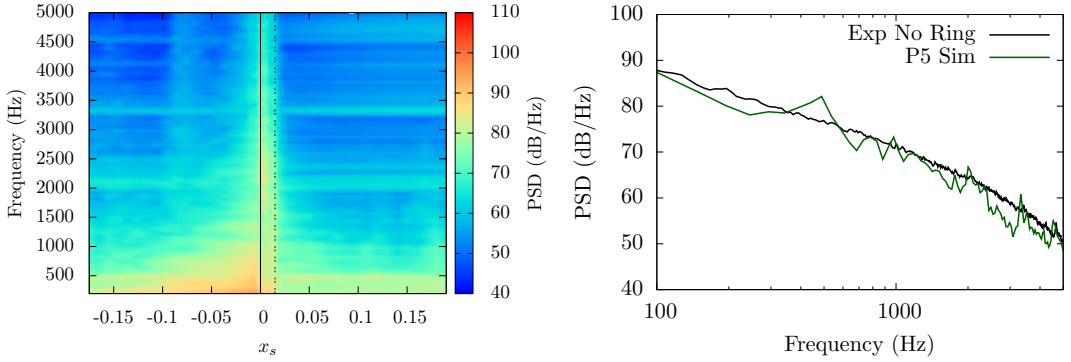

(a) Orifice face contour (b) Single point orifice face

Figure 5.32: Variation of the wall pressure spectra across the orifice face and comparison to experimental data wall pressure spectra for a single point at a radius of 35mm from the duct centreline for the ring in position P5. The solid line represents the upstream corner of the orifice and the double dashed line represents the downstream corner of the orifice.

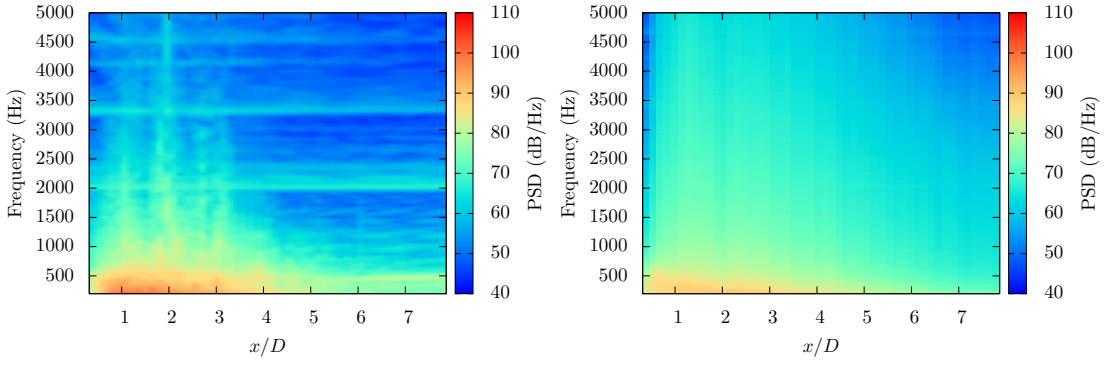

(a) Simulation (b) Experiment

Figure 5.33: Comparison of the experimental and simulated wall pressure spectra for sampled points along the the duct wall for the ring in position P5.

On the duct wall, there are also large wall pressure fluctuations in the low frequency range along the length of the duct wall, but concentrated around the recirculation region. High fluctuations are also surprisingly seen between 3-5D downstream of the orifice. This position coincides with the maximum skin friction values along the duct wall after reattachment of the jet flow. Therefore, it is possible that this noise is caused by the

newly reattached and highly turbulent boundary layer. The comparison between the simulated and experimental wall pressure along the duct is satisfactory in terms of the development of the spectra with downstream distance. However, the magnitude of the spectra predicted by the simulation is seen to be significantly higher (∼10dB) at distances less than x/D=4 at frequencies less than 1kHz. Across the rest of the duct and at higher frequencies, the simulation underpredicts by up to 10dB. The is most likely an effect of the overpredicted turbulence within the shear layers interacting with the walls.

Overall, the comparison of the simulated and experimental data gives confidence in the modelling approach and the representation of the flow both in the near field, based on the results presented in this section, and in the farfield, based on the results presented in Section 5.4.3. This enables the prediction of the flow with additional upstream turbulence, where less in depth validation will be performed of the basic flow properties.

In order to analyse the frequency components of the source term of Curle's analogy, the square of the time derivative of the hydrodynamic pressure was across the entire surface of the duct and orifice at each timestep. This enables processing of the data via an FFT, the results of which are shown as contour plots of the orifice face and duct wall in Figure 5.34. The large magnitude of the noise source along the upstream face of the orifice near the upstream corner becomes immediately apparent. This source clearly dominates the other sources present on the orifice face for the case of orifice self noise. The dominant noise source on the duct wall is less noticeable, however, the source term spectra appears to remain high even far downstream of the orifice.

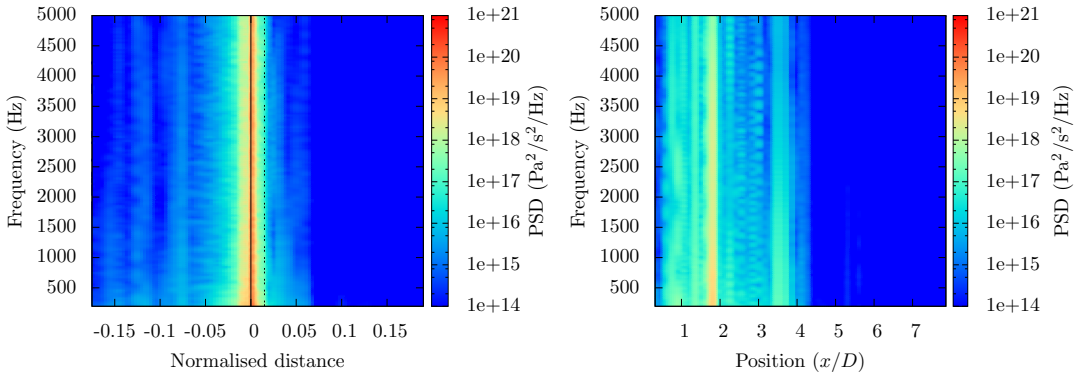

(a) Orifice face

(b) Duct wall

Figure 5.34: Variation of the square of the time derivative of the hydrodynamic pressure spectra for sampled points along the orifice face and the duct wall for the ring in position P5. The solid line represents the upstream corner of the orifice and the double dashed line represents the downstream corner of the orifice.

5.4.4.5 Orifice self noise mechanism

Whilst the primary noise source for the orifice self noise appears to have been identified, no attempt has yet been made to explain the noise source mechanism. Based on the results presented here, it is clear to see that the noise source is located within a region where the gradient of the pressure and density is very large, see Figures 5.26 and 5.28. This by itself is not the noise source, however, when this large gradient is combined with the unsteadiness of the mass flow rate through the orifice opening (caused by the flapping motion of the shear layer [204]), the pressure will vary with relatively small changes over time of the mass flow rate. Due to the fact that nearly all of the pressure drop leading into the orifice occurs in the region close to the upstream corner, it is the place on the wall that will see the largest effect from mass flow variations. The relationship between the mass flow rate through the orifice and the pressure drop is given by Equation 2.3. The instantaneous values and the spectra of the mass flow rate across the orifice opening, taken as an average across the cell centres of the most upstream cells within the orifice opening, are presented in Figure 5.35.

The instantaneous mass flow rate shows variations of up to 0.2% of the mean mass flow rate. From the spectra of the mass flow rate it can be seen that the primary fluctuations are at lower frequencies, further suggesting that the flapping of the shear layer is the dominant driving mechanism. However, the lack of any mid- to high-frequency content (>5kHz) in the spectra of the mass flow rate suggests that it may be a more local mechanism which is contributing to the higher frequency fluctuations seen in the acoustic pressure spectra. This effect may have been lost through the process of averaging across the orifice opening. Based on Equation 2.3, the fluctuations in the mass flow rate could result in fluctuations in the pressure of up to 28Pa with this orifice and flow rate. The actual fluctuations seen in the pressure drop value are approximately 32Pa. The high frequency local fluctuations may account for the difference between the predicted and the actual pressure fluctuations through the orifice opening.

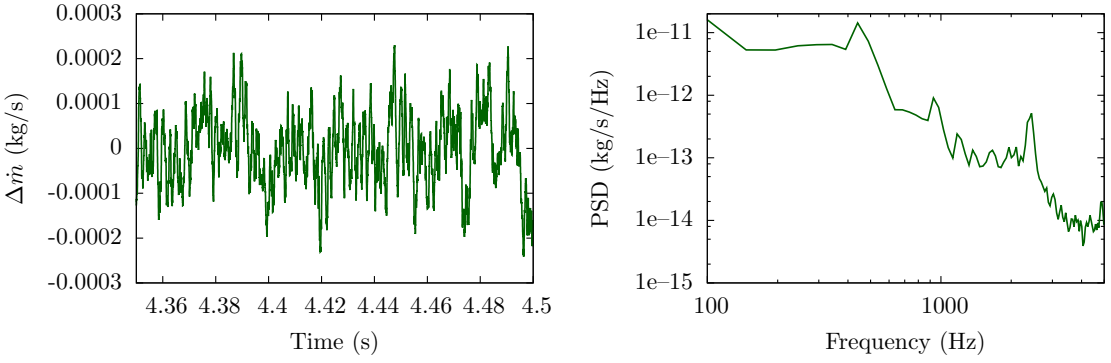

(a) Instantaneous (b) Spectra

Figure 5.35: Instantaneous and spectral values of the unsteady mass flow rate taken as an average across the orifice opening.

As mass flow rate changes do not fully explain the unsteadiness around the upstream corner of the orifice, a second effect which must be considered is the unsteady separation which occurs from the upstream corner of the orifice and the secondary separation seen over much of the upstream orifice face. The noise source is located directly between these two points and therefore will be influenced by the unsteadiness of both of these regions.

The position of this noise source, being located on the upstream face of the orifice, suggests that the radiation may not be dominant downstream and in that case may not be the primary source of noise for downstream locations. This point has been addressed in Section 6.3, where an idealised monopole and dipole noise source, at plane wave frequencies, was propagated from a location coinciding with the dominant source on the upstream face of the orifice. The directivity of the radiation was quantified.

5.5 Single orifice cases with additional turbulence

In the previous section, an attempt was made to identify and characterise the self noise source of an orifice (when only fully developed conditions exist in the duct). The next part of this study focuses on the additional noise generation by a highly turbulent incoming flow, when it interacts with the orifice. The method of increasing the turbulence levels within the duct is documented in Section 5.2. Within this section, this method of modifying the inflow conditions will be validated, and an attempt will be made to identify and characterise the additional noise mechanism.

5.5.1 Validation of inflow conditions

In order to increase the turbulence levels within the duct, the position of the ring was varied upstream of the orifice. The positioning of the rings does not correspond exactly to the experimental configuration, with slight differences to account for the differences in the turbulence decay rate seen between the experiment and the simulations. This was assessed with data collected from a precursor simulation of an isolated ring, with measurements of the turbulence intensity at various spanwise planes downstream of the ring. It was not known how the orifice may affect the decay of the turbulence and therefore, it was necessary to perform a further validation of the inflow conditions when using a ring/orifice pairing. The result of this validation is shown for ring positions P1 and P2 in Figures 5.36 and 5.37, where the spanwise profiles of mean normalised velocity and turbulence intensity are plotted at a position $0.3D$ upstream of the orifice. The result of this validation is that the mean velocities are well predicted, but the turbulence intensity is slightly underpredicted for ring position P1. This underprediction is more noticeable near the walls of the duct and is most likely related to the same difficulties as seen in the prediction of the orifice flow, noted in Section 5.4.1.1. These results suggest that the blockage of the orifice has the effect of slightly reducing the turbulence intensity

upstream, probably due to the large acceleration and straightening of the flow which is passing through the orifice. A similar effect is seen in wind tunnel contraction sections, where the flow acceleration has the effect of straightening the flow and reducing its turbulence intensity [205].

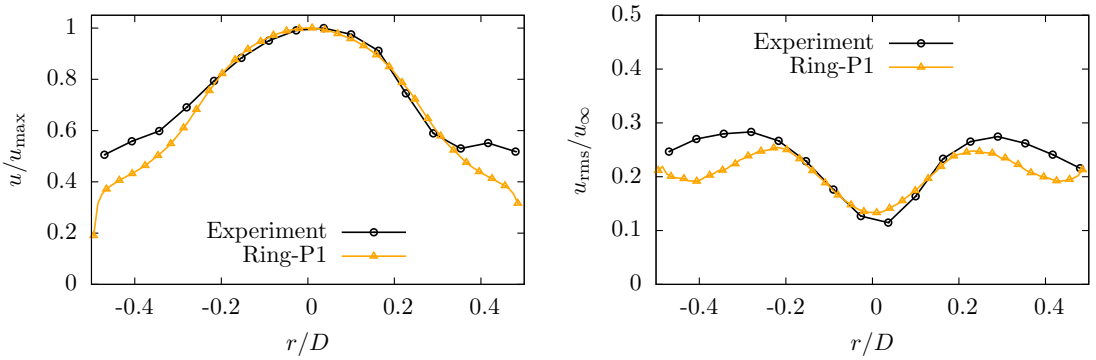

(a) Mean normalised velocity (b) Turbulence intensity

Figure 5.36: Comparison of the experimental and simulated mean velocity profiles and turbulence intensity profiles at a position $0.3D$ upstream of the orifice with a ring placed at $1.4D$ upstream of the orifice (Position P1).

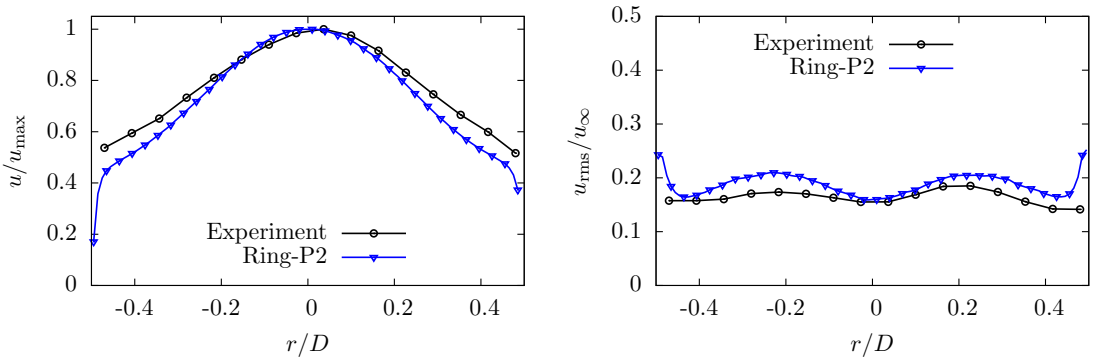

(a) Mean normalised velocity (b) Turbulence intensity

Figure 5.37: Comparison of the experimental and simulated mean velocity profiles and turbulence intensity profiles at a position $0.3D$ upstream of the orifice with a ring placed at $3D$ upstream of the orifice (Position P2).

The result of the other ring positions, is shown in Figure 5.38. The validation of these positions is based on their relative turbulence generation compared to the other positions, as there was not experimental data for comparison. It is seen that as the ring is moved further upstream, the turbulence intensity upstream of the orifice is reduced. This follows that the turbulence has a longer streamwise distance to decay and results in the lower levels. As expected, the mean velocity profile is seen to recover more upstream of the orifice as the ring separation distance is increased.

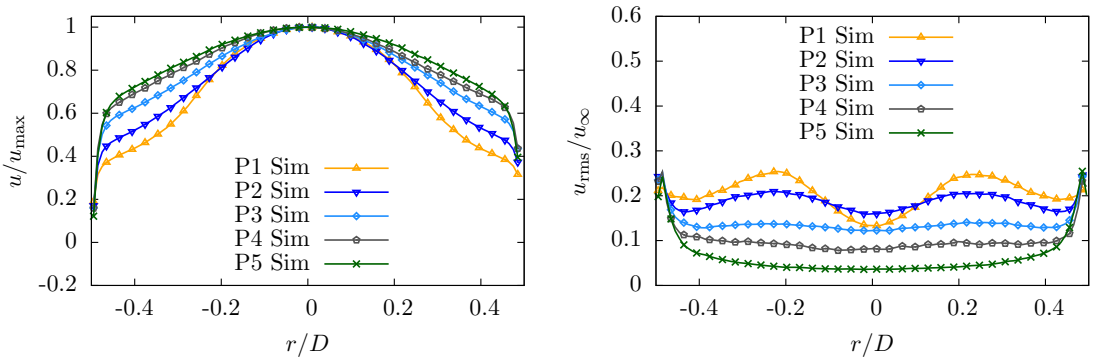

(a) Mean normalised velocity

(b) Turbulence intensity

Figure 5.38: Comparison of the simulated mean velocity profiles and turbulence intensity profiles at a position $0.3D$ upstream of the orifice with a ring placed in positions P1-P5.

Despite the slight underprediction of the turbulence intensity, it is clear that the introduction of the ring into the ducting has had the desired effect of dramatically increasing the turbulence levels. The turbulence intensity is seen to easily be controlled through positioning of the ring. The good comparison of the upstream flow will provide the basis for an investigation of the effects of increased turbulence levels on the flow.

5.5.2 Velocity results

From the previous section, it is clear that the rings provide a suitable method for increasing the turbulence levels within the ducting upstream of the orifice. The effect of this increased upstream turbulence is now assessed at a location downstream of the orifice, in an effort to link the upstream and downstream flow properties. This data is presented for ring positions P1 and P2 with comparison to experimental data in Figures 5.39 and 5.40, respectively.

The results indicate that in both cases, the mean velocity profile stays relatively unchanged despite the increased levels of turbulence. The turbulence intensity profiles show a more significant change, especially within the recirculation region and through the centre of the jet. The increased upstream turbulence intensity presents itself as an increase in downstream turbulence intensity within these regions. The shear layers are less noticeably affected by the increased turbulence, suggesting that the turbulence produced within the shear layers dominates the effect of the upstream turbulence. The relative turbulence intensity is higher when the ring is placed in position P1, which corresponds to the higher upstream turbulence levels.

The results for the additional ring positions is shown in Figure 5.41. The mean velocity profile is seen to be almost completely unchanged, and there are only noticeable differences in the turbulence intensity profile through the centre of the jet. The differences

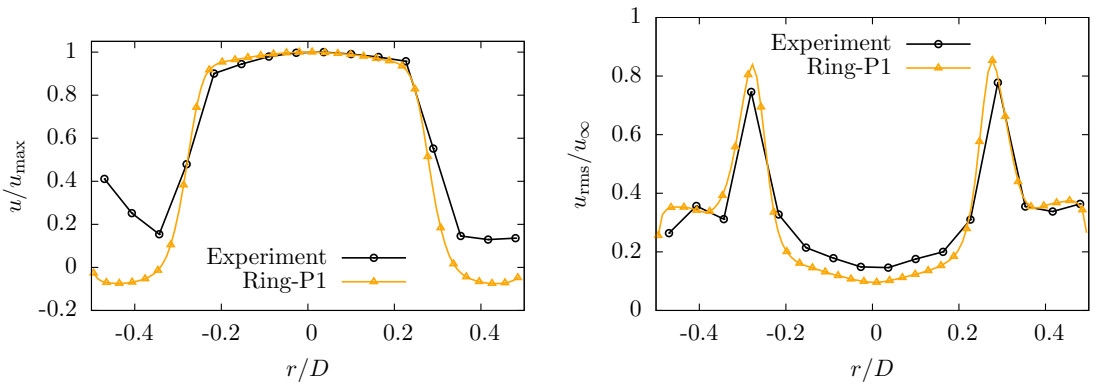

(a) Mean normalised velocity

(b) Turbulence intensity

Figure 5.39: Comparison of the experimental and simulated mean velocity profiles and turbulence intensity profiles at a position $0.3D$ downstream of the orifice with a ring placed at $1.4D$ upstream of the orifice (Position P1).

across the span will become more noticeable further downstream as the turbulence diffuses throughout the duct. Overall, it appears that the turbulence levels within the jet and the shear layers can be directly related to the upstream turbulence levels, whereas the turbulence levels within the recirculation region have relatively increased less, probably due to the less efficient transfer of turbulence from the shear layer into the separated region.

The recirculation length is seen to be affected by the position of the ring. For the five ring positions, the predicted recirculation lengths are x/D= 2.05, 2.1, 2.15, 2.2 and 2.3 respectively, all of which show an overprediction based on the experimental data of Bull and Agarwal [7]. The effect can be explained by looking at the mean velocity and mean k-fields along the centreline of the duct, which are plotted in Figure 5.42. The results show that the centreline velocity increases as it passes through the ring and then decays quickly to a lower centreline velocity than upstream of the ring. This is caused by the ring introducing a higher velocity close to the walls which eventually creates a more uniform flow across the duct span and reduces the centreline velocity further downstream. For ring positions P1-P3, the centreline velocity is high when entering the orifice due to the orifice jet, which means that less flow deviation is required and the recirculation regions are therefore shorter. This effect is also coupled with an increase in the LES content of the upstream flow which then interacts with the upstream corners of the orifice. This would provide a faster development of the shear layers and a reduced recirculation length. The k-field on the centreline shows elevated values approximately $2D$ downstream of each ring location as it takes some distance for the turbulence created within the shear layers of the ring to diffuse towards the centreline. This explains the higher centreline values seen for ring position P2 when compared to P1 in Figure 5.42(b).

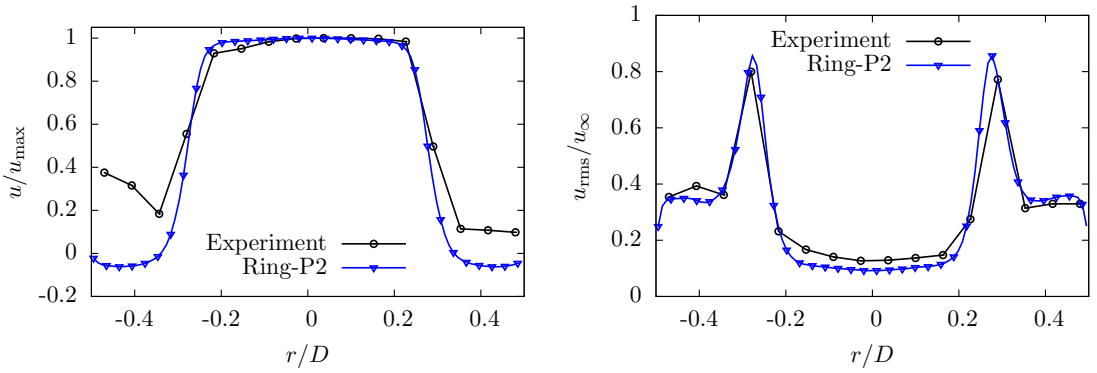

(a) Mean normalised velocity (b) Turbulence intensity

Figure 5.40: Comparison of the experimental and simulated mean velocity profiles and turbulence intensity profiles at a position $0.3D$ downstream of the orifice with a ring placed at $3D$ downstream of the orifice (Position P2).

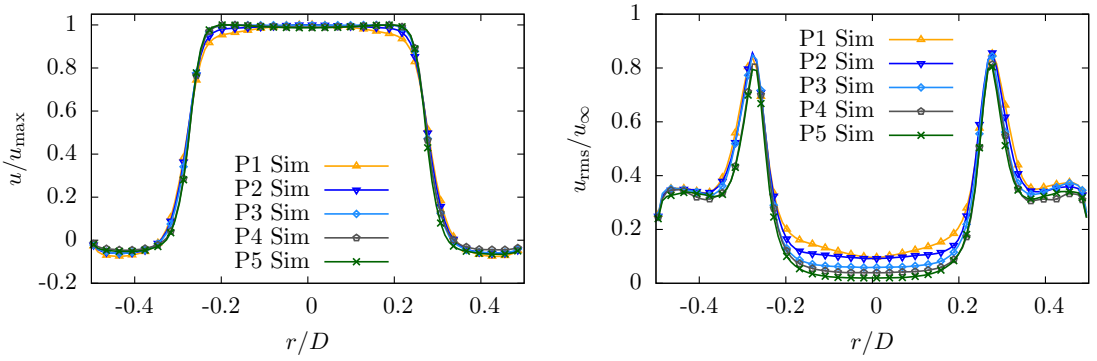

(a) Mean normalised velocity (b) Turbulence intensity

Figure 5.41: Comparison of the simulated mean velocity profiles and turbulence intensity profiles at a position $0.3D$ downstream of the orifice with a ring placed in positions P1-P5.

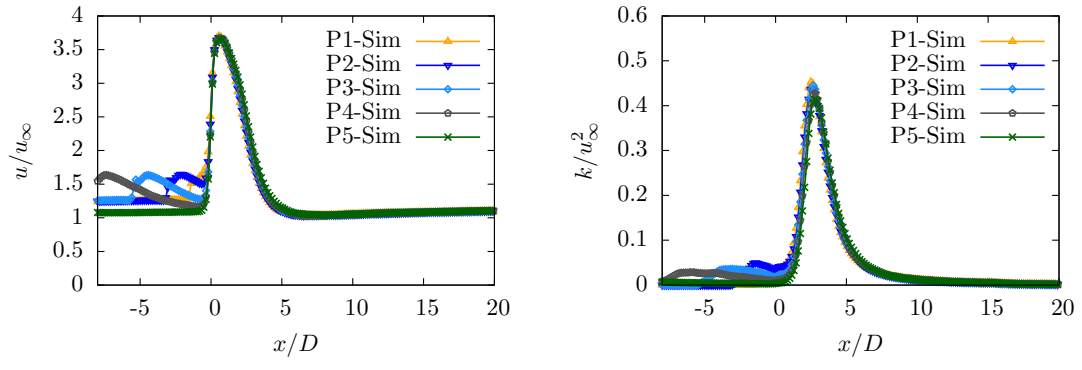

(a) Mean velocity (b) Turbulent kinetic energy

Figure 5.42: Comparison of the mean velocity and turbulent kinetic energy on the centreline of the duct for ring positions P1-P5.

5.5.3 TKE results

Prior to this, the turbulence intensity has been used as the primary method for measuring the turbulence levels within the duct. The reason for this was the desire to validate the turbulence properties against experimental data which were collected using a single wire hotwire probe. Turbulent kinetic energy information can be easily extracted from the simulation and provides a more complete view of the magnitude of the turbulence within the flow. The turbulent kinetic energy is shown in Figure 5.43 for positions $0.3D$ upstream and downstream of the orifice for ring positions P1, P2 and P5. The results show a very similar trend to the turbulence intensity plots, with an increase of the TKE throughout the duct downstream when the ring is introduced. Based on the similarities, it is suggested that the streamwise fluctuations dominate the turbulent kinetic energy profiles. From these plots it is not possible to understand the effect of the additional turbulence, but it is clear that the levels are significantly higher.

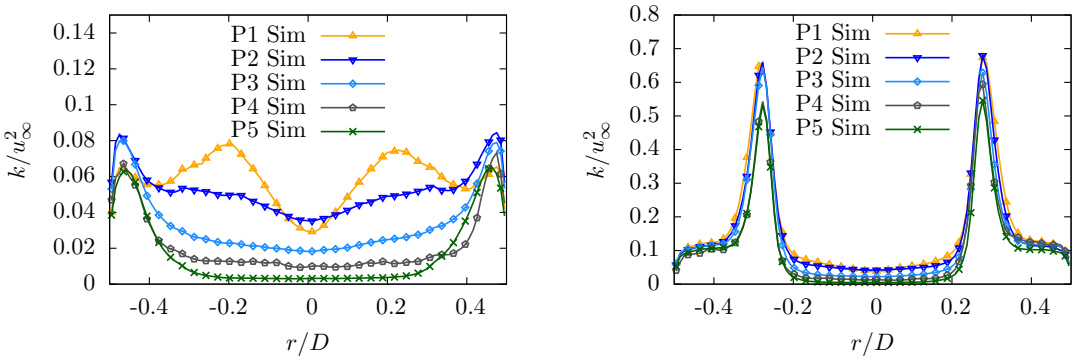

(a) $0.3D$ upstream

(b) $0.3D$ downstream

Figure 5.43: Comparison of the turbulent kinetic energy for ring positions P1-P5.

5.5.4 Acoustic validation

As previously, the acoustic validation will be performed using wall pressure spectra at a distance sufficiently far downstream that it can be assumed that the hydrodynamic fluctuations no longer dominate. Unfortunately, there is no experimental wall pressure spectra with rings available for validation, as it was deemed that farfield sound power measurements were more useful in the experimental program [6]. Therefore, comparison here is performed between the wall pressure spectra of the five ring positions to identify in which cases the noise levels have changed. This comparison can be seen in Figure 5.44.

The wall pressure spectra shows that as the ring is placed closer to the orifice, additional noise is produced. This effect is most noticeable with the ring placed in position P1, but additional low and mid frequency noise is also noted with ring position P2. When the ring is placed in positions P3-P5, the additional noise is negligible, suggesting that

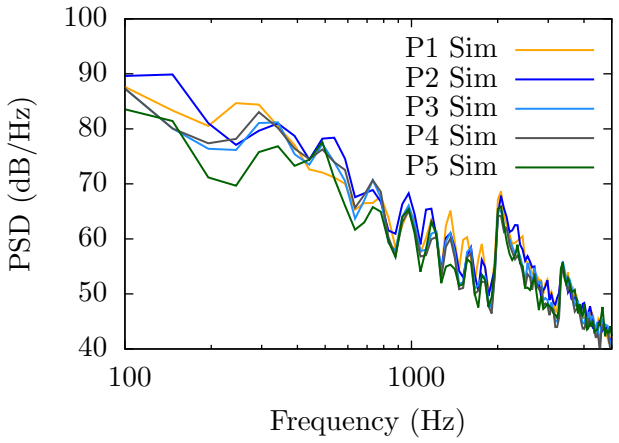

Figure 5.44: Comparison of the simulated wall pressure spectra at a distance of $12D$ downstream of the orifice for ring positions P1-P5.

in these cases the interaction noise is dominated by the orifice self noise. The critical turbulence intensity for this particular geometry appears to be approximately 15%, however, this does not take into account the different turbulence length scales or the presence of vortices in the flow.

It is possible that the reason for the larger increase at low frequencies, is a result of the dominant source being on the front face of the orifice and radiating both upstream and downstream. Then the lower frequency waves would easily pass through the orifice opening, and the higher frequencies would be more significantly refracted and may radiate much better in the upstream direction than downstream. This could be the cause of the larger increase in wall pressure spectra throughout the lower frequencies when the noise in the acoustically dominated region was measured ($12D$ downstream). This point is investigated further in Section 6.3.

Due to the lack of additional noise present in cases P3 and P4, relative to P5, these cases will not be considered further in this investigation. The findings here are in keeping with the farfield experimental results noted by Tao [6], where the ring is in position P1 provided increased noise across the whole frequency range and ring P2 increased the noise in just the low to mid frequency range. The other rings were seen to produce negligible interaction noise.

Unlike when the ring is placed in position P5, the ratio of the upstream and downstream wall pressures could not be compared at the other ring positions. This is due to the scattering of the upstream travelling waves by the ring which would make an accurate estimation of the upstream wall pressure spectra difficult.

5.5.5 Sound source identification

It has been confirmed that the additional interaction noise can be seen in the simulations, providing that the ring is placed sufficiently close to the orifice. In the sections that

follow, the mechanisms responsible for the interaction noise will be investigated using cases P1 (140mm), P2 (300mm) and P5 (2000mm). The ring in position P1 provides the highest turbulence intensity and the most noticeable change in the noise levels when compared to ring position P5. The methodology used for noise source identification will focus on the same procedure as used previously for the orifice self noise, although, the volume sources will not be considered for these configurations.

5.5.5.1 Initial sound source identification

The additional turbulence has a significant effect on the results. Firstly, the pressure drop through the orifice is decreased, as shown in Figure 5.45(a), although this may be a secondary effect from underdeveloped flow within the duct following the ring. The presence of the ring and its wakes have caused a lower pressure region to exist upstream of the orifice. Secondly, the pressure fluctuations throughout the duct have been increased by placing the ring in position closer to the orifice.

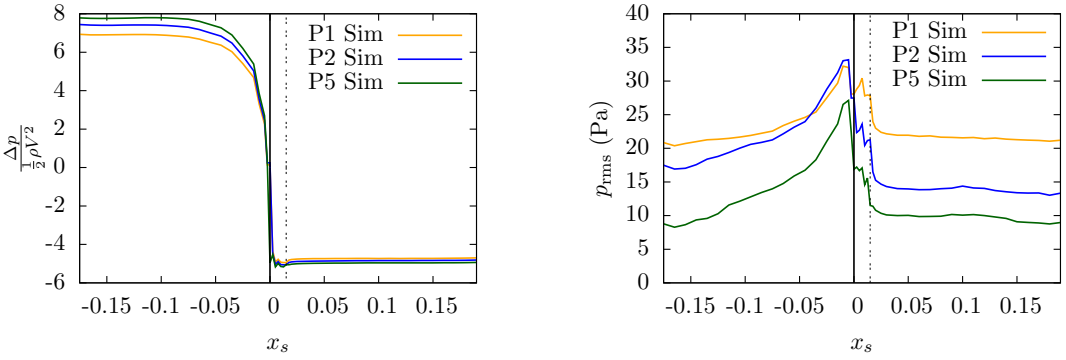

(a) Normalised mean pressure

(b) RMS pressure

Figure 5.45: Comparison of the simulated mean and RMS pressure on the face of the orifice for ring positions P1, P2 and P5.

Figures 5.45(b), 5.46(a) and 5.46(b), which show the RMS pressure fluctuations on the orifice, duct wall and the centreline, all indicate larger pressure fluctuations as the ring is moved closer to the orifice. This effect is most noticeable on the orifice face and on the duct wall, in regions away from the jet impingement location. The increase of the pressure fluctuations near the jet interaction point is small, suggesting that this secondary noise source may be minimally effected by the additional turbulence within the jet. The fluctuations are significantly increased across the whole face of the orifice, although most noticeably in the region around the previously suggested dominant noise source. This suggests that whilst the turbulence has some effect on the noise sources across the rest of the upstream face and the whole of the downstream face of the orifice, the majority of the additional noise comes from an increase in the dominant noise source.

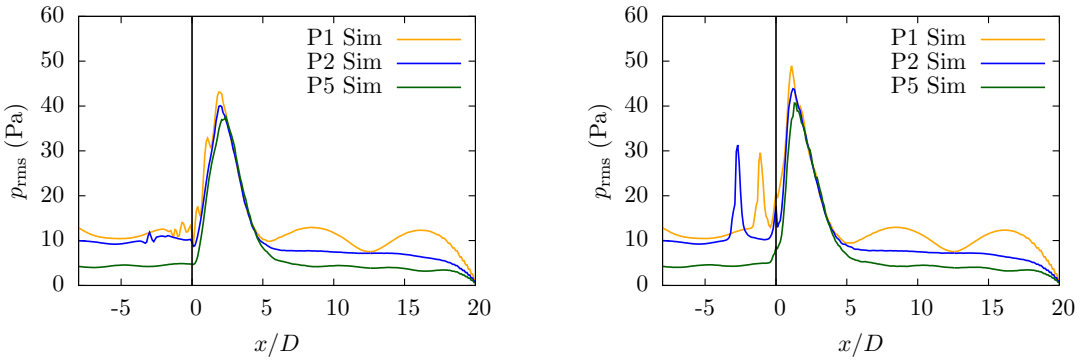

(a) Centreline (b) Duct wall

Figure 5.46: Comparison of the simulated RMS pressure along the duct centreline and the duct wall for ring positions P1, P2 and P5.

5.5.5.2 Surface sound source identification

The magnitude of the square of the derivative of the hydrodynamic wall pressure (source term in Curle's analogy) on the orifice face and duct wall for different ring positions, is shown in Figure 5.47. When the rings are introduced, the source term is increased, primarily in the region around the upstream corner dominant source. With the ring placed in positions P1 and P2, the source term is seen to be increased across the whole orifice face compared to position P5, however, around the upstream corner of the orifice is seen to be almost unchanged, whereas the source term on the other parts of the upstream and downstream faces of the orifices is higher with the ring in position P1. This suggests that the effect of the turbulence is to produce additional interaction noise over specific parts of the orifice face.

On the duct wall around the jet impingement location, the source term is seen to be relatively insensitive to the position of the ring. The source term downstream of the impingement region shows higher values as the ring is placed closer to the orifice, caused by both the interaction of the additional turbulence with the duct walls and the propagation of the higher noise levels produced by the orifice. In all cases, it is seen that an increase in the source term downstream of the orifice is coupled with a similar increase in the source term upstream of the orifice.

The vorticity magnitude on the orifice face and duct wall in shown in Figure 5.48. It is clear that the vorticity on the orifice face is insensitive to the positioning of the rings.

5.5.5.3 Frequency resolved surface sound source identification

The comparison of the frequency resolved noise sources on the orifice surface shows some significant differences between cases P1, P2 and P5. Before discussing the differences between the cases, a validation of the wall pressure spectra for ring position P1 is conducted. Figure 5.49 shows the wall pressure spectra across the whole face of the orifice

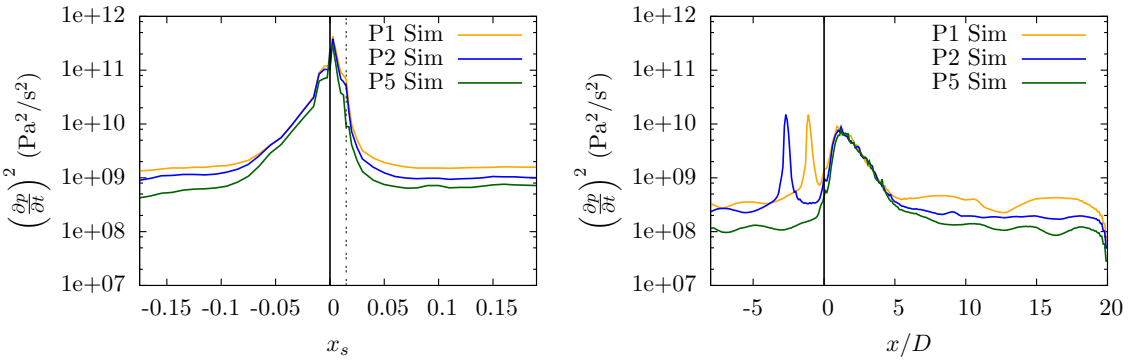

(a) Orifice face (b) Duct wall

Figure 5.47: Profiles of the mean squared time derivative of the hydrodynamic wall pressure on the face of the orifice and the duct wall for ring positions P1, P2 and P5. The solid line represents the upstream corner of the orifice and the double dashed line represents the downstream corner of the orifice.

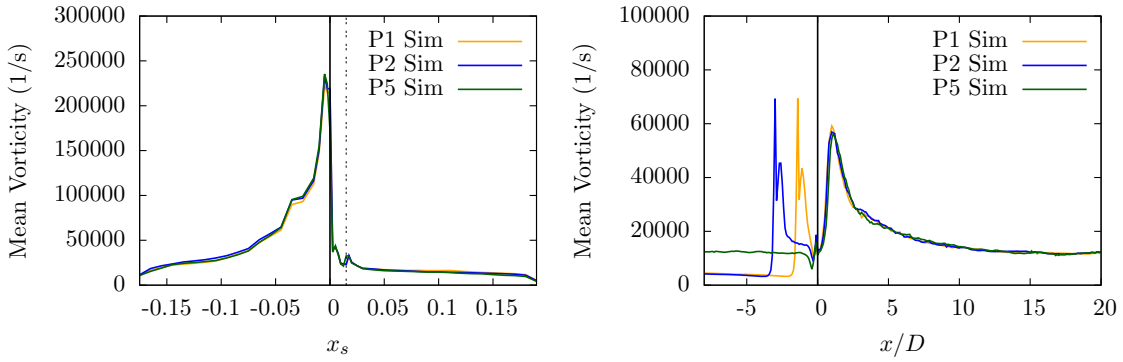

(a) Orifice face (b) Duct wall

Figure 5.48: Comparison of the simulated mean vorticity for points along the orifice and the duct wall for ring positions P1 and P5. The solid line represents the upstream corner of the orifice and the double dashed line represents the downstream corner of the orifice.

and a comparison to the experimental data for a single point on the orifice face. The comparison of the wall pressure spectra is very good throughout the whole frequency range (max 10dB) and even captures the low frequency tonal peak to within 3dB, although this could be greatly improved with a better frequency resolution. The tonal peak occurs at approximately 270Hz and is seen at measurement points both on the upstream and downstream faces of the orifice. It is thought that this frequency may be excited by the unsteadiness of the shear layers within the wake of the ring. The same tonal peak is seen in both the experimental and numerical data, which gives good confidence that the correct physics is being captured in the numerical data. Furthermore, these validations give a good basis for confidence in the noise predictions presented in Section 5.5.4.

The comparison of the pressure spectra on the duct wall is given in Figure 5.50. This

comparison shows a good agreement to the shape of the experimental wall pressure spectra, although there is a little overprediction (∼5dB) in the low frequency fluctuations around the location of the jet and strong shear layers. There is also an underprediction at higher frequencies across the duct wall, however, this can be explained by the lower frequency resolution of the FFT of the simulated data.

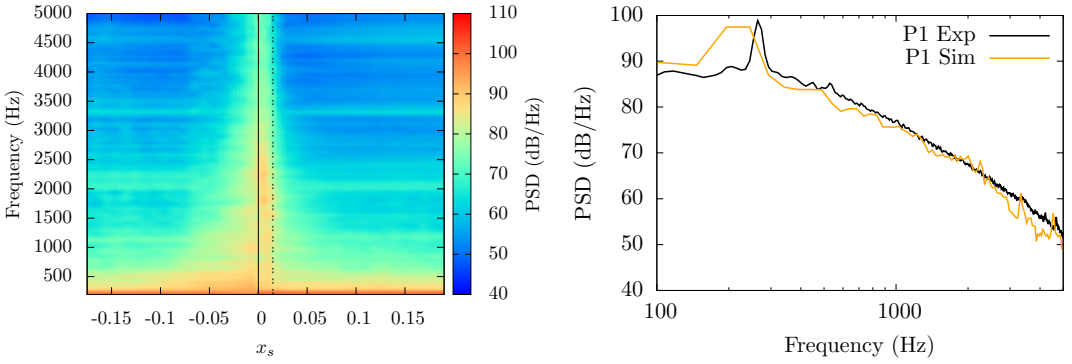

(a) Orifice face contour

(b) Single point orifice face

Figure 5.49: Variation of the wall pressure spectra across the orifice face and comparison to experimental data wall pressure spectra for a single point at a radius of 35mm from the duct centreline for the ring in position P1. The solid line represents the upstream corner of the orifice and the double dashed line represents the downstream corner of the orifice.

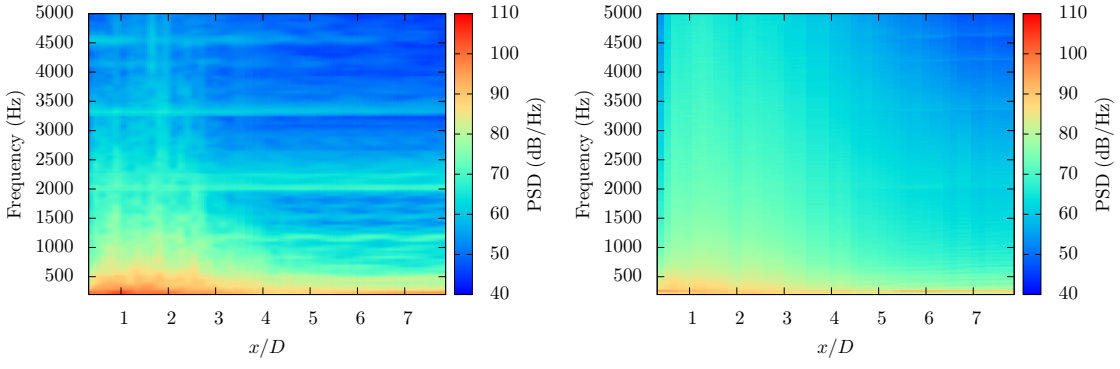

(a) Simulation

(b) Experiment

Figure 5.50: Comparison of the experimental and simulated wall pressure spectra for sampled points along the duct wall for the ring in position P1.

In order to assess the effect of additional turbulence, the differences in the wall pressure spectra, on the orifice, between cases P1 and P2, relative to case P5 have been plotted in Figure 5.51. The variation in the orifice wall pressure spectra suggests that the turbulence acts to increase the total pressure fluctuations over a large part of the orifice

face. What is seen is that the mid to high frequency fluctuations (1-5kHz) are increased around the location of the dominant orifice self noise source and the low frequency increase (<1kHz) is dominated by the downstream face and the upstream face at $r/D >$ 0.375. There is no part of the orifice face where a noticeable reduction in the wall pressure spectra is seen. How this increase in wall pressure fluctuations corresponds to an increase in noise source is discussed in the following section.

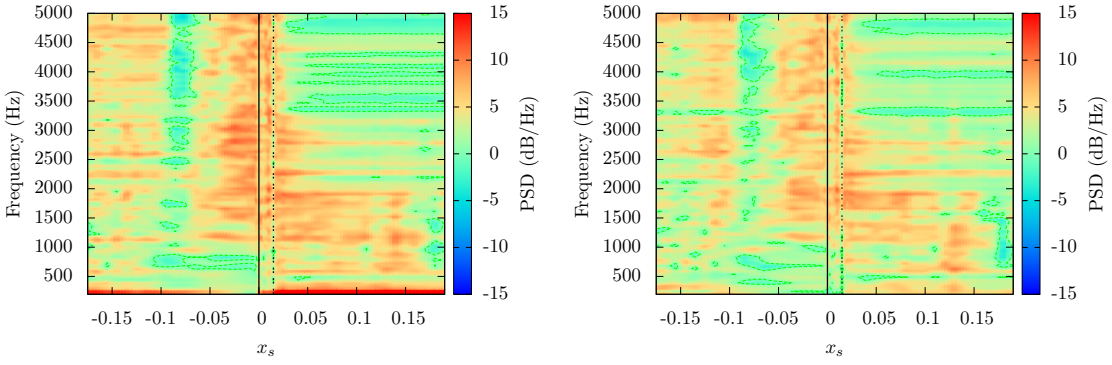

(a) Position P1

(b) Position P2

Figure 5.51: Differences between the wall pressure spectra on the orifice face for ring positions P1 and P2 relative to the spectra in position P5. The solid line represents the upstream corner of the orifice and the double dashed line represents the downstream corner of the orifice.

5.5.5.4 Identification of additional noise generation mechanism

A comparison was also made to the noise source term from Curle's analogy for ring positions P1 and P2. These are presented in Figure 5.52. For both of these ring configurations, it becomes clear that the increase in sound is produced by the orifice face. The increased magnitude of the source term is seen to be heavily concentrated around the upstream corner of the orifice, suggesting that the majority of the noise, and the majority of the interaction noise is generated in this location. Furthermore, the noise source is increased for both cases at x_s=0.07-0.19, the majority of the downstream face. For ring position P1, the same increase is also seen across the majority of the upstream face, with only small regions where the noise source is relatively unchanged (the blue contour data). For ring position P2, there are larger regions across the upstream face and in the region at x_s=0.02-0.06, where the noise source is relatively unchanged. However, in all cases, these areas are so small that they can be considered negligible when compared to the increase around the upstream corner. The increases seen over large parts of the orifice face for both positions P1 and P2 are also negligible when compared to the large change in the corner noise source. Therefore, it is suggested that the increased wall pressure fluctuations seen in the results both on the orifice face and within the duct

further downstream of the orifice are the result of an increase in the noise radiating from the close to the upstream corner of the orifice. The similarity of the noise sources spectra in this region for ring positions P1 and P2 does help explain the similarities in the wall pressure fluctuations measured at $12D$ downstream, and may help to confirm that the other changes in the sources do not have a large effect on the overall pressure fluctuations within the duct.

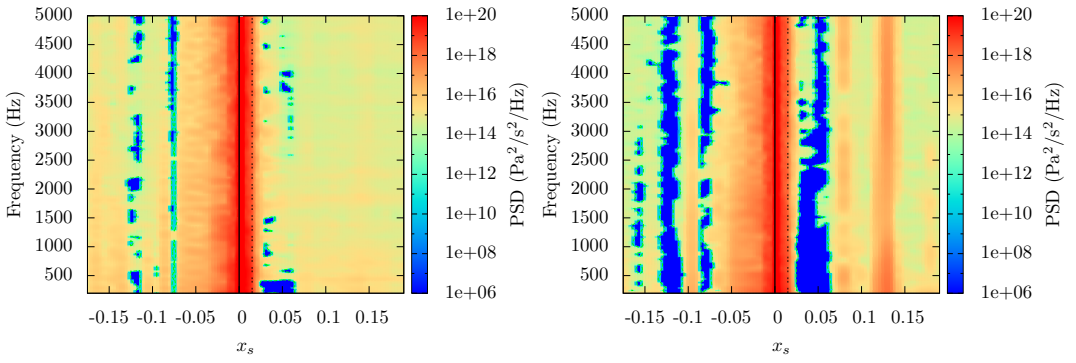

(a) Position P1 (b) Position P2

Figure 5.52: Differences between the magnitude of the source term of Curle's equation on the orifice face for positions P1 and P2, relative to the magnitude for position P5. The solid line represents the upstream corner of the orifice and the double dashed line represents the downstream corner of the orifice.

It is clear that the additional noise source is related to the additional turbulence. The effect of this is most noticeable on the upstream face of the orifice, where it is suggested that the turbulent flow and vortices within the wake of the ring, directly impinge onto the walls of the orifice. On the inside edge of the orifice, the scrubbing of turbulent eddies along the surface may be related to increases in the wall pressure across the frequency range. Furthermore, increased unsteadiness of the mass flow rate through the orifice may help to explain the increase in the dominant noise source region. On the downstream face of the orifice, the wall pressure increase may be attributed to a feedback mechanism, related to the upstream convection of turbulent eddies by the recirculation region, which then impinge on the orifice, as noted by [57].

Proving the underlying mechanisms of these sources is difficult. It is known that the additional turbulence produces additional unsteady forces of the faces of the orifice which then radiate a dipole sound source. From the turbulence intensity plots in Sections 5.5.1 and 5.5.2, it is known that the additional turbulence upstream leads to additional turbulence throughout the duct downstream of the orifice as well. This increase in the turbulence levels within the shear layer has a direct impact on the turbulence levels within the recirculation region.

5.6 Summary

The effect of varying levels of turbulence on the noise produced by a ducted orifice have been investigated using an IDDES based numerical method. The properties of the turbulence upstream of the orifice are modified by changing the position of a ring relative to a single hole orifice. As the turbulence levels are increased, the wall pressure is seen to be increased both on the orifice face and duct wall, and also at locations far downstream of the orifice. The noise sources are estimated using the source term from Curle's analogy, which suggests that the vast majority of the noise is produced from the surface of the orifice, close to the upstream corner. As the turbulence levels are increased, there is little change to the noise sources on the duct walls, but a large change on parts of the orifice face, which contribute to the higher wall pressure spectra. The increase is primarily seen in the source region close to the upstream orifice corner and on other parts of the upstream face, where direct impingement of turbulence is seen. Furthermore, a smaller increase is seen on the downstream face of the orifice, where it is suggested that turbulent eddies are convected within the recirculation region to cause the impingement. However, the sources caused by impingement are generally small compared to the dominant noise source and it is suggested that these will have minimal impact on the pressure fluctuations within the duct. Therefore, the increased wall pressure fluctuations are suggested to be from the increased noise production from the dominant upstream corner source.

Chapter 6

Sound Propagation Through the Air Distribution System

6.1 Introduction

In addition to producing sound, components within the ADS are also responsible for the scattering of existing sound. This existing sound can be produced by other components upstream and downstream of the orifices and may also be the result of the scattering of orifice noise by other components. Studying the propagation of noise within the ducting of the ADS provides information on how existing noise acts to increase noise levels within other parts of the system.

There are a number of advantages to the numerical simulation of sound propagation. Firstly, the amplitude and frequency of the noise source can be easily controlled, to investigate the scattering characteristics at individual frequencies. Furthermore, the placement and the propagation direction of the noise source can be better defined. In terms of the disadvantages of this numerical method, there is one key point. The LEE do not take into account the effects of viscosity, meaning that the production of sound induced vortices at the corners of the orifice, and their corresponding absorption of sound energy, will not be properly accounted for. However, this effect has been studied and for large orifice sizes, the vortices created are weak and dissipate quickly after shedding. The incident sound then propagates with minor distortion whilst passing through the orifice [77]. The sound absorption was predicted to be highest at the lower frequencies, where the underprediction by the LEE is expected to be most significant.

This chapter give details of the simulations performed to investigate the propagation of acoustic waves through in-duct components of an ADS. The simulations in the first section aims to give a better understanding of the reflection of sound waves as they pass through a single orifice. The results presented within this section show the effect of varying parameters of the duct and orifice geometry on different frequency plane waves. The aim of the second section is to estimate how a sound source from the orifice face

will propagate upstream and downstream through the ducting of the ADS. For this purpose, idealised monopole and dipole sources are placed on the wall of the orifice, at the estimated location of the dominant noise source.

6.2 Propagation of existing noise

This section details the studies conducted into the downstream propagation of existing sound in the ducting and its interaction with the single orifice geometry. The following sections details the studies conducted using a clean geometry and a single orifice and the effect of various geometrical parameters of the orifice and flow conditions on the propagation and reflection.

6.2.1 Methodology

The geometries used for this study share the same 100mm diameter cylindrical ducting as used for the noise generation studies in chapter 5. Two separate configurations have been investigated, firstly a clean duct has been simulated to serve as a benchmark case, and then a series of isolated single orifices, with varying internal diameters, d, of between 30-90mm have been quantified in terms of their ability to reflect incoming sound waves. Additionally, the effect of varying thickness and non-uniform meanflow is considered using a d=80mm orifice, along with the effects of incoming wave amplitude.

The simulations performed here solve the Linearised Euler Equations in the time domain using a high order in-house code called SotonLEE (see section 3.8.1). The code uses buffer zones at inlet and outlet of the straight duct to control the properties of the flow entering and leaving the domain. The buffer zone at inlet additionally allows for the specification of incoming acoustic waves. The incoming acoustic waveform is solved on a separate grid and the solution transferred onto the final meshes prior to initialising the simulations. This additional mesh is required to account for the presence of multiple mesh blocks across the span at the inflow. The solution on this mesh is then updated at each computational timestep to force the propagation of these acoustic waves through the duct.

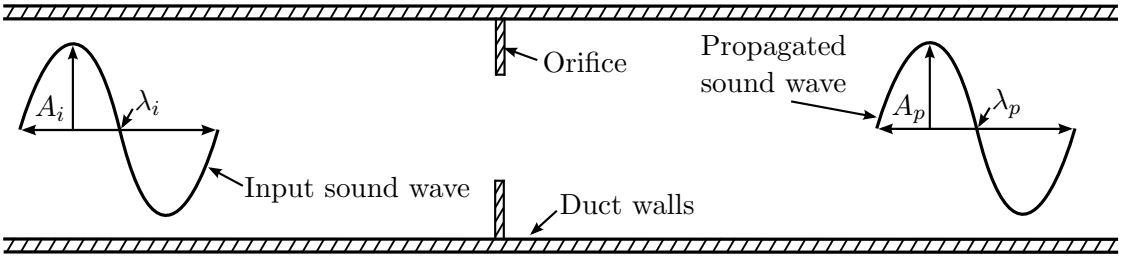

Figure 6.1: Schematic of the computational domain for the study of the transmission and reflection of an incoming sound wave by a single orifice.

The outer walls of the duct are designated as slip walls and the centreline of the duct is defined as a symmetry plane. The simulations are performed in axisymmetric coordinates, which allows for modes which are constant in the span, e.g. plane waves (n=0, m=0) to be solved in 2D at reduced computational cost. These simulations require additional postprocessing routines to take the results and reconstruct a full duct domain with the radial variation in flow quantities. For all studies performed in this section, the coordinate system is defined as follows: x is the flow direction, y is the vertical direction, z is the spanwise direction and r is the radial direction.

Non-dimensional timesteps (based on the speed of sound and an arbitrary length scale of 1m) of 1×10^{-4} and 1×10^{-5} were used for the clean duct and single orifice cases, respectively. These provided maximum CFL values of 0.6 and 0.4, were sufficient to ensure the stability of the code. Each simulation is run for a initial period of a minimum of 10 wavelengths of the highest frequency considered, after which, sampling was performed for a minimum of an additional 10 wavelengths.

All of the meanflows utilised in this chapter are created with OpenFOAM [206] version 2.2.2 using a compressible solver (see section 3.8.2). The clean duct meanflow is taken directly from the CFD simulations described in Section 4.3. The meanflow for the 80mm orifice is developed from the same methodology and mesh topology as used for the single orifice case in Section 4.4. The mean profiles of density, pressure and the velocity components are interpolated from the CFD mesh onto the LEE mesh using the Kriging method in Tecplot 360 [207] 2013. The solution is then converted to the correct format by subroutines within SotonLEE.

One of the problems with the use of the LEE's, are stability issues for flows with shear layers where a large velocity gradient occurs (see section 3.8.1). Unfortunately, the flow through an orifice is dominated by a high velocity jet and recirculation regions, creating a strong shear layer between them. This flow feature caused significant problems in the higher velocity non-uniform mean flows (>10m/s) which were attempted in the early simulations. There were two options for reducing the impact of the problem; removal of terms from the LEE and reduction of the Mach number of the meanflow, to reduce the velocity gradients within the shear layer. Both of these methods were eventually used, with the bulk velocity being reduced to a maximum of 10m/s for all cases considered and the gradient term suppression form of the LEE being utilised.

6.2.2 Clean duct geometry

The clean duct cases have been run without any components present within the duct. These cases are expected to provide a reference point for the other components of the ADS and have also been used to identify important parameters within the LEE simulation setup. Preliminary studies were performed to assess the effect of mesh refinement, the meanflow (Mach number and uniformity) and the order and amount of numerical filtering.

The meshes used for these simulations are presented in Figure 6.2. There are three refinement levels, with the 'medium' mesh resolving the acoustic waves with a minimum of 10 points-per-wavelength (PPW) (suitable for higher order codes [208]), the 'fine' mesh providing 20PPW at the higher frequency (the required resolution for a low order code [99, 101]) and the 'finest' mesh using 40PPW (only used for the mesh validation). The meshes have been designed specifically for SotonLEE and therefore have no boundary layer mesh on the slip walls. Due to the simple nature of the clean duct geometry, a low aspect ratio can be used for all cells and the mesh resolution is uniform throughout the domain. Buffer zones are applied over the whole of the inlet and outlet blocks which have a length of $2D$, sufficient to accept a quarter of a wavelength of even at the lowest frequencies considered.

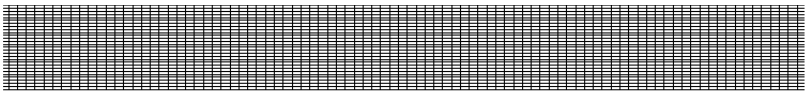

(a) Medium mesh

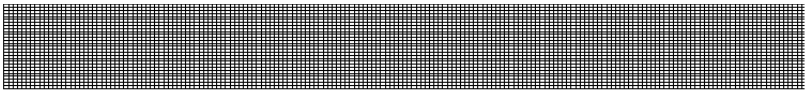

(b) Fine mesh

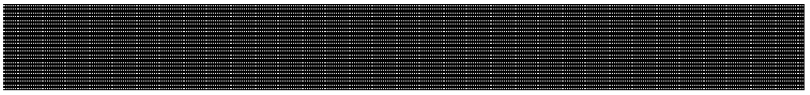

(c) Finest mesh

Figure 6.2: Comparison of the three mesh refinement levels for the clean duct.

These cases were run with both a low and higher frequency plane wave (200Hz and 2000Hz), where the higher frequency wave was chosen to be just below the cut-on frequency for the first spinning duct mode (2041Hz). This would provide information about the suitability of the mesh refinement as it was close to the theoretical maximum frequency for which the medium mesh was designed. Unless stated otherwise, all of the simulations are performed using the medium mesh.

The results of the mesh refinement study and the effect of the numerical filtering order can be seen in Figures 6.3(a) and 6.3(b), respectively. The results show that there is a negligible difference seen for the mesh refinement and the effect of the numerical filter, despite the increased simulation stability provided by the 6th order filter. The most significant difference was seen for the switch between the uniform and non-uniform meanflows (shown in Figure 6.4). The non-uniform mean flow is taken from the data presented in Section 4.3.1. For the low frequency case, the effect of the non-uniform mean flow is still negligible, however, as the frequency is increased to 2000Hz, there is a small difference. The RMS pressure is increased slightly near the walls of the duct and

decreased slightly towards the centreline of the duct. This is caused by the difference in the meanflow velocities in the centre of the duct and towards the walls, where the boundary layer has an influence. Overall however, this effect is still small, but may become more significant for the orifice geometry and will be investigated further there.

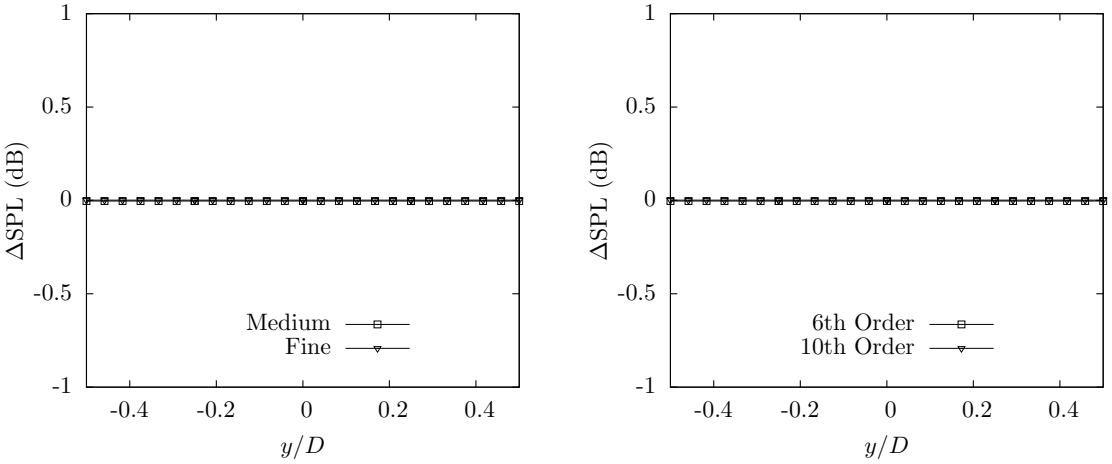

(a) Mesh refinement

(b) Filter order

Figure 6.3: Comparison of the effect of the levels of mesh refinement and filter order on the propagation of a 2000Hz plane wave.

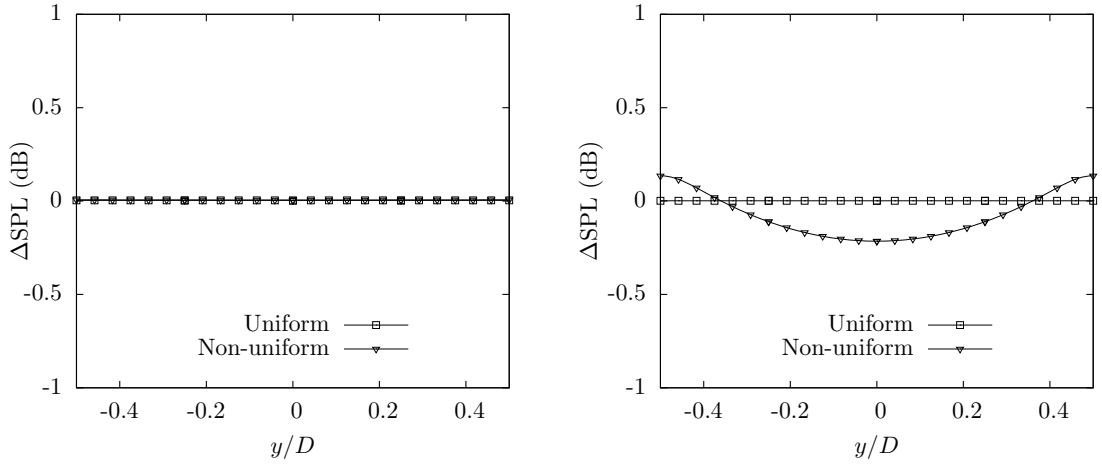

(a) 200Hz plane wave

(b) 2000Hz plane wave

Figure 6.4: Comparison of the effect of uniform and non-uniform meanflows on the propagation of acoustic plane waves.

6.2.3 Single orifice geometry

When these simulations were first considered, the idea was to perform a parameter study of the orifice geometry and flow conditions, to investigate optimum configurations for noise attenuation. However, the large range of parameters and the realisation that

many of these parameters may have little effect, meant that the most important ones for noise attenuation needed to be selected using preliminary studies. This included a study of the importance of orifice diameter and thickness, Mach number of the non-uniform meanflow and amplitude of the input waves. The frequency has been identified as an important parameter in the clean duct studies and will be considered in detail for the orifice studies. However, the presence of the orifice is expected to have a greater effect at higher frequencies, so the preliminary comparison studies are performed using a 2000Hz plane wave only. Varying the duct diameter was discounted prior to these simulations, due to the experimental rig having a single fixed diameter and the need to limit the number of variables where possible.

6.2.3.1 Initial simulations

Based on the initial clean duct simulations, it was decided that the 6th order filter would be used as it provided better stability without significant affect on the results and that a non-uniform meanflow may be important in order to achieve accurate results.

The preliminary single orifice simulations were all run using the d=80mm orifice. This geometry was chosen as it was shown to be stable in the early stages of using the SotonLEE code and provided reasonable interaction between the acoustic waves and the geometry. This was the first geometry that was considered, and therefore had seen a number of mesh revisions to produce a stable mesh. The main difficulties experienced in meshing the geometries were around the corners of the orifice. In the original meshing procedure, shown in Figure 6.5(a), a square block structured had been produced to mesh the orifice face. This led to there being a node on the lower corners of the orifice being shared by three blocks, one of which was unaware that this node belonged to a boundary, along which a slip wall condition was enforced. This is a common problem when using sharp edged geometries with a finite difference code. There are a number of possible solutions; the geometry can be modified, for example by rounding the corners of the orifice, although this changes the physics of the problem and is therefore undesirable; by copying point values from the other two blocks that are aware of the presence of the slip wall boundary; and finally, to redesign the block structure of the mesh. The first attempt was made by copying the nodes values from one of the other two blocks onto the node located on the third block, however, this was unsuccessful and still ultimately led to the divergence of the simulation. Secondly, the block structure of the mesh was modified, which led to the intermediate block structure, shown in Figure 6.5(b). This was produced by making three blocks around the orifice, unlike the original mesh which used five, and using connectors emanating at 45° angles from the corners of the orifice. By using this new topology, the edges of the three blocks surrounding the orifice were all prescribed with a slip wall boundary and the points on the corners of the orifice were only shared by two blocks. This intermediate meshing topology was used for all of the preliminary simulations in this section, as it was found to be stable for the larger

d=80/90mm orifices, where the shear layers were weaker and the acoustic waves were deformed only minimally. This topology did have its disadvantages, leading to a more complex mesh with poorer cell quality (than the low aspect ratio, orthogonal cells in the original mesh) in the vicinity of the orifice faces.

As the internal diameter of the orifice was reduced to 70mm or less, the simulations became unstable even with the intermediate mesh topology. This necessitated a third mesh redesign, this time with a slight geometry change. Although it was undesirable to redesign the edges of the orifice, it was necessary to help the work in this part of the project progress. The modified geometry can be seen in Figure 6.5(c), where it is clear that the changes are relatively small, but allow for a much higher quality mesh around the lower edge of the orifice. The original, intermediate and final meshes near to the orifice are shown in Figure 6.6.

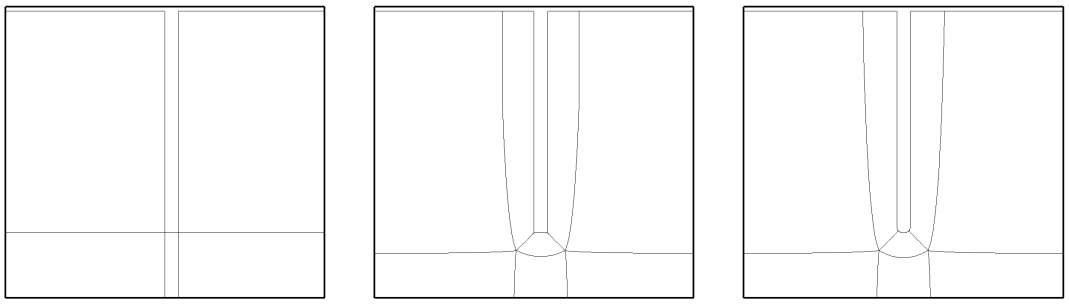

(a) Original (b) Intermediate (c) Final (changed geometry)

Figure 6.5: Comparison of the block topologies used for the three single orifice meshes.

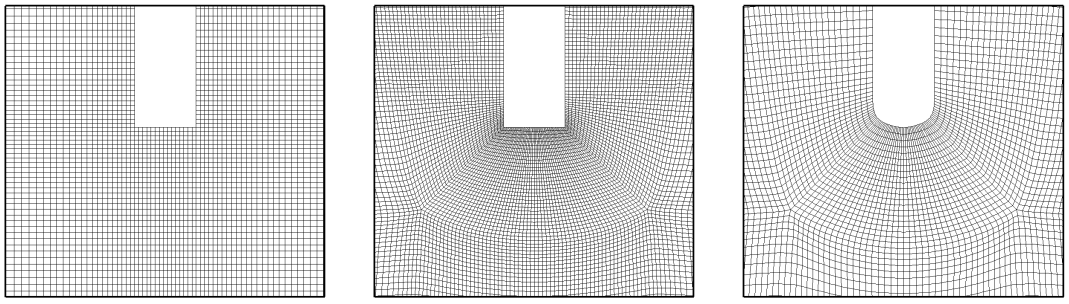

(a) Original (b) Intermediate (c) Final (changed geometry)

Figure 6.6: Comparison of the three meshes used in the nearfield of the single orifice.

Effect of upstream reflections The aim of studying the orifice geometry is to better understand some of the parameters which govern the reflection and transmission of sound waves through the single orifice. The reflections are best seen in the time domain using a plane wave impulse. What became clear from the first sets of results from these studies is that there was an decrease in the sound power downstream, compared to the SPL

of the input wave. There was also an increase in the upstream sound power. Within an LEE simulation, due to the absence of thermal and viscous effects, there should be no loss of sound power from the propagation of the waves. The presence of reflections is confirmed through the snapshots of the domain, shown in Figure 6.7, taken at fixed time intervals of t_a=6.76 $\times 10^{-8}$ (except for the difference of t_a=3.38 $\times 10^{-7}$ between the first and second snapshots). The figures show that a plane wave of half a period is input to the domain. This travels downstream until it interacts with the normal face of the orifice. Part of the wave, which is significantly less than half of the amplitude of the original wave for this orifice diameter, is reflected and travels upstream towards the inlet. The reflected wave does not propagate only in the normal direction to the face and is seen to have some velocity towards the centreline of the duct. The original wave continues downstream, although it is deformed by the orifice and takes a significant distance to once again resemble a plane wave. The upstream wave continues to travel upstream, and the power is spread over approximately 1.5 wavelengths of the original input frequency.

The reflections can not be confirmed using just these snapshots of a plane wave impulse. The best way to confirm the conservation of sound power is to use a full plane wave simulation in the time domain. In order to do this, a 2000Hz plane wave is input at the duct inlet and is averaged over the domain for an equal distance upstream and downstream of the orifice, as shown schematically in Figure 6.8. The instantaneous average and the simple moving average (defined as the unweighted average of the previous data) of the domain for an area of $2D$ upstream/downstream of the orifice is shown in Figure 6.9. The results show that the sum of the pressure within this region is cyclic, as the waves enter/leave the domain and are reflected from the orifice. The average over the iterations shown is approximately zero, which is confirmed by the moving average which tends to zero. This confirms that the sound power is conserved and that any losses downstream of the orifice are seen as increases upstream of the orifice.

Effect of wave amplitude The effect of wave amplitude is shown in Figure 6.10. The data shows a spanwise cut across the entire duct at a distance of $0.2D$ downstream of the orifice. For the three input waves of 50, 75 and 100dB, it is clear to see that the ratio of the reflected and transmitted wave is the same regardless of the amplitude. This confirms that the wave amplitude is within the linear propagation range. Therefore, for all future studies, a single wave amplitude of 100dB is used.

Effect of non-uniform meanflow The effect of uniform meanflow is not investigated here as it is assumed to have a minimal effect in comparison to the non-uniform meanflow. Furthermore, it is wholly unrepresentative of the actual meanflow present within the ducting and was seen to cause stability issues on the parts of the orifice which were normal to the flow. It is therefore neglected from these investigations.

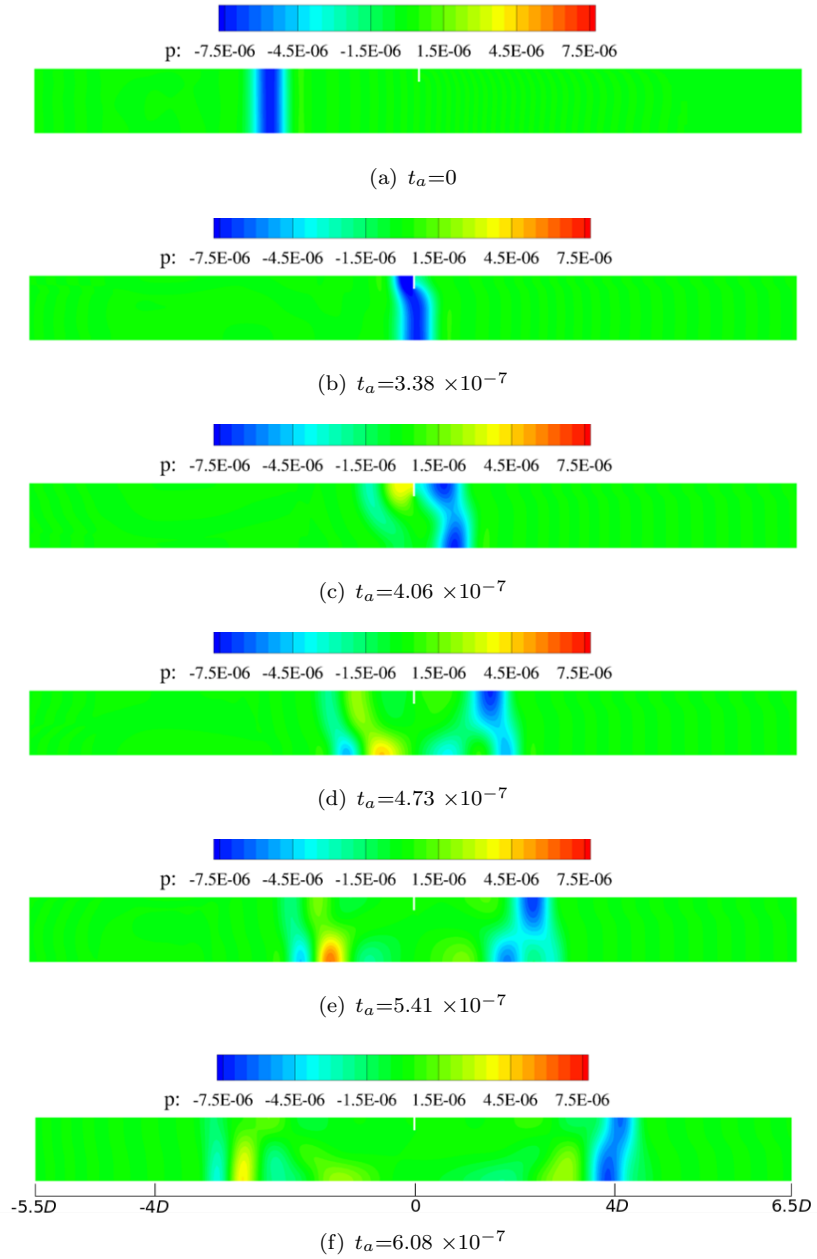

Figure 6.7: Comparison of the propagation of a 2000Hz impulse of a half sine pulse through the d=80mm single orifice at six different time instances.

The effect of non-uniform meanflow was seen to be one of the most significant parameter changes in the clean duct test cases. In the single orifice case, the effect of non-uniform meanflow is investigated using the d=80mm orifice with a 10m/s non-uniform meanflow. The results for the non-uniform meanflows can be seen in Figures 6.12 and 6.13, and the difference between the velocity fields of the two meanflows is shown in Figure 6.11. The meanflow is seen to have the most significant effect on the propagating waves in the recirculation region and the jet. The SPL of the plane waves is increased within the recirculation region due to convective amplification, which also causes a reduction in the SPL within the jet. This effect is relatively small at lower frequencies, but is a

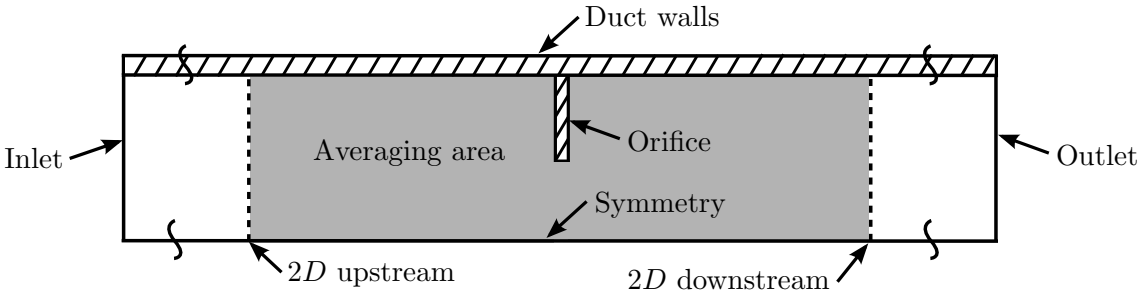

Figure 6.8: Schematic of the domain used for averaging of the incoming and outgoing plane wave.

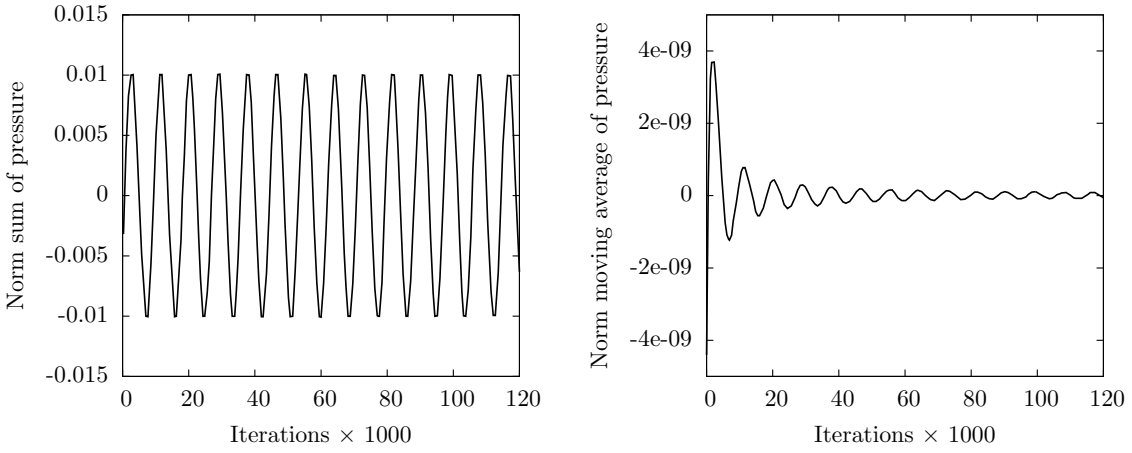

(a) Sum of pressure

(b) Moving average

Figure 6.9: Comparison of the instantaneous and moving averages of the pressure summed over a region of $2D$ upstream/downstream of the d=80mm orifice.

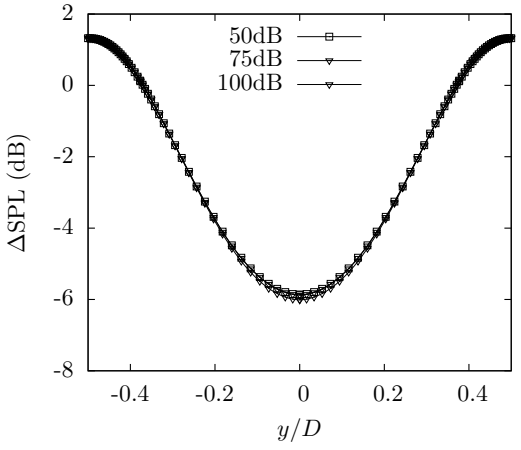

Figure 6.10: Comparison of the spanwise SPL for three different amplitude (50, 75 and 100dB) 2000Hz input waves to a d=80mm orifice. Measurement location is $0.2D$ downstream of the orifice.

noticeable 1dB reduction in the jet at 2000Hz.

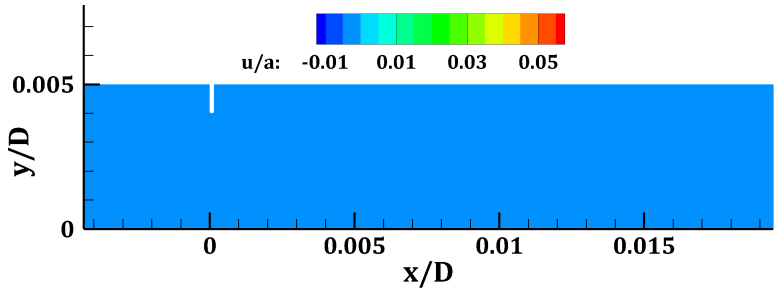

(a) Uniform no flow

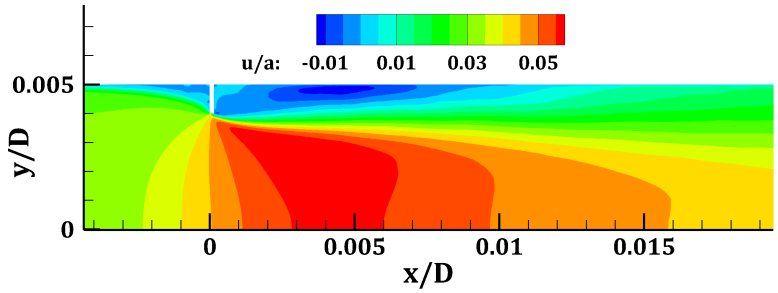

(b) Non-uniform

Figure 6.11: Comparison of the uniform no flow condition and the 10m/s non-uniform meanflow for the d=80mm orifice.

Effect of orifice thickness The effect of varying the orifice on the reflection of plane waves can be seen in Figure 6.14. The figures show the results for four different thicknesses of the d=80mm orifice (1.5, 3, 5 and 10mm) at two different downstream locations across the span. The results show that the thickness of the orifice does play a role in the amount of the wave reflected. As the thickness is increased, the amount of upstream reflection is increased for all of the cases considered here, resulting in a lower SPL downstream of the thicker orifices. Overall however, the effect is relatively small, leading to a increase in reflection of less than 1dB between the thinnest and thickest orifices at a downstream distance of $4D$. This effect will be neglected for the final simulations.

6.2.3.2 Final simulations

Following the studies to investigate the most important parameters governing the propagation of acoustic waves through the single orifice geometry, the order of the problem can be reduced, with the neglected parameters listed in Table 6.1. The primary quantities for these studies are the orifice diameter and the input wave frequencies.

The problem can be further reduced by running multiple frequencies within a single simulation. The waves that propagate through the orifice, do so at the same frequency as the input wave. Therefore, the frequency of each wave is known, and through the use of a Fast Fourier Transform (FFT), the SPL of the individual frequencies can be extracted from the pressure time history during postprocessing. The main requirement to note is

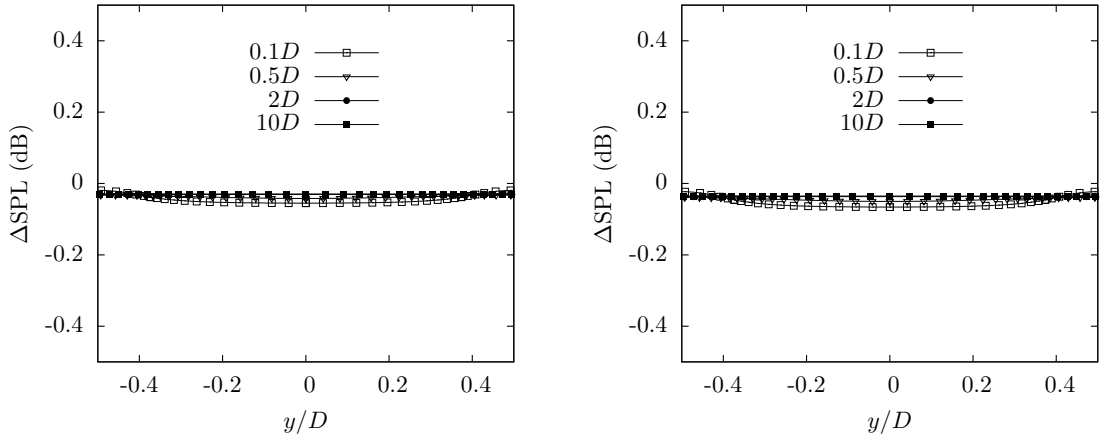

(a) 500Hz Uniform

(b) 500Hz Non-uniform

(c) 1000Hz Uniform

(d) 1000Hz Non-uniform

Figure 6.12: Comparison of the propagation of 500Hz and 1000Hz plane waves through the d=80mm single orifice with no flow and 10m/s non-uniform meanflows.

that the mesh and timestep must be fine enough to resolve the highest frequency waves and the simulation must be run for long enough such that enough wavelengths of the lowest frequency are sampled to ensure a good average.

Variable name/orifice diameter (mm)	**30**	**40**	**50**	**60**	**70**	**80**	**90**	**Clean duct**
Orifice thickness	X	X	X	X	X	X	X	X
Orifice diameter	✔	✔	✔	✔	✔	✔	✔	✔
Wave amplitude	X	X	X	X	X	X	X	X
Wave frequency	✔	✔	✔	✔	✔	✔	✔	✔
Mach number	✔	✔	✔	✔	✔	✔	✔	✔
Duct modes	X	X	X	X	X	X	X	X
Duct diameter	X	X	X	X	X	X	X	X

Table 6.1: Table of the reduced order simulations to quantify the effect of the orifice geometry on the propagation of acoustic waves.

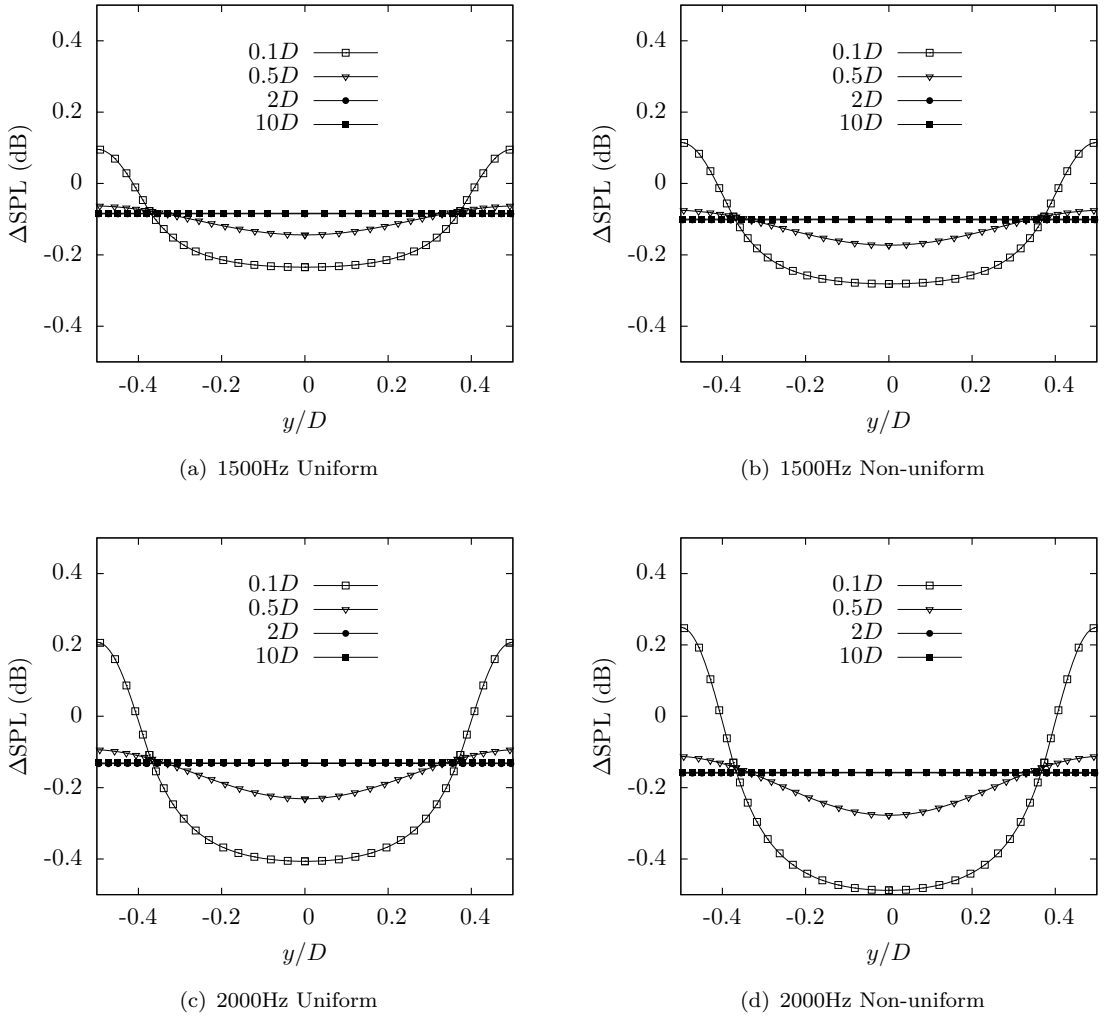

(a) 1500Hz Uniform

(b) 1500Hz Non-uniform

(c) 2000Hz Uniform

(d) 2000Hz Non-uniform

Figure 6.13: Comparison of the propagation of 1500Hz and 2000Hz plane waves through the d=80mm single orifice with no flow and 10m/s non-uniform meanflows.

For each of the orifice diameters, seven frequencies were input to the simulation, equally spaced in the range from 500Hz to 2000Hz. The results have been presented based on the SPL of the acoustic wave at a distance of $10D$ downstream. The waves are seen to change shape as they pass through the orifice but quickly return to a plane wave shape as they reach distances greater than $4D$ downstream. The contour plot, shown in Figure 6.15, shows the reflection caused by orifices of various diameters (Note that Figures 6.12 and 6.13 show typical results, but Figure 6.15 shows all frequencies). There is a clear trend showing that higher frequency waves and smaller diameter orifices lead to larger ratios of the propagating sound wave being reflected. This is as expected, as the open area ratio reduces in the smaller diameter orifices and the high frequency waves are known to be more heavily influenced by the thickness to wavelength ratio of the orifice. It must be made clear here though, that the results neglect the absorption caused by viscosity in the mouth of the orifice, and are therefore only considering part

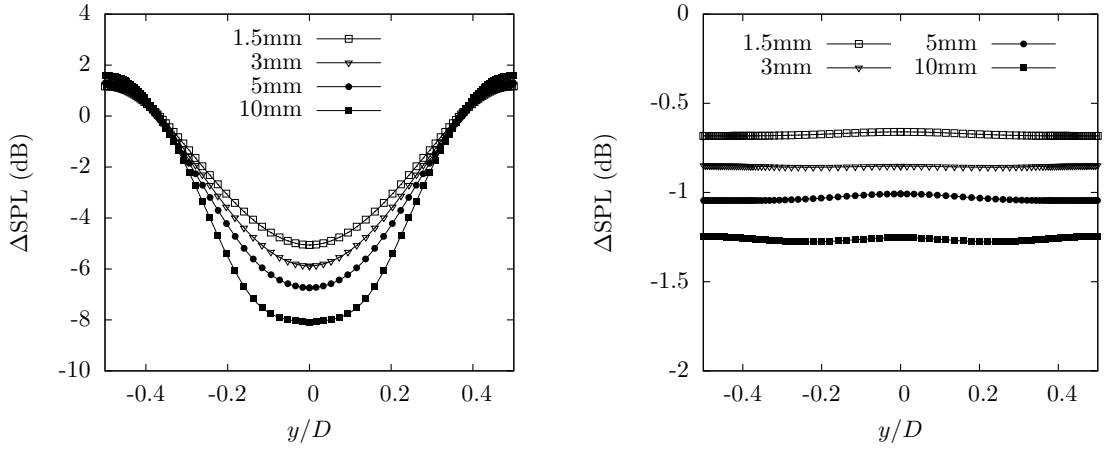

(a) $0.2D$ downstream (b) $4D$ downstream

Figure 6.14: Comparison of SPL at orifice thickness's of 1.5, 3, 5 and 10mm for a d=80mm orifice.

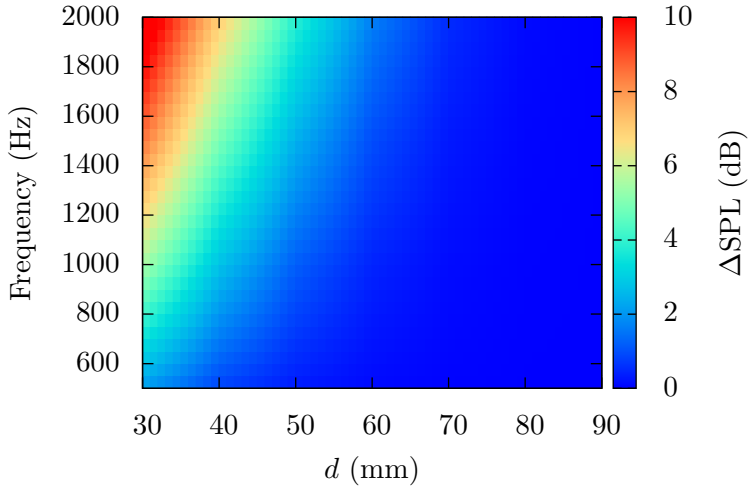

Figure 6.15: Insertion loss of various frequency incoming sound waves by single orifices of a range of internal diameters.

of the mechanism by which the waves are reflected by the orifice. This explains the differences seen between these results and some previous works [77].

6.3 Noise source propagation

In the previous section, the passive properties of the orifice were investigated when an upstream sound source propagated through the orifice. However, in most cases, the orifice will be the primary source of noise within the local vicinity of the orifice. This

means that the most significant effect will be in the scattering of the orifice noise sources by the orifice. Within this section, the orifice source propagation, within the plane wave region, will be investigated through the use of the placement of idealised sources (a monopole and a dipole) on the face of the orifice. The placement of the source matches the estimated dominant source position of the orifice self noise identified in Section 5.4.4.2. This setup is shown schematically in Figure 6.16.

6.3.1 Methodology

The monopole and dipole sources, used in these studies, were implemented following similar methods to those described in [209] and [210], respectively. A validation of the implementation of the source types is shown in Figure 6.17. The distribution of the sources when they are placed on the surface of a wall is displayed in Figure 6.18.

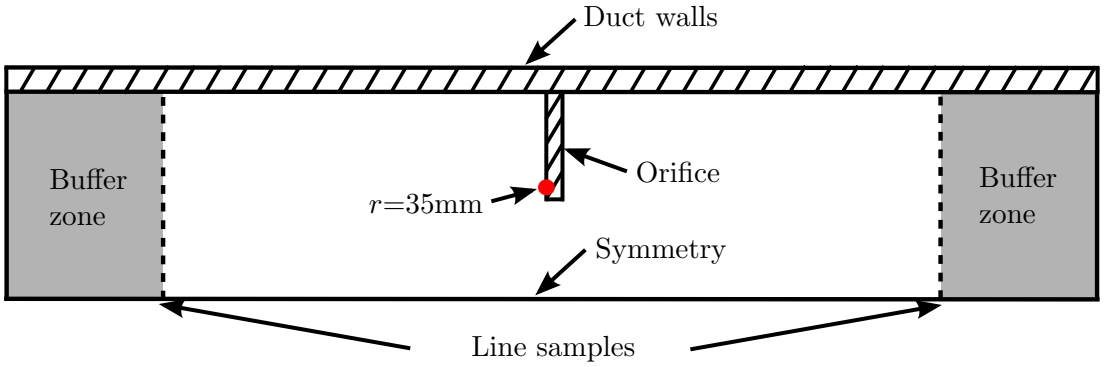

Figure 6.16: Schematic of the geometry, boundary conditions and point source location for the orifice noise source propagation study.

The frequency of the sources is selected to fall within the plane wave frequency range of 250-2000Hz, with an interval of 250Hz. The usage of SotonLEE is identical to the numerical setup described in Section 3.8.1. A two dimensional slice of the duct and orifice is simulated, where a one diameter section upstream and downstream of the d=65mm orifice is meshed. The mesh is a multi-block fully structured design, using the final orifice geometry shown in Figure 6.2(b). This mesh resolution matches that used for the validated medium mesh, which was found to be suitable for propagation problems in the plane wave frequency range. The non-dimensional timestep size is 1×10^{-5}, which provided a maximum CFL number of 0.4.

Buffer zones are applied at the boundaries upstream and downstream of the orifice, a slip wall is applied along the upper boundary and the orifice and a symmetry boundary conditions is applied along the centreline of the duct. The coordinate system is the same as described in Section 6.2.1. No background mean flow is applied to these cases. The domain is initialised using zero perturbations and the sources are distributed over a finite area close to the orifice surface. As the simulation progresses, the distribution of the source is updated and the sound waves propagate through the domain. An initial

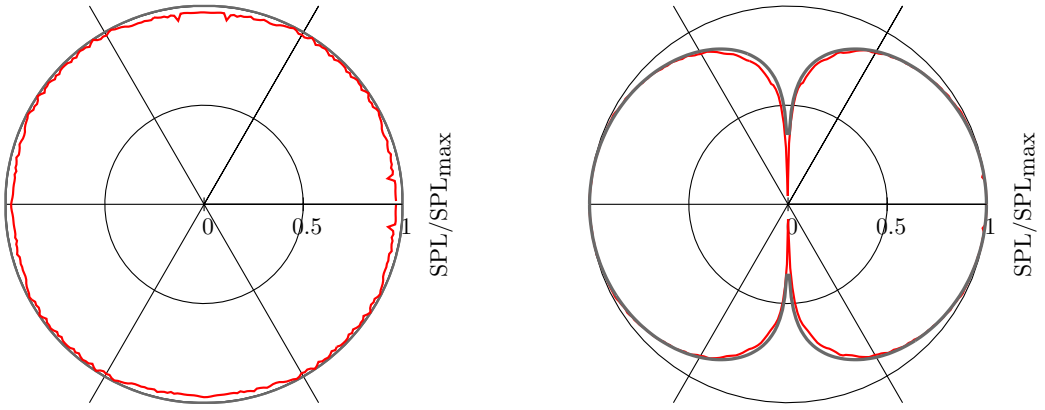

(a) Monopole (b) Dipole

Figure 6.17: Validation of the implementation of the monopole and dipole sound sources in the freefield (red line) plotted with the analytical solution (dark grey line).

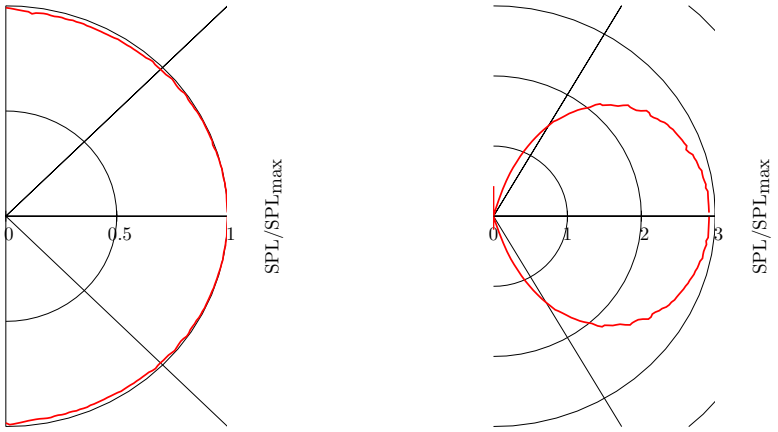

(a) Monopole (b) Dipole

Figure 6.18: Directivity pattern of the monopole and dipole sources when placed on a solid surface and radiating into a hemispherical freefield. The surface is placed along the vertical axis through the origin and extends to infinity in both directions to create the hemispherical freefield.

transient period is used to allow the source waves to propagate up to a distance of $4D$ from the source position. After this initial period is passed, sampling is performed to provide a minimum of 10 periods of each frequency. The time history of the pressure is sampled every 20 timesteps at locations of $0.8D$ upstream and downstream of the orifice. A total of 33 points in each location are sampled, equally spaced along the y-direction. This data is then used to calculate the SPL across the span of the duct and the difference between the locations upstream and downstream is calculated. In both cases, the sources are placed on the upstream face of the orifice. Therefore, it is

expected that the upstream sound pressure levels will be higher across the frequency range investigated, resulting in a positive ΔSPL in the upstream direction.

The location of the primary source of the orifice self noise was identified as part of the simulations in Section 5.4.4.2. It was identified to be dominant on the upstream face of the orifice, in the region from approximately r=32.5-37.5mm near the upstream corner of the orifice. It has also been noted, that the wall pressure spectra upstream of the orifice shows higher levels than at the equivalent downstream location. This therefore suggests that the source radiates more in the upstream direction than the downstream direction with a significant difference $\approx$ 10dB. In order to investigate the source propagation characteristics, an idealised noise source is placed at a location of r=35mm, near to the upstream corner of the orifice on the upstream face. In SotonCAA, the monopole and dipole implementation is not a point source, but is distributed over a small source region encompassing a number of cells close to the intended source centre. The distributed source region of the monopole and dipole sources is chosen such that it approximately corresponds to the estimated dominant source region.

6.3.2 Monopole source

The results of the SPL difference between upstream and downstream locations across the span of the duct is shown in Figure 6.19. The results show that as the frequency of the wave is increased, the difference between the upstream and downstream SPL increases. This would be expected, due to the change in the ratio of the thickness of the orifice, to the wavelength of the propagating acoustic wave. For a monopole, the difference within the whole plane wave frequency is relatively low and doesnt explain the large differences seen between upstream and downstream wall pressure spectra. However, for the monopole source, it is known that this is not a good representation of the acoustic source on the face of the orifice, which is actually a dipole noise source with its dominant radiation direction normal to the orifice faces. In order to estimate the SPL difference from a more realistic source, a dipole noise source is placed at the same location of r=35mm and distributed over the same range as in the previous case. The simulation and sampling procedure is then repeated.

6.3.3 Dipole source

The results of the analysis for the dipole sound source is presented in Figure 6.20. The strong directivity of the dipole, with dominant radiation in the upstream direction, has not resulted in a larger difference as expected. However, the largest difference between upstream and downstream propagation is at low frequencies. This is probably due to the more limited ability for the low frequency sound waves to turn within the ducting to be able to propagate downstream. The maximum difference at 250Hz is approximately 1.1dB and becomes negligible at frequencies above 750Hz. However, the

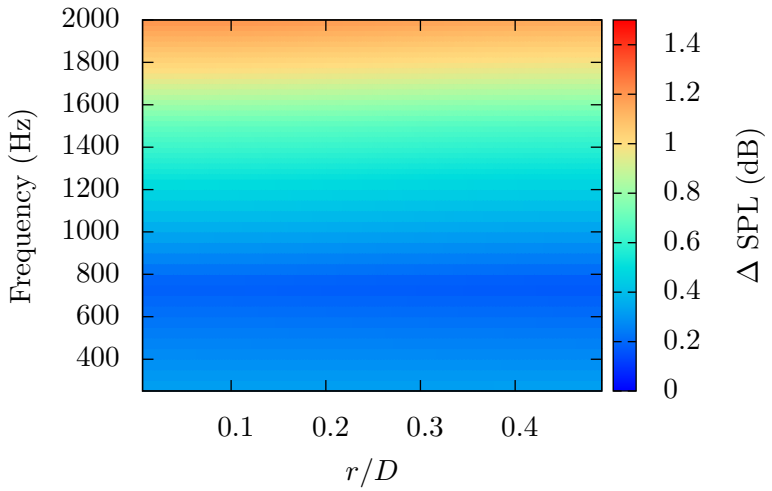

Figure 6.19: Difference between the SPL of upstream and downstream locations for a d=65mm orifice when using a monopole source placed on the upstream surface of the orifice at r=35mm.

higher frequencies appear to be significantly less affected by the orifice when using a dipole source. This is potentially because the sound waves radiating from the more highly directional dipole source have less interaction with the corner of the orifice and therefore, experience less reflection of the high frequency wave. This finding suggests that it would be possible for a dipole noise source on the upstream face of the orifice to efficiently propagate both upstream and downstream of the orifice, raising the noise levels in both directions. This is somewhat in contradiction to the higher noise levels seen in the upstream directions for the LES cases in Figure 5.24. Possible causes for these differences may be the lack of a representation meanflow, although this had a minor effect when considered for a d=80mm orifice, the idealised nature of the source or through the absence of absorption due to viscosity in the mouth of the orifice. The absorption around the corner of the orifice would have contributed to a larger difference between upstream and downstream directions across the frequency range [77].

6.4 Summary

This chapter is comprised of two studies investigating the propagation of plane waves through a clean duct and single orifice. The first study looks at the propagation of downstream travelling acoustic waves through a clean duct and orifice geometry. The primary quantities affecting this propagation are found to be the frequency of the waves and the orifice diameter. Other parameters such as wave amplitude, filter order, meanflow, mesh refinement (within the refinement range considered) and orifice thickness were seen to have a negligible effect. It was shown that higher frequency waves were more easily

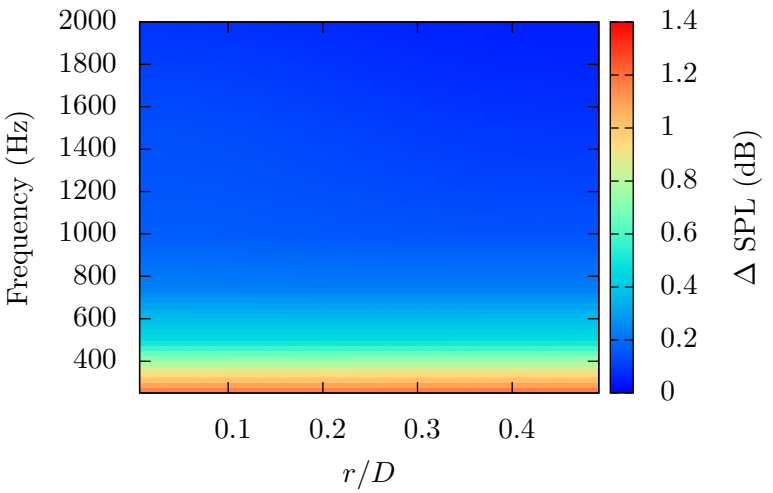

Figure 6.20: Difference between the SPL of upstream and downstream locations for a d=65mm orifice when using a dipole source placed on the upstream surface of the orifice at r=35mm

reflected by the orifice and the reflection increased with reducing orifice diameter. The reflection was largest with a small orifice and a high frequency wave.

The second section of this chapter investigated the propagation of sound produced by the orifice, through the introduction of idealised sound sources. The sources were placed such that they coincided with the calculated position of the dominant noise source from the simulations in Chapter 5. Two types of idealised source, a monopole and a dipole, were placed on the face of the orifice and the relative upstream and downstream propagation was quantified. For the monopole source, the difference between upstream and downstream propagation was found to be largest at the highest frequencies and negligible at low frequencies. For the dipole source, with the strong directivity pattern, the opposite was found to be true, where the lowest frequency waves showed the largest difference. The differences were small and even negligible at higher frequencies, suggesting that the propagation of sound waves from a source on the upstream face of the orifice would see little difference in the upstream and downstream directions for both of these source types. This is in contradiction to the higher noise levels seen in the upstream direction in Section 5.4.3 and is most probably a result of neglecting the effects of viscosity from these simulations.

Chapter 7

Summary and Recommendations

7.1 Summary

Computational studies of a clean duct and ducts with single orifice and double orifices have been performed. The studies performed cover the turbulence, noise and sound propagation of these configurations, with the aim of improving the understanding of the governing mechanisms. The effect of separation distance between an identical orifice pair is first investigated. The study for this included a clean duct and single orifice, both of which helped with the development of suitable boundary conditions and provided reference values for comparison to the results of the orifice pairs. The investigation of the double orifice configuration provided information on the turbulence and velocity fields within the duct and identified the critical separation distance of $2D$, where the maximum turbulence is generated. The study also highlighted the fast recovery of the velocity profiles downstream of the orifice, but the persistence of increased turbulence levels even at $10D$ downstream.

The second area of investigation was that of the effect of varying turbulence levels, where the additional turbulence is generated by a ring, rather than an upstream orifice. The reason for this subtle but key difference is that the additional noise generated by an upstream orifice could be significant and make it hard to isolate the noise produced by the downstream orifice. The ring provided increased turbulence levels and was therefore ideal for a study into the affects of turbulence on the noise generated by an orifice. The turbulence levels were controlled by changing the distance between the upstream ring and the orifice and all cases showed that as the ring was placed closer to the orifice, the turbulence both upstream and downstream of the orifice was increased. This increase in turbulence was accompanied by an increase in the pressure fluctuations both upstream and downstream of the orifice, suggesting that the noise may also be increased by the orifice. This was confirmed using the source term from Curle's analogy, which highlighted the dominant noise source as being present on the upstream face of the orifice, close to the upstream corner of the orifice. The additional noise due to turbulence was also noted

to act predominantly in this region of the orifice face, due to the increased unsteadiness in the mass flow rate through the orifice. Additional interaction noise was also suggested to be caused by impingement of turbulent eddies on the upstream face of the orifice and convection of eddies within the recirculation regions which impinge on the downstream face of the orifice.

The third and final study was performed to investigate the propagation of acoustic waves through components of the ADS. The first part of this study considered the propagation of downstream travelling acoustic waves which have been created by other parts of the ADS. The propagation through a clean duct and single orifice highlighted the parameters important to the reflection of acoustic waves as the wave frequency and the orifice diameter. Other parameters investigated were found to have negligible effect on the wave reflection. The final conclusions were that higher frequency waves were more easily reflected by the orifice and the reflection was a function of the internal diameter of the orifice, such that a small diameter and a high frequency wave produced the largest reflection. In addition to a study of existing noise, the influence of the orifice on the propagation of sound waves generated by the surface of the orifice was also investigated. Idealised monopole and dipole sources were placed at the approximate location identified as the dominant noise source from the studies performed using Curle's analogy. The relative magnitude of the upstream and downstream propagating sound waves was quantified. It was found that the position of the source and its directivity results in significant changes in the upstream and downstream propagation of a source placed on the upstream face of the orifice. This is attributed to the differences in the ability for low frequency waves to turn with the duct when they are emitted in a particular direction. It was noted that the effect of the orifice on the propagation was small for both idealised sources cases and was not the cause of the differences in upstream and downstream noise seen in the LES simulations. The differences were postulated to be caused by neglecting viscosity from the propagation simulations.

7.2 Future work

The future work detailed here focuses around the unanswered questions which have arisen as part of this work. The primary area of future work is centred around the confirmation of the orifice noise sources. The methods that have been applied in this work only provide information about the separated parts of the problem of noise generation and propagation. The ideal study would focus on the hybrid coupling of the unsteady sound generation with a propagation code to better understand the interaction between the flow, noise and geometry. The major advantage of the hybrid coupling of a CFD solver with a linearised propagation solver, is to allow for a realistic modelling of the propagation of the sound sources on the walls of the orifice and duct. This would lead to improved understanding of the source mechanisms including identification of the dominant noise source and an improvement of the understanding of the propagation

characteristics of the orifice noise sources. A simplified attempt at this type of study has been made in the final chapter of this work, but this only extended to idealised noise sources and will only provide realistic information when the variation of the sound sources in time and space across the orifice faces is accounted for. Furthermore, the effect of the mean flow has not be investigated for the propagation of the noise sources from the orifice face and the duct wall. This would require the use of a Linearised Navier-Stokes (LNS) code, to allow for the effect of the strong shear layers and acoustically induced vortex shedding to be quantified, something that wasn't available to this research. The quantification of the mean flow would be interesting, as it was shown to have some effect for the downstream propagating sound waves through the orifice, even at a low Mach number and for a large orifice diameter, where the jet velocity was relatively low. Furthermore, the use of a LNS would be essential to properly account for the effect of viscosity near to the orifice. This would be particularly important when the noise sources were placed on the face of the orifice.

To the authors knowledge, this hybridised method has not been applied to an orifice geometry, despite being previously noted to provide valuable information on the noise sources of a forward-backward facing step [115]. Therefore, at the very least, this method would go some way to proving or disproving the noise sources suggested in this work.

A further area of interest is to attempt to account for the propagation effect of the exponential flare used in the experimental configurations. Existing researchers have accounted for propagation through the clean duct using a tailored Green's function, however, this is unable to predict sound propagation outside of the ducting. This modification would then allow for comparison to the farfield sound power levels measured in the experimental configuration.

References

[1] F. Landis and A. Shapiro, "The Turbulent Mixing of Coaxial Gas Jets," *Proceeding of the Heat Transfer and Fluid Mechanics Institution, Stanford University Press*, 1951.

[2] Dirac Delta Consultants Limited, "Aerodynamic noise." `AerodynamicNoise,www.diracdelta.co.uk/science/source/a/e/aerodynamic%20noise/source.html`, 2011. [Online; accessed 22-Feb-2011].

[3] I. Vér and L. Beranek, *Noise and Vibration Control Engineering: Principles and Applications*. John Wiley & Sons, 2nd Edition, 2005.

[4] G. Ferrara, L. Ferrari, and G. Lenzi, "An Experimental Methodology for the Reconstruction of Three-Dimensional Acoustic Pressure Fields in Ducts," *Journal of Engineering for Gas Turbines and Power*, vol. 136, no. 1, 2013.

[5] M. Shur, P. Spalart, M. Strelets, and A. Travin, "A Hybrid RANS-LES Approach with Delayed-DES and Wall-Modelled LES Capabilities," *International Journal of Heat and Fluid Flow*, vol. 29, pp. 1638–1649, 2008.

[6] F. Tao, "Experimental study of noise generation of ventilation system," *MPhil/PhD Transfer Report*, 2014.

[7] M. Bull and N. Agarwal, "Characteristics of the Flow Separation due to an Orifice Plate in Fully Developed Turbulent Pipe-Flow," *Eighth Australian Fluid Mechanics Conference, University of Newcastle, N.S.W.*, 1983.

[8] P. Spalart, W. Jou, M. Strelets, and S. Allmaras, "Comments on the Feasibility of LES for Wing and on a Hybrid RANS/LES Approach," *Advances in LES/DNS, First AFOSR International Conference on DNS/LES*, 1997.

[9] W. Dobrzynski, "Almost 40 Years of Airframe Noise Research: What Did We Achieve?," *Journal of Aircraft*, vol. 47, no. 2, pp. 353–367, 2010.

[10] European Commission, "The Challenge of the Environment," tech. rep., Advisory Council for Aeronautics Research in Europe, 2002.

[11] European Commission, "Flightpath 2050 - Europe's Vision for Aviation," tech. rep., Advisory Council for Aeronautics Research in Europe, 2011.

[12] T. Spangenberg, W. Schroder, and M. Siercke, "Numerical and experimental analysis of the turbulence and the noise generated by flow through restrictors in an aircraft cabin air distribution system," Master's thesis, RWTH Aachen, 2012.

[13] D. Gray, *A First Course in Fluid Mechanics for Civil Engineers*. Water Resources Publications, 2000.

[14] P. Nelson and C. Morfey, "Aerodynamic Sound Production in Low Speed Flow Ducts," *Journal of Sound and Vibration*, vol. 79, no. 2, pp. 263–289, 1981.

[15] C. Gordon, "Spoiler Generated Flow Noise. II: Results," *Journal of the Acoustical Society of America*, vol. 45, no. 1, pp. 214–223, 1969.

[16] L. F. Moody, "Friction Factors for Pipe Flow," *Transactions of the ASME*, vol. 66, no. 8, pp. 671–684, 1944.

[17] C. Tam, "Computational Aeroacoustics: Issues and Methods," *AIAA Journal*, vol. 33, no. 10, pp. 1788–1796, 1995.

[18] G. Batchelor and A. Gill, "Analysis of the Stability of Axisymmetric Jets," *Journal of Fluid Mechanics*, vol. 14, no. 529, pp. 529–551, 1962.

[19] A. Hussain and M. Zedan, "Effects of the Initial Condition on the Axisymmetric Free Shear Layer: Effect of the Initial Fluctuation Level," *Physics of Fluids*, vol. 21, pp. 1475–1481, 1978.

[20] A. Hussain and M. Zedan, "Effects of the Initial Condition on the Axisymmetric Free Shear Layer: Effect of the Initial Momentum Thickness," *Physics of Fluids*, vol. 21, pp. 1100–1112, 1978.

[21] G. Raman, E. Rice, and E. Reshotko, "Mode Spectra of Natural Disturbances in a Circular Jet and the Effect of Acoustic Forcing," *Experiments in Fluids*, vol. 17, no. 6, pp. 415–426, 1994.

[22] E. Gutmark and C. Ho, "Preferred Modes and the Spreading Rates of Jets," *Physics of Fluids*, vol. 26, no. 10, pp. 2932–2938, 1983.

[23] L. Facciolo, "A Study on Axially Rotating Pipe and Swirling Jet Flows," tech. rep., Royal Institute of Technology, KTH, 2006.

[24] E. Alenius, *Flow Duct Acoustics - An LES Approach*. PhD thesis, Royal Institute of Technology, KTH, 2012.

[25] S. Komori and H. Ueda, "Turbulent Flow Structure in the Near Field of a Swirling Round Free Jet," *Physics of Fluids*, vol. 28, pp. 2075–2082, 1985.

[26] G. Mattingly and C. Chang, "Unstable Waves on an Axisymmetric Jet Column," *Journal of Fluid Mechanics*, vol. 65, pp. 541–560, 1974.

[27] J. Citriniti and W. George, "Reconstruction of the Global Velocity Field in the Axisymmetric Mixing Layer Utilizing the Proper Orthogonal Decomposition," *Journal of Fluid Mechanics*, vol. 418, pp. 137–166, 2000.

[28] D. Jung, S. Gamard, and W. George, "Downstream Evolution of the Most Energetic Modes in a Turbulent Axisymmetric Jet at High Reynolds Number. Part 1. the Near-Field Region," *Journal of Fluid Mechanics*, vol. 514, pp. 173–204, 2004.

[29] J. Bridges and A. Hussain, "Roles of Initial Condition and Vortex Pairing in Jet Noise," *Journal of Sound and Vibration*, vol. 117, pp. 289–311, 1987.

[30] C. Schram, S. Taubitz, J. Anthoine, and A. Hirschberg, "Theoretical/Empirical Prediction and Measurement of the Sound Produced by Vortex Pairing in a Low Mach Number Jet," *Journal of Sound and Vibration*, vol. 281, pp. 171–187, 2005.

[31] C. Bogey, O. Marsden, and C. Bailly, "A Computational Study of the Effects of Nozzle Exit Turbulence Level on the Flow and Acoustic Fields of a Subsonic Jet," *AIAA Paper 2011-2837*, 2011.

[32] C. Bogey, O. Marsden, and C. Bailly, "Effects of Initial Shear Layer Thickness on Turbulent Subsonic Jets at Moderate Reynolds Numbers," *AIAA Paper 2012-2249*, 2012.

[33] A. Anderson, "A Jet Tone Orifice Number for Orifices of Small Thickness-Diameter Ratio," *The Journal of the Acoustical Society of America*, vol. 26, pp. 21–25, 1954.

[34] W. Quinn, "Upstream Nozzle Shaping Effects on Near Field Flow in Round Turbulent Free Jets," *European Journal of Mechanics-B/Fluids*, vol. 25, no. 3, pp. 279–301, 2006.

[35] J. Mi, P. Kalt, G. Nathan, and C. Wong, "PIV Measurements of a Turbulent Jet Issuing from Round Sharp-Edged Plate," *Experiments in Fluids*, vol. 42, no. 4, pp. 625–637, 2007.

[36] B. Khoo, T. Chew, P. Heng, and H. Kong, "Turbulence Characterisation of a Confined Jet Using PIV," *Experiments in Fluids*, vol. 13, no. 5, pp. 350–356, 1992.

[37] N. Agarwal, "The Sound Field in a Fully Developed Turbulent Pipe Flow due to Internal Flow Separation, Part 2: Modal Amplitude and Cut-off Frequencies," *Journal of Sound and Vibration*, vol. 175, no. 1, pp. 65–76, 1994.

[38] F. Durst and A. Wang, "Experimental and Numerical Investigations of the Axisymmetric Turbulent Pipe Flow over a Wall-Mounted Thin Obstacle," *Proceedings of 7th Symposium on Turbulent Shear Flows*, pp. 10.4.1–10.4.6., 1989.

[39] F. Shan, A. Fujishiro, T. Tsuneyoshi, and Y. Tsuji, "Particle Image Velocimetry Measurements of Flow Field Behind a Circular Square-Edged Orifice in a Round Pipe," *Experiments in Fluids*, vol. 54, no. 1553, 2013.

[40] M. Reader-Harris and J. Sattary, "The Orifice Plate Discharge Coefficient Equation," *Flow Measurement and Instrumentation*, vol. 1, no. 2, pp. 67–76, 1990.

[41] J. Holmgren, "Method for Calculating Restrictor Noise in Ducts, Airbus Report X21ME1100251," tech. rep., Airbus Operations GmbH, 2011.

[42] H. Heller and S. Widnall, "Sound Radiation from Rigid Flow Spoilers Correlated with Fluctuating Forces," *Journal of the Acoustical Society of America*, vol. 47, pp. 924–936, 1970.

[43] H. Ribner, "The Generation of Sound by Turbulent Jets," *Advanced Applied Mechanics*, vol. 8, pp. 103–182, 1964.

[44] C. Gordon, "Spoiler Generated Flow Noise. I: The Experiment," *Journal of the Acoustical Society of America*, vol. 43, no. 5, pp. 1041–1048, 1968.

[45] J. Davies, H.and Ffowcs-Williams, "Aerodynamic Sound Generation in a Pipe," *Journal of Fluid Mechanics*, vol. 14, pp. 765–778, 1968.

[46] D. Oldham and A. Ukpoho, "A Pressure-Based Technique for Predicting Regenerated Noise Levels in Ventilation Systems," *Journal of Sound and Vibration*, vol. 140, no. 2, pp. 259–272, 1990.

[47] M. Åbom, S. Allam, and S. Boij, "Aeroacoustics of Flow Duct Singularities at Low Mach Numbers," *AIAA Paper 2006-2687*, 2006.

[48] J. Cissoni, K. Nozaki, A. van Hirtum, X. Grandchamp, and S. Wada, "Numerical Simulation of the Influence of the Orifice Aperture on the Low Around a Teeth-Shaped Obstacle," *Fluid Dynamics Research*, vol. 45, no. 2: 025505, pp. 445–476, 2013.

[49] M. Krane, "Aeroacoustic Production of Low Frequency Unvoiced Speech Sounds," *Journal of the Acoustical Society of America*, vol. 118, pp. 410–427, 2005.

[50] N. Stevens, "Airflow and Turbulence Noise for Fricative and Stop Consonants: Static Considerations," *Journal of the Acoustical Society of America*, vol. 50, pp. 1180–1192, 1971.

[51] C. Shadle, *The Acoustics of Fricative Consonants*. PhD thesis, Massachusetts Institute of Technology, 1985.

[52] X. Gloerfelt and P. Lafon, "Direct Computation of the Noise Induced by a turbulent Flow through a Diaphragm in a Duct at Low Mach Numbers," *Computers and Fluids*, vol. 37, pp. 388–401, 2008.

[53] J. Rossiter, "Wind Tunnel Experiments on the Flow Over Rectangular Cavities at Subsonic and Transonic Speeds," tech. rep., Aeronautical Research Council Reports and Memoranda, 1964.

[54] C. Ho and N. Nosseir, "Dynamics of an Impinging Jet. Part 1. The Feedback Phenomenon," *Journal of Fluid Mechanics*, vol. 105, no. 1, pp. 119–142, 1981.

[55] J. Laufer and P. Monkewitz, "On Turbulent Jet Flows - A new Perspective," *AIAA Journal*, 1980.

[56] E. Villermaux and E. Hopfinger, "Self-Sustained Oscillations of a Confined Jet: a Case Study for the Non-Linear Delayed Saturation Model," *Physica D: Nonlinear Phenomena*, vol. 72, no. 3, pp. 230–243, 1994.

[57] V. Ahuja, A. Hosangadi, M. Hitt, and D. Lineberry, "Numerical Simulations of Instabilities in Single-Hole Orifice Elements," *AIAA Paper 2013-4058*, 2013.

[58] R. Lacombe, P. Moussou, and Y. Auregan, "Whistling of an Orifice in a Reverberating Duct at Low Mach Number," *Journal of the Acoustical Society of America*, vol. 130, no. 5, pp. 2662–2672, 2011.

[59] P. Testud, Y. Aurégan, P. Moussou, and A. Hirschberg, "The Whistling Potentiality of an Orifice in a Confined Flow Using an Energetic Criterion," *Journal of Sound and Vibration*, vol. 325, no. 4-5, pp. 769–780, 2009.

[60] C. Ho and P. Huerre, "Perturbed Free Shear Layers," *Annual Review of Fluid Mechanics*, vol. 16, pp. 365–424, 1984.

[61] C. Mak, "A Prediction Method for Aerodynamic Sound Produced by Multiple Elements in Air Ducts," *Journal of Sound and Vibration*, vol. 287, no. 12, pp. 395–403, 2005.

[62] N. Han, X. Qin, and C. Mak, "A Further Study of the Prediction Method for Aerodynamic Sound Produced by Two in-Duct Elements," *Journal of Sound and Vibration*, vol. 294, no. 12, pp. 374–380, 2006.

[63] C. Mak and W. Au, "A Turbulence Based Prediction Technique for Flow - generated Noise Produced by in-Duct Elements in a Ventilation System," *Applied Acoustics*, vol. 70, no. 1, pp. 11–20, 2009.

[64] L. Bell and D. Bell, *Industrial Noise Control: Fundamentals and Applications, Second Edition.* Marcel Dekker, Inc, 1993.

[65] M. Fink, "Investigation of Scrubbing and Impingement Noise, CR-134762," tech. rep., NASA, 1975.

[66] P. Russell and A. Hatton, "Turbulent Flow Characteristics of an Impinging Jet," *Heat and Fluid Flow*, vol. 3, no. 1, pp. 1–12, 1973.

[67] A. Petric, "An Experimental Investigation of the Noise Production by Air Jet Impingment on Flat Plates," *Applied Acoustics*, vol. 7, pp. 117–126, 1974.

[68] D. Boldman and P. Brinich, "Mean Velocity, Turbulence Intensity, and Scale in a Subsonic Turbulent Jet Impinging Normal toa Large Flat Plate, Technical Paper 1037," tech. rep., NASA, 1977.

[69] A. Marsh, "Noise Measurements Around a Subsonic Air Jet Impinging on a Plane Rigid Surface," *Journal of Acoustical Society of America*, vol. 33, no. 8, pp. 1065–66, 1961.

[70] N. Nosseir and C. Ho, "Dynamics of an Impinging Jet. Part 2. The Noise Generation," *Journal of Fluid Mechanics*, vol. 116, pp. 379–391, 1982.

[71] R. Paterson and R. Amiet, "Acoustic Radiation and Surface Pressure Characteristics of an Airfoil Due to Incident Turbulence, CR-2733," tech. rep., NASA, 1976.

[72] A. Sengissen, B. Caruelle, P. Souchotte, E. Jondeau, and T. Poinsot, "LES of Noise Induced by Flow Through a Double Diaphragm System," *AIAA Paper 2009-3357*, 2009.

[73] A. Belanger, M. Meskine, B. Caruelle, and K. Debatin, "Aero-Acoustic Simulation of a Double Diaphragm Using Lattice Boltzmann Method," *AIAA Paper 2005-2917*, 2005.

[74] F. Mendonca, A. Read, S. Caro, K. Debatin, and B. Caruelle, "Aeroacoustic Simulation of Double Diaphragm Orifices in an Aircraft Climate Control System," *AIAA Paper 2005-2976*, 2005.

[75] Q. Yang, *Computational Study of Sound Generation by Surface Roughness in Turbulent Boundary Layers*. PhD thesis, University of Notre Dame, April 2012.

[76] M. Salikuddin and K. Ahuja, "Acoustic Power Dissipation on Radiation Through Duct Terminations: Experiments," *Journal of Sound and Vibration*, vol. 91, pp. 479–485, 1983.

[77] R. Leung, M. Wang, X. Li, R. So, and P. Student, "In-Duct Orifice and its Effect on Sound Absorption," *Journal of Sound and Vibration*, vol. 299, no. 4-5, pp. 990–1004, 2007.

[78] J. Rupp, J. Carrotte, and A. Spencer, "Interaction Between the Acoustic Pressure Fluctuations and the Unsteady Flow Field Through Circular Holes," *Journal of Engineering for Gas Turbines and Power*, vol. 132, no. 6, p. 061501, 2010.

[79] A. Cummings and I. Chang, "The Transmission of Intense Transient and Multiple Frequency Sound Waves Through an Orifice Plate with Mean Flow," *Revue de Physique Appliquee*, vol. 21, pp. 151–161, 1986.

[80] J. Wendoloski, "Sound Absorption by an Orifice Plate in a Flow Duct," *Journal of the Acoustical Society of America*, vol. 104, pp. 122–132, 1998.

[81] P. Durrieu, G. Hofmans, G. Ajello, R. Boot, Y. Aurégan, A. Hirschberg, and M. Peters, "Quasisteady Aeroacoustic Response of Orifices," *The Journal of the Acoustical Society of America*, vol. 110, no. 4, pp. 1859–1872, 2001.

[82] E. de Villiers, *The Potential of Large Eddy Simulation for the Modelling of Wall Bounded Flows*. PhD thesis, Imperial College, 2006.

[83] Y. Kim, I. Castro, and Z. T. Xie, "Divergence-Free Turbulence Inflow Conditions for Large-Eddy Simulations with Incompressible Flow Solvers," *Journal of Computational Fluids*, vol. 84, pp. 56–68, 2013.

[84] N. Jarrin, S. Benhamadouche, D. Laurence, and R. Prosser, "A Synthetic-Eddy Method for Generating Inflow Conditions for Large-Eddy Simulations," *International Journal of Heat and Fluid Flow*, vol. 27, pp. 585–593, 2006.

[85] M. Pamies, P. Weiss, E. Garnier, S. Deck, and P. Sagaut, "Generation of Synthetic Turbulent Inflow Data for Large Eddy Simulation of Spatially Evolving Wall-bounded Flows," *Journal of Physical Fluids*, vol. 21, 2009.

[86] Z. T. Xie and I. Castro, "Efficient Generation of Inflow Conditions for Large Eddy Simulations of Street-scale Flow," *Journal of Flow, Turbulence and Combustion*, vol. 81, pp. 449–470, 2008.

[87] Y. Kim, I. Castro, and Z. T. Xie, "Divergence-Free Turbulence Inflow Conditions for Large-Eddy Simulations of Flows Around an Airfoil," *UK WES Conference*, 2012.

[88] P. Roach, "The Generation of Nearly Isotropic Turbulence by Means of Grids," *International Journal of Heat and Fluid Flow*, vol. 8, no. 2, pp. 82–92, 1987.

[89] S. Laizet and J. Vassilicos, "DNS of Fractal-Generated Turbulence," *Flow, Turbulence and Combustion*, vol. 87, pp. 673–705, 2011.

[90] M. Lighthill, "On Sound Generation Aerodynamically. I. General Theory," *Proceedings of the Royal Society of London. Series A, Mathematical and Physical Sciences*, vol. 211, no. 1107, pp. 564–587, 1952.

[91] N. Curle, "The Influence of Solid Boundaries upon Aerodynamic Sound," *Proceedings of the Royal Society of London. Series A, Mathematical and Physical Sciences*, vol. 231, no. 1187, pp. 505–514, 1955.

[92] J. E. Ffowcs Williams and D. L. Hawkings, "Sound Generation by Turbulence and Surfaces in Arbitrary Motion," *Philosophical Transcripts of the Royal Society of London*, vol. 342, pp. 261–321, 1969.

[93] X. Gloerfelt, F. Perot, C. Bailly, and D. Juve, "Flow Induced Cylinder Noise Formulated as a Diffraction Problem for Low Mach Numbers," *Journal of Sound and Vibration*, vol. 287, pp. 129–151, 2005.

[94] M. Norton, *Fundamentals of Noise and Vibration Analysis for Engineers.* Cambridge Publications, 1989.

[95] E. Rice, "Multimodal Farfield Acoustic Radiation Pattern Using Mode Cut-off Ratio," *AIAA Journal*, vol. 16, pp. 906–911, 1978.

[96] P. Roe, "Technical Prospects for Computational Aeroacoustics," *AIAA Paper 92-02-032*, 1992.

[97] C. Tam, "Computational Aeroacoustics: An Overview of Computational Challenges and Applications," *International Journal of Computational Fluid Dynamics*, vol. 18, no. 6, pp. 547–567, 2004.

[98] J. Ferzinger and M. Peric, *Computational Methods for Fluid Dynamics.* Springer, 3rd Edition, 2002.

[99] P. Spalart, M. Shur, M. Strelets, and A. Travin, "Towards Noise Prediction for Rudimentary Landing Gear," *IUTAM Symposium on Computational Aero-Acoustics for Aircraft Noise Prediction*, 2010.

[100] T. Van de Ven, "Computational and Aeroacoustic Analysis of 1/4 Scale G550 Nose Landing Gear," *AIAA Paper 2009-3359*, 2009.

[101] M. Brio, G. Webb, and A. Zakharian, *Numerical Time-Dependent Partial Differential Equations for Scientists and Engineers.* Elsevier Academic Press, 2010.

[102] R. Courant, K. Friedrichs, and H. Lewy, "On the Partial Difference Equations of Mathematical Physics," *IBM Journal of Research and Development*, vol. 11, no. 2, pp. 215–234, 1967 [1928].

[103] J. Freund, S. Lele, and P. Moin, "Direct Numerical Simulation of a Mach 1.92 Turbulent Jet and its Sound Field," *AIAA Journal*, vol. 38, no. 11, pp. 2023–2031, 2000.

[104] J. Freund, "Noise Sources in a Low-Reynolds-Number Turbulent Jet at Mach 0.9," *Journal of Fluid Mechanics*, vol. 438, pp. 277–305, 2001.

[105] H. Ran and T. Colonius, "Numerical Simulation of Sound Radiated by a Turbulent Vortex Ring," *AIAA Paper 2004-2918*, 2004.

[106] J. Freund, S. Lele, and P. Moin, "Matching of Near/Far-field Equation Sets for Direct Computation of Aerodynamic Sound," *AIAA Paper 93-4326*, 1993.

[107] E. Gröschel, W. Schröder, P. Renze, M. Meinke, and P. Comte, "Noise Prediction for a Turbulent Jet Using Different Hybrid Methods," *Computers and Fluids*, vol. 37, no. 4, pp. 414–426, 2008.

[108] T. Imamura, T. Hirai, K. Amemiya, Y. Yokokawa, S. Enomoto, and K. Yamamoto, "Aerodynamic and Aeroacoustic Simulations of a Two-wheel Landing Gear," *Procedia Engineering, IUTAM Symposium on Computational Aero-Acoustics for Aircraft Noise Prediction,*, 2009.

[109] T. Colonius and S. Lele, "Computational Aeroacoustics: Progress on Nonlinear Problems of Sound Generation," *Progress in Aerospace Sciences*, vol. 40, pp. 345–416, 2004.

[110] X. Zhang, X. Chen, and C. Morfey, "Acoustic Radiation from a Semi-Infinite Duct with a Subsonic Jet," *International Journal of Aeroacoustics*, vol. 4, no. 1-2, pp. 169–184, 2005.

[111] E. Richards, X. Chen, X. Huang, and X. Zhang, "Computation of fan noise radiation through an engine exhaust geometry with flow," *International Journal of Aeroacoustics*, vol. 6, no. 3, pp. 223–241, 2007.

[112] X. Zhang, X. Chen, C. Morfey, and P. Nelson, "Computation of Spinning Modal of Radiation from an Unflanged Duct," *AIAA Journal*, vol. 42, no. 9, pp. 1795–1801, 2004.

[113] X. Zhang, X. Chen, J. Gill, and X. Huang, "Gradient Term Filtering for Stable Sound Propagation with Linearised Euler Equations," *AIAA Paper 2014-3306*, 2014.

[114] R. Ewert and W. Schröder, "Acoustic Perturbation Equations Based on Flow Decomposition via Source Filtering," *Journal of Computational Physics*, vol. 188, no. 2, pp. 365–398, 2003.

[115] Y. Addad, D. Laurence, C. Talotte, and M. Jacob, "Large Eddy Simulation of a Forward-Backward Facing Step for Acoustic Source Identification," *International Journal of Heat and Fluid Flow*, vol. 24, pp. 562–571, 2003.

[116] S. Deck, "Recent Improvements in the Zonal Detached Eddy Simulation (ZDES) formulation," *Theoretical and Computational Fluid Dynamics*, vol. 26, pp. 523–550, 2012.

[117] S. Menon and V. Chakravarthy, "Large Eddy Simulation of Premixed Flames in Couette Flow," *AIAA Paper 96-3077*, 1996.

[118] B. Panjwani, I. Ertesvag, A. Gruber, and K. Rian, "Large-Eddy Simulation of Backward Facing Step Flow," *Fifth National Conference on Computational Mechanics*, 2009.

[119] P. Voke, N. Sandham, and L. Kleiser, *Direct and Large Eddy Simulation III*. Springer Science and Business Media, 2009.

[120] L. Larcheveque, P. Sagaut, T.-H. Le, and P. Comte, "Large-Eddy Simulation of a Compressible Flow in a Three-Dimensional Open Cavity at High Reynolds Number," *Journal of Fluid Mechanics*, vol. 516, pp. 265–301, 2004.

[121] L. Larcheveque, P. Sagaut, and O. Labbe, "Large-Eddy Simulation of a Subsonic Cavity Flow Including Asymmetric Three-Dimensional Effects," *Journal of Fluid Mechanics*, vol. 577, pp. 105–126, 2007.

[122] H. Lai and K. Luo, "A Three-Dimensional Hybrid LES-Acoustic Analogy Method for Predicting Open-Cavity Noise," *Flow, Turbulence and Combustion*, vol. 79, no. 1, pp. 55–82, 2007.

[123] S.-H. Peng and S. Leicher, "DES and Hybrid RANS-LES Modelling of Unsteady Pressure Oscillations and Flow Features in a Rectangular Cavity," *Notes on Numerical Fluid Mechanics-Advances in Hybrid RANS-LES Modelling*, vol. 97, pp. 132–141, 2008.

[124] R. Ashworth, "Prediction of Acoustic Resonance Phenomena for Weapons Bays Using Detached Eddy Simulation," *The Aeronautical Journal*, vol. 109, no. 1102, pp. 631–638, 2005.

[125] T. Kobayashi, Y. Morinishi, and K. Oh, "Large Eddy Simulation of Backward-Facing Step Flow," *Communications in Applied Numerical Methods*, vol. 8, pp. 431–441, 1992.

[126] J. Aider and A. Danet, "Large-Eddy Simulation of Upstream Boundary Conditions Influence upon a Backward Facing Step Flow," *Comptes Rendus Mechanique*, vol. 334, no. 7, pp. 447–453, 2006.

[127] S. Saric, S. Jakirlic, and C. Tropea, "A Periodically Perturbed Backward-Facing Step Flow by Mean of LES, DES and T-RANS: An Example of Flow Separation Control," *Journal of Fluids Engineering*, vol. 127, pp. 879–887, 2005.

[128] B. Singer and Y. Guo, "Development of Computational Aeroacoustics Tools for Airframe Noise Calculations," *International Journal of Computational Fluid Dynamics*, vol. 18, no. 6, pp. 455–469, 2004.

[129] Z. Ma, "Experimental Data Base for a Single Landing Gear Wheel," tech. rep., University of Southampton, 2007.

[130] W. Liu, J. Kim, X. Zhang, and B. Caruelle, "Simulation of a Generic Two-Wheel Nose Landing Gear Using High-order Finite Difference Schemes," *AIAA Paper 2012-2278*, 2012.

[131] M. Khorrami, "Towards Establishing a Realistic Benchmark for Airframe Noise Research: Issues and Challenges," *IUTAM Symposium on Computational Aero-Acoustics for Aircraft Noise Prediction*, 2010.

[132] F. Douglas, J. Gasoriek, J. Swaffield, and L. Jack, *Fluid Mechanics*. Prentice Hall, 5th Edition, 2005.

[133] L. Prandtl, "Uber die ausgebildete Turbulenz," *ZAMM*, vol. 5, pp. 136–139, 1925.

[134] V. Kármán, "Mechanische ahnlichkeit und turbulenz," pp. 85–105, 1930.

[135] A. Favre, "Turbulence: Space-Time Statistical Properties and Behaviour in Supersonic Flows," *Physics of Fluids A*, vol. 26, no. 10, pp. 2851–2863, 1983.

[136] J. Boussinesq, "Essai sur la Théorie des Eaux Courantes," *Mémoires Pésentés par Divers Savants à l'Académie des Sciences*, vol. 23, no. 1, 1887.

[137] C. Heschl, K. Inthavong, and J. Tu, "Evaluation of Eddy Viscosity Turbulence Models to Predict Convective Heat Transfer," *Ninth International Conference on CFD in the Minerals and Process Industries*, 2012.

[138] P. Spalart and S. Allmaras, "A One-Equation Turbulence Model for Aerodynamic Flows," *La Recherche Aerospatiale*, vol. 1, no. 5, 1994.

[139] B. Launder and D. Spalding, "The Numerical Computation of Turbulent Flows," *Computer Methods in Applied Mechanics and Engineering*, vol. 3, no. 2, pp. 269–289, 1974.

[140] D. Wilcox, "Re-Assessment of the Scale-Determining Equation for Advanced Turbulence Models," *AIAA Journal*, vol. 26, no. 11, pp. 1299–1310, 1988.

[141] F. Menter, "Two Equation Eddy-Viscosity Turbulence Models for Engineering Applications," *AIAA Journal*, vol. 32, no. 8, pp. 1598–1605, 1994.

[142] E. Manoha, J. Bulte, and B. Caruelle, "LAGOON: An Experimental Database for the Validation of CFD/CAA Methods for Landing Gear Noise Prediction," *AIAA Paper 2008-2816*, 2008.

[143] A. Kolmogorov, "The Local Structure of Turbulence in Incompressible Viscous Fluid for Very Large Reynolds Number," *Doklady Akademii Nauk SSSR*, vol. 30, pp. 9–13, 1941.

[144] A. Kolmogorov, "On Degeneration (Decay) of Isotropic Turbulence in an Incompressible Viscous Liquid," *Doklady Akademii Nauk SSSR*, vol. 31, pp. 538–540, 1941.

[145] P. Moin, K. Squires, W. Cabot, and S. Lee, "A Dynamic Subgrid-Scale Model for Compressible Turbulence and Scalar Transport," *Physics of Fluids*, vol. 3, pp. 2746–2757, 1991.

[146] J. Smagorinsky, "General Circulation Experiments with the Primitive Equations, I, The basic experiment," *Monthly Weather Review*, vol. 91, pp. 99–165, 1963.

[147] E. Van Driest, "On Turbulent Flow near a Wall," *AIAA Journal*, vol. 23, no. 11, pp. 1007–1011, 1956.

[148] M. Germano, U. Piomelli, P. Moin, and W. Cabot, "A Dynamic Subgrid-Scale Eddy Viscosity Model," *Physics of Fluids A*, vol. 3, no. 7, pp. 1760–1765, 1991.

[149] S. Shi, *Large Eddy Simulation of Ship Wakes*. PhD thesis, West Virginia University, 2001.

[150] S. Pope, *Turbulent Flows*. Cambridge Publications, 2000.

[151] D. You and P. Moin, "A Dynamic Global-Coefficient Subgrid-Scale Eddy-Viscosity Model for Large-Eddy Simulations in Complex Geometries," *Physics of Fluids*, vol. 19: 065110, no. 6, 2007.

[152] S. Deck, E. Garnier, and P. Guillen, "Turbulence Modelling Applied to Space Launcher Configurations," *Journal of Turbulence*, vol. 3, 2002.

[153] F. Menter, M. Kuntz, and L. Durand, "Adaptation of Eddy Viscosity Turbulence Models to Unsteady Separated Flows Behind Vehicles," *The Aerodynamics of Heavy Vehicles: Trucks, Buses and Trains*, 2002.

[154] R. Allen and F. Mendonca, "DES Validation of Cavity Acoustics Over the Subsonic to Supersonic Range," *AIAA Paper 2004-2862*, 2004.

[155] P. Spalart, S. Deck, M. Shur, K. Squires, M. Strelets, and A. Travin, "A New Version of Detached-Eddy Simulation Resistant to Ambiguous Grid Densities," *Theoretical and Computational Fluid Dynamics*, vol. 20, pp. 181–195, 2006.

[156] N. Nikitin, F. Nicoud, B. Wasistho, K. Squires, and P. Spalart, "An Approach to Wall Modelling in Large-Eddy Simulations," *Physics of Fluids*, vol. 12, no. 7, pp. 1629–1632, 2000.

[157] C. Mockett, M. Fuchs, and F. Thiele, "Progress in DES for Wall-Modelled LES of Complex Internal Flows," *Computers and Fluids*, vol. 65, pp. 44–55, 2012.

[158] M. Gritskevich, A. Garabaruk, J. Schutze, and F. Menter, "Development of DDES and IDDES Formulations for the k-ω Shear Stress Transport Model," *Journal of Flow, Turbulence and Combustion*, vol. 88, no. 3, pp. 431–449, 2012.

[159] P. Spalart, "Strategies for Turbulence Modelling and Simulations," *International Journal of Heat Fluid Flow*, vol. 21, pp. 252–263, 2000.

[160] P. Spalart, S. Deck, M. Shur, K. Squires, M. Strelets, and A. Travin, "Young-Persons Guide to Detached-Eddy Simulation Grids, CR-2001-211032," tech. rep., NASA, 2001.

[161] J. Chung, "Rejection of Flow Noise Using a Coherence Function Method," *Journal of Acoustical Society of America*, vol. 62, no. 2, pp. 388–395, 1977.

[162] N. Agarwal, "The Sound Field in a Fully Developed Turbulent Pipe Flow due to Internal Flow Separation, Part 1: Wall-pressure Fluctuation," *Journal of Sound and Vibration*, vol. 169, no. 1, pp. 89–109, 1992.

[163] N. Agarwal, "Mean Separation and Reattachment in Turbulent Pipe Flow due to an Orifice Plate," *Journal of Fluids Engineering*, vol. 116, no. 2, pp. 373–376, 1994.

[164] A. Powell, "Aerodynamic Noise and the Plane Boundary," *Journal of the Acoustical Society of America*, vol. 32, no. 982, pp. 962–990, 1960.

[165] V. Koschatzky, J. Westerweel, and B. Boersma, "Comparison of Two Acoustic Analogies Applied to Experimental PIV Data for Cavity Sound Emission Estimation," *AIAA Paper 2010-3812*, 2010.

[166] S. Rienstra and B. Tester, "An Analytical Green's Function for a Lined Circular Duct Containing Uniform Mean Flow," *Journal of Sound and Vibration*, vol. 317, pp. 994–1016, 2008.

[167] M. Goldstein, *Aeroacoustics*. New York: McGraw-Hill, 1976.

[168] M. Wang, "Aerodynamic Sound of Flow Past an Airfoil," *Center for Turbulence Research, Annual Research Briefs*, 1995.

[169] C. Morfey, "The Role of Viscosity in Aerodynamic Sound Generation," *International Journal of Aeroacoustics*, vol. 2, no. 3-4, pp. 225–240, 2003.

[170] Y. Maruta and S. Kotake, "Separated Flow Noise of a Flat Plate," *Tokyo University, Institute of Space and Aeronautical Science, Report no. 592*, vol. 46, pp. 105–174, 1981.

[171] A. Lida, A. Mizuno, and R. Brown, "Identification of Aerodynamic Sound Source in the Wake of a Rotating Circular Cylinder," *Proceedings of 15th Australasian Fluid Mechanics Conference*, 2004.

[172] Y. Wang, J. Chen, H. Lee, and K. Li, "Accurate Simulation of Surface Pressure Fluctuations and Flow-Induced Noise Near Bluff Body at Low Mach Numbers," *Proceedings of 7th International Colloquium on Bluff Body Aerodynamics and Applications*, 2012.

[173] C. Hamman, J. Klewicki, and R. Kirby, "On the Lamb Vector Divergence in Navier-Stokes Flows," *Journal of Fluid Mechanics*, vol. 610, pp. 261–284, 2008.

[174] A. Powell, "Theory of Vortex Sound," *Journal of the Acoustical Society of America*, vol. 36, pp. 177–195, 1964.

[175] M. Howe, *Acoustics of Fluid-Structure Interactions*. Cambridge University Press, 1998.

[176] M. Howe, *Theory of vortex sound*. Cambridge University Press, 2003.

[177] J. Cissoni, K. Nozaki, A. Van Hirtum, and S. Wada, "A Parametrised Geometric Model of the Oral Tract for Aero Acoustic Simulations of Fricatives," *International Journal of Information and Electronics Engineering*, vol. 1, no. 3, pp. 223–228, 2011.

[178] D. Violato and F. Scarano, "Three-Dimensional Vortex Analysis and Aeroacoustic Source Characterization of Jet Core Breakdown," *Physics of Fluids*, vol. 25, no. 015112, 2013.

[179] I. Proudman, "The Generation of Noise by Isotropic Turbulence," *Proceedings of the Royal Society*, vol. A214:119, 1952.

[180] S. Sarkar and M. Hussaini, "Computation of the Sound Generated by Isotropic Turbulence, Contract Report 93-74," tech. rep., NASA, 1993.

[181] P. Croaker, A. Skvortsov, and N. Kessessoglou, "A Simple Approach to Estimate Flow-Induced Noise from Steady State CFD Data," *Paper Number 54, Proceedings of ACOUSTICS 2011*, 2011.

[182] J. Gill, X. Zhang, P. Joseph, and T. Node-Langlois, "Symmetric Airfoil Geometry Effects on Leading Edge Noise," *Journal of the Acoustical Society of America*, vol. 134, no. 4, pp. 2669–2680, 2013.

[183] R. Hixon, "Prefactored Small-Stencil Compact Schemes," *Journal of Computational Physics*, vol. 165, pp. 522–541, 2000.

[184] F. Hu, M. Hussaini, and J. Manthey, "Low-Dissipation and Low-Dispersion Runge-Kutta Schemes for Computational Acoustics," *Journal of Computational Physics*, vol. 124, pp. 177–191, 1996.

[185] M. Visbal and D. Gaitonde, "High-Order Accurate Methods for Unsteady Vortical Flows on Curvilinear Meshes," *AIAA Paper 98-0131*, 1998.

[186] B. Wasistho, B. Guerts, and J. Kuerten, "Simulation Techniques for Spatially Evolving Instabilities in Compressible Flow over a Flat Plate," *Journal of Computers and Fluids*, vol. 7, pp. 713–739, 1997.

[187] K. Stuben, "A Review of Algebraic Multigrid," *Journal of Computational and Applied Mechanics*, vol. 128, pp. 281–309, 2001.

[188] T. Poinsot and S. Lele, "Boundary Conditions for Direct Simulations of Compressible Viscous Reacting Flows," *Journal of Computational Physics*, vol. 101, pp. 103–129, 1992.

[189] A. Moitra, "Automated CFD Analysis of Two-Dimensional High Lift Flows," *Journal of Wind Engineering and Industrial Aerodynamics*, vol. 39, no. 4, pp. 662–667, 2002.

[190] P. Spalart, "Trends in Turbulence Treatments," *AIAA Paper 2000-2306*, 2000.

[191] Pointwise-Inc, "Gridgen user manual version 15." `http://www.pointwise.com`, 2003. [Online; accessed 16-Oct-2014].

[192] F. Tao, X. Zhang, P. Joseph, O. Stalnov, M. Siercke, and H. Scheel, "Experimental study of the mechanisms of sound generation due to an in-duct orifice plate," *AIAA Paper 2015-2231*, 2015.

[193] A. Keating, U. Piomelli, E. Balaras, and H. Kaltenbach, "a Priori and a Posteriori Tests of Inflow Conditions for Large-Eddy Simulation," *Physics of Fluids*, vol. 16, pp. 4696–4712, 2004.

[194] P. Batten, U. Goldberg, and S. Chakravarthy, "Interfacing Statistical Turbulence Closures with Large-Eddy Simulation," *AIAA Journal*, vol. 42, pp. 485–492, 2004.

[195] F. Menter, "Zonal Two Equation k-ω Turbulence Models for Aerodynamic Flows," *AIAA Paper 93-2906*, 1993.

[196] C. Schram, J. Anthoine, and A. Hirschberg, "Calculation of Sound Scattering Using Curle's Analogy for Non-Compact Bodies," *AIAA Paper 2005-2836*, 2005.

[197] R. Issa, "Solution of the Implicitly Discretized Fluid Flow Equations by Operator-Splitting," *Journal of Computational Physics*, vol. 62, pp. 40–65, 1986.

[198] J. Van Doormall and G. Raithby, "Enhancements of the SIMPLE Method for Predicting Incompressible Fluid Flows," *Numerical Heat Transfer Applications*, vol. 7, pp. 147–163, 1984.

[199] H. Versteeg and W. Malalasekera, *An Introduction to Computational Fluid Dynamics - Second Edition*. Prentice Hall, 2007.

[200] B. Tester and C. Morfey, "Developments in Jet Noise Modelling-Theoretical Predictions and Comparisons with Measured Data," *Journal of Sound and Vibration*, vol. 46, no. 1, pp. 79–103, 1976.

[201] S. Koh, G. Geiser, and W. Schroder, "Reformulation of Acoustic Entropy Source Terms," *AIAA Paper 2011-2927*, 2011.

[202] G. Muller and M. Moser, *Handbook of Engineering Acoustics*. Springer Science and Business Media, 2012.

[203] A. Khavaran, "Influence of Mean-Density Gradient on Small-Scale Turbulence Noise," *AIAA Paper 2000-2059*, 2000.

[204] Y. Moon, Y. Bae, and M. Cho, "Numerical Investigation of the Aerodynamic Noise from a Forward-Facing Step," *ECCOMAS CFD*, 2006.

[205] Y. Han, W. George, and J. Hjarne, "Effect of a Contraction on Turbulence. Part 1: Experiment," *AIAA Paper 2005-1119*, 2005.

[206] OpenFOAM Foundation, "User guide." `http://www.openfoam.com`, 2013. [Online; accessed 13-Oct-2014].

[207] Tecplot, Inc, "User guide, release 1." `http://www.tecplot.com`, 2013. [Online; accessed 07-June-2015].

[208] J. Jin, *The Finite Element Method in Electromagnetics*. Wiley, 2nd Edition, 2002.

[209] C. Bailly and D. Juve, "Numerical Solution of Acoustic Propagation Problems Using Linearised Euler Equations," *AIAA Journal*, vol. 38, no. 1, pp. 22–29, 2000.

[210] S. Maciel and B. Carmo, "Development of High-Order Computational Tool to Solving Acoustic Propagation Problems," *Proceedings of COBEM 2013, ISSN 2176-5480*, 2013.

[211] I. Celik, U. Ghia, P. Roache, C. Freitas, H. Coleman, and P. Raad, "Procedure for Estimation and Reporting of Uncertainty Due to Discretization in CFD Applications," *Journal of Fluids Engineering*, vol. 130, no. 7, p. 078001, 2008.

Appendix A

Single Orifice Grid Independent Study

A.1 Introduction

A number of sources of error exist in a numerical simulation. Some of these are related to factors beyond the control of the engineer, such as the rounding errors from the precision of the computer and modelling errors arising from the small approximations introduced by the governing equations. However, the single largest source of error in most simulations is in the discretisation of the equations and the flow variables. This error arises from the spatial resolution of the mesh, the temporal resolution from the timestep and the numerical schemes used to solve the problem. Therefore, due to the fixed second order accuracy provided by the spatial and temporal discretisation schemes, and the temporal resolution (as discussed in Section 5.3), the emphasis of this grid study is placed on ensuring that the spatial resolution is suitable. As a final note, a grid convergence study has been performed for the propagation cases in Section 6.2.2, so only the DES studies on the sound generation will be considered here.

A.2 Methodology

The error estimation procedure used here is based on that of Celik *et al.* [211]. The method involves using the cell volumes to define a representative grid size for a three-dimensional problem. Three different grids are then constructed and simulations performed using the same initial and boundary conditions to determine key variables for the problem of interest. The grid refinement factors are defined as $\vartheta_{21} = h_2/h_1$ and $\vartheta_{32} = h_3/h_2$, where h_1, h_2 and h_3 are the representative grid sizes for the coarse, medium and fine meshes, respectively. These refinement factors are recommended to be at least 1.3.

The apparent order of the method, O, can be calculated using the expression:

$$O = \frac{1}{\ln(\vartheta_{21})}\Big|\ln|\xi_{32}/\xi_{21}| + \ln\Big(\frac{\vartheta_{21}^{O} - s}{\vartheta_{32}^{O} - s}\Big)\Big|, \tag{A.1}$$

where $s = 1 \cdot \text{sign}(\xi_{32}/\xi_{21})$, $\xi_{32} = \Phi_3 - \Phi_2$ and $\xi_{21} = \Phi_2 - \Phi_1$, where Φ_k denotes the solution variable on the kth grid. The second term above cancels if the grid refinement factors are constant (ϑ_{32}=ϑ_{21}). The above equation is solved using fixed point iteration, with an initial guess taken as equal to the first term. The values of the extrapolated correct solution can be calculated from:

$$\Phi_{ext}^{21} = (\vartheta_{21}^{O}\Phi_1 - \Phi_2)/(\vartheta_{21}^{O} - 1), \tag{A.2}$$

where the same follows for Φ_{ext}^{32}. The method produces three error estimates in addition to the apparent order O;

The approximate relative error:

$$e_a^{21} = \Big|\frac{\Phi_1 - \Phi_2}{\Phi_1}\Big|, \tag{A.3}$$

the extrapolated relative error:

$$e_{ext}^{21} = \Big|\frac{\Phi_{ext}^{12} - \Phi_1}{\Phi_{ext}^{12}}\Big| \tag{A.4}$$

and the fine-grid convergence index:

$$\text{GCI}_{fine}^{21} = \frac{1.25e_a^{21}}{\vartheta_{21}^{O} - 1} \tag{A.5}$$

A.3 Mesh convergence

For this mesh convergence study, three meshes have been created for the isolated d=65mm orifice case; One providing a theoretical mesh cut off of 3.33kHz in the region of interest (4.8 million cells), the second providing a theoretical mesh cut off frequency of 5kHz in the region of interest (9.8 million cells) and the third providing a theoretical mesh cut off frequency of 8.5kHz (19.9 million cells). The mesh topology and domain size for all three is the same as that described in Section 5.3. The refinement factor used between the meshes is constant at 1.27, which whilst slightly below the recommended value, it should be noted that the mesh outside the region of interest was not refined between meshes and the chosen mesh sizes also provided a 'nice' set of values in terms of the theoretical mesh cut-off frequency.

Details of the calculation of the discretisation error can be found in Table A.1. The two most important convergence variables have been chosen which are the pressure drop

through the orifice and the orifice jet reattachment location. Details of the measurements locations and methods are described in Sections 5.4.1.1 and 5.4.2, respectively.

	Φ=normalised pressure drop (C_D)	Φ=normalised reattachment length
N_1, N_2, N_3 (million)	4.8, 9.8, 19.9	4.8, 9.8, 19.9
ϑ_{21}	1.27	1.27
ϑ_{32}	1.27	1.27
Φ_1	432.7	$2.19D$
Φ_2	427.8	$2.31D$
Φ_3	415.7	$2.61D$
O	3.80	3.83
Φ_{ext}^{21}	436.01	$2.11D$
e_a^{21}	1.13%	5.48%
e_{ext}^{21}	0.76%	3.79%
GCI_{fine}^{21}	0.96%	4.57%

Table A.1: Calculations of the variables used in the error estimation for the normalised pressure drop and the normalised reattachment point.

Overall, as discussed in Section 5.4.1.1, the experimental comparison for the pressure drop and reattachment location is poor. The mesh refinement has made a small difference to both of the quantities, although the extrapolated values suggest that even with infinite mesh refinement, the solution would converge to values approximately 9.8% and 11.1%, respectively, over the experimental data. Therefore, these results suggest that another factor besides mesh density, such as turbulence model and inflow conditions, is responsible for the majority of the discrepancy. However, the resulting errors of less than 4% for both cases indicate that the discretisation error is at low levels and gives further confidence in the results, in addition to the extensive experimental validation conducted in Chapter 5.

Alongside the data presented in Table A.1, additional comparisons of the mean velocity and turbulence intensity, at a spanwise slice of x=1D downstream of the orifice, and the wall pressure spectra, at a location of x=12D, are shown in Figures A.1 and A.2, respectively.

Neither the mean velocity nor the turbulence intensity shows a significant difference between the profiles for the three mesh refinement levels. The 'Fine' mesh is less well averaged in both cases due to the large increase in cost leading to a shorter averaging period. Overall, it appears that the mesh resolution does little to improve the problem of the over prediction of turbulence intensity within the recirculation regions.

The wall pressure spectra, which is a crucial quantity to this research, is presented in Figure A.2 and shows the spectra at x=12D for the three mesh refinement levels with comparison to the experimental data with no ring present for a d=65mm orifice. The results show a significant improvement between the coarse and medium meshes but a much less noticeable change from the medium to fine mesh. This suggests that for the wall pressure spectra, using the current simulation methodology, there is little to be

gained from mesh improvements alone, although coupling a redesign with improvements to the numerical schemes and initial conditions may provide larger benefits.

In conclusion, it is believed that the current mesh design and refinement levels provide sufficiently accurate results for studying the effects of incoming turbulence on a single orifice. The results may be improved by further mesh refinements, however, these must always be balanced against the increase in computational costs that these improvements lead to. For that reason, the meshes designed for the orifice and ring configurations will use a mesh refinement equivalent to the 'Medium' meshes presented here, giving a maximum resolution of 5kHz.

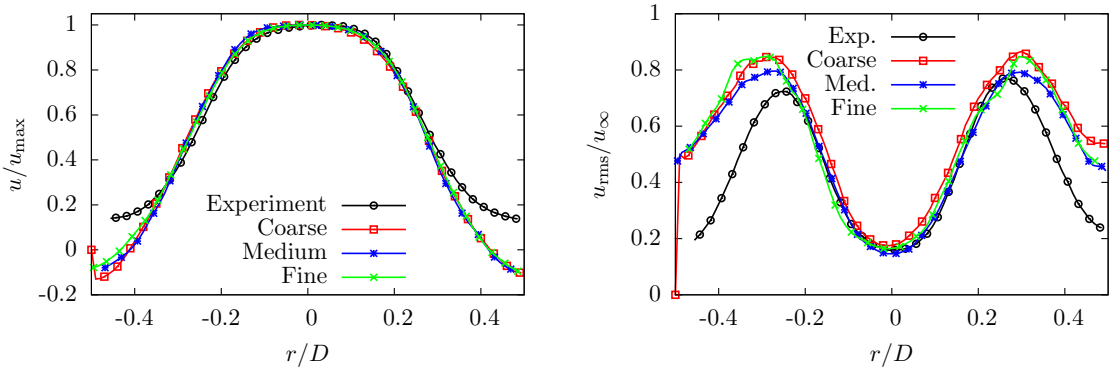

(a) Mean velocity

(b) Turbulence intensity

Figure A.1: Comparison of the mean velocity and turbulence intensity at a spanwise slice of x=1D downstream of a single orifice with no ring present, for three different mesh refinement levels.

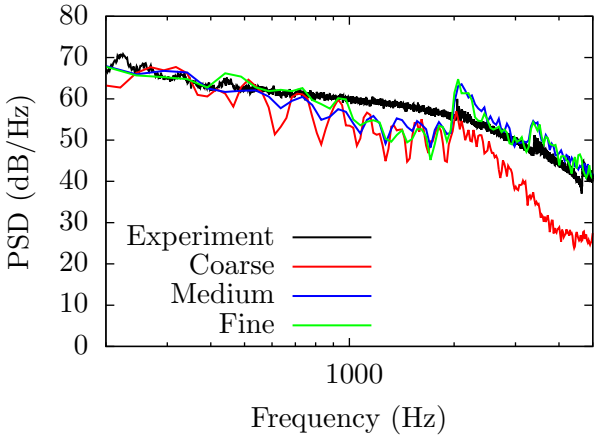

Figure A.2: Comparison of the wall pressure spectra at a steamwise distance of x=12D downstream from the orifice for three different mesh refinement levels.